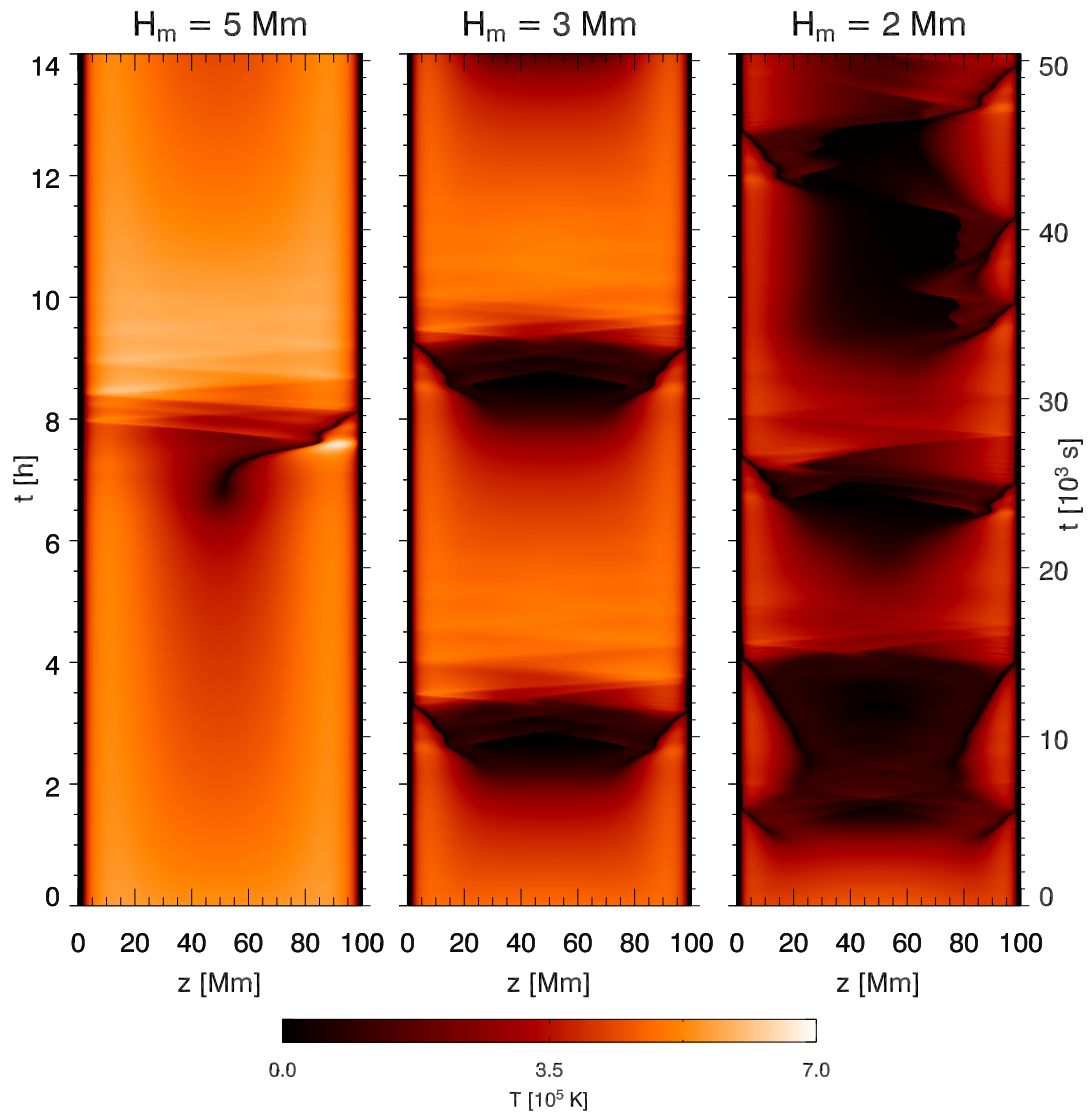


Catastrophic Cooling in Solar Coronal Loops

Thermal Instability as a Road to Complex Evolution



Daniel Müller

The cover illustration shows space-time plots of the modeled temperature distribution along a magnetic loop in the solar corona. The damping length, H_m , of the energy dissipation in the loop controls the onset of thermal instabilities. Regions of cool, dense plasma result from these catastrophic cooling events and propagate towards the footpoints of the loop, seen as dark lanes in the temperature plots. The left and right footpoints of the loop are located at $z = 0$ Mm and $z = 100$ Mm, respectively.

Dissertation zur Erlangung des Doktorgrades der Fakultät für Mathematik
und Physik der Albert-Ludwigs-Universität
Freiburg im Breisgau

Catastrophic Cooling in Solar Coronal Loops

Thermal Instability as a Road to Complex Evolution

Daniel Müller

Kiepenheuer Institute for Solar Physics, Freiburg &
Institute of Theoretical Astrophysics, Oslo
October 2004

Dekan:	Prof. Dr. J. Honerkamp
Referent:	PD Dr. H. Peter
Korreferent:	Prof. Dr. V. H. Hansteen
Datum der mündlichen Prüfung:	20.12.2004

In the context of this thesis the following articles have been/will be published:

Papers in Refereed Journals

- I. D.A.N. Müller, V.H. Hansteen & H. Peter,
Dynamics of Solar Coronal Loops:
I. Condensation in Cool Loops and its Effect on Transition Region Lines,
Astronomy & Astrophysics 411, 605–613 (2003)
- II. D.A.N. Müller, H. Peter & V.H. Hansteen
Dynamics of Solar Coronal Loops:
II. Catastrophic Cooling and High-Speed Downflows,
Astronomy & Astrophysics 424, 289–300, (2004)
- III. D.A.N. Müller, A. De Groof, V.H. Hansteen & H. Peter,
High-Speed Coronal Rain
Astronomy & Astrophysics, submitted (2004)
- IV. D.A.N. Müller, H. Peter & V.H. Hansteen,
Coronal Loops out of Equilibrium: Paths Towards Instability
Astronomy & Astrophysics, in preparation (2004)

Conference Proceedings

- I. D.A.N. Müller, H. Peter & V.H. Hansteen,
Condensation in Cool Coronal Loops and its Effect on Transition Region Lines,
Astronomische Nachrichten 324/3, 108 (2003)
- II. D.A.N. Müller, V.H. Hansteen & H. Peter,
Dynamics of Coronal Loops: “Catastrophic Cooling” and High-Speed Downflows,
Astronomische Nachrichten 324/3, 13 (2003)
- III. D.A.N. Müller, V.H. Hansteen & H. Peter,
Plasma Condensation in Coronal Loops: I. Basic Processes,
in: *Proceedings of the SOHO-13 Workshop*, ESA SP-547, 285–290 (2004)
- IV. D.A.N. Müller, H. Peter & V.H. Hansteen,
Plasma Condensation in Coronal Loops: II. “Catastrophic Cooling” and High-Speed Downflows, in: *Proceedings of the SOHO-13 Workshop*, ESA SP-547, 199–204 (2004)
- V. D.A.N. Müller, H. Peter & V.H. Hansteen,
Catastrophic Cooling and High-Speed Downflows in Solar Coronal Loops,
in: *Stars as Suns: Activity, Evolution and Planets*, Eds. A.K. Dupree & A.O. Benz, Astr. Soc. Pacific, ASP, ISBN 1-58381-163-X (2004)

- VI. A. De Groof, D.A.N. Müller, D. Berghmans, & S. Poedts,
Downflows of Cool Plasma in Coronal Loops: Observations and Modeling
in: *Physicalia Magazine*, *in press* (2004)
- VII. D.A.N. Müller, A. De Groof, V.H. Hansteen & H. Peter,
Thermal Non-Equilibrium in Coronal Loops: A Road to Complex Evolution,
in: *Multi-Wavelength Investigations of Solar Activity*, Eds. A.V. Stepanov,
E.E. Benevolenskaya, A.G. Kosovichev, Cambridge University Press, *in press* (2005)
- VIII. A. De Groof, D.A.N. Müller, D. Berghmans, & S. Poedts,
Downflows of Cool Plasma in Coronal Loops: Observations and Modeling
in: *Multi-Wavelength Investigations of Solar Activity*, Eds. A.V. Stepanov,
E.E. Benevolenskaya, A.G. Kosovichev, Cambridge University Press, *in press* (2005)
- IX. D.A.N. Müller, A. De Groof, V.H. Hansteen & H. Peter,
Thermal Instability as the Origin of High-Speed Coronal Rain,
in: *Proceedings of the SOHO-15 Workshop*, ESA SP-575, *in press* (2005)

Contents

Abstract	1
1 Introduction	5
1.1 The Solar Atmosphere	5
1.1.1 The Radiative Core and the Convection Zone	5
1.1.2 The Photosphere	5
1.1.3 The Chromosphere	8
1.1.4 The Transition Region	9
1.1.5 The Corona	10
1.1.6 The Solar Wind	12
1.2 Magnetic Loops in the Solar Corona	12
1.2.1 Theoretical Concept	12
1.2.2 Observations of Coronal Loops	13
1.2.3 Loop Models	15
1.3 Motivation and Scope of this Work	17
2 Model Equations and their Solution	19
2.1 Model Equations	19
2.2 Implicit Integration Methods	20
2.2.1 Implicit Integration of First-Order Partial Differential Equations	20
2.3 Conservative Methods	21
2.4 Upwind Schemes	21
2.5 Staggered Grid	23
2.6 Boundary Conditions	24
2.7 Conservation Laws on an Adaptive Mesh	25
2.7.1 Examples	26
2.8 Implementation of an Adaptive Grid	27
2.9 Solving the Model Equations	29
3 Emission Line Spectroscopy	33
3.1 Atomic Processes	33
3.1.1 Important Atomic Processes in the Transition Region and Corona	34
3.2 Formation of Optically-Thin Emission Lines	35
3.2.1 Excitation and Deexcitation	36
3.2.2 The Two-Level Atom Approximation	38
3.2.3 Ionization	39

3.2.4	Atomic Data	39
3.2.5	The Spectral Line Profile	39
4	Plasma Condensation in Cool Loops and its Effect on Transition Region Lines	41
4.1	Introduction	41
4.2	Loop Heating	43
4.3	Results: Condensation due to Thermal Instability	43
4.3.1	Initial State	43
4.3.2	Loop Evolution	44
4.3.3	Energy Balance Analysis	46
4.3.4	The Role of the Damping Length	46
4.3.5	Limit Cycle of Loop Evolution	51
4.3.6	Remarks on Rayleigh-Taylor Instability	52
4.3.7	Spectral Signature of Condensation in Transition Region Lines	53
4.4	Discussion	53
5	Catastrophic Cooling and High-Speed Downflows	57
5.1	Introduction	57
5.1.1	Loop Heating	58
5.1.2	Initial State	58
5.2	Plasma Condensation due to Thermal Instability	60
5.3	Results	62
5.3.1	Different Types of Loop Evolution	62
5.3.2	Classification of Loop Evolution	65
5.3.3	Where in a Coronal Loop do Condensation Regions Form?	65
5.3.4	Formation of a Shock Front	68
5.3.5	Velocity Profiles and Acceleration of the Condensation Region	68
5.3.6	Spectral Signature of Catastrophic Cooling and Downflows	71
5.4	Comparison to Observations and Discussion	75
5.5	Summary	78
6	High-Speed Coronal Rain	79
6.1	Introduction	79
6.1.1	Loop Heating	80
6.1.2	Initial State	80
6.2	Effect of the Damping Length on the Loop Evolution	80
6.2.1	Recurrent Condensations in Long Loops	80
6.2.2	Slow and Fast Blobs	83
6.2.3	Formation of the Second Condensation Region	83
6.3	Comparison with Observations	87
6.4	Spectral Signature of Fast Downflows	90
6.4.1	Footpoint Brightening	91
6.5	Summary	92
7	Coronal Loops as Non-Linear Systems	95

8 Families of Loops: A Parameter Study	99
8.1 Introduction and Setup	99
8.2 Classes of Solutions and Periods	100
8.3 Temperature and Density Variations	102
8.4 Overheated Loops	106
8.5 Comparison with Hydrostatic Models	108
8.6 Plots of Loop-Averaged Variables	109
8.6.1 Time Evolution of Mean Temperature	110
8.6.2 Pressure-Temperature Diagrams	115
9 Recent Multi-Wavelength Observations of Coronal Loops	121
10 Discussion & Outlook	127
A Appendix	131
A.1 Effect of Atomic Composition on Instabilities in Shock Waves	131
A.2 Further Data From the Parameter Study	132
A.2.1 Time Evolution of Mean Electron Density	132
A.2.2 Time Evolution of Mean Pressure	137
A.3 List of Physical Constants	142
Bibliography	143
Acknowledgments	149

Abstract

Satellite observations with high spatial and temporal resolution have revealed the highly dynamic nature of the solar corona and enabled us to study physical processes in the outer atmosphere of our mother star in great detail. This thesis deals with dynamic processes in coronal loops, i.e. magnetic structures which may be thought of as the elementary building blocks of the solar corona. Using computational fluid dynamics as a tool, I calculate time-dependent models of solar coronal loops in order to address the following questions: Are dynamic processes in coronal loops, such as flows and transient brightenings, necessarily the result of a time-dependent driving mechanism? Can various observations of fast downflows be explained by a common mechanism? Which parameters determine the dynamics of coronal loops?

It is found that coronal loops which are predominantly heated around their footpoints can develop a thermal instability in the upper part of the loop. This instability results in a self-amplifying “catastrophic cooling” process and leads to the formation of dense, cool plasma condensations. The first part of the work focuses on plasma condensations in short cool loops, which presumably constitute the solar transition region, and describes how the catastrophic cooling process leads to transient brightenings in spectral lines formed in the transition region. In the second part of the work, the model is extended to larger coronal loops, and the conclusion is reached that the damping length of the energy dissipation acts as a control parameter of this non-linear system. While a long damping length results in stable, static loops, damping lengths below a critical value give rise to a dynamic evolution. The dynamic evolution can be understood on the basis of an evaporation-condensation cycle: Plasma is first evaporated by coronal heating from the cool and dense chromosphere into the corona, then condenses in the coronal part of the loop as a result of thermal instability, drains towards the footpoints of the loop and finally evaporates again. When applying the catastrophic cooling scenario to long active region loops, I find that the draining process is accompanied by fast downflows which can reach flow speeds of up to several 100 km/s. Also the proper motions of the dense plasma blobs themselves are of the order of 100 km/s, which offers an explanation for the recent observations of moving bright blobs in coronal loops.

In contrast to earlier models it is suggested that the process of catastrophic cooling does not have to be initiated by a drastic decrease of the total loop heating but rather results from a loss of equilibrium at the loop apex as a natural consequence of footpoint-centered heating which can be constant in time. To obtain a broader picture, a parameter study is carried out which describes the evolution of coronal loops as a function of different lengths, heating rates and damping lengths. A connection between the thermal instability in coronal loops and global relaxation oscillations of stellar coronae is pointed out.

Zusammenfassung

Satellitenbeobachtungen mit hoher räumlicher und zeitlicher Auflösung zeigen die dynamische Natur der Sonnenkorona und ermöglichen uns, physikalische Prozesse in der äußeren Atmosphäre der Sonne mit großer Genauigkeit zu untersuchen. Die vorliegende Arbeit beschäftigt sich mit dynamischen Prozessen in koronalen Bögen, d.h. magnetischen Strukturen, die einen wichtigen Bestandteil der Sonnenkorona bilden. Zeitabhängige numerische Modelle koronaler Bögen werden berechnet, um die folgenden Fragen zu beantworten: Verlangen dynamische Prozesse in koronalen Bögen, wie z.B. Strömungen und kurzzeitige Helligkeitsvariationen, notwendigerweise nach einem externen Antriebsmechanismus? Können unterschiedliche Beobachtungen von schnellen Abströmungen in koronalen Bögen mit einem einzigen Mechanismus erklärt werden? Welche Parameter bestimmen die Dynamik koronaler Bögen?

Es zeigt sich, dass koronale Bögen, die vorwiegend in der Nähe der Fußpunkte geheizt werden (worauf sowohl Beobachtungen als auch theoretische Überlegungen hindeuten) eine thermische Instabilität im oberen Teil des Bogens entwickeln können. Diese Instabilität hat einen selbstverstärkenden Kühlungsprozess („catastrophic cooling“) zur Folge, der zur Bildung dichter, kühler Plasmakondensationen führt. Der erste Teil dieser Arbeit beschäftigt sich mit Plasmakondensationen in kleinen magnetischen Bögen relativ niedriger Temperatur, aus denen sich vermutlich die solare Übergangsregion zusammensetzt, und beschreibt, wie der drastische Kühlungsprozess zu starken Helligkeitsvariationen in Spektrallinien der Übergangsregion führt. Im zweiten Teil der Arbeit werden Modelle für längere koronale Bögen vorgestellt, die zeigen, dass die Dämpfungslänge der Energiedissipation im Bogen einen Kontrollparameter dieses nichtlinearen Systems darstellt. Während eine große Dämpfungslänge stabile, statische Bögen liefert, führen Dämpfungslängen unterhalb einer kritischen Schwelle zu einer dynamischen Entwicklung. Diese kann auf der Basis eines Evaporations-Kondensations-Zyklus verstanden werden: Plasma wird zuerst durch einen koronalen Heizungsmechanismus von der kühlen, dichten Chromosphäre in die Korona verdampft, kondensiert dann im koronalen Teil des Bogens in Folge thermischer Instabilität, fließt zu den Fußpunkten des Bogens ab und verdampft schließlich erneut. Eine Anwendung des „catastrophic cooling“-Modells auf lange Bögen aktiver Regionen zeigt, dass beim Abströmen des Plasmas Geschwindigkeiten von mehreren 100 km/s erreicht werden und auch die dichten Plasmawolken selbst sich mit Geschwindigkeiten von bis zu 100 km/s bewegen. Dies liefert eine Erklärung für Beobachtungen von wandernden hellen Strukturen und schnellen Abströmungen in koronalen Bögen.

Im Gegensatz zu früheren Modellen legt diese Arbeit nahe, dass der selbstverstärkende Kühlungsprozess nicht durch eine drastische Verringerung der Heizung eines koronalen Bogens angetrieben werden muss, sondern vielmehr aus einer thermischen Instabilität des Bogens resultiert. Dies ist die natürliche Konsequenz eines vorrangig im unteren Teil des Bogens wirkenden Heizungsmechanismus, der nicht zeitabhängig sein muss. Um die verschiedenen Lösungsregime zu lokalisieren, wurde eine Parameterstudie durchgeführt, die die Entwicklung koronaler Bögen in Abhängigkeit ihrer Länge, Heizungsrate und Dämpfungslänge beschreibt. Dabei wird eine Verbindung zwischen der thermischen Instabilität in koronalen Bögen und globalen Relaxationsoszillationen in stellaren Koronen aufgezeigt.

Resymé

Satellittobservasjoner med høy rom- og tidsoppløsning har avslørt solkoronaens dynamiske natur, og har gjort det mulig å studere de fysiske prosessene i solas ytre atmosfære med høy presisjon. Dette arbeidet omhandler de dynamiske prosessene i koronaløkker, d.v.s. magnetiske strukturer som er en viktig bestanddel av solkoronaen. Tidsavhengige numeriske modeller av koronaløkker beregnes for å gi svar på de følgende spørsmål: Krever dynamiske prosesser i koronaløkker, f.eks. strømnings og raske intensitetsvariasjoner, nødvendigvis en ekstern drivmekanisme? Kan forskjellige observasjoner av raske nedstrømninger i koronaløkker forklares med én eneste mekanisme? Hvilke parametere bestemmer dynamikken til koronaløkker?

Det viser seg at koronaløkker som oppvarmes i nærheten av fotpunktene kan utvikle en termisk ustabilitet i den øvre delen av løkken. Denne ustabiliteten har en selvforsterkende kjølingsprosess («catastrophic cooling») som følge, som fører til at tette, kjølige plasmakondensasjoner utvikles. Den første delen av arbeidet omhandler plasmakondensasjoner i små magnetiske løkker, som formentlig det solare transisjonslaget består av, og beskriver hvordan den dramatiske kjølingsprosessen fører til store intensitetsvariasjoner i spektrallinjer som dannes i transisjonslaget. I den andre delen av arbeidet presenteres modeller av større koronaløkker som viser at dempelengden til energidissipasjonen i løkken er en kontrollparameter i dette ikke-lineære systemet. Mens en stor dempelengde gir stabile, statiske løkker, fører dempelengder kortere enn en kritisk terskel til en dynamisk utvikling. Denne utviklingen kan forklares med en evaporasjons-kondensasjons-syklus: Plasma fordampes først på grunn av en koronal oppvarmingsmekanisme fra den kjølige, tette kromosfæren til koronaen, kondenserer i den koronale delen av løkken som følge av termisk ustabilitet, strømmer ned til fotpunktene av løkken og prosessen gjentas. En anvendelse av «catastrophic cooling»-modellen på lange løkker viser at hastigheter på flere 100 km/s oppnås ved nedstrømning av plasma og også at de tette plasmaskyene selv beveger seg med hastigheter opp til 100 km/s. Det gir en forklaring på observasjoner av små, intense strukturer som beveger seg og raske nedstrømninger i koronaløkker.

I motsetning til tidligere modeller blir det i dette arbeidet foreslått at den selvforsterkende kjølingsprosessen ikke skyldes en drastisk nedsatt oppvarming av en koronaløkke, men snarere den termiske ustabiliteten i løkken. Det er den naturlige konsekvensen av en oppvarmingsmekanisme som hovedsakelig virker i den lavere delen av en koronaløkke og som kan være tidsavhengig. For å lokalisere de forskjellige løsningsområder ble en parameterstudie gjennomført som undersøker utviklingen av koronaløkker i forhold til deres lengde, oppvarming og dempelengde. Dessuten påvises en forbindelse mellom den termiske ustabiliteten i koronaløkker og «global relaxation oscillations» av stellare koronaer.

1 Introduction

The sun is in many respects a very ordinary star of medium size, age and activity. It is classified as a star of spectral class G2 V, has a radius of $6.96 \cdot 10^8$ m, a mass of $1.99 \cdot 10^{30}$ kg and a luminosity of $3.8 \cdot 10^{26}$ W (for comparison: the earth has a radius of 6378 km and a mass of $5.97 \cdot 10^{24}$ kg.). What makes it so important to us is its relative vicinity: At a mean distance of 150 million kilometers from earth, it is around 100 000 times closer than the next neighboring star, α Centauri. It is the only star for which a reasonable attempt can be made to resolve the important physical length scales in order to understand in detail how a star works. Even more important for us is the fact that the variation of the sun's irradiance has a measurable impact on the earth's atmosphere, and a detailed understanding of the origin and manifestations of solar activity is of vital importance to assess its role regarding the earth's climate. In this respect, the variability of the ultraviolet part of the solar spectrum is of particular interest since the radiation in this wavelength range has a strong effect on thermal and chemical processes in the earth's upper atmosphere. The aim of the following section is to give a brief general introduction to the sun's atmosphere and to highlight some of its prominent features. For a thorough and detailed treatment of this subject the reader is referred to the textbook of [Stix \(2002\)](#).

1.1 The Solar Atmosphere

1.1.1 The Radiative Core and the Convection Zone

In the solar core, nuclear fusion transforms hydrogen into helium at a central temperature of $15.7 \cdot 10^6$ K. This energy is almost entirely produced within the inner 25 % of the radius, which encloses merely 1.5 % of the sun's volume. In the inner 70 % of the solar radius, energy is transported by radiation. In the outer shell, where the temperature drops from $2.2 \cdot 10^6$ K to an effective temperature of 5778 ± 3 K, energy is transported by convection. The stratification of the convection zone is superadiabatic and hence unstable. At the lower boundary of the convection zone, the convective motions "overshoot" into the stably stratified radiation zone. According to our current understanding, it is this overshoot region where dynamo processes take place which generate the sun's magnetic field. The magnetic field influences and often dominates the physical processes on all spatial scales of the sun, and manifests itself e.g. by sunspots and coronal loops. Figure 1.1 shows a cut-away view of the sun.

1.1.2 The Photosphere

Almost all radiation from the sun is emitted from the *photosphere*, a thin layer of several 100 km thickness which lies at the upper boundary of the convection zone. The photosphere exhibits a regular pattern of convection cells, the granules, of around 1000 km diameter which change on the time scale of minutes. Occasionally, the peaceful "quiet sun" is interrupted by dark sunspots.

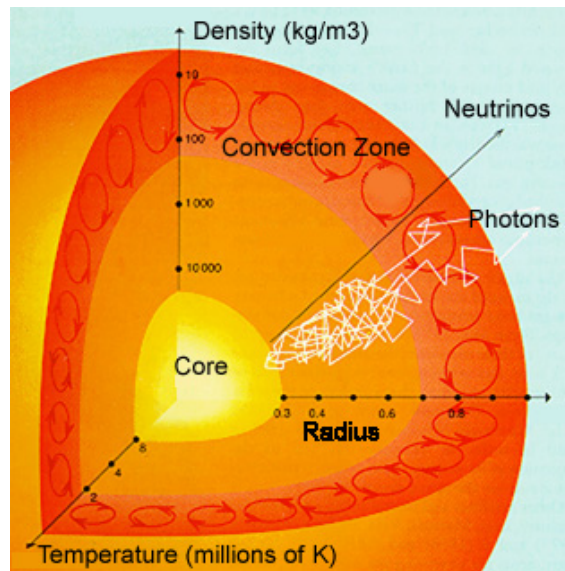


FIGURE 1.1: A cut-away view of the Sun. The tickmarks on the axes illustrate how the temperature and density vary as a function of the solar radius (Credit: UCB Science Education Gateway).

Sunspots had already been reported in the antique, and also Kepler observed a sunspot in 1607, but misinterpreted it as a transit of the planet mercury. Shortly after the invention of the telescope, [Fabricius \(1611\)](#) and [Scheiner \(1611\)](#) announced independently the “discovery” of sunspots. Almost 300 years later the astronomer G. E. Hale ([Hale 1908a,b](#)) discovered that sunspots possess strong magnetic fields. In these and also later observations ([Hale & Nicholson 1938](#)) he found that lines in the spectra of sunspots are split due to the Zeeman effect and that this effect could be used to measure magnetic field strengths. In the center of sunspots he measured field strengths of several hundred mT (i.e. several thousand Gauss)¹ which decreased to under hundred mT towards the boundary of the spots.

According to our current understanding sunspots are formed when magnetic flux concentrations rise from the bottom of the convection zone and penetrate the photosphere as magnetic loops. They appear dark because the convective energy transport is hampered by the magnetic field as the plasma is forced to move along the field lines ([Biermann 1941](#); [Alfvén 1942](#)). Figure 1.2 shows an image of a sunspot, observed in the G-band ($\lambda = 430.5 \pm 0.5$ nm). The dark central region of the spot, the *umbra*, is surrounded by the brighter *penumbra*, which has a complex filamentary structure and harbors the outward-directed Evershed flow. Further indications of strong magnetic field in the solar photosphere are the small bright points and structures in the intergranular lanes, which are particularly prominent in the G-band.

¹1 Gauss = 10^{-4} Tesla. For historical reasons, magnetic fields are commonly measured in units of Gauss in solar physics. However, in this thesis SI units will be used throughout.

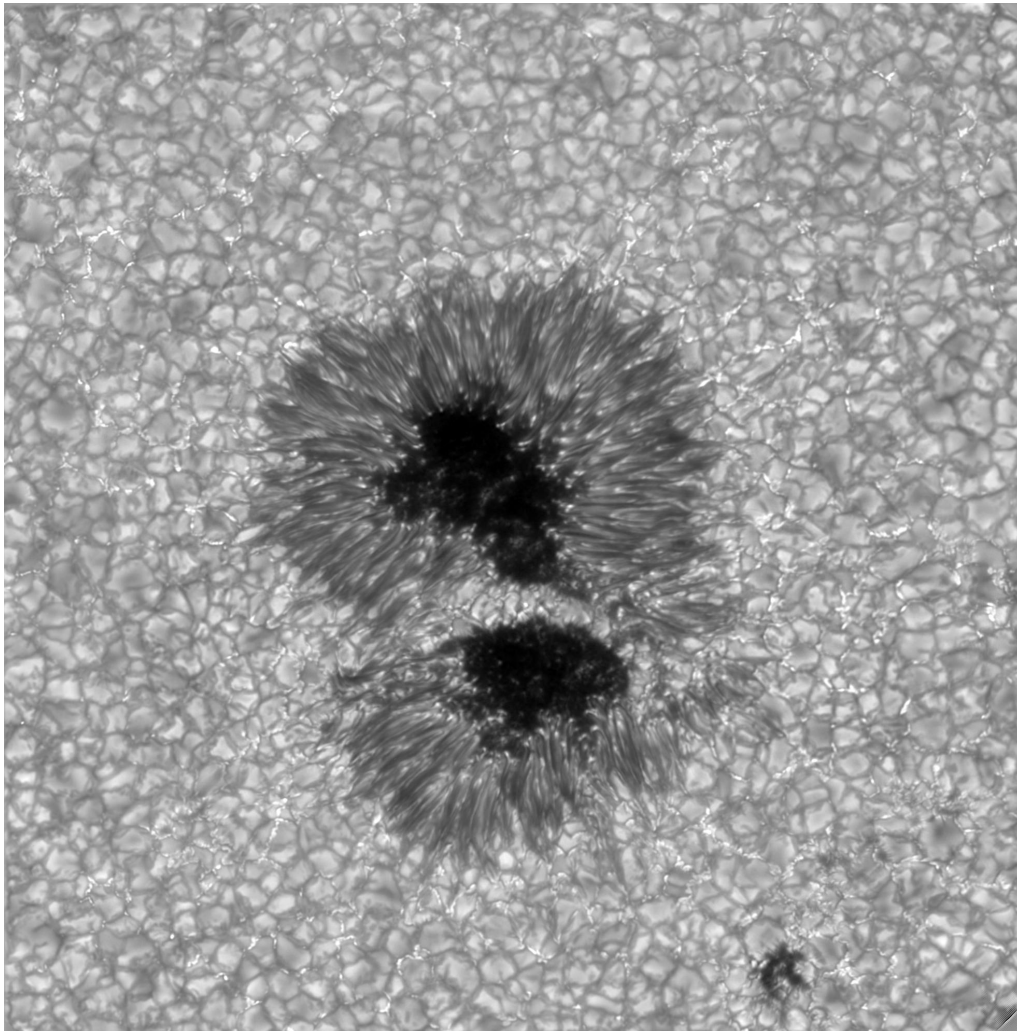


FIGURE 1.2: A sunspot, observed in the G-band ($\lambda = 430.5 \pm 0.5$ nm) with the Swedish 1-m Solar Telescope. The dark center, the umbra, is surrounded by the highly structured penumbra. A light-bridge crosses the lower part of the spot. The area surrounding the spot is covered with convection cells, the solar granulation. Bright points and structures of presumably magnetic origin are seen in the intergranular lanes. Image scale: $80''8 \times 81''6$, corresponding to $\approx 58\,000$ km \times $59\,000$ km (approximately 0.2 % of the solar disk). The earth would easily fit into the sunspot. Courtesy of L. Rouppe van der Voort.

1.1.3 The Chromosphere

Going upwards in the solar atmosphere, the photosphere connects to the *chromosphere*, which has a mean thickness of 1000 – 2000 km and a temperature of 4 000 – 25 000 K. It bears its name (*chromosphere*: the “colored sphere”) due to the colorful appearance of the solar limb shortly before and after a total solar eclipse, which originates from the red hydrogen Balmer- α line, often referred to as H_α , at $\lambda = 656.3$ nm. In the so-called *flash spectrum* strong spectral lines which are usually seen in absorption in the solar spectrum on the disk appear in emission above the limb. Figure 1.3 shows an image of an active solar region, observed in the H_α line. This image shows that the solar chromosphere is already much more structured by the magnetic field than the photosphere. Movies recorded in this spectral line show that the solar plasma is in constant motion along thin filamentary paths which outline the magnetic field. In the upper left of the image a sunspot with a bright light-bridge and an extended superpenumbra is seen, and thin structures connect this region to another sunspot seen in the lower right. The lower part of the image shows a filament in absorption as a thin dark structure.

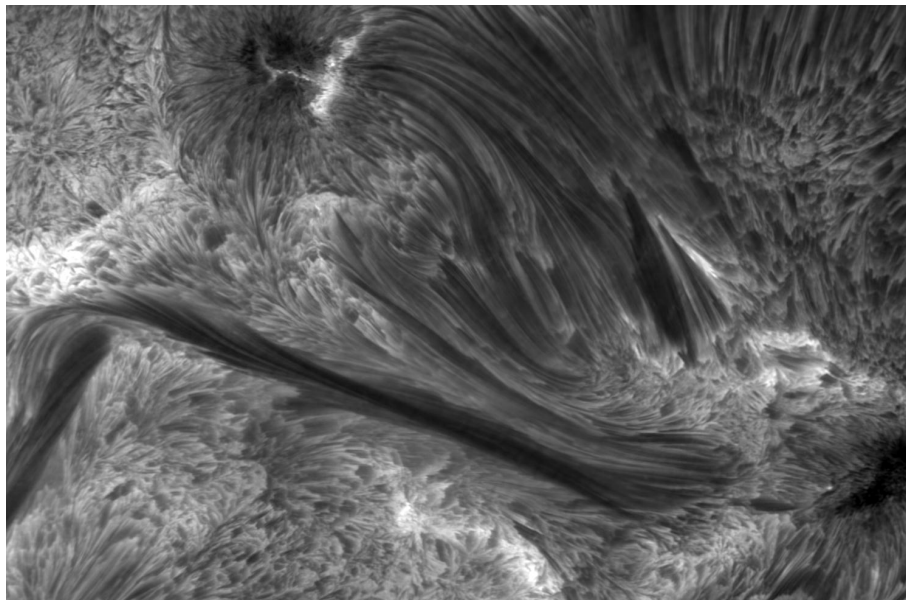


FIGURE 1.3: An active solar region, observed in the hydrogen Balmer- α line ($\lambda = 656.3$ nm) with the Swedish 1-m Solar Telescope. In the upper left a sunspot with a bright light-bridge and an extended superpenumbra is seen. The lower part of the image shows a filament in absorption as a thin dark structure. Image scale: $95''.6 \times 63''.0$, corresponding to $\approx 69\,000$ km \times $45\,000$ km. Courtesy of L. Rouppe van der Voort.

The highly dynamic nature of the chromosphere cannot be adequately described by simple stratified atmospheric models. Carlsson & Stein (1995) proposed that the observed enhanced chromospheric emission, which is usually attributed to a temperature rise in the chromosphere, may be the result of propagating waves without any increase in the mean gas temperature. They showed that the radiation temperature represents predominantly the peaks in the gas temperature rather than its mean temperature and concluded that the sun may not have a classical chromosphere in

the magnetic field-free internetwork regions at all.

1.1.4 The Transition Region

Above the chromosphere, a thin transition region is found. In this transition region, which should be thought of as a temperature regime rather than a geometric layer, the temperature rises rapidly from around 25 000 K to around 10^6 K. The transition region thus links the lower atmospheric layers to the solar corona, where the temperature amounts to several 10^6 K and can be as high as 10^7 K. While the convection zone and partly also the solar photosphere are dominated by flows which are capable of moving regions of strong magnetic flux around, the solar transition region and corona are dominated by the magnetic field which forces the plasma to move predominantly along field lines.

The emission from this temperature regime is governed by spectral lines in the extreme ultraviolet (EUV) range of the solar spectrum. These emission lines originate from various ions at different temperatures and are thus well suited to probe the structure and dynamics of the transition region. Figure 1.4 shows the temperature and density stratification in the solar atmosphere after the semi-empirical one-dimensional model of Vernazza et al. (1981). The approximate formation temperature of several prominent transition region and low coronal lines are indicated by shaded circles, with wavelengths given in Ångström.² The shaded box indicates the source region of the EUV continuum in the low corona.

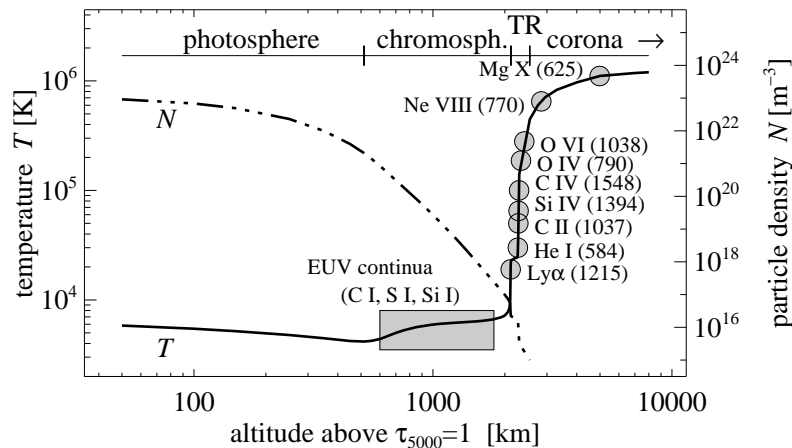


FIGURE 1.4: Temperature and density stratification in the solar atmosphere after the semi-empirical one-dimensional model of Vernazza et al. (1981). The approximate formation temperature of several prominent transition region and low coronal lines are indicated by shaded circles, with wavelengths given in Ångström. The shaded box indicates the source region of the EUV continuum in the low corona. Courtesy of H. Peter.

Reeves (1976) found that the chromospheric network which harbors most magnetic flux is clearly seen in lines formed in the lower transition region, but disappears gradually towards the lower corona. The model of Gabriel (1976) gave an explanation for this in terms of an expansion of photospheric magnetic flux tubes towards the corona. The model is based on the fact that the low

²1 Ångström = 0.1 nm

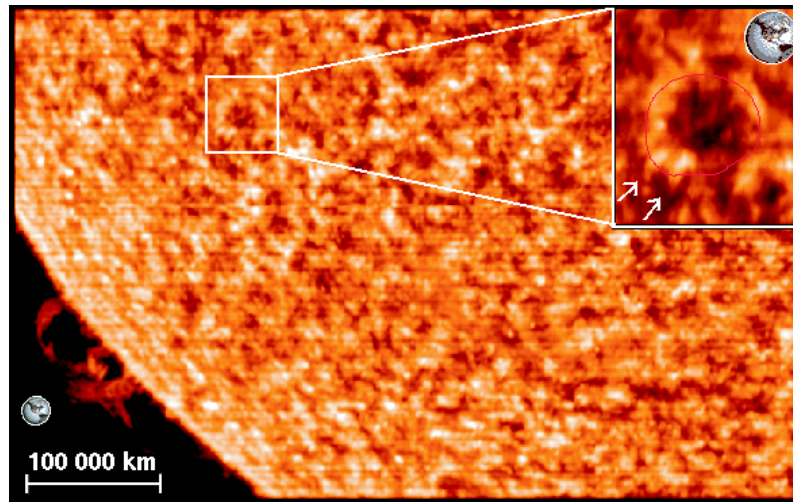


FIGURE 1.5: The chromospheric network in the spectral line of C III (97.7 nm), formed around $T = 80\,000$ K. The bright network cells have a diameter of around 20 000 km. The upper right shows a magnification of one such cell. Very small coronal loops of only several 1000 km length are seen that straddle the chromospheric network. For comparison, the earth's size is indicated (raster scan with the SUMER instrument on SOHO, courtesy of H. Peter).

gas pressure in the corona can no longer confine the magnetic flux so that it expands into so-called coronal funnels, which are rooted in the chromospheric network and then expand upwards to fill the entire corona. However, it was shown that for this model an “emission measure problem” arises, i.e. the emission from low-temperature regions (lower than around 10^5 K) is strongly underestimated by this model. For this reason, Dowdy et al. (1986) proposed a hierarchy of magnetic loops with different temperatures which could resolve this problem. Within the last years, this idea has been supported observationally by raster scans of the SUMER³ instrument on SOHO⁴ which show structures that may be interpreted as cool loops in the network (cf. Fig. 1.5).

UV observations of transition region lines often show line profiles with enhanced wings which may be interpreted as a two-component emission from a narrow bright component from coronal loops and a broader weaker component from coronal funnels (Peter 2000). This led Peter (2001) to the proposal of a multi-component transition region which is sketched in Fig. 1.6. According to this picture, the solar transition region is composed of a mixture of closed-field regions, i.e. small network loops and large loops that connect different patches of the network, and open-field regions, i.e. coronal funnels which form the base of the solar wind.

1.1.5 The Corona

The most puzzling aspect about the solar corona is its very existence. Naively, one would not assume that a star with its hot core and a temperature that is steadily decreasing towards its visible surface may be surrounded by an extremely hot outer shell of several million degrees temperature.

³SUMER is the Solar *U*ltraviolet *M*easurements of *E*mitted *R*adiation instrument onboard SOHO.

⁴SOHO: The *S*olar and *H*eliospheric *O*bservatory is a joint project of the European Space Agency, ESA, and the National Aeronautics and Space Administration, NASA.

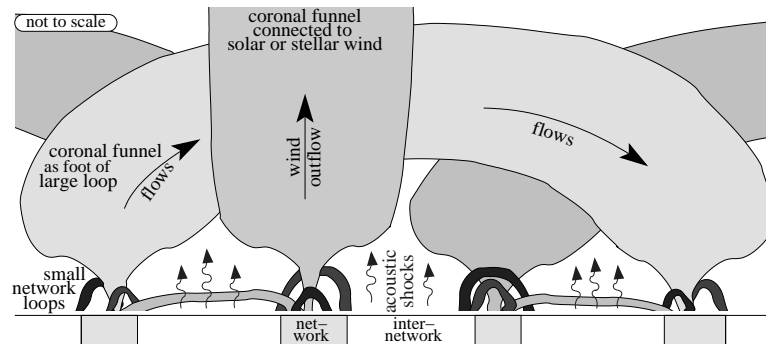


FIGURE 1.6: Sketch of the multi-component transition region. Small loops dominate the emission from the network. Coronal funnels either connect to other network elements or extend outwards to form the base of the solar wind (after Peter 2001).

It turns out that most stars harbor coronae, but a unique explanation of the processes that heat this low-density outer region of a star to such high temperatures has not been identified yet. Numerous heating mechanisms have been proposed, involving heating by different types of waves (sound waves, magneto-acoustic waves, Alfvén waves), Joule heating by dissipation of electric currents, and reconnection events such as nanoflares (Parker 1988, 1991). A very promising idea is provided by the recent numerical models of Gudiksen & Nordlund (2002) and Gudiksen (2004) who demonstrated explicitly that photospheric motions which shear the magnetic field are capable of dissipating sufficient energy to heat the corona.

Figure 1.7 shows an image of the solar corona during a total solar eclipse. The emitting plasma is structured by magnetic field lines which are predominantly radial and guide energetic particles outwards to form the solar wind. The optical coronal radiation (white-light corona) is traditionally divided into the F-corona and the K-corona. The F-corona is named after the prominent Fraunhofer lines seen in the spectrum and stems from light scattered on dust particles. The spectrum of the K-corona, on the other hand, is highly polarized and arises from Thomson scattering by free electrons. The letter “K” in K-corona stems from the German “Kontinuum”. Due to the high thermal speed of the scattering electrons, the spectral lines are smeared out to broad and shallow dips and only a continuous spectrum is seen. The nature of the corona remained mysterious for a long time. Several emission lines in the corona had been measured and could not be attributed to any known atomic transition, so that exotic explanations such as emission from a new element “coronium” were proposed. Grotian (1939) was the first who identified two coronal emission lines at 637.4 nm and 789.2 nm as forbidden transitions of Fe X and Fe XI and thereby showed that the solar corona must have a temperature of the order of a million degrees. However, it was only after Edlén (1942) had identified 19 further lines as forbidden transitions of highly ionized atoms that the high temperature of the corona was generally recognized.

Observations of the solar corona at EUV and X-ray wavelengths reveal a wealth of different structures. In general, one can distinguish between open-field regions such as coronal holes and helmet streamers, and closed-field regions, which are commonly referred to as coronal loops. These loops will be described in detail in the next section. The open-field regions form the base of the solar wind, a continuous stream of energetic particles that is accelerated outwards.

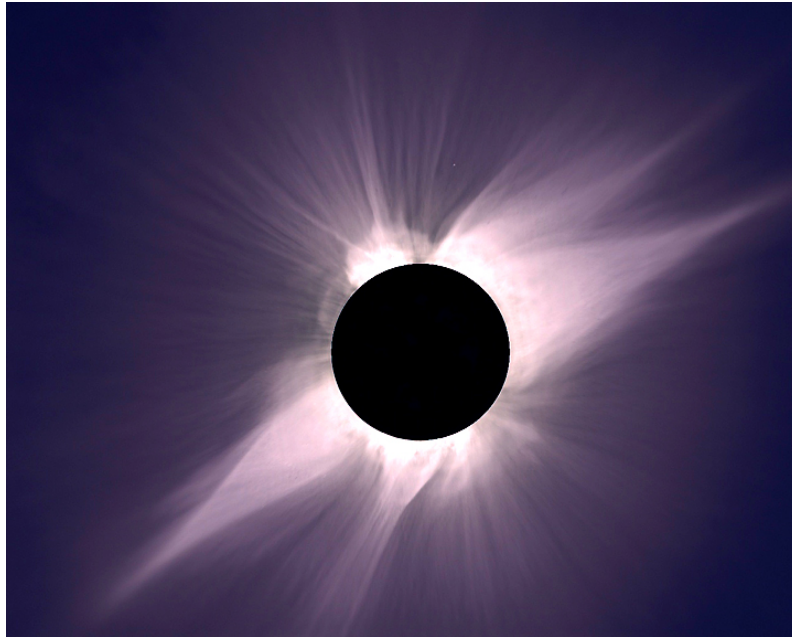


FIGURE 1.7: Image of the total solar eclipse in 1991, taken from Mauna Kea, Hawaii. As the moon masks the solar disk, the highly structured solar corona becomes visible. Around the equator of the sun, two “helmet streamers” are seen (Credit: High Altitude Observatory/ National Center for Atmospheric Research, Boulder, CO).

1.1.6 The Solar Wind

The first evidence for the solar wind was inferred from observations of the ion tails of comets. These tails point roughly in the direction opposite to the sun, but Hoffmeister (1943) noticed a small systematic difference: The ion tail is inclined by a small angle (less than 5°) with respect to the solar radius vector, trailing the direction of the comet’s motion around the sun. Biermann (1951) realized that the radiation pressure of the sun’s radiation field could not account for this deviation and proposed a corpuscular radiation instead. This could explain Hoffmeister’s discovery, and from subsequent measurements it was found that this corpuscular radiation, later named *solar wind*, was a particle stream continuously blowing outwards from the sun in all directions.

1.2 Magnetic Loops in the Solar Corona

1.2.1 Theoretical Concept

It has been seen earlier in this chapter that the solar magnetic field plays a dominant role for the structuring and organization of the plasma in the solar atmosphere. Regions of concentrated magnetic flux, so-called flux tubes, rise through the convection zone and penetrate through the photosphere, giving rise to the formation of sunspots and active regions. Such a bundle of magnetic field lines exerts a lateral magnetic pressure, $p_B = B^2/2\mu_0$, on the plasma in which it is embedded, which has to be balanced by the hydrostatic pressure (or gas pressure), p , of the sur-

rounding material. In the lower layers of the solar atmosphere, the gas pressure is high so that regions of concentrated flux are advected by the surrounding plasma flow. Going upwards in the atmosphere, however, the pressure decreases exponentially while the decrease of the magnetic field strength follows approximately a power law so that the magnetic field fans out with height until it eventually fills the whole corona.

A useful parameter to decide whether hydrodynamic or magnetic forces govern the dynamics of the plasma is the so-called plasma- β , the ratio between the hydrostatic pressure, p , and the magnetic pressure, p_B :

$$\beta = \frac{2\mu_0 p}{B^2}. \quad (1.1)$$

In this expression, $\mu_0 = 4\pi \cdot 10^{-7} \text{ V s A}^{-1} \text{ m}^{-1}$ is the magnetic permeability of the vacuum and B denotes the magnetic field strength.⁵ For $\beta \ll 1$, the magnetic forces are much larger than the gas forces so that the magnetic field dominates the dynamics of the plasma. If, on the other hand, $\beta \gg 1$, the gas forces reign over the magnetic forces and the magnetic field is advected by the plasma if there is a gas pressure gradient perpendicular to the magnetic field.

The high temperature of the upper solar atmosphere results in a large number of free electrons which give rise to a high electrical conductivity. In a similar way the electrons also provide a high thermal conductivity. If the electrical conductivity is high, the magnetic field is “frozen” in the plasma (cf. [Stix 2002](#)). Combined with the much higher efficiency of thermal conduction parallel to the magnetic field compared to perpendicular to the field, this explains why the plasma in the upper transition region and corona traces the structure of the magnetic field. While some field lines extend radially outwards and form the base of the solar wind, the major part of the field lines closes back to the solar surface to connect photospheric regions of opposite polarity. If these bundles of closed field lines are filled with plasma, they become visible through the emission of radiation, and are referred to as *coronal loops*.⁶ Coronal loops are observed to be structured down to the smallest spatial scales which can be observed with the currently available space instruments. It is therefore probable that the observed loops are composed of smaller-scale structures, which are often referred to as *strands*. The corona is filled with loops of very different sizes, ranging from small inter-network loops of several Mm length to large trans-equatorial loops which can reach lengths of several 100 Mm.

1.2.2 Observations of Coronal Loops

Impressive drawings of coronal loops after observations in the hydrogen Balmer- α line above the solar limb were already made in the 19th century, for example by the Italian astronomer A. Secchi. An example is given in [Fig. 1.8](#), which already illustrates the dynamic nature of these loops which will be studied in the course of this thesis. Confined regions of enhanced emission were observed to fall towards the solar surface, seemingly coming out of nothing. The term *coronal rain* was coined to describe these findings.

⁵ If the velocities are of the order of the sound speed or larger, this plasma- β may no longer be a relevant parameter. Instead, it is replaced by a “kinetic” β which gives the ratio between the kinetic energy density of the plasma (with density ρ and velocity v) and the magnetic pressure: $\beta_{\text{kin}} = \mu_0 \rho v^2 / B^2$.

⁶ Sometimes the closed magnetic structures themselves are referred to as coronal loops, but since only those structures can be observed which are emitting light, it seems more reasonable to use the term in the above definition.

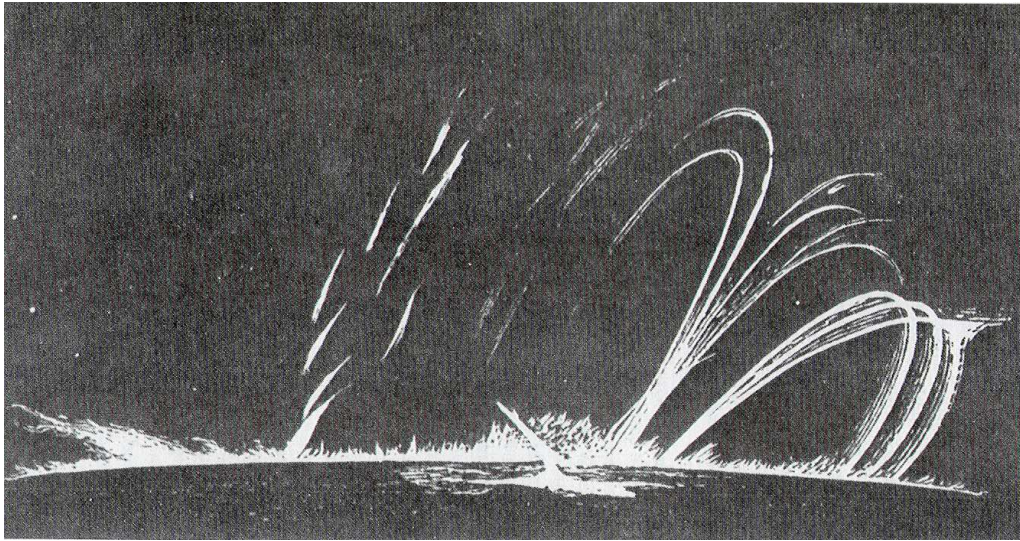


FIGURE 1.8: Coronal loops drawn by A. Secchi from spectrohelioscope observations in the hydrogen Balmer- α line on October 5, 1871. From [Young \(1895\)](#).

With the advent of the satellite era, the solar corona could be imaged from space in ever increasing detail. Analyzing *Skylab* data, [Levine & Withbroe \(1977\)](#) found that coronal loops may undergo “dramatic evacuation” on time scales of less than one hour. Since 1996, the *Solar and Heliospheric Observatory*, SOHO, has provided us with long uninterrupted time series of both images and spectra of the sun, and since 1998 the superior spatial resolution of the *Transition Region and Coronal Explorer*⁷, TRACE, (which has a spatial resolution of 1”, corresponding to roughly 725 km on the sun) revealed even smaller structures in the sun’s outer atmosphere. These structures are dynamic and are observed to change significantly on time scales down to minutes and probably less. Figure 1.9 shows a TRACE image of coronal loops, taken in the 17.1 nm pass band, which is dominated by emission lines from the iron ions Fe X and Fe XI, characteristic of plasma at a temperature of 1 MK.

[Schrijver \(2001\)](#) analyzed image sequences taken in different spectral passbands with TRACE and found that loop evacuation occurs frequently after plasma in the upper parts of the loops has cooled to temperatures around 10^5 K or below. The cooling process is often accompanied by emission in the hydrogen Ly $_{\alpha}$ and the CIV (154.8 nm) lines, developing initially near the loop top. Thereafter, cool plasma is observed to slide down on both sides of the loop, forming clumps which move with velocities of up to 100 km/s. The downward acceleration of these plasma clumps as inferred from these observations is significantly less than the gravitational acceleration on the solar surface.

Further observational evidence of “blobs” of plasma falling down towards the solar surface along magnetic field lines is presented by [De Groof et al. \(2004\)](#), based on high-cadence data taken in the He II 30.4 nm band with the Extreme-Ultraviolet Imaging Telescope (EIT) and Big Bear H_{α} images.

⁷TRACE is a mission of the Stanford-Lockheed Institute for Space Research, and part of the NASA Small Explorer program.

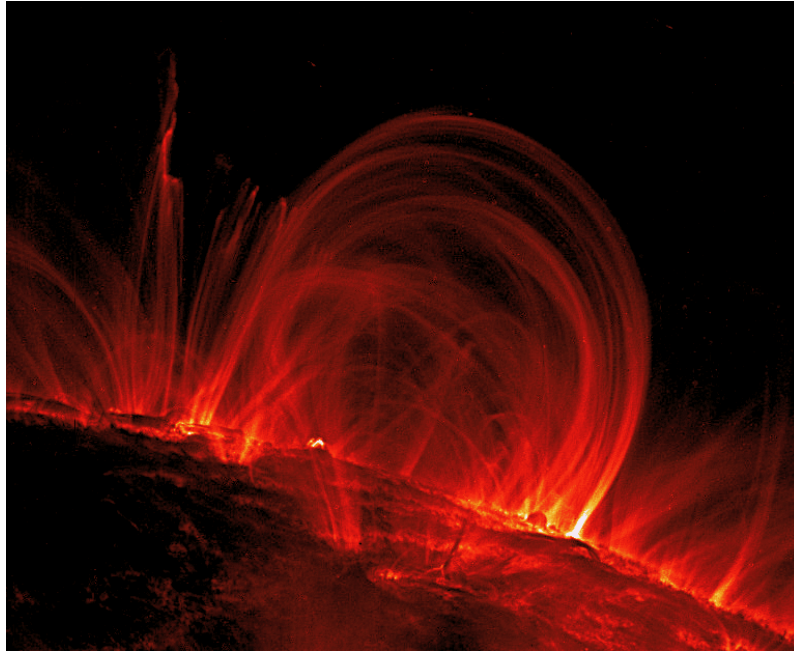


FIGURE 1.9: TRACE image of coronal loops, taken in the 17.1 nm pass band, characteristic of plasma at 1 MK.

Using the Coronal Diagnostic Spectrometer (CDS) on SOHO, [Kjeldseth-Moe & Brekke \(1998\)](#) found that even in quiescent, non-flaring conditions, coronal loops show strong temporal variability of emission in UV spectral lines and substantial plasma flows. They reported significant changes of coronal loops over a period of one hour, in particular seen in emission lines in the temperature range between $T = 1 - 5 \cdot 10^5$ K. This variability is accompanied by large Doppler shifts, typically around $v = 20 - 100$ km/s.

Furthermore, [Dere et al. \(1989\)](#) studied spectra of the CIV lines at 154.8 nm and 155.0 nm, taken with the rocket-borne *High Resolution Telescope and Spectrograph*, HRTS. The authors found non-Gaussian spectral line shapes which they identified as explosive events, accompanied by velocities of up to 100 km/s for the plasma at a temperature of around 10^5 K. These observations indicate dynamics on even smaller spatial scales which are below the current observational limits of resolution.

1.2.3 Loop Models

The fact that the magnetic field confines the motion of the coronal plasma along field lines facilitates the construction of coronal loop models considerably. To a good approximation, a coronal loop can be modeled as a one-dimensional hydrodynamical system with a parametrized gravitational acceleration along the loop. Due to the insufficient knowledge about the coronal heating mechanism itself, the energy input into the coronal loop is accomplished by prescribing a heating function which depends on the assumed heating mechanism and is often parametrized as a function of distance along the loop. The most crucial aspects for a model are the implementation of

physically correct boundary conditions at the footpoints of the model, corresponding to the solar chromosphere, and the resolution of the steep temperature gradient of the solar transition region.

Early modeling attempts consisted of static, symmetric loop models with a prescribed constant pressure along the entire loop and a spatially constant heating. Under these assumptions, [Rosner et al. \(1978\)](#) derived a scaling law which relates the maximal loop temperature to the pressure and the loop length. This scaling law has been used widely in the last decades for loops of all sizes and temperatures, although it only applies to loops which have a height which is small compared to the pressure scale height. [Serio et al. \(1981\)](#) extended this scaling law to loops higher than the pressure scale height and also parametrized for the first time an exponential energy dissipation function which allowed the heating to be concentrated around the loop's footpoints. For energy dissipation scale heights below around 1/4 to 1/6 of the total loop length, the authors found that stable solutions are possible which have a local temperature minimum at the loop apex, while for very small energy dissipation scale heights no static solutions were found.

As was already pointed out, however, observations showed from the very beginning strong evidence that coronal loops are inherently dynamic and thus time-dependent models are needed to obtain a more detailed understanding of their nature. The main energetic agents that determine the evolution of a loop are *thermal conduction*, which is proportional to $T^{5/2} \cdot \nabla T$, the *radiative losses*, which scale approximately with the square of the electron density times a temperature-dependent radiative loss function that peaks around $T = 2 - 3 \cdot 10^5$ K, and the *coronal heating* term. The interplay between the three terms makes coronal loops react like a thermostat to a changing energy input: If a hot loop experiences a slight increase in the heating rate, the temperature and the pressure of the loop plasma increase. In the corona, this will reduce the radiative losses and the temperature will rise even further. In the chromosphere, on the other hand, the radiative losses will increase and the chromosphere will cool even further. This results in an even steeper temperature gradient which leads to an enhanced conductive flux from the corona into the chromosphere. This excess energy heats up the chromosphere and results in a larger negative pressure gradient towards the corona, which drives chromospheric plasma in the coronal part of the loop. This process is called *chromospheric evaporation*. The evaporated material then increases the density in the coronal part of the loop which in turn increases the radiative losses there. This process continues until a new balance between the increased heating rate and the adjusted radiative losses of the now hotter and denser loop is achieved. The opposite process occurs if the heating rate is decreased slightly. In this case, coronal material cools and flows down towards the chromosphere. This so-called *condensation* results in a new stable loop configuration with a lower temperature and density. It has become customary to use the term condensation to describe the process of rapid cooling accompanied with a strong density enhancement, although no phase transition in the physical sense takes place. This is emphasized here since I will use this expression in several occasions throughout this work.

The dynamical energy balance between the heat flux from the corona into the chromosphere and the chromospheric evaporation of plasma into the corona adjusts the location of the transition region and sets the coronal base pressure. Therefore, including a chromosphere in a loop model is very important, even if this chromosphere is an oversimplified model of the real chromosphere.

1.3 Motivation and Scope of this Work

The classic interpretation of observations like the “dramatic evacuation” or “catastrophic cooling” of coronal loops has been so far that drastic changes of the emission from loops or loop systems occur as a result of strong changes in the total amount of loop heating. In this picture, turning off the heating of a loop or reducing it significantly leads to catastrophic cooling and draining of the whole loop. However, it has been discussed by [Hood & Priest \(1980\)](#) whether or not the resulting cool loops would be stable.

The question arises whether it is actually necessary to impose strong changes of the heating rate or other quantities to account for the dynamic evolution of coronal loops. In this thesis I investigate this problem using a numerical approach: A coronal loop is modeled as a one-dimensional hydrodynamical system including heat conduction and self-consistent radiative losses. The coronal heating is parametrized as a function of distance along the loop, which can be used to study the effect of the spatial energy deposition on the loop’s evolution. By calculating the non-equilibrium ionization of several atomic species consistently with the hydrodynamic equations, not only can the total radiative losses be calculated, but also the emission in a large number of optically-thin emission lines which can then be directly compared with observations. Specifically, I address the following questions in this thesis:

- Are dynamic processes in coronal loops, such as flows and transient brightenings, necessarily the result of a time-dependent driving mechanism?
- Can recent observations of fast downflows in coronal loops, as reported e.g. by [Schrijver \(2001\)](#) and [De Groof et al. \(2004\)](#) be explained by a common mechanism?
- Which parameters determine the dynamics of coronal loops?

In the course of this work, I will show that coronal loops can exhibit very dynamic evolution even under the assumption of a temporally constant energy supply, which proves that no time-dependent driving mechanism is needed to account for fast downflows and transient brightenings. It is found that the scale height of the energy dissipation acts as a control parameter of this non-linear system which determines whether a coronal loop is stable or unstable.

In the next chapter, the equations governing the coronal loop model and the numerical methods used to solve them will be introduced. Chapter 3 gives an overview over the physical processes in the solar transition region and corona which lead to emission in the ultraviolet spectral range and describes how optically-thin spectral lines are synthesized from the model. In Chap. 4 the concepts of thermal instability in coronal loops and the evaporation-condensation cycle are established and applied to the evolution of short, cool magnetic loops which presumably constitute the solar transition region. Numerical calculations are presented which show that, depending on the damping length of the heating function, plasma condensations can form in these short, cool loops. I will study the evolution of these loops, discuss static as well as dynamic solutions and finally calculate the time-dependent emission of transition region lines arising from this model. In Chap. 5, this concept is applied to longer coronal loops, and it is found that it can account for transient brightenings in prominent spectral lines and leads to fast downflows. Chapter 7 reviews the obtained results in the framework of non-linear systems. It is described how these results compare to the early model of [Kuin & Martens \(1982\)](#) and the advantages as well as the limitations of simplified

models are assessed. In Chap. 6 it is shown which implications the evaporation-condensation cycle has for long, hot active region loops and how these findings relate to the recent observations of [De Groof et al. \(2004\)](#). Finally, Chap. 8 consists of a parameter study which covers a broad range of loop sizes and heating rates and describes the different types of evolution that coronal loops can undergo. Apart from outlining the parameter regime in which footpoint-heated loops are inherently dynamic, this chapter compares the results from our time-dependent models to the parameter study of hydrostatic loop models by [Aschwanden et al. \(2001\)](#). Furthermore, I propose a connection between the thermal instability in coronal loops and models of global relaxation oscillations of stellar coronae.

2 Model Equations and their Solution

The numerical code which is used for the calculations in this thesis is a one-dimensional time-dependent code that solves the hydrodynamic equations of continuity, motion and energy, together with the ionization rate equations for a given number of atomic species. It has been developed by V. H. Hansteen (cf. Hansteen 1993) and is based on an *implicit conservative upwind* method. In this chapter I will first introduce the model equations, then introduce the numerical methods, partly following the description given by Korevaar (1989), and finally describe how the model equations are solved numerically.

2.1 Model Equations

The equations for mass conservation, momentum, energy, and ionization and recombination rates which are going to be solved read as follows:

- Mass conservation:

$$\frac{\partial \rho}{\partial t} + \frac{\partial}{\partial z}(\rho v) = 0, \quad (2.1)$$

- Momentum equation:

$$\rho \frac{\partial v}{\partial t} + \rho v \frac{\partial v}{\partial z} = \frac{\partial}{\partial z}(p + \Lambda) - \rho g_{\parallel}, \quad (2.2)$$

- Energy equation:

$$\frac{\partial}{\partial t}(\rho e) + \frac{\partial}{\partial z}(\rho v e) + (p + \Lambda) \frac{\partial v}{\partial z} = -\frac{\partial F_c}{\partial z} + Q_m - L_{\text{rad}} + Q_o, \quad (2.3)$$

- Rate equations:

$$\frac{\partial n_{ij}}{\partial t} + \frac{\partial}{\partial z}(n_{ij} v) = n_e [n_{i,j-1} q_{i,j-1} - n_{ij} (q_{ij} + \alpha_{ij}) + n_{i,j+1} \alpha_{i,j+1}]. \quad (2.4)$$

In these equations v denotes the velocity along the curvilinear loop coordinate, z , g_{\parallel} the component of the gravitational acceleration that is parallel to the magnetic field, Q_m the “mechanical” heating rate which parametrizes the energy supply to the loop, L_{rad} the radiative loss rate per unit volume, and Q_o a small “opacity heating” term that is included in order to maintain chromospheric temperatures at roughly 7 000 K. The internal energy, e , is calculated as the sum of the thermal and internal energy including only ionization states since the contribution from the excitation energy is negligible. The population of the ionization state j of element i is denoted by n_{ij} , while ionization rates and recombination rates are represented by q_{ij} and α_{ij} , respectively.

To ensure a continuous solution through the shocks an artificial viscosity term $\partial\Lambda/\partial z$ is introduced in Eq. (2.3). Following the treatment of von Neumann & Richtmyer (1950) we write

$$\Lambda = \begin{cases} \frac{4}{3}\rho l_g^2 (\partial v/\partial z)^2 & \text{for } (\partial v/\partial z) < 0, \\ 0 & \text{for } (\partial v/\partial z) \geq 0, \end{cases} \quad (2.5)$$

where l_g is chosen to be some fraction of the average grid spacing. The artificial viscosity will result in a shock thickness of order l_g while reproducing the correct jump in the dynamic variables, as well as the correct propagation speed of the shock. The thermal conduction is set to $F_c = \kappa_0 T^{5/2} dT/dz$ (Spitzer 1962) with $\kappa_0 = 1.1 \times 10^{-11} \text{ W m}^{-1} \text{ s}^{-1} \text{ K}^{-7/2}$.

Radiative losses are computed assuming that the plasma is effectively thin. While, ideally, one should solve the equation of radiative transport in order to calculate the radiative losses, comparisons with models where this has been done (Carlsson 2003; Kun & Poland 1991) indicate that the errors incurred by assuming effectively thin losses in the Ly_α line are not significant to the energetics of the system in the upper chromosphere and above. Radiative losses are due to collisional excitation of the various ions comprising the plasma. The elements hydrogen, helium, carbon, oxygen, neon, silicon, and iron have been included in the calculation of the radiative losses, as well as thermal bremsstrahlung. If computing time is an issue, as it is e.g. the case for very long simulations or extensive parameter studies, some of the metals can be treated by assuming ionization equilibrium and then deriving an *a priori* radiative loss curve as a function of electron temperature. For the simulations presented in this work, the radiative losses from hydrogen, helium, carbon and oxygen were computed consistently with full time dependent rate equations, while precalculated radiative losses were used for neon, silicon and iron, if not otherwise mentioned.

2.2 Implicit Integration Methods

An implicit time integration uses the variables of the solution after the time step as well as at the beginning of the time step, and then the equations are solved to determine the values of the variables after the time step. In general this requires simultaneous equations to be solved at each time step. Implicit methods have several advantages over explicit methods. One advantage is that they are absolutely stable, regardless of the time step, while explicit methods are absolutely stable only for time steps smaller than the Courant-Friedrichs-Lewy limit (Courant et al. 1928).¹ Implicit methods also prove to work better for very non-linear or stiff problems like the one treated in this thesis, because information about the variables after the time step is used in the calculation of the solution. On the contrary, explicit methods are simpler to implement than implicit methods and use less computing-time per time step. An explicit integration with respect to time uses only the knowledge of the solution available at the beginning of the time step.

2.2.1 Implicit Integration of First-Order Partial Differential Equations

In general, any set of partial differential equations (PDEs) can be written in the form

$$\frac{\partial}{\partial t} \mathbf{x} = \mathbf{f}(\mathbf{x}, t). \quad (2.6)$$

¹The Courant-Friedrichs-Lewy condition states that the time step times the sound speed must be less than the distance of the smallest grid spacing in the problem. If this condition is not met, an explicit method is unstable.

We associate the independent variable t with time, but any other variable can be used as well. The vector \mathbf{x} consists of N independent unknown variables. The operator \mathbf{f} may contain first derivatives with respect to other independent variables, such as $\partial/\partial x$. When \mathbf{f} contains no such derivatives, Eq. (2.6) reduces to a set of ordinary differential equations. In some cases a higher order differential equation can be reduced to a set of first order differential equations by a suitable substitution. The numerical integration of the set of PDEs given by Eq. (2.6) requires discretization in space and time. One way to discretize these equations is by a finite difference scheme. This approach was taken in this work, but other methods such as finite elements or spectral methods exist. If we denote the numerical approximations of \mathbf{x} and \mathbf{f} at time level t^n by \mathbf{x}^n and \mathbf{f}^n , a possible discretization of Eq. (2.6) is given by

$$\frac{\mathbf{x}^{n+1} - \mathbf{x}^n}{\Delta t^n} = (1 - \alpha)\mathbf{f}^n + \alpha\mathbf{f}^{n+1}. \quad (2.7)$$

At first sight, $\alpha = \frac{1}{2}$ may appear as the most intuitive choice, but depending on the situation other values of α can be preferable. Schemes with $\alpha = 0$ are called *explicit*, schemes with $\alpha = 1$ are called *fully implicit*. The special case $\alpha = \frac{1}{2}$ is called *central time differencing*. In the numerical code used in this thesis, α is a free parameter which is set to $\alpha = 0.55$ unless otherwise mentioned (in some situations, the fully implicit setting $\alpha = 1.0$ is used). For $\alpha \approx 1/2$, the integration scheme is second-order accurate in time, otherwise only first-order accuracy is reached.

2.3 Conservative Methods

The temporal evolution of any fluid may be described by means of differential equations for the conservation of mass, momentum and energy. A numerical method is called conservative if it uses these conservation equations explicitly, i.e. the numerical scheme guarantees the conservation of mass, momentum and energy. In practice this is achieved by dividing the space coordinate into zones, and by considering the integral values of quantities within each zone rather than the values at the center of it.

2.4 Upwind Schemes

In the one-dimensional Eulerian description of a fluid there are three characteristic velocities: $v - c$, v , and $v + c$, where v is the fluid velocity and c is the speed of sound. Information of the hydrodynamic system is transported at these three velocities. If we would like to model the temporal evolution of the fluid, it is necessary to know in which direction the information propagates. For instance, if the fluid is at rest, an equal amount of information streams into both directions because the characteristic velocities are $-c$, 0 , and c . If the flow is supersonic, all hydrodynamic information propagates in one direction because the three characteristic velocities are of equal sign. An upwind method is a numerical method that consistently takes into account the direction of the flow of information.

Let us first consider the simplest case, the first-order upwind scheme. In this scheme, we determine first the direction of the flow at the boundary of a zone. The flux through the boundary $j + 1/2$ is then set equal to the velocity $v_{j+1/2}$ at the boundary times the transported quantity F upstream (or upwind) from that boundary, i.e.

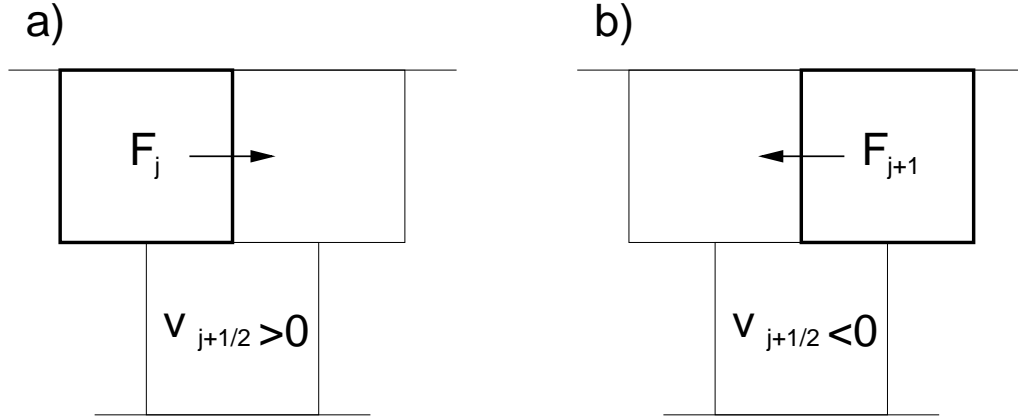


FIGURE 2.1: Illustration of the upwind scheme. The direction of the flow speed v determines how the flux of the quantity F through the boundary $j + 1/2$ is calculated.

$$\text{flux}_{j+1/2} = \begin{cases} v_{j+1/2} F_j & \text{for } v_{j+1/2} > 0, \\ v_{j+1/2} F_{j+1} & \text{for } v_{j+1/2} < 0. \end{cases} \quad (2.8)$$

This is illustrated in Fig. 2.1. The advantage of this scheme is that it is very stable and very simple. Its disadvantage is that it introduces diffusion errors: If the transported quantity has a strong gradient, the calculated flux will always be either too small or too large since the scheme is “upwind-weighted”. An approach to reduce the diffusion error is the transport scheme of [Wilson \(1978\)](#) which involves averaging of the transported quantity over neighboring zones, followed by an extrapolation into the upwind zone. This yields a more accurate scheme, but at the expense of stability: With this scheme it can happen that the volume of fluid transported out of a zone exceeds the total amount of fluid in this zone.

It would thus be desirable to have a scheme which has a high accuracy and is stable at the same time. One such scheme is the second-order upwind method of [Van Leer \(1974\)](#), a monotonic transport scheme which is used in our numerical code to calculate particle and momentum fluxes.

We will follow the treatment of [Hawley et al. \(1984\)](#) to derive the monotonic transport scheme of [Van Leer \(1974\)](#) by considering the analytic transport equation

$$\frac{\partial f}{\partial t} + v \frac{\partial f}{\partial x} = 0. \quad (2.9)$$

For simplicity we assume a constant transport velocity, v . For a given initial value distribution $f(x, t_0)$, we establish a finite difference grid, with F_j being zone averages of that initial value function. We can write the discrete version of the transport equation in integral form as

$$\left[\int_{x_j}^{x_{j+1}} f(x, t) dx \right] \Big|_{t_n}^{t_{n+1}} + \left[\int_{t_n}^{t_{n+1}} v f(x, t) dt \right] \Big|_{x_j}^{x_{j+1}} = 0. \quad (2.10)$$

This is equivalent to

$$(F_{j+1/2}^{n+1} - F_{j+1/2}^n) \Delta x + (\langle v f \rangle_{j+1} - \langle v f \rangle_j) \Delta t = 0, \quad (2.11)$$

where $\langle vf \rangle_j$ is a time average, which has the role of the flux through boundary j . Let

$$\langle vf \rangle_j = \frac{1}{2}v \left[F(x_j, t_{n+1}) + F(x_j, t_n) \right], \quad (2.12)$$

where the function $F(x, t_{n+1})$ is approximately equal to $F(x, t_n)$ advected over a distance $v\Delta t = \sigma\Delta x$, where $\sigma = v\Delta t/\Delta x$ (assume $v > 0$) is the Courant number. Thus, we can write

$$F(x_j, t_{n+1}) = F(x_j - \sigma\Delta x, t_n). \quad (2.13)$$

Hence, we are averaging the function $F(x, t)$ at $x = x_j$ at the beginning of the time step and at the end after advection. Now we move back to the zone center location by replacing $F(x_j, t_n)$ with $F(x_{j-1/2} + \frac{1}{2}\Delta x, t_n)$:

$$\langle vf \rangle_j = \frac{1}{2}v \left[F(x_{j-1/2} + \frac{1}{2}\Delta x - \sigma\Delta x, t_n) + F(x_{j-1/2} + \frac{1}{2}\Delta x, t_n) \right]. \quad (2.14)$$

A Taylor expansion of $F(x_{j-1/2} + \frac{1}{2}\Delta x - \sigma\Delta x, t_n)$ and substitution into Eq. (2.14) yields

$$\langle vf \rangle_j = v \left[F_{j-1/2} + \frac{1}{2}(1 - \sigma)\Delta_{j-1/2}F \right]. \quad (2.15)$$

$\Delta_{j-1/2}F/\Delta x$ is the gradient of F centered at $j - 1/2$. The accuracy of the scheme can vary depending on the choice of the gradient of $F(x, t)$. The final difference equation is given by

$$F_{j+1/2}^{n+1} = F_{j+1/2}^n - \sigma \left[F_{j+1/2} - [F_{j-1/2} + \frac{1}{2}(1 - \sigma)(\Delta_{j+1/2}F - \Delta_{j-1/2}F)] \right]. \quad (2.16)$$

The real advantage of Van Leer's scheme is realized when the condition of monotonicity is used in the definition of the gradient $\Delta_{j-1/2}F$: We require that the local slope of the function $F(x, t)$ must be the same after advection as before advection. Figure 2.2 shows two different discrete functions, one which is nonmonotonic at the zone boundaries, and one that this monotonic. We thus have to choose the gradient $\Delta_{j-1/2}F$ such that monotonicity is maintained at the zone boundaries. Van Leer finds that the following definition for the slope satisfies this criterion:

$$\Delta_{j-1/2}F = \begin{cases} \frac{2(F_{j-1/2} - F_{j-3/2})(F_{j+1/2} - F_{j-1/2})}{F_{j+1/2} - F_{j-3/2}} & \text{if } (F_{j-1/2} - F_{j-3/2})(F_{j+1/2} - F_{j-1/2}) > 0, \\ \Delta_{j-1/2}F = 0 & \text{otherwise.} \end{cases} \quad (2.17)$$

2.5 Staggered Grid

Our numerical code uses a *staggered grid* (see, e.g., [Hawley et al. 1984](#)), which means that the grids on which scalar quantities (like temperature and density) and vector-valued quantities (fluxes, momentum and velocity) are defined are shifted by half a grid point with respect to each other (cf. Fig. 2.3). Scalars are located at the center of a zone, while vectors are located at the zone boundaries. Since the vector-valued quantities are formed out of differences (derivatives) of scalar quantities, placing a vector-valued quantity centered between two scalar quantities is a natural choice. Formally, such a centered difference has the advantage of a second-order accuracy as opposed to the first-order accuracy of a forward or backward difference.

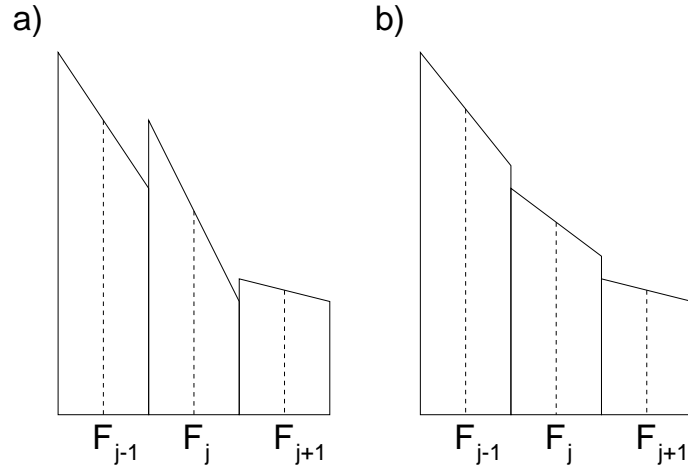


FIGURE 2.2: Three finite difference zones and the distributions $F(x, t)$ used to represent the unknown analytic density distribution. In (a) the function $F(x, t)$ is nonmonotonic at the boundaries. In (b) monotonicity has been restored by altering the slope $\Delta F/\Delta x$.

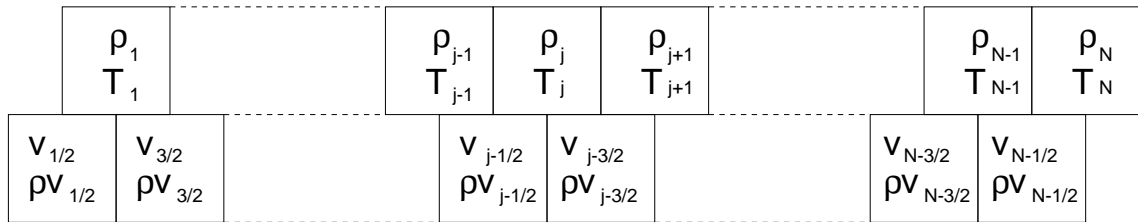


FIGURE 2.3: The staggered grid. Scalar quantities is defined on the upper grid, vector-valued quantities on the lower grid, which is shifted by half a grid point with respect to the upper one. Scalars are thus defined in the zone centers, vectors on the zone boundaries. Note that for simplicity the grid cells are drawn in equal sizes, while the width of the grid cells is in fact variable.

2.6 Boundary Conditions

The proper treatment of boundary conditions is important as the boundaries of the computational domain must represent the rest of the physical system. The numerical boundaries must not behave as physical boundaries, i.e. disturbances moving towards the boundaries of the computational domain should not be reflected, while information about the physical system outside the computational domain must pass into it. For example, during the temporal evolution of the loop model, sound waves are generated. They propagate along the loop and should pass through the boundaries without reflection. In this code the transparent boundary conditions as described by [Korevaar & van Leer \(1988\)](#) are implemented where the physical variables are extrapolated outside the numerical grid, using the characteristic variables.

2.7 Conservation Laws on an Adaptive Mesh

In numerical simulations of fluid dynamics, one often encounters the problem that in certain regions of the computational domain the physical variables change much more rapidly than in others. In our application, the large temperature gradient of the solar transition region and possible shocks which are moving in the coronal loop have to be resolved, while in other regions the spacing of the numerical grid may be wider to make the code more efficient in terms of computing-time. To achieve this goal, adaptive-mesh techniques have proven to be very effective (the terms “mesh” and “grid” are used synonymously in this work). Unlike Eulerian coordinates, which are fixed in the laboratory frame, or Lagrangean coordinates (fixed in the moving fluid), an adaptive mesh is fixed neither in the laboratory frame nor in the fluid but is free to evolve in such a way as to track significant features in the flow. This facilitates the simulation of shocks and results in robust computational algorithms. In particular, adaptive-mesh methods allow one to resolve fronts (e.g. shocks, ionization and radiation fronts) naturally, and are designed to use the grid points efficiently by redistributing them in space in response to the time evolution of the flow. [Winkler et al. \(1984\)](#) showed that similar to the general Reynolds transport theorem, a *mesh transport theorem* can be derived for equations formulated on an adaptive mesh. In this section, the description of [Winkler et al. \(1984\)](#) is presented in order to motivate this mesh transport theorem.

In an adaptive coordinate system, three different time derivatives have to be distinguished: (1) the Eulerian derivative, $(\partial/\partial t)$, taken with respect to fixed coordinates in the laboratory frame, (2) the Lagrangean (or comoving) derivative, (D/Dt) , taken with respect to a definitive fluid element, and (3) the adaptive-mesh derivative, (d/dt) , taken with respect to fixed values of the adaptive-mesh coordinates, which, in general, are neither fixed in the laboratory frame nor in the fluid. The Eulerian *fluid velocity* is

$$\mathbf{v} = D\mathbf{r}/Dt, \quad (2.18)$$

where $\mathbf{r} = \mathbf{r}(\mathbf{r}_0, t)$ is the position of a definitive point (“molecule”) in the fluid, and the *grid velocity* is

$$\mathbf{v}_{\text{grid}} = d\mathbf{r}/dt, \quad (2.19)$$

where $\mathbf{r} = \mathbf{r}(\mathbf{k}, t)$ is the position of a definitive set of grid coordinates (specified by \mathbf{k}). The *relative velocity* of the fluid with respect to the adaptive grid is then given by

$$\mathbf{v}_{\text{rel}} = \mathbf{v} - \mathbf{v}_{\text{grid}}. \quad (2.20)$$

The Lagrangean and Eulerian derivatives of any quantity f are related by

$$(Df/Dt) = (\partial f/\partial t) + (\mathbf{v} \cdot \nabla)f, \quad (2.21)$$

where ∇ denotes the gradient with respect to the lab-frame (Eulerian) coordinates. Analogously,

$$(df/dt) = (\partial f/\partial t) + (\mathbf{v}_{\text{grid}} \cdot \nabla)f. \quad (2.22)$$

If J_f denotes the Jacobian of the transformation between the coordinates defining an initial volume dV_{fluid}^0 and the volume $dV_{\text{fluid}} = J_f dV_{\text{fluid}}^0$ of the same fluid at a later time, the *Euler expansion formula*

$$D(\ln J_f)/Dt = \nabla \cdot \mathbf{v} \quad (2.23)$$

can be derived (Aris 1962; Owczarek 1964), which then leads to the *Reynolds transport theorem*

$$\frac{D}{Dt} \left(\int_{V_{\text{fluid}}} f dV_{\text{fluid}} \right) = \int_{V_{\text{fluid}}} \left[\frac{\partial f}{\partial t} + \nabla \cdot (\mathbf{v}f) \right] dV_{\text{fluid}}. \quad (2.24)$$

In this equation, V_{fluid} is a definitive volume of *fluid*. In the same way, these theorems can be extended to the adaptive coordinate system. Writing $dV = JdV^0$ to relate an adaptive-mesh volume dV to its original volume dV^0 we obtain the *adaptive-mesh expansion formula*

$$d(\ln J)/dt = \nabla \cdot \mathbf{v}_{\text{grid}} \quad (2.25)$$

and the *adaptive-mesh transport theorem*

$$\begin{aligned} \frac{d}{dt} \left(\int_V f dV \right) &= \int_V \left[\frac{\partial f}{\partial t} + \nabla \cdot (\mathbf{v}_{\text{grid}} f) \right] dV \\ &= \int_V \frac{\partial f}{\partial t} dV + \int_{\partial V} f \mathbf{v}_{\text{grid}} \cdot \mathbf{dS}. \end{aligned} \quad (2.26)$$

In this equation V denotes a definite volume corresponding to *fixed values of the adaptive coordinates*, and \mathbf{dS} is an outwards-pointing element on the surface ∂V of this volume.

It is interesting to note that the transformation to an adaptive coordinate system comprises a field of local Galilean transformations (Winkler et al. 1984). The frame in which the dependent variables, i.e. the fluid properties, are measured is not changed, but only the underlying coordinate system on which the equations are specified. Because the physical quantities are not transformed to and measured with respect to the moving mesh, the grid velocity can be arbitrarily large. In particular, the grid velocity may exceed the speed of light without violating physical causality. In our application to the dynamics of the solar corona, this is of no importance, but the same adaptive-mesh technique can also be applied to relativistic flows.

2.7.1 Examples

As an example, let us transform some conservation laws to adaptive coordinates. In the following equations, ρ denotes density, p pressure and e internal energy.

- a) The Lagrangean equation of continuity

$$(D\rho/Dt) = -\rho(\nabla \cdot \mathbf{v}) \quad (2.27)$$

transforms into

$$\frac{d}{dt} \left(\int_V \rho dV \right) + \int_{\partial V} \rho \mathbf{v}_{\text{rel}} \cdot \mathbf{dS} = 0. \quad (2.28)$$

- b) Euler's equation of motion with an external force \mathbf{f}

$$\rho \frac{D\mathbf{v}}{Dt} + \nabla p = \rho \mathbf{f} \quad (2.29)$$

becomes

$$\frac{d}{dt} \left(\int_V \rho \mathbf{v} dV \right) + \int_{\partial V} (\rho \mathbf{v}) \mathbf{v}_{\text{rel}} \cdot d\mathbf{S} + \int_{\partial V} p \mathbf{n} \cdot d\mathbf{S} = \int_V \rho \mathbf{f} dV, \quad (2.30)$$

and the

c) Adiabatic gas energy equation

$$\rho \left[\frac{De}{Dt} + p \frac{D}{Dt} \left(\frac{1}{\rho} \right) \right] = 0 \quad (2.31)$$

is written as

$$\frac{d}{dt} \left(\int_V \rho e dV \right) + \int_{\partial V} (\rho e) \mathbf{v}_{\text{rel}} \cdot d\mathbf{S} + \int_V p (\nabla \cdot \mathbf{v}) dV = 0. \quad (2.32)$$

2.8 Implementation of an Adaptive Grid

Having shown that conservation laws can be formulated on an adaptive grid, a prescription of how this grid should adapt to changes of the physical system has to be chosen. A simple and effective way of implementing an adaptive grid for one-dimensional initial value problems was suggested by [Dorfi & Drury \(1987\)](#) and is used in our numerical code. The idea is that for a given function f , the data points should be distributed uniformly along the graph of f . This suggests that the desired resolution of the numerical grid, R , should be given by $R = \sqrt{1 + (df/dx)^2}$. This is generalized to several functions, f_1, \dots, f_M , and discretized in the form

$$R_k = \left(1 + \sum_{j=1}^M \left(\frac{Z}{F_j} \frac{f_{j,k+1} - f_{j,k}}{z_{k+1} - z_k} \right)^2 \right)^{1/2}, \quad (2.33)$$

where Z is a natural length scale (in our case chosen to be the mean grid spacing), F_j is a natural scale associated with the function f_j , and $f_{j,k} = f_j(z_k)$. The normalization constant F is used to preferentially weight those quantities for which a correct resolution is most important. The grid density at grid point k with normalization Z is defined by

$$c_k \equiv Z / (z_{k+1} - z_k). \quad (2.34)$$

The idea is to set $c_k \propto R_k$. In practice, information on the variation of the first and second derivatives and the maximal allowed variation of the grid density with respect to time are included in the grid equation. Eq. (2.33) is therefore extended to

$$R_k = \left(1 + \sum_{j=1}^M \left(\frac{Z}{F_j} \left(\frac{\partial f_j}{\partial z} \right)_k^2 + \frac{Z^2}{F_j^2} \left(\frac{\partial^2 f_j}{\partial z^2} \right)_k^2 \right) \right)^{1/2}. \quad (2.35)$$

To prevent large spatial jumps in the grid density, it is redefined as

$$\tilde{c}_k = c_k - \alpha(\alpha + 1)(c_{k+1} - 2c_k + c_{k-1}), \quad (2.36)$$

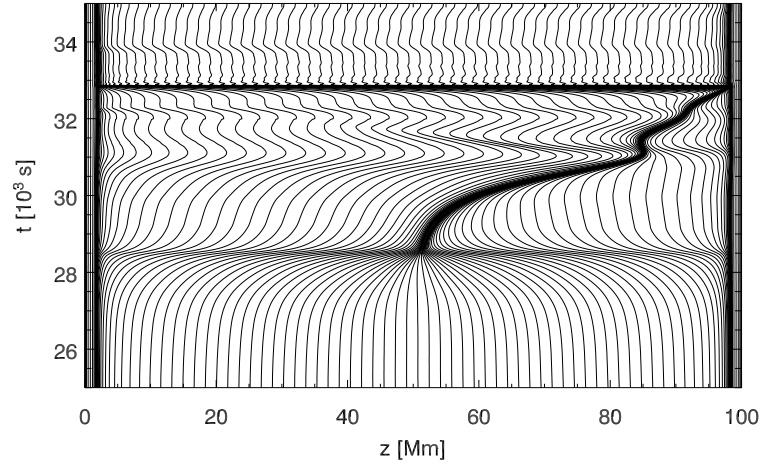


FIGURE 2.4: Evolution of the grid points with time. The lines track the location of a given grid point which changes as a result of the dynamic evolution of the coronal loop. In the domain shown here, a cool plasma condensation forms and moves towards the right, leading to a shock wave when it hits the transition region. For clarity, only every second point of the numerical grid is plotted.

which constricts the grid density gradient to

$$\frac{\alpha}{1 + \alpha} \leq \frac{c_{k+1}}{c_k} \leq \frac{\alpha + 1}{\alpha}. \quad (2.37)$$

Furthermore, a time scale τ is introduced by redefining

$$\hat{c}_k = \tilde{c}_k + \frac{\tau}{\Delta t} (\tilde{c}_k - \tilde{c}_k^o), \quad (2.38)$$

where the superscript o indicates the value of the grid density at the last time step and Δt the length of this time step. The grid will then respond to changes of the corresponding variables with a characteristic time scale τ . The final grid equation can then be written as

$$\frac{\hat{c}_k}{R_k} = \frac{\hat{c}_{k+1}}{R_{k+1}}. \quad (2.39)$$

This equation for the grid density is solved simultaneously with the equations for the conservation of mass, momentum and energy. As an example, Fig. 2.4 displays the numerical grid for a time interval of the simulation of a coronal loop of 100 Mm length. The left footpoint is located at $z = 0$ Mm, the right footpoint at $z = 100$ Mm. The plot shows that the grid points are initially concentrated in the transition region close to the footpoints of the loop where the gradients of temperature, density and pressure are largest. Around $t = 28\,000$ s, a region of cool and dense plasma forms and then falls down towards the right side of the loop. In order to resolve the large gradients around this condensation region, the grid points are redistributed rapidly towards the center of the loop. They then move downwards (i.e. to the right) with the falling condensation region and follow it closely during its deceleration around $t = 31\,000$ s. When the condensation

region encounters the dense plasma of the transition region, a shock occurs which is moving upwards along the loop. Again the grid points adjust rapidly and follow the shock through the loop around $t = 33\,000$ s. Afterwards, the grid relaxes into a configuration close to its initial state. For a description of the physical processes, the reader is referred to Chap. 5.

2.9 Solving the Model Equations

Our model contains M coupled partial differential equations for M variables (density, momentum, energy, ion populations) which are discretized as difference equations on a spatial grid with N points. In the case of the continuity equation,

$$\frac{\partial \rho}{\partial t} + \frac{\partial}{\partial z}(\rho v) = 0, \quad (2.40)$$

the discretized equation at the grid point i reads

$$(\rho_i^{n+1} - \rho_i^n)\Delta z + (F(\rho_{i+1/2}^{n+1/2} v_{i+1/2}^{n+1/2}) - F(\rho_{i-1/2}^{n+1/2} v_{i-1/2}^{n+1/2}))\Delta t = 0. \quad (2.41)$$

In this equation, F denotes an operator to calculate the momentum fluxes. In this code, the monotonic transport scheme of [Van Leer \(1974\)](#) is used which is described in Sect. 2.4. For a given time t^n , the M difference equations at N grid points are written as a vector \mathbf{f} containing $M \cdot N$ elements:

$$\mathbf{f} = \begin{pmatrix} f_{\rho_1} \\ f_{v_1} \\ \vdots \\ f_{T_1} \\ \vdots \\ f_{\rho_N} \\ f_{v_N} \\ \vdots \\ f_{T_N} \end{pmatrix}. \quad (2.42)$$

We write down the equations in the form $\mathbf{f}(\mathbf{x}^n) = 0$, where \mathbf{x}^n is a given solution at time t^n . This solution, i.e. the values of the M variables at N grid points is also written as a vector \mathbf{x} with $M \cdot N$ elements:

$$\mathbf{x}^n = \begin{pmatrix} \rho_1^n \\ v_1^n \\ \vdots \\ T_1^n \\ \vdots \\ \rho_N^n \\ v_N^n \\ \vdots \\ T_N^n \end{pmatrix}. \quad (2.43)$$

The goal is now to find the solution \mathbf{x}^{n+1} at the next time step, t^{n+1} . This is done by means of the *Newton-Raphson method*. Assume we have a guess $\mathbf{x}_{\text{guess}}$ at t^{n+1} which is close to the correct solution. We then perform a Taylor expansion around $\mathbf{f}(\mathbf{x}_{\text{guess}}^{n+1})$:

$$\mathbf{f}(\mathbf{x}_{\text{guess}}^{n+1} + \delta\mathbf{x}) = \mathbf{f}(\mathbf{x}_{\text{guess}}^{n+1}) + \frac{\partial\mathbf{f}}{\partial\mathbf{x}} \cdot \delta\mathbf{x}, \quad (2.44)$$

where $\delta\mathbf{x} = \mathbf{x}^{n+1} - \mathbf{x}_{\text{guess}}^{n+1}$ is the difference between our guessed solution and the correct solution. Since we have constructed the equations such that $\mathbf{f}(\mathbf{x}_{\text{guess}}^{n+1} + \delta\mathbf{x}) = \mathbf{f}(\mathbf{x}) = 0$, Eq. (2.44) is equivalent to

$$-\mathbf{f}(\mathbf{x}_{\text{guess}}^{n+1}) = \frac{\partial\mathbf{f}}{\partial\mathbf{x}} \cdot \delta\mathbf{x}. \quad (2.45)$$

This equation is then solved iteratively for $\delta\mathbf{x}$. As long as our guess is sufficiently close to the solution, the inversion of the Jacobian matrix $\partial\mathbf{f}/\partial\mathbf{x}$ will converge quadratically. The Jacobian matrix $\partial\mathbf{f}/\partial\mathbf{x}$ is a $(M \cdot N) \times (M \cdot N)$ matrix containing the derivative of each equation with respect to each variable at each grid point:

$$\frac{\partial\mathbf{f}}{\partial\mathbf{x}} = \begin{pmatrix} \frac{\partial f_{\rho_1}}{\partial \rho_1} & \frac{\partial f_{\rho_1}}{\partial v_1} & \cdots & \frac{\partial f_{\rho_1}}{\partial T_1} & \cdots & \frac{\partial f_{\rho_1}}{\partial \rho_N} & \frac{\partial f_{\rho_1}}{\partial v_N} & \cdots & \frac{\partial f_{\rho_1}}{\partial T_N} \\ \frac{\partial f_{v_1}}{\partial \rho_1} & \frac{\partial f_{v_1}}{\partial v_1} & \cdots & \frac{\partial f_{v_1}}{\partial T_1} & \cdots & \cdots & \cdots & \cdots & \cdots \\ \vdots & \vdots & \vdots & \vdots & \vdots & \vdots & \vdots & \vdots & \vdots \\ \frac{\partial f_{T_N}}{\partial \rho_1} & \frac{\partial f_{T_N}}{\partial v_1} & \cdots & \cdots & \cdots & \cdots & \cdots & \cdots & \frac{\partial f_{T_N}}{\partial T_N} \end{pmatrix}. \quad (2.46)$$

However, as only the two neighboring grid points on each side are used to calculate these derivatives, this matrix is very sparse and consists of 5 $M \times M$ submatrices in N rows, centered around the diagonal of $\partial\mathbf{f}/\partial\mathbf{x}$ (for the first and the last row only grid points on one side exist so that ghost cells are used in these cases). This can be illustrated as follows:

$$\frac{\partial\mathbf{f}}{\partial\mathbf{x}} = \begin{pmatrix} \square & \square & \square & \cdots & \cdots & \cdots & \cdots & \cdots & \cdots & \cdots \\ \square & \square & \square & \square & \cdots & \cdots & \cdots & \cdots & \cdots & \cdots \\ \square & \square & \square & \square & \square & \cdots & \cdots & \cdots & \cdots & \cdots \\ \cdots & \square & \square & \square & \square & \square & \cdots & \cdots & \cdots & \cdots \\ \cdots & \cdots & \cdots & \cdots & \cdots & \cdots & \cdots & \cdots & \cdots & \cdots \\ \cdots & \cdots & \cdots & \cdots & \cdots & \cdots & \cdots & \cdots & \cdots & \cdots \\ \cdots & \cdots & \cdots & \cdots & \cdots & \square & \square & \square & \square & \square \\ \cdots & \cdots & \cdots & \cdots & \cdots & \cdots & \square & \square & \square & \square \\ \cdots & \cdots & \cdots & \cdots & \cdots & \cdots & \cdots & \square & \square & \square \\ \cdots & \cdots & \cdots & \cdots & \cdots & \cdots & \cdots & \cdots & \square & \square \end{pmatrix}. \quad (2.47)$$

For example, the box in row N_1 and column N_2 contains the derivatives of all M equations $f_{i,i=\{1,\dots,M\}}$ at grid point N_1 with respect to all M variables at grid point N_2 . For computational reasons, we solve for the relative corrections rather than for the absolute corrections and therefore define a vector $\mathbf{e} = \delta\mathbf{x}/x_{\text{guess}}^{n+1}$ and a modified matrix $\mathbf{m} = \partial\mathbf{f}/\partial\mathbf{x} \cdot \mathbf{x}_{\text{guess}}^{n+1}$ by multiplying each column by the respective value of $\mathbf{x}_{\text{guess}}^{n+1}$. In the case of the velocity, v , we divide by and multiply

with the local sound speed, c_s , since the velocity can be zero:

$$\mathbf{m} = \begin{pmatrix} \frac{\partial f_{\rho_1}}{\partial \rho_1} \cdot \rho_1 & \frac{\partial f_{\rho_1}}{\partial v_1} \cdot c_{s1} & \cdots & \frac{\partial f_{\rho_1}}{\partial T_1} \cdot T_1 & \cdots & \frac{\partial f_{\rho_1}}{\partial \rho_N} \cdot \rho_N & \cdots & \frac{\partial f_{\rho_1}}{\partial T_N} \cdot T_N \\ \frac{\partial f_{v_1}}{\partial \rho_1} \cdot \rho_1 & \frac{\partial f_{v_1}}{\partial v_1} \cdot c_{s1} & \cdots & \frac{\partial f_{v_1}}{\partial T_1} \cdot T_1 & \cdots & \cdots & \cdots & \cdots \\ \vdots & \vdots & \vdots & \vdots & \vdots & \vdots & \vdots & \vdots \\ \frac{\partial f_{T_N}}{\partial \rho_1} \cdot \rho_1 & \frac{\partial f_{T_N}}{\partial v_1} \cdot c_{s1} & \cdots & \cdots & \cdots & \cdots & \cdots & \frac{\partial f_{T_N}}{\partial T_N} \cdot T_N \end{pmatrix}. \quad (2.48)$$

We start with our initial guess, $\mathbf{x}_{\text{guess}}^{n+1}$, and then invert the block-pentadiagonal matrix \mathbf{m} to solve for the relative correction,

$$\mathbf{e} = -\mathbf{m}^{-1}\mathbf{f}. \quad (2.49)$$

A new approximated solution is then computed as $\mathbf{x}_{\text{guess,new}} = \mathbf{x}_{\text{guess}}(1 + \mathbf{e})$, and this procedure is iterated until the relative correction is smaller than a predefined value, typically of the order of 10^{-3} . We then proceed to the next time step and iterate again until a sufficiently accurate solution has been obtained. In order to accelerate the time integration, the size of the consecutive time step is made dependent on the number of iterations needed to reach convergence for the last time step. Thus, the size of the time step is controlled efficiently and can be very large if the system is close to equilibrium and adjusts quickly to smaller values if the values of the physical variables change drastically, e.g. due to the formation of shocks.

3 Emission Line Spectroscopy

In the hot plasma of the solar transition region and corona, many different atomic processes can excite and deexcite atomic energy levels and give rise to ionization and recombination. In this section I will first list the most important ionization and excitation processes for hot plasmas, then focus on those important for the solar transition region and corona, and finally describe how optically-thin emission lines can be calculated from the atomic parameters. To a large extent the description follows the textbook by [Mariska \(1992\)](#), and the reader is referred to this textbook and to [Beyer & Shevelko \(2003\)](#) for a more detailed treatment.

3.1 Atomic Processes

The main processes which can change the states of ionization and excitation of atoms and ions are listed below. The symbol X^{q+} refers to an q -times ionized atom, and excited states are denoted by an asterisk.

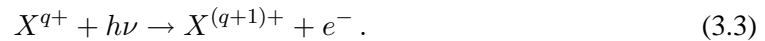
Radiative excitation (Photoexcitation) takes place if a photon is absorbed and the ion makes a transition to an excited state, $[X^{q+}]^*$:



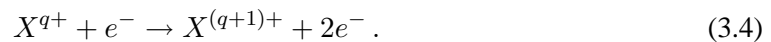
Collisional excitation is induced by an electron, e^- , impacting on ion, X^{q+} :



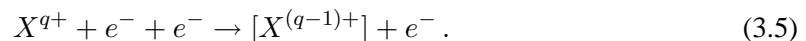
Photoionization is connected with the ejection of an electron after a photon with energy $h\nu$ has been absorbed:



Collisional ionization by electron impact releases an additional electron:



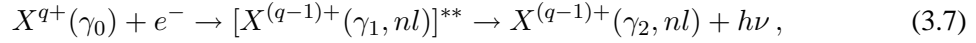
Three-body recombination is the inverse process to collisional ionization by electron impact:



Radiative recombination (Photorecombination) is the recombination of an electron and an ion under the emission of a photon:

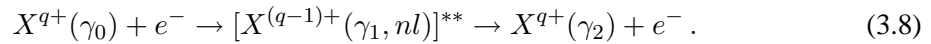


Dielectronic Recombination is a two-step resonance process involving the capture of a free electron with simultaneous excitation of a bound electron plus a subsequent radiative deexcitation:

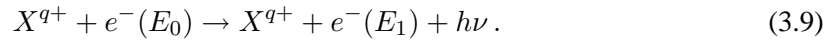


where γ_i ($i = 0, 1, 2$) denote the electronic core configurations involved. This process is only possible if the ion X^{q+} has at least one bound electron. If it is completely stripped, $q = Z$, the only two possibilities for an electron and an ion to recombine while fulfilling momentum and energy conservation are three-body and radiative recombination.

Autoionization is an alternative decay mode of the doubly excited state in the dielectronic capture process (3.7) which leads to the emission of an electron:



Free-free emission is produced when an electron interacts with a charged particle X^{q+} and makes a transition from an energy E_0 to an energy E_1 releasing a photon of energy $h\nu$:



For a Maxwellian velocity distribution of electrons this process is called *thermal Bremsstrahlung*. *Spontaneous radiative decay* is an efficient process by which excited levels are depopulated.¹



The rate for this process is given by $n_j A_{ji}$, where n_j denotes the population of an atomic energy level j and A_{ji} is the Einstein coefficient for a spontaneous transition from level j to a lower level i .

3.1.1 Important Atomic Processes in the Transition Region and Corona

Not all of the mentioned processes are equally important in the solar transition region and corona. Table 3.1 lists the expressions for the rates with which the different processes take place, together with characteristic time scales. The given values have been calculated for the CIV ion at a temperature of 10^5 K and an electron density of 10^{16} m^{-3} and are taken from the textbook of Mariska (1992). While collisional excitation is very common, only very few ions are excited radiatively due to the relatively weak solar radiation field at UV wavelengths. For the same reason stimulated emission is negligible, while spontaneous radiative decay is the fastest deexcitation process. Collisional excitation is important to populate some lines, but in most cases spontaneous radiative decays are much more efficient in depopulating excited levels.

Most ions in the solar transition region can only be ionized by collisions since the UV radiation field is too weak to make photoionization efficient, while radiative recombination is the dominating recombination mechanism. At the low densities of the solar transition region and corona, the rate for three-body recombination is negligible. Autoionization and dielectronic recombination can be important for the ionization state of the plasma, but are only effective at higher temperatures. Table 3.1 illustrates the important fact that the characteristic time scales for ionization and recombination processes are on the order of tens to hundreds of seconds which is much longer than the time scales for excitation processes.

¹In fact, spontaneous emission is not quite spontaneous but can be understood as stimulated emission induced by a virtual photon.

Process	Rate [m ⁻³ s ⁻¹]	Characteristic Time [s]
Collisional excitation	$n_i n_e C_{ij}$	$2 \cdot 10^{-3}$
Collisional deexcitation	$n_j n_e C_{ji}$	$2 \cdot 10^{-3}$
Spontaneous radiative decay	$n_j A_{ji}$	$4 \cdot 10^{-9}$
Collisional ionization	$n_e n_{\text{ion}} q_{\text{coll}}$	107
Autoionization	$n_e n_{\text{ion}} q_{\text{auto}}$	–
Total ionization rate	$n_e n_{\text{ion}} q_{\text{tot}}$	107
Radiative recombination	$n_e n_{\text{ion}} \alpha_{\text{rad}}$	88
Dielectronic recombination	$n_e n_{\text{ion}} \alpha_{\text{diel}}$	–
Total recombination rate	$n_e n_{\text{ion}} \alpha_{\text{tot}}$	88

TABLE 3.1: Important atomic processes in the solar transition region. The given values have been calculated for the CIV ion at a temperature of 10⁵ K and an electron density of 10¹⁶ m⁻³. For autoionization and dielectronic recombination no characteristic time scales are given since these processes are only effective for CIV at much higher temperatures. After [Mariska \(1992\)](#).

3.2 Formation of Optically-Thin Emission Lines

Let us consider an arbitrary ion which emits a photon of energy $h\nu_{ji}$ by a spontaneous transition from an upper level j to a lower level i . The rate for this process to occur in a volume of plasma is given by the Einstein coefficient, A_{ji} , multiplied by the number density of ions in the upper level, n_j . The volume emissivity, ε_ν , of the plasma for the transition from j to i is then given by

$$\varepsilon_{\nu,ji} = h\nu_{ji} A_{ji} n_j \Phi(\nu) \quad [\text{W m}^{-3} \text{ Hz}^{-1}]. \quad (3.11)$$

where $\Phi(\nu)$ denotes the normalized emission profile which will be described in Sect. 3.2.5. Integrating over the emission profile, we obtain the total emissivity:

$$\varepsilon_{ji} = h\nu_{ji} A_{ji} n_j \quad [\text{W m}^{-3}]. \quad (3.12)$$

Due to the low density of the coronal plasma, opacity effects can in most cases be neglected, so that we can integrate the emission from a given volume of plasma, ΔV , to obtain a flux at earth, where R_A is the sun-earth distance:

$$F_{ji} = \frac{1}{4\pi R_A^2} \int_{\Delta V} \varepsilon_{ji} dV \quad [\text{W m}^{-2}]. \quad (3.13)$$

It is sometimes convenient to express the number density of ions in the excited level j in terms of the other parameters of the solar plasma. Specifically, if we denote the relative population of the excited level by n_j/n_{ion} , the relative abundance of the ionic species by $n_{\text{ion}}/n_{\text{el}}$, the abundance of the element relative to hydrogen by $n_{\text{el}}/n_H \equiv A_{\text{el}}$, and the number density of hydrogen atoms relative to the number density of electrons by n_H/n_e , we can write

$$n_j = \frac{n_j}{n_{\text{ion}}} \frac{n_{\text{ion}}}{n_{\text{el}}} \frac{n_{\text{el}}}{n_H} \frac{n_H}{n_e} n_e. \quad (3.14)$$

Inserting this relation into Eqn. (3.13) we obtain

$$F_{ji} = \frac{h\nu_{ji}A_{ji}}{4\pi R_A^2} \int_{\Delta V} \frac{n_j}{n_{\text{ion}}} \frac{n_{\text{ion}}}{n_{\text{el}}} A_{\text{el}} \frac{n_H}{n_e} n_e dV. \quad (3.15)$$

This equation contains all the parameters necessary to calculate the total flux at the earth (or at the location of a satellite) for an optically-thin spectral line. The general problem is, however, to infer the physical state of the observed plasma from the measured flux in a spectral line, since all factors in the integral depend on the thermodynamic state of the plasma. In order to understand observed fluxes, one must therefore understand the physical processes which determine the different factors in this equation.

3.2.1 Excitation and Deexcitation

It was pointed out in the previous section that in the low-density plasma of the outer solar atmosphere, excitation and deexcitation processes generally take place on much shorter time scales than ionization and recombination processes. We can therefore separate the problem of calculating the population of excited levels from the problem of calculating the ionization balance. Let us first consider the population of excited levels.

A given energy level can be both populated by collisional excitation from lower levels and by collisional deexcitation and spontaneous radiative decay from higher levels. At the same time, it can also be depopulated by collisional excitation to higher energy levels and by collisional deexcitation and radiative decay to lower energy levels. To obtain the total population of this level, we must therefore solve a rate equation which describes the balance between the different processes.

The collisional transition rate from an energy level i to a level j is given by $n_i n_e C_{ij}$, where n_i is the number density of atoms in level i , n_e the electron number density, and C_{ij} the collisional rate coefficient. Radiative transitions from level i to level j take place at a rate of $n_i A_{ij}$ (both transition rates have units of $\text{m}^{-3} \text{s}^{-1}$). For each level i in the ion, the rate equation reads:

$$\frac{dn_i}{dt} = \underbrace{\sum_{j \neq i} n_j n_e C_{ji}}_{\text{coll. excit.}} - \underbrace{n_i \sum_{j \neq i} n_e C_{ij}}_{\text{coll. deexcit.}} + \underbrace{\sum_{j > i} n_j A_{ji}}_{\text{spont. dec. } j \rightarrow i} - \underbrace{n_i \sum_{j < i} A_{ij}}_{\text{spont. dec. } i \rightarrow j}. \quad (3.16)$$

To calculate level populations, we require that the sum of the level populations equals the ion number density,

$$n_{\text{ion}} = \sum_i n_i. \quad (3.17)$$

The electron collisional rate coefficient, C_{ij} , can be calculated by integrating the cross-section, σ_{ij} , for excitations by collisions with electrons of velocity v_e over their velocity distribution, $f(v_e)$. The collision rate between lower level i and upper level j then reads

$$n_e n_i C_{ij} = n_e n_i \int_{v_{e,0}}^{\infty} \sigma_{ij}(v_e) f(v_e) dv_e, \quad (3.18)$$

where $v_{e,0}$ is the velocity that corresponds to the threshold energy for the transition. Under the conditions of local thermodynamic equilibrium (LTE), the velocities follow a Maxwell distribution,

$$f(v_e) = 4\pi \left(\frac{m_e}{2\pi k T_e} \right)^{3/2} v^2 \exp\left(\frac{-m_e v^2}{2k T_e} \right). \quad (3.19)$$

Collision cross-sections are often expressed in terms of the collision strength $\Omega_{ij}(E_e)$, which is usually given as a function of the kinetic energy, E_e , of the exciting electron. The relation between the two is

$$\sigma_{ij} = \frac{\pi a_0^2 \Omega_{ij}(E_e)}{\omega_i E_e}, \quad (3.20)$$

where a_0 is the Bohr radius and ω_i is the statistical weight of level i . Combining the previous expressions, we obtain

$$C_{ij} = \frac{C_0}{\omega_i k T_e^{3/2}} \int_{\Delta E_{ij}}^{\infty} \Omega_{ij}(E) \exp\left(\frac{-E_e}{k T_e} \right) dE_e, \quad (3.21)$$

where ΔE_{ij} is the threshold energy for the transition and $C_0 = 8.63 \cdot 10^{-6}$ is a dimensionless constant. If one assumes that the collision strength is independent of the incident electron energy, this equation simplifies to

$$C_{ij} = \frac{C_0 \bar{\Omega}_{ij}}{\omega_i T_e^{1/2}} \exp\left(\frac{-\Delta E_{ij}}{k T_e} \right). \quad (3.22)$$

This approximation can be improved by substituting the energy-independent $\bar{\Omega}_{ij}$ by a thermally-averaged collisional strength, Γ_{ij} :

$$\Gamma_{ij}(T_e) = \int_0^{\infty} \Omega_{ij} \exp\left(-\frac{E_j}{k T_e} \right) d\left(\frac{E_j}{k T_e} \right), \quad (3.23)$$

where E_j is the energy of the scattered electron relative to the final energy state of the ion. The collisional deexcitation rates are obtained from the *principle of detailed balance*, which states that in thermodynamic equilibrium each microscopic process is balanced by its inverse process. In the case of collisional excitations and deexcitations, this means that the number of excitations caused by electrons in the velocity interval $[v_1, v_1 + dv_1]$ is balanced by collisional deexcitations by electrons in the range $[v_2, v_2 + dv_2]$, where

$$\frac{1}{2} m v_1^2 = \frac{1}{2} m v_2^2 + \Delta E_{ij}. \quad (3.24)$$

Applying this principle, one obtains

$$n_e n_i \sigma_{ij}(v_1) f(v_1) v_1 dv_1 = n_e n_i \sigma_{ji}(v_2) f(v_2) v_2 dv_2. \quad (3.25)$$

In thermodynamic equilibrium, the ratio of the level populations can be calculated with the Boltzmann equation:

$$\frac{n_j}{n_i} = \frac{\omega_j}{\omega_i} \exp\left(\frac{-\Delta E_{ij}}{k T} \right), \quad (3.26)$$

which yields for the collisional deexcitation rate

$$C_{ji} = \frac{\omega_i}{\omega_j} C_{ij} \exp\left(\frac{\Delta E_{ij}}{k T} \right). \quad (3.27)$$

3.2.2 The Two-Level Atom Approximation

For optically allowed, electric dipole transitions the assumption can be made that the population of the upper level occurs mainly via collisional excitation from the ground state and that the spontaneous radiative decay dominates over all other depopulation processes. This assumption is also called the *coronal model approximation*. The statistical equilibrium equations (3.16) then reduce to the two-level atom approximation:

$$n_e n_l C_{lu} = n_u A_{ul}, \quad (3.28)$$

where l denotes the lower and u the upper level. Since $n_e C_{lu} \ll A_{ul}$, the population of the upper level is negligible in comparison with the ground level, and we may identify the population of the lower level with the total population of the radiating ion, $n_l \approx n_{\text{ion}}$. Then the expression for the flux in the spectral line reduces to

$$F_{ul} = \frac{h\nu_{ul}}{4\pi R_A^2} \int_{\Delta V} n_e n_{\text{ion}} C_{lu} dV. \quad (3.29)$$

This simplifies the calculations of line fluxes considerably since we do not have to solve the complete set of level population equations for the specific ion, but only the ionization rate equations. If we assume that the collision strength is independent of the incident electron energy, Eqns. (3.14) and (3.22) can be used to obtain

$$F_{ul} = \frac{h\nu_{ul}}{4\pi R_A^2} \frac{C_0 \Omega_{lu}}{\omega_l} \frac{n_H}{n_e} A_{\text{el}} \int_{\Delta V} n_e^2 \frac{n_{\text{ion}}}{n_{\text{el}}} T^{-1/2} \exp\left(\frac{-h\nu_{ul}}{kT}\right) dV, \quad (3.30)$$

where the hydrogen-to-electron number density ratio, n_H/n_e , is approximately 0.8. The temperature dependent terms can be grouped together into a so-called contribution function, $G(T)$:

$$G(T) = \frac{n_{\text{ion}}}{n_e} T^{-1/2} \exp\left(\frac{-h\nu}{kT}\right). \quad (3.31)$$

This function has a sharp peak at a specific temperature because of the strong temperature sensitivity of the relative ion abundances. The temperature at which $G(T)$ peaks is often referred to as the *formation temperature*, T_f , of the spectral line. Table 3.2 lists the formation temperatures of several transition region lines which will be studied in this work, along with their atomic transitions and wavelengths.

λ [nm]	Ion	Transition	$\log T_f$ [K]
62.97	O V	$2s^2 \ ^1S_0 - 2s2p \ ^1P_1$	5.40
103.19	O VI	$2s \ ^2S_{1/2} - 2p \ ^2P_{3/2}$	5.50
154.82	C IV	$2s \ ^2S_{1/2} - 2p \ ^2P_{3/2}$	5.00
155.08	C IV	$2s \ ^2S_{1/2} - 2p \ ^2P_{1/2}$	5.00

TABLE 3.2: Wavelengths, transitions and formation temperatures for some prominent emission lines formed in the solar transition region. After Mariska (1992).

3.2.3 Ionization

The ion number densities in the low-density plasma of the solar transition region and corona are determined by a balance between electron impact ionization and radiative and dielectronic recombinations. We saw in the previous section that the time scales for ionization and recombination are of the order of tens to hundreds of seconds, compared to around 10^{-3} s for collisional excitation and deexcitation. Because ionization and recombination proceed so slowly, significant departures from an equilibrium population of the different ionization stages is possible. Therefore, we have to solve the ionization rate equations together with the dynamic equations describing the plasma, which in our case are the hydrodynamic equations, Eqns. (2.1) - (2.3).

For an ion z of an element with nuclear charge Z , electron impact ionizations to the next ionization stage $z + 1$ are governed by the ionization rate coefficient, q_z , and recombinations to ion $z - 1$ by a total recombination rate coefficient, α_z . The ionization rate equations thus read:

$$\frac{dn_z}{dt} = n_e \left[n_{z-1} q_{z-1} - n_z (q_z + \alpha_z) + n_{z+1} \alpha_{z+1} \right]. \quad (3.32)$$

This equation is complemented by the requirement that the total number density of ions of a given element is the sum of the number densities of all ionization stages.

3.2.4 Atomic Data

As already stated in Chap. 2, the numerical code used in this work includes atomic models for the elements hydrogen, helium, carbon, oxygen, neon, silicon, and iron. The ionization and recombination rates given by [Arnaud & Rothenflug \(1985\)](#) and [Shull & van Steenberg \(1982\)](#) are implemented, and the collisional excitation rates are calculated using the HAO-DIAPER atomic data package ([Judge & Meisner 1994](#)). The collisional excitation rate from the ground state of hydrogen to its first excited state is computed from coefficients found in [Janev et al. \(1987\)](#). The spontaneous and dielectronic recombination rates are calculated according to [Aldrovandi & Pequignot \(1973\)](#), and the recombination rates of the hydrogen-like ions were taken from [Allen \(1973\)](#).

3.2.5 The Spectral Line Profile

In an ensemble of atoms, each atom has a velocity ξ with respect to the observer's line-of-sight, which results in a Doppler-broadened emission profile due to the uncorrelated superposition of their individual motions (applying the principle of detailed balance, this also holds for absorption profiles). Under the conditions of local thermodynamical equilibrium (LTE), the velocities follow a Maxwell distribution, which states that the probability of finding an atom with a line-of-sight velocity ξ in the interval $(\xi', \xi' + d\xi')$ is given by

$$W(\xi) d\xi = \frac{1}{\sqrt{\pi} \xi_0} \exp \left[-(\xi/\xi_0)^2 \right] d\xi, \quad (3.33)$$

where $\xi_0 = \sqrt{2kT/m_{\text{ion}}}$ is the most probable velocity at a temperature T and a mass m_{ion} of the radiating ion. With the definition of the Doppler width, $\Delta\nu_D$, of a spectral line with rest frequency ν_0 ,

$$\Delta\nu_D \equiv \nu_0 \xi_0 / c, \quad (3.34)$$

this velocity distribution leads to a Doppler broadening of

$$\Phi_D(\nu) = \frac{1}{\sqrt{\pi}\Delta\nu_D} \exp\left[-(\Delta\nu/\Delta\nu_D)^2\right], \quad (3.35)$$

where $\Delta\nu = \nu - \nu_0$ is the frequency difference with respect to the rest frequency, ν_0 . In general the resulting profile function of a spectral line is obtained by a convolution of the Doppler broadening function with the damping profile, Φ_L , of the atomic transition, which has the form of a Lorentzian. However, for optically-thin spectral lines in the solar corona, this damping profile is much narrower than the thermal Doppler broadening so that the profile function is to a good approximation given by the thermal Doppler broadening itself, i.e. $\Phi(\nu) = \Phi_D(\nu)$.

If the emitting plasma is not at rest, the emergent spectral lines are shifted by the Doppler effect. When one takes into account the projection of a velocity field (here assumed to be a one-dimensional flow with a velocity v) onto the line-of-sight, \vec{n} , the spectral profile at a location z is given by

$$\Phi(\nu, z, \vec{n}) = \frac{1}{\sqrt{\pi}\Delta\nu_D} \exp\left[-\left(\frac{\Delta\nu - \nu \cos\theta v(z)/c}{\Delta\nu_D}\right)^2\right], \quad (3.36)$$

where $\theta = \vec{e}_z \cdot \vec{n}$ is the aspect angle, defined by the scalar product of the local vector of the flow field, \vec{e}_z , and the normalized line-of-sight vector, \vec{n} . The emergent intensity of a spectral line in an optically-thin plasma can then be calculated as

$$I(\nu) = \frac{h\nu_{ul}}{4\pi} \int_0^{s_0} \Phi(\nu) n_e n_{zk} C_{lu} ds, \quad (3.37)$$

where the integration is carried out along the line-of-sight, $[0, s_0]$, parametrized by the path length, s . In this expression, n_e denotes the electron density, n_{zk} the population of the ionization state z of element k , and C_{lu} is the collisional rate.²

²It is assumed that the complete volume one is looking at is filled with plasma with the given properties. If this is not the case, the emergent intensity from a combination of different structures can be calculated by assigning an appropriate filling factor to each of the constituents.

4 Plasma Condensation in Cool Loops and its Effect on Transition Region Lines

Abstract

In this chapter, numerical calculations of the condensation of plasma in short coronal loops are reported which have several interesting physical consequences. Firstly, I propose a connection between small, cool loops ($T < 10^6$ K), which constitute one of the basic components of the solar transition region, and prominences, in the sense that the same physical mechanism governs their dynamics: Namely the onset of instability and runaway cooling due to strong radiative losses. Secondly, it is shown that the temporal evolution of these loop models exhibits a cyclic pattern of chromospheric evaporation, condensation, motion of the condensation region to either side of the loop, and finally loop reheating with a period of 4000 – 8000 s for a loop of 10 Mm length. Thirdly, transition region lines have been synthesized from these calculations which show strong periodic intensity variations, making condensation in loops a candidate to account for observed transient brightenings of solar transition region lines. Remarkably, all these dynamic processes take place for a heating function which is *constant* in time and has a simple exponential height dependence.

4.1 Introduction

Since the era of the *Skylab* project, loops have been recognized as a vital ingredient in coronal structure and coronal energetics. Indeed, one could imagine that the corona is entirely composed of nested loops with varying lengths, temperatures, heating rates, and activity levels. A nested structure of low-lying cool loops was suggested by [Dowdy et al. \(1986\)](#) to explain the temperature dependence of the emission measure. Thus, building an understanding of loop energetics is obviously a desirable objective. There are alternative scenarios for the structure of the transition region (see, e.g., [Mariska 1992](#)). As recent SOHO/SUMER results have shown, however, small cool loops to constitute one of the basic building blocks of the transition region ([Feldman et al. 2000](#)), this chapter will concentrate on the dynamics and energetics of cool loops.

The main components in the energy balance of *static* loops were identified by [Rosner et al. \(1978\)](#): They consist of a coronal heating term whose exact form is so far unknown, thermal conduction and radiative losses in the loop itself and at the transition region/chromosphere boundary. Roughly speaking one can understand static loop behavior quite well by assuming that the heat deposited by the heating mechanism in the corona is largely conducted back towards the chromosphere where it is radiated away. Due to the strong temperature dependence of the thermal conduction coefficient, this scenario almost invariably leads to apex loop temperatures of roughly 1 MK bounded by a geometrically small transition region as the temperatures fall towards 10^4 K

and chromospheric densities at the loop footpoints. Variations in the heating rate are dealt with in this type of loop by chromospheric evaporation or coronal condensation such that the radiative losses at the top of the chromosphere balance the thermal conductive flux from above (Hansteen 1993). This behavior is almost independent of the details of the heat deposition – as long as radiative losses near the loop apex are not an important factor in the energy budget.

Clear as the model above seems, serious difficulties are encountered as soon as loop model predictions are confronted with the observations themselves. These difficulties are various and sundry (Mariska 1992) but might be summarized as follows: The differential emission measures predicted by the models gives a much lower line emission from the lower transition region, below 10^5 K, than what is observed (alternatively one could say that the line emission from the upper transition region, above 10^5 K, is predicted much too high). In addition it is very difficult to account for the pervasive *average* redshift of up to 10 km/s seen in lower transition region lines and blueshifts in the upper transition region and low corona (Peter & Judge 1999).

Several proposals have been put forward to answer the difficulties outlined above. Dowdy et al. (1986) suggested a two-component transition region, consisting of magnetic funnels and a nested structure of low-lying, cool coronal loops. This new class of static loop solutions had been discussed by Antiochos & Noci (1986). Cally & Robb (1991) argued, however, that these cool loop solutions were unstable, and Cally (1990) proposed turbulent thermal conduction as an alternative hypothesis to explain the enhanced transition region emission. As for the spectral diagnostics of transition region lines, loop dynamics due to downward-propagating magneto-acoustic waves were shown to be a candidate to account for the pervasive redshifts (Hansteen 1993). However, it was first with the observations by the SOHO and TRACE instruments that the importance of cool loops and loop dynamics has belatedly come to the foreground. Peter (2000) gives evidence for a multi-component structure of the transition region, and Feldman et al. (2001) reach the conclusion that regions of hotter and cooler plasma in the solar atmosphere are essentially disconnected from each other.

The question that is raised is what implications these new ideas have on our understanding of the structure and energetics of both cool and hot coronal loops. Obviously a time-dependent heating will produce a number of dynamic phenomena such as waves or material motions through evaporation or condensations. But as will be shown below it is also found that within a certain parameter range of static mechanical energy deposition quite violent dynamics can ensue. Numerous mechanisms of coronal heating have been proposed (e.g. wave heating, nanoflares, magnetic reconnection), but independent of the detailed process of energy release there is now observational evidence that coronal loops are predominantly heated at the footpoints (Aschwanden et al. 2000, 2001). With heating concentrated near the loop footpoints it is no longer certain that sufficient energy to counter radiative losses is deposited near the loop apex. In fact, for such loops static solutions with a hot midpoint may no longer exist as the radiative loss rate increases strongly in the loop center when the temperature decreases towards $T \approx 2 \cdot 10^5$ K. If the magnetic field topology is such that the loop has a dip in the center, footpoint heating can lead to the condensation of plasma in the loop center and hence give rise to prominence formation (Antiochos et al. 1999). It was also found by Antiochos et al. (2000) that this type of prominence formation shows a cycle of formation, motion, and destruction. Recently, it was demonstrated by Karpen et al. (2001) that the condition of a “dipped” geometry is indeed not a necessary condition for prominence formation in long loops (their work describes a loop of 340 Mm length). A key element in their prominence scenario is the large ratio of loop length to the damping length of the heating function, and the

authors argue that shorter loops with a smaller ratio should therefore behave differently.

In this chapter numerical calculations are presented which show that, depending on the damping length of the heating function, condensation is also possible in short, cool coronal loops. I study the evolution of these loops, discuss static as well as dynamic solutions and finally calculate the time-dependent emission of transition region lines arising from this model.

4.2 Loop Heating

In order to parametrize the energy input into the coronal loop, the energy flux amplitude at the footpoints of the loop, F_{m0} , is specified and a mechanical heat flux is assumed that is constant up to a height z_1 and then decreases for $z \geq z_1$ as

$$F_m(z) = F_{m0} \exp[-(z - z_1)/H_m] \quad (4.1)$$

with a damping length H_m . In the models presented below H_m will be varied between 0.25 and 3.25 Mm. For the mechanical energy flux the value of $F_{m0} = 150 \text{ W m}^{-2}$ is adopted (the same as the one used by [Hansteen & Leer 1995](#)) and z_1 is set to 1.75 Mm for a loop of 10 Mm length. The heating rate, i.e. the energy deposition per unit time and unit volume, is given by the divergence of the energy flux:

$$Q_m(z) = -\frac{A_0}{A} \frac{dF_m(z)}{dz} = \frac{A_0}{A} \frac{F_m(z)}{H_m}. \quad (4.2)$$

The plasma- β is assumed to be $\ll 1$ and a constant cross section of the loop, i.e. $A = A_0 = \text{const}$ is assumed. This parametrization of the heating function was first suggested by [Serio et al. \(1981\)](#) and seems to be supported by recent observations ([Aschwanden et al. 2000, 2001](#)). Special care was taken to normalize the heating rate to a given energy flux in order to separate effects from changes of the amplitude of the energy flux to changes in its spatial distribution.

4.3 Results: Condensation due to Thermal Instability

4.3.1 Initial State

The model coronal loop has a total length of 10 Mm, consisting of a semicircular arch of 8 Mm length and a vertical stretch of 1 Mm length at both ends. Figure 4.1 shows the initial loop configuration. The temperature and density are plotted as a function of distance, z , along the loop. The total particle density at the base is $n_{\text{base}} = 8.8 \cdot 10^{20} \text{ m}^{-3}$. This density corresponds (very) roughly to a height of $h = 605 \text{ km}$ above $\tau_{500\text{nm}} = 1$ in the [Vernazza et al. \(1981\)](#) quiet sun model. The ionization degree of hydrogen is $\approx 0.3\%$ at this height and the base temperature is set to $T_{\text{base}} = 7000 \text{ K}$.

In the chromosphere, the temperature remains constant while the density falls off exponentially with a scale height of about 190 km until the transition region is encountered at 1.6 Mm. Here the temperature rises rapidly reaching 10^5 K at 1.63 Mm and $5 \cdot 10^5 \text{ K}$ at 2.81 Mm. The loop apex temperature is $6.55 \cdot 10^5 \text{ K}$. Energy losses by radiation are $L_{\text{rad}} \approx 10^{-4} \text{ W m}^{-3}$ in the coronal and transition region portions of the loop while conductive losses to the top of the chromosphere account for $\nabla Q \approx 8 \cdot 10^{-4} \text{ W m}^{-3}$, i.e. the loop is essentially a ‘‘hot loop’’ in that the

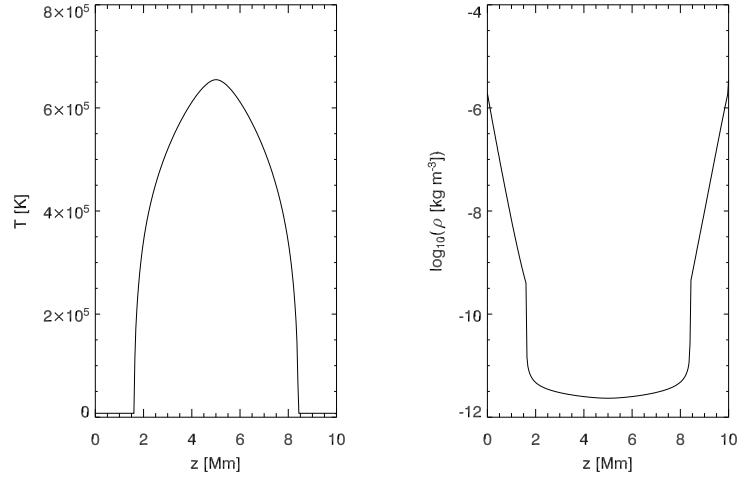


FIGURE 4.1: Initial configuration: temperature, T (left), and particle density, ρ (right), along the loop with a total length of 10 Mm.

energetics are dominated by conduction. The sound crossing time for the loop is 7 min and a low-amplitude acoustic wave is initially bouncing in the coronal portion of the loop between the two steep temperature gradients. This wave had been triggered by a temporally and spatially localized energy deposition (*nanoflare*) in the upper part of the loop. This episodic heating mechanism was switched off before the start of the simulation, and replaced by the continuous heating function given by Eq. (4.2). All calculations presented here could have equally well been initialized with a static loop model, but I decided to start with this perturbed model in order to illustrate that the formation of recurrent condensations is not only possible when starting from an analytic solution, but also for dynamic, and therefore more ‘realistic’ circumstances.

4.3.2 Loop Evolution

Starting from the initial loop model, a *time-independent* heating function is prescribed as given by Eq. (4.2) with a damping length of $H_m = 1.25$ Mm, which results in a heating rate at the loop center that is 15% of the maximal heating rate, $Q_m(z_1)$. At $z = z_1 = 1.75$ Mm, the ratio of mechanical heating to radiative losses is 0.26 at $t = 0$, while at the loop apex, it is 2.10.

The evolution of the loop temperature, velocity, and density is shown in Fig. 4.2. During the first 2300 s the loop cools down from $T_{\text{top}}(t = 0) = 6.5 \cdot 10^5$ K to $T_{\text{top}}(t = 900 \text{ s}) = 2 \cdot 10^5$ K, while the density stratification remains roughly constant and the low-amplitude acoustic wave continues to bounce between the two transition regions. At $t = 2300$ s there is a sudden change: The temperature at the loop apex is no longer the maximal loop temperature, and this dip in the temperature stratification amplifies rapidly. At the same time, a flow towards the cooling loop apex sets in, which reaches $v \approx 2$ km/s at $t = 3200$ s. At $t = 3400$ s, a clump of cool (10^4 K) material with rapidly increasing mass content has formed at the loop apex. This clump, which I will call the *condensation region* hereafter, eventually starts moving slowly towards one loop leg and is accelerated to $v \approx 3$ km/s before draining into the chromosphere at $t = 5300$ s. As

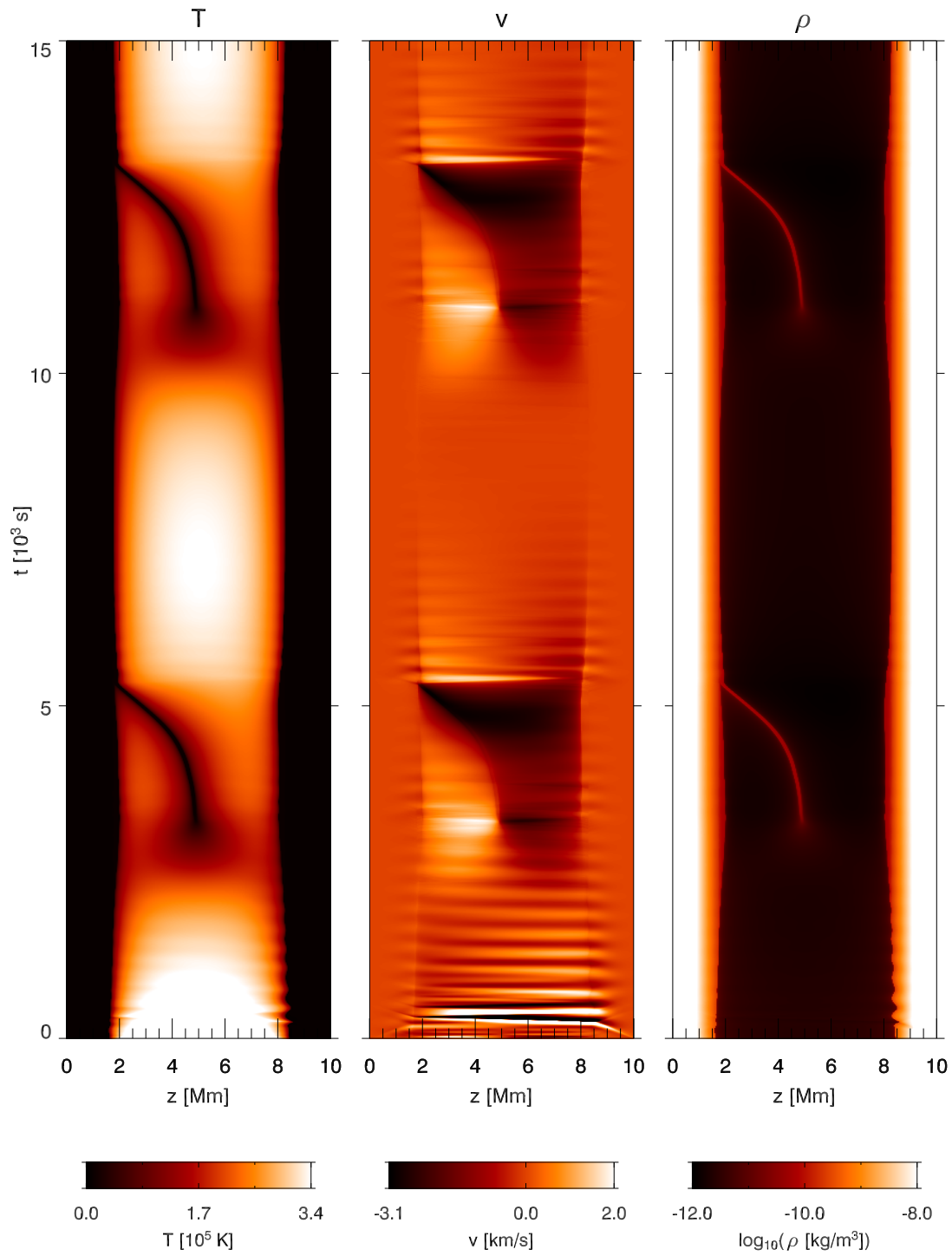


FIGURE 4.2: Temporal evolution of temperature (*left*), velocity (*center*), and density (*right*) along the loop. The heating rate for the loop shown is characterized by $F_{m0} = 150 \text{ W m}^{-2}$ and a scale height of $H_m = 1.25 \text{ Mm}$.

a result, a weak rebound shock forms on the left side, followed by a phase of chromospheric evaporation which refills the evacuated loop with plasma. This upflow decreases with time from $v(t = 5400 \text{ s}) \approx 1.5 \text{ km/s}$ to $v(t = 8000 \text{ s}) \approx 0$. In the mean time, the apex temperature of the loop has reached its maximum of $T_{\text{max,top}} = 3.4 \cdot 10^5 \text{ K}$ at $t = 7200 \text{ s}$. The subsequent decline in temperature is first slow and then becomes faster towards $t = 10\,000 \text{ s}$. At this time a dip in the temperature profile forms again at the loop apex, and the whole process repeats.

In the case of the model run shown in Fig. 4.2, a slow magneto-acoustic wave of low amplitude passes through the loop in the beginning of the simulation and leads to a leftward motion of the condensation region. Alternatively, an asymmetry of 1% between the deposited energy in both legs proved to be sufficient to dictate the draining direction: the condensation region then moves to the side on which less energy is supplied.

4.3.3 Energy Balance Analysis

The formation of the central dip of the temperature stratification results from the concentration of heating near the footpoints of the loop or, to put it differently, from insufficient heating at the top. In order to better understand the evolution of the loop, let us consider the energy balance at the loop apex for a damping length of $H_m = 1.25 \text{ Mm}$. The relevant terms for this are the mechanical energy supply, Q_m , the radiative losses, L_{rad} , the adiabatic compression, $p\nabla v$, and the divergence of the conductive flux, ∇F_c . As the density in the coronal part of the loop increases, the mechanical heating *per particle*, Q_m/n_e , decreases (the ion density, n_{ion} , equals approximately the electron density, n_e). This is displayed in the top row of Fig. 4.3. At the same time, the radiative losses per particle, L_{rad}/n_e (Fig. 4.3, center), increase as the temperature drops to $T = 2 \cdot 10^5 \text{ K}$, which is predominantly due to the temperature dependence of the radiative losses.

The time dependence of the total energy balance at the apex is dominated by two interacting processes, namely the increase of radiative losses and the increase of density. The *bottom* plot of Fig. 4.3 shows that, as a result of this interplay, the energy supply at the loop top becomes negative at $t = 2000 \text{ s}$, which explains the developing dip in the temperature profile. The simultaneous decrease of the gas pressure initiates a symmetric flow towards the center of the loop, so that more and more mass is advected and a condensation region forms. Once the temperature dip has formed as a consequence of the described loss of equilibrium, a thermal instability sets in as $L_{\text{rad}} \propto n_e^2$. This process of runaway cooling has been described, e.g., by Antiochos & Klimchuk (1991). As our model loop is of semicircular shape, the configuration with a condensation region located at the very center of the loop is gravitationally unstable. Therefore, the slightest perturbation forces the condensation region to move downward in either direction, where it experiences increasing acceleration as described below.

4.3.4 The Role of the Damping Length

A plausible hypothesis is that the major factor in determining the cyclic behavior of the loop lies in the damping length, H_m , of the heating function because this critically influences the heat deposition at the loop top. The influence of the damping length on the thermal evolution of the loop has been studied by varying H_m from 0.25 Mm to 3.25 Mm and in each case letting the loop model evolve for 20 000 s. In Fig. 4.4, the mechanical heating function, $Q_m(z)$, is plotted for different values of H_m . The temporal evolution of the mean loop temperatures, $\langle T \rangle$, is displayed for these

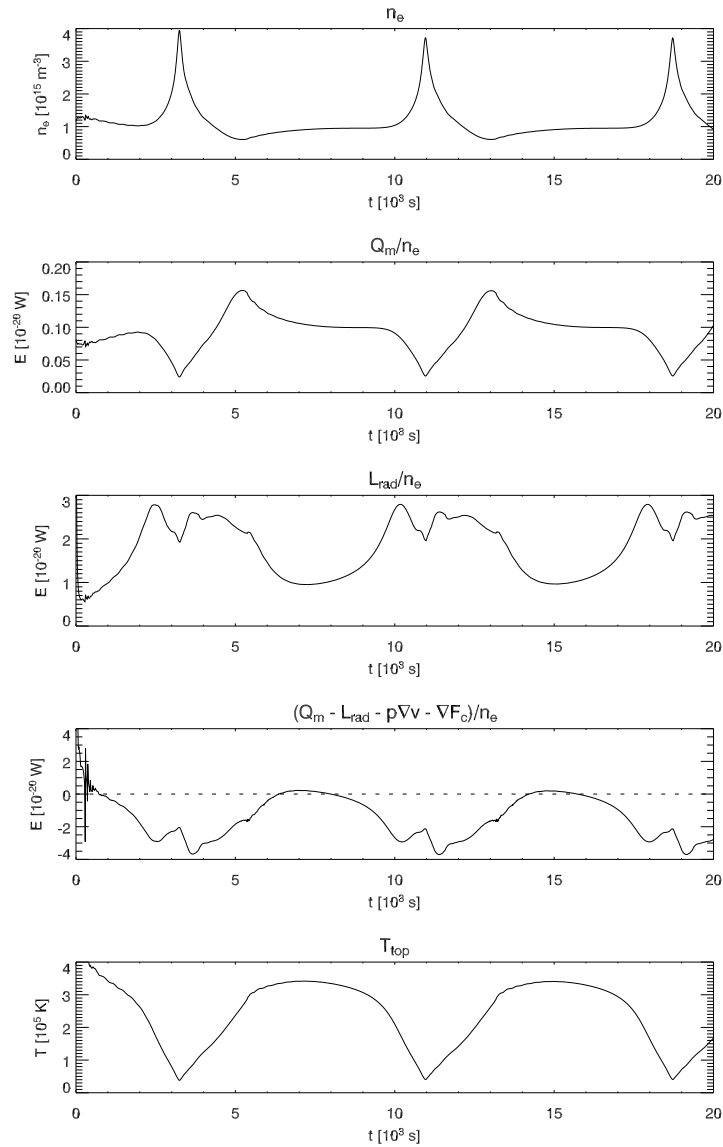


FIGURE 4.3: Energy balance at the loop apex for a damping length of $H_m = 1.25$ Mm. From *top to bottom*: electron density, n_e , mechanical heating per particle, radiative losses per particle, the sum $(Q_m - L_{\text{rad}} - p\nabla v - \nabla F_c)/n_e$ per particle (negative values mean that the loop apex is losing energy), and the temperature at the loop top.

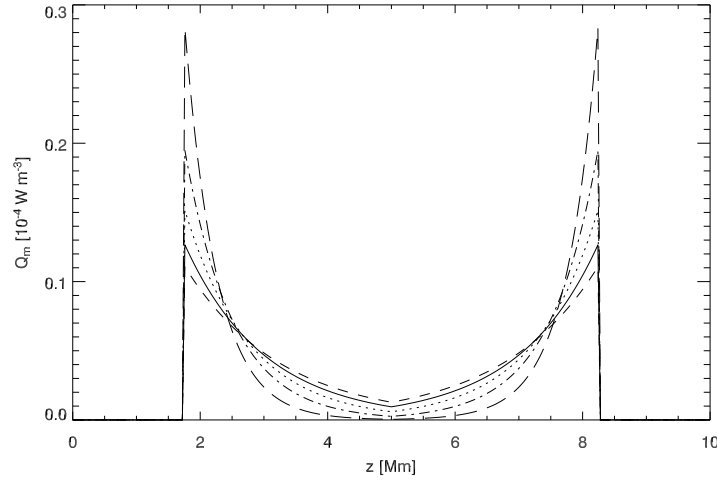


FIGURE 4.4: The mechanical heating function, $Q_m(z)$, plotted for different values of H_m . *Dashed line:* $H_m = 1.5$ Mm, *solid line:* $H_m = 1.25$ Mm, *dotted line:* $H_m = 1.0$ Mm, *dash-dotted line:* $H_m = 0.75$ Mm, *long-dashed line:* $H_m = 0.5$ Mm.

models in Fig. 4.5. For this plot, the mean temperature is defined as the average temperature over the central half of the loop, i.e. from $z = 2.5$ Mm to $z = 7.5$ Mm.

Let us consider the limiting cases first: For short damping lengths of $H_m \lesssim 0.5$ Mm, the loop decays as not enough energy is deposited in the upper part of the loop to balance the radiative and conductive losses. In this case the temperature in the loop falls during the first 15000 s to roughly 10^4 K and stays at that level for the remainder of the model run, maintained in part by the "opacity" heating term that is included in order to maintain chromospheric temperatures at roughly 7000 K. On the other hand, for longer damping lengths with $H_m \geq 1.5$ Mm, the energy deposition at the loop center is large enough to sustain a stable loop against radiative and conductive losses and an average loop temperature of $3.6 \cdot 10^5$ K (for $H_m = 1.5$ Mm) is reached and maintained (see Fig. 4.5, *dashed*). Even longer damping lengths lead to stable loops with slightly higher temperatures. The regime in between, with intermediate damping lengths of $0.75 \text{ Mm} \leq H_m < 1.5$ Mm, shows the cyclic behavior described above. In these cases, the loop exhibits a dynamic behavior, triggered by the onset of thermal instability as described in Sect. 4.3.2.

Let us focus on the *solid* line in Fig. 4.5, for a damping length of $H_m = 1.25$ Mm. The first minimum of this curve with $\langle T \rangle_{\min} = 1.4 \cdot 10^5$ K is attained at $t = 3000$ s, corresponding to the formation of the condensation region. This is followed by an increase in temperature towards a temporary plateau at $\langle T \rangle = 1.8 \cdot 10^5$ K. During this phase, the condensation region is moving down one loop leg, while the top of the loop is already reheating. After the condensation region has left the loop, the temperature rises rapidly to $\langle T \rangle_{\max} = 3.7 \cdot 10^5$ K at $t = 7200$ s. At this point in time, the net energy supply at the loop top decreases (cf. Sect. 4.3.3), and the loop starts to cool gradually. When the temperature approaches $T = 2 \cdot 10^5$ K, the radiative losses increase strongly which drastically accelerates the cooling process. As a result, a new condensation region forms, and a second minimum in mean temperature is attained at $t = 10800$ s. The period of this

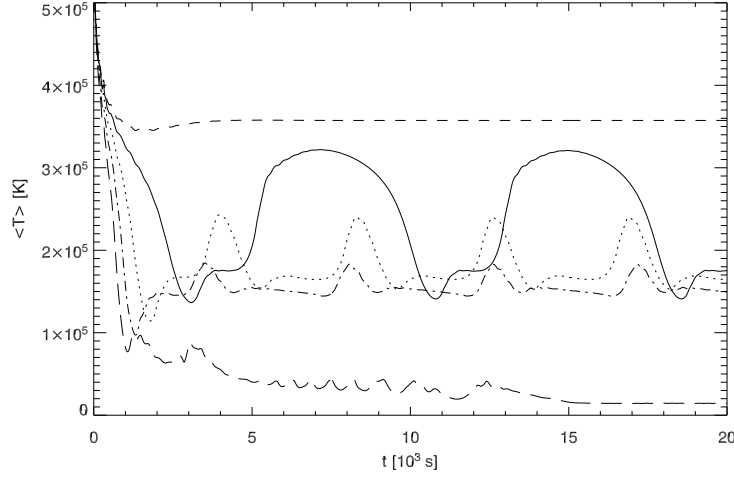


FIGURE 4.5: The influence of the damping length, H_m , on the thermal evolution of the loop. *Dashed line:* $H_m = 1.5$ Mm, *solid line:* $H_m = 1.25$ Mm, *dotted line:* $H_m = 1.0$ Mm, *dash-dotted line:* $H_m = 0.75$ Mm, *long-dashed line:* $H_m = 0.5$ Mm.

condensation cycle is $P = 7800$ s.

For the cases of shorter damping lengths, $H_m = 0.75$ Mm and $H_m = 1.0$ Mm, the formation of a condensation region works qualitatively in the same way. Let us therefore focus on the differences: As the heating is more strongly concentrated towards the footpoints of the loop, the net energy supply per particle at the loop top starts to decrease at an earlier point in time so that the maximum loop temperature attained is lower, namely $T_{\max} = 2.2 \cdot 10^5$ K for $H_m = 0.75$ Mm, and $T_{\max} = 2.6 \cdot 10^5$ K for $H_m = 1.0$ Mm compared to $T_{\max} = 3.4 \cdot 10^5$ K for $H_m = 1.25$ Mm. Due to the strong radiative losses towards $T = 2 \cdot 10^5$ K, these loops subsequently also cool faster than the hotter loop, so that the period of the condensation cycle is shorter than for $H_m = 1.25$ Mm: $P = 4600$ s for $H_m = 0.75$ Mm and $P = 4100$ s for $H_m = 1.0$ Mm. The cooling rate, $\Delta T / \Delta t$, in the temperature range $1.5 \cdot 10^5$ K $< T < 2.5 \cdot 10^5$ K is very similar for all three cases, which allows the conclusion that the increased period for the damping length of $H_m = 1.25$ Mm is mostly due to the longer duration of loop reheating and loop cooling at temperatures $T > 2.5 \cdot 10^5$ K. Simulations for longer and hotter loops (see Chap. 8) support the finding that the cooling phase from $T = T_{\max}$ up to the development of a deep dip in the temperature profile is indeed much longer than any other phase of the condensation cycle. Table 4.1 summarizes the relevant parameters for different damping lengths.

It should be noted that for all loops which form a condensation region, the minimum mean temperature is very similar, $\langle T \rangle_{\min} = 1.4\text{--}1.5 \cdot 10^5$ K. This minimum temperature is attained when the condensation region has just formed, which happens shortly after the dip in the temperature profile has developed. At this point in time, the energy balance, as discussed in Sect. 4.3.2, is very similar for all loops. This is illustrated in Fig. 4.6, which displays the temperature profiles of three different loops corresponding to the respective minimal mean temperatures. As shown in Fig. 4.5, the period of the condensation cycle depends on the damping length – the more the heating is

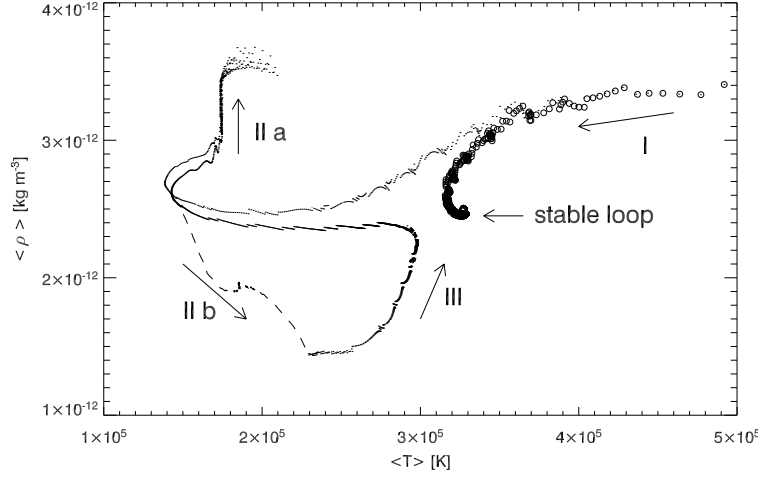


FIGURE 4.7: Limit cycle of loop evolution for a damping length of $H_m = 1.25 \text{ Mm}$ (dots) and $H_m = 1.50 \text{ Mm}$ (open circles). The phases of evolution are indicated as follows: (I) initial cooling, (II a) condensation, (II b) simultaneous evolution of the hot part of the loop (dashed line), (III) loop reheating and chromospheric evaporation.

localized near the footpoints, the sooner the thermal instability sets in.

4.3.5 Limit Cycle of Loop Evolution

As pointed out previously, the thermal evolution of the model coronal loop shows periodicity for a significant parameter range of the damping length. To illustrate this cyclic pattern, Fig. 4.7 shows the mean density, $\langle \rho \rangle$, of the loop as a function of mean loop temperature, $\langle T \rangle$. From here on, the mean values are defined as the average quantities over the region of the loop which lies above the transition region, bounded by the points where the temperature crosses $T = 10^5 \text{ K}$ in both loop legs. The exact choice of this cut-off value does not significantly influence the results and could be set to any temperature $T > 2 \cdot 10^4 \text{ K}$. In contrast to the convention used in the previous section, this definition is independent of motions of the chromosphere–transition region boundary, while the former definition was used to describe the decaying loop together with the other solutions. Figure 4.7 displays the loop evolution for two different damping lengths: For $H_m = 1.50 \text{ Mm}$, the loop approaches a stationary solution (open circles), while for $H_m = 1.25 \text{ Mm}$ (dots), the loop enters a limit cycle after its initial cooling, expressing the fact that the loop evolution becomes independent of the initial boundary conditions. The evolution can be divided into four parts:

- I The 10 Mm loop first cools down from its initial mean temperature of $\langle T \rangle_0 = 5 \cdot 10^5 \text{ K}$ to $\langle T \rangle \approx 1.4 \cdot 10^5 \text{ K}$.
- II a The onset of condensation is seen as an increase in the mean density of the loop. The mean temperature starts to rise again shortly before the condensation region leaves the loop, which is due to the fact that one side of the loop is already reheating while the condensation region is moving to the other side. The stage of evolution when the condensation region

drains from the loop is seen as a sudden drop in density from $\langle \rho \rangle = 3.6 \cdot 10^{-12} \text{ kg m}^{-3}$ to $\langle \rho \rangle = 1.4 \cdot 10^{-12} \text{ kg m}^{-3}$. One point is plotted for each 10 s of the evolution, and the lack of points in this fairly large interval of mean density illustrates that the condensation region leaves the loop very quickly (but still with a velocity that is much slower the free-fall velocity of $v_{\text{ff}} = 31.2 \text{ km/s}$ for this loop).

- II b As the mean density of the loop during the condensation phase is dominated by the condensation region itself, also the density in the hot part of the loop alone is evaluated: Due to the formation of a condensation region, the density in the adjacent parts of the coronal loop decreases which leads to an increase in temperature. The mean values of the hot part of the loop for this stage of evolution is plotted as a *dashed line* in Fig. 4.7.
- III After the condensation region has drained, the evacuated loop reheats and chromospheric matter is evaporated, as indicated by the increase in mean density. When the loop reaches $\langle T \rangle = 3 \cdot 10^5 \text{ K}$, the radiative losses at the loop top are no longer balanced by the energy supply through mechanical heating, conductive flux, and enthalpy flux, so that the temperature starts to decrease and the cycle repeats.

Cyclic evolution of coronal loops was studied for the first time by [Kuin & Martens \(1982\)](#). In their semi-analytical model, they treated the coronal loop as a zero-dimensional system, characterized by a mean temperature and density, which is coupled to the underlying chromosphere. Depending on the strength of the coupling, the authors obtained different classes of solutions, namely solutions converging towards a fixed point and solutions approaching a limit cycle. As the loop was treated as one zero-dimensional system, however, Kuin & Martens were not able to model any spatially localized condensation which in our work leads to the upward-arching branch in the $\langle \rho \rangle (\langle T \rangle)$ diagram of Fig. 4.7. Considering the hot coronal part of the loop alone, in contrast, reconciles our spatially resolved loop model with the semi-analytical approach of Kuin & Martens (cf. Fig. 4.7, *dashed line*). More details about the work of Kuin & Martens will be given in Chap. 7.

4.3.6 Remarks on Rayleigh-Taylor Instability

Loop configurations with a density inversion at the center are unstable against Rayleigh-Taylor instability if $\nabla \rho \cdot \vec{g} < 0$. The question is: Would a Rayleigh-Taylor instability inhibit the condensation of plasma in the upper part of a coronal loop? To estimate the importance of Rayleigh-Taylor instability compared to the dynamic time scale of our model loop, I followed the work of [Chandrasekhar \(1961\)](#) and calculated the growth rate, ω , of the amplitude of normal modes of the form $A(\vec{x}, t) \propto \exp[i(k_x x + k_y y) + \omega t]$ as a result of a density perturbation near the boundary between two incompressible, inviscid fluids of uniform densities, ρ_2 and ρ_1 ($\rho_2 > \rho_1$), permeated by a uniform magnetic field parallel to the direction of the gravitational force. One finds that an upper limit for the growth rate, ω , of the perturbation is given by

$$\omega_{\text{max}} = \frac{\sqrt{4\pi\mu}g_{\parallel}}{B_0} (\sqrt{\rho_2} - \sqrt{\rho_1}). \quad (4.3)$$

Inserting typical values for the formation of a condensation region of $\rho_1 = 3 \cdot 10^{-12} \text{ kg m}^{-3}$, $\rho_2 = 4 \cdot 10^{-11} \text{ kg m}^{-3}$, $g_{\parallel} = 0.04 \cdot g_{\odot}$ (corresponding to a width of the condensation region of

0.2 Mm), and $B_0 = 1$ mT, a time scale of $T = \frac{2\pi}{\omega} \approx 22\,000$ s is obtained, which is more than an order of magnitude larger than the time scale over which the condensation region evolves. I thus conclude that the onset of Rayleigh-Taylor instability does not fundamentally affect the formation of the condensation region. It might eventually lead to a dissolution of the condensation region, but at that stage, this region is already moving towards the loop footpoint, which would also happen if the condensation region were split up in pieces. Moreover, it was checked that the perturbation of the loop geometry due to the accumulation of mass in the center of the loop is negligible.

4.3.7 Spectral Signature of Condensation in Transition Region Lines

The fact that the numerical code used in this work self-consistently solves the non-equilibrium ionization rate equations for different atomic species offers the possibility of synthesizing optically-thin transition region lines. The inclusion of non-equilibrium ionization effects is of vital importance when studying the spectral signature of a plasma in a *dynamic* state like in the present case.

Figure 4.8 displays the intensity variations of the lines C IV (154.8 nm, formed at $T_f \approx 1 \cdot 10^5$ K), O V (63.0 nm, $T_f \approx 2.2 \cdot 10^5$ K), and O VI (103.2 nm, $T_f \approx 3.2 \cdot 10^5$ K) during the evolution of the loop. The spectral lines are calculated by integrating the emission of the entire loop as seen vertically from the top, the line widths are given in velocity units. All three lines show periodic brightenings which have their origin in the condensation process. In the case of the C IV line, the strong increase in density at the beginning of the condensation results in high radiative losses and hence an intensity maximum. A second maximum of slightly smaller amplitude is attained when the condensation region has grown to its maximum, shortly before draining down the loop leg. Right after the condensation region has left the loop, the intensity is minimal as the loop is devoid of plasma at this stage. In the following evolution, the intensity gradually increases as chromospheric evaporation sets in again. In contrast to this, the intensity of the O VI line is maximal when the temperature is highest as the line is formed around $T \approx 3.2 \cdot 10^5$ K. When the condensation sets in and the maximal loop temperature temporarily sinks below $T = 2 \cdot 10^5$ K, the intensity in O VI almost drops to zero. The O V line, formed around $T \approx 2.2 \cdot 10^5$ K, can be considered as an intermediate case.

For a damping length of $H_m = 1.25$ Mm, the C IV total intensity varies between 1.1 W/(m² sr) and 3.8 W/(m² sr), the O V total intensity varies between 2.0 W/(m² sr) and 6.9 W/(m² sr), while the O VI total intensity varies between 0.1 W/(m² sr) and 4.8 W/(m² sr). For shorter damping lengths, the maximum temperatures of the loop are lower which results in a *decreased intensity for lines which are formed at higher temperatures*. The O VI line, for example, shows bright periodic intensity maxima for $H_m = 1.25$ Mm, while it is almost invisible for a damping length of $H_m = 0.75$ Mm. In contrast to this, the intensity range of the C IV line remains almost unaffected by a change of the damping length as the maximum loop temperature exceeds in all cases its formation temperature.

4.4 Discussion

It has been shown in this chapter that cool coronal loops can exhibit inherently dynamic behavior even under the simple assumption of a mechanical energy flux into the loop that is dissipated expo-

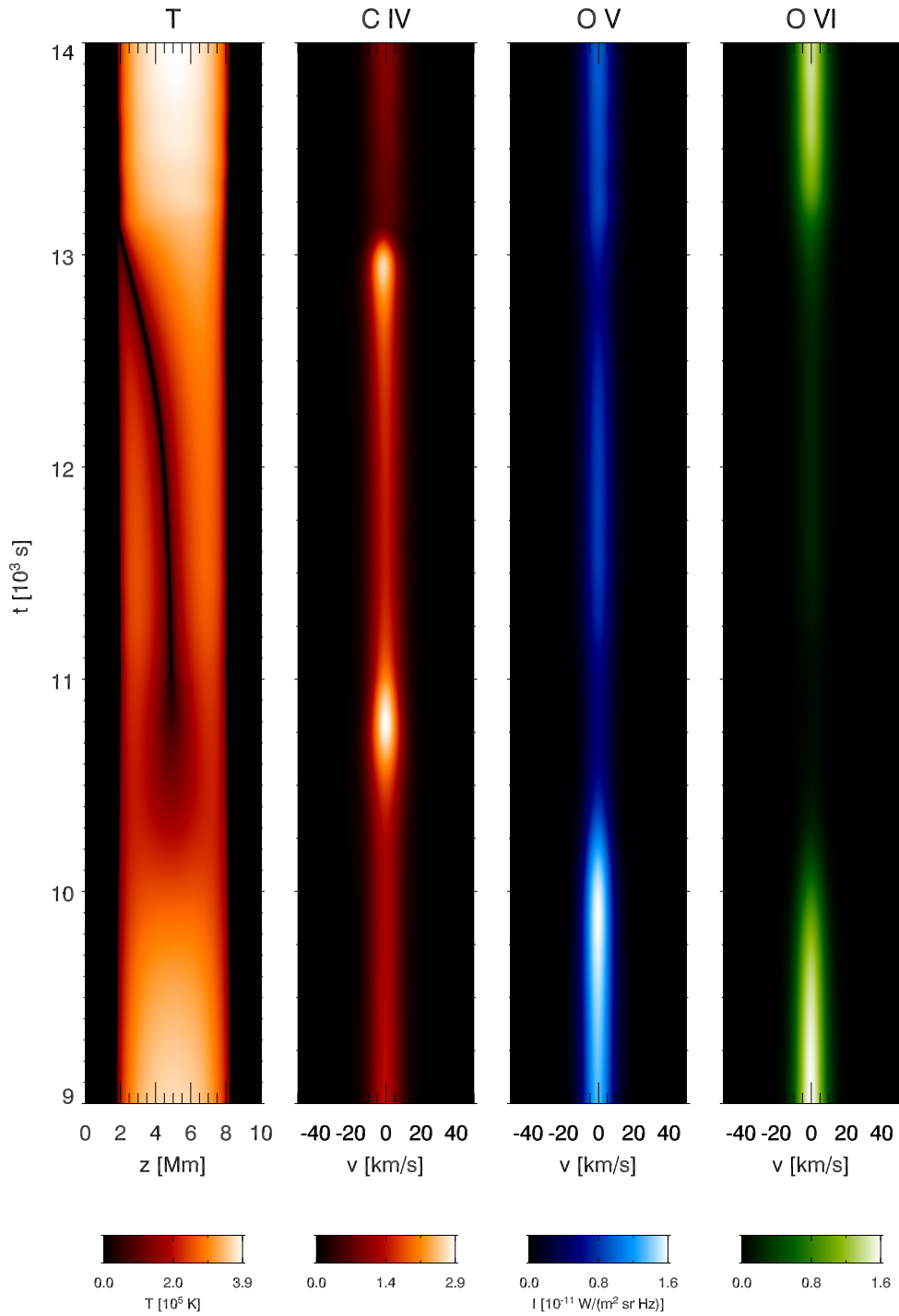


FIGURE 4.8: From left to right: Space-time plot of the loop temperature and the corresponding variations of the lines of C IV (154.8 nm), O V (63.0 nm), O VI (103.2 nm) for a damping length of $H_m = 1.25$ Mm.

nentially with a given scale height but constant in time. This scenario is interesting in the sense that no time-dependent driving mechanism is needed to generate transient brightenings in transition region lines. Simultaneous observations of, e.g., the C IV (154.8 nm) and the O VI (103.2 nm) lines would be advantageous in order to verify if this phenomenon is as ubiquitous as it seems. Recent TRACE observations of Schrijver (2001) indeed show frequent “catastrophic cooling” and evacuation of coronal loops over active regions and enhanced emission of C IV, developing initially near the loop top, followed by quick draining. Furthermore, CDS observations by Fredvik (2002) show localized brightenings in coronal loops in O V (63.0 nm) on the limb which move quickly towards the solar surface and could be interpreted as cooling plasma close to a condensation region. As most of these recent observations refer to loops that are about one order of magnitude larger than those considered here, models for longer loops will be studied in Chaps. 5 and 6. This could also help to better understand and disentangle loops of different lengths in active regions, as observed, e.g., by Spadaro et al. (2000).

The fact that the dynamic loop models described in this chapter can show strong emission in lines formed at $T \leq 10^5$ K and at the same time relatively weak emission in lines formed at higher temperatures seems promising with respect to the outstanding problem that current models predict an emission measure that is either much lower than the emission observed at $T < 10^5$ K or much higher than what is observed at $T > 10^5$ K. Further observational confirmation of the dynamics predicted here, preferably concentrating on shorter loops, would lead to a strengthening of the hypothesis that coronal heating is concentrated towards the footpoints of loops. Such knowledge would be very useful to limit the number of possible coronal heating mechanisms.

5 Catastrophic Cooling and High-Speed Downflows

Abstract

In this chapter the problem of plasma condensation and “catastrophic cooling” in solar coronal loops of 100 Mm length is addressed. I have carried out numerical calculations of coronal loops and find several classes of time-dependent solutions (static, periodic, irregular), depending on the spatial distribution of a temporally constant energy deposition in the loop. Dynamic loops exhibit recurrent plasma condensations, accompanied by high-speed downflows and transient brightenings of transition region lines, in good agreement with features observed with TRACE. Furthermore, these results also offer an explanation for the recent EIT observations of [De Groof et al. \(2004\)](#) of moving bright blobs in large coronal loops. In contrast to earlier models, it is suggested that the process of catastrophic cooling is not initiated by a drastic decrease of the total loop heating but rather results from a loss of equilibrium at the loop apex as a natural consequence of heating concentrated at the footpoints of the loop, but constant in time.

5.1 Introduction

Recent observations of the solar transition region and corona, especially with the Solar and Heliospheric Observatory (SOHO) and the Transition Region And Coronal Explorer (TRACE), have shown that magnetically closed structures in the upper solar atmosphere, commonly referred to as coronal loops, exhibit intrinsically dynamic behavior. Even in quiescent, non-flaring conditions, loops show strong temporal variability of emission in UV spectral lines and substantial plasma flows. An overview of observations of the temporal variability of active region loops with the Coronal Diagnostic Spectrometer (CDS) is given by [Kjeldseth-Moe & Brekke \(1998\)](#). They report significant changes of coronal loops over a period of one hour, in particular seen in emission lines in the temperature range between $T = 1 - 5 \cdot 10^5$ K. This variability is accompanied by large Doppler shifts, typically around $v = 20 - 100$ km/s. Recent observations with CDS and the Extreme ultraviolet Imaging Telescope (EIT) with high temporal cadence ([Fredvik 2002](#), private communication, [De Groof et al. 2004](#)) furthermore reveal spatially localized brightenings in coronal loops, moving rapidly down towards the footpoints of the loops. The fact that coronal loops can undergo rapid evacuation has been known for decades: [Levine & Withbroe \(1977\)](#), for example, report *Skylab* spectroscopic observations, compatible with “dramatic evacuation” of active region loops triggered by rapid, radiation dominated cooling. A detailed study of “catastrophic cooling” and evacuation of quiescent coronal loops observed with the TRACE instrument is presented by [Schrijver \(2001\)](#). He analyzes image sequences taken in different spectral passbands and finds that loop evacuation occurs frequently after plasma in the upper parts of the loops has cooled to

transition region or lower temperatures. The cooling process is often accompanied by emission in Ly_α and CIV (154.8 nm), developing initially near the loop top. Thereafter, cool plasma is observed to slide down on both sides of the loop, forming clumps which move with velocities of up to 100 km/s. The downward acceleration of these plasma clumps as inferred from these observations is significantly less than the gravitational acceleration on the solar surface. According to the observations of Schrijver (2001), this process of dramatic cooling and evacuation is a rather common one. Further observational evidence of “blobs” of plasma falling down towards the solar surface along magnetic field lines is presented by De Groof et al. (2004), based on high-cadence time series of simultaneous EIT (30.4 nm) and Big Bear H_α data.

In this chapter, numerical models of coronal loops are presented which exhibit a wide range of dynamics using a very simple heating function that is exponentially decreasing with height, but *constant* in time. A key feature of these models is the recurrent formation of plasma condensations, followed by loop evacuation, as described in Chap. 4 and in Müller et al. (2003), which offers a unifying explanation for different aspects of recent observations.

5.1.1 Loop Heating

The energy input into the coronal loop is parametrized in the same way as in Chap. 4 by specifying the energy flux at the footpoints of the loop, F_{m0} , and assuming a mechanical energy flux that is constant up to a height z_1 and then decreases exponentially for $z \geq z_1$ as

$$F_m(z) = F_{m0} \exp[-(z - z_1)/H_m] \quad (5.1)$$

with a damping length H_m . In the models presented below, H_m will be varied between 2 and 12.5 Mm for a loop of 100 Mm length. A mechanical energy flux of $F_{m0} = c \cdot 150 \text{ W/m}^2$ is used, with the normalization constant $c = 1/(1 - \exp[-(L/2 - z_1)/H_m])$ and $z_1 = 1.75 \text{ Mm}$. The normalization constant ensures that the total energy input into the loop is the same, irrespective of the damping length H_m . The heating rate, i.e. the energy deposition per unit time and unit volume, is given by the divergence of the energy flux, $Q_m = -\nabla F_m$. Figure 5.1 displays graphs of the heating rate for different values of the damping length, H_m . The damping length H_m controls whether the heating is concentrated near the footpoints or more evenly distributed along the loop. An exponentially decaying heating function was first suggested by Serio et al. (1981) and seems to be supported by recent observations (Aschwanden et al. 2000, 2001) as well as by numerical simulations of Gudiksen & Nordlund (2002).

5.1.2 Initial State

The coronal loop model studied here has a total length of 100 Mm, composed of a semicircular arch of 98 Mm length and a vertical stretch of 1 Mm length at each end. A static initial state is obtained by prescribing a large energy dissipation length of $H_m = 12.5 \text{ Mm}$, which results in a loop apex temperature of $T = 6.8 \cdot 10^5 \text{ K}$. The temperature along the loop of the initial state is plotted in Fig. 5.2.

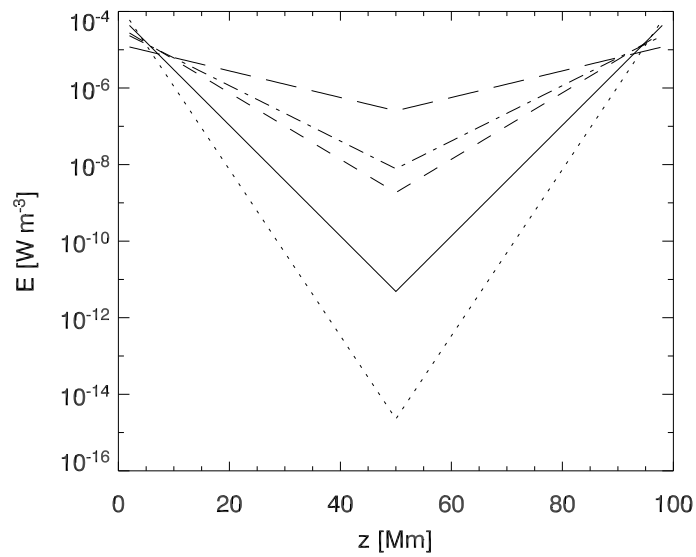


FIGURE 5.1: Prescribed heating rate for different values of the damping length: $H_m = 2$ Mm (*dotted*), $H_m = 3$ Mm (*solid*), $H_m = 5$ Mm (*dashed*), and $H_m = 6$ Mm (*dash-dotted*), and $H_m = 12.5$ Mm (*long dashes*, heating function for static initial model). The total heat input into the loop is the same for all cases.

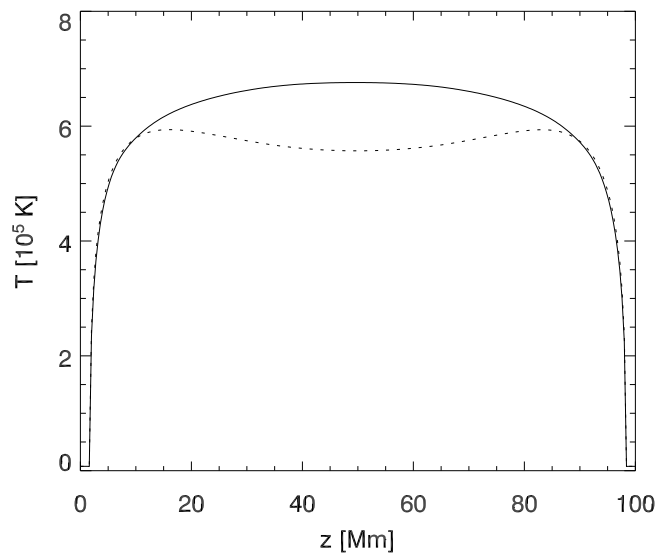


FIGURE 5.2: Temperature along the coronal loop. Initial state (*solid line*, $H_m = 12.5$ Mm) and stable solution for $H_m = 6$ Mm (*dotted line*).

5.2 Plasma Condensation due to Thermal Instability

For very short damping lengths of the heating function, solutions with a hot loop apex may no longer exist due to the insufficient energy supply to the center, i.e. the top of the loop, as shown by Antiochos et al. (1999), Karpen et al. (2001) and Müller et al. (2003). In this case, a thermal instability occurs and leads to a runaway cooling process, also called *catastrophic cooling*, accompanied by plasma condensation. This process has been discussed in detail in Chap. 4. Unless this condensation region is gravitationally supported, for example by means of a dip in the magnetic field lines, to maintain a stable prominence-like state, such a configuration is unstable and the dense condensation region eventually moves down the loop legs and drains through the footpoints. The depleted loop then reheats quickly as its heat capacity is very low (at this stage there is much less mass in the loop but the heating remains constant) and is filled again by chromospheric evaporation. Exactly how this cycle of plasma condensation, draining, and chromospheric evaporation is realized depends strongly on the spatial dependence of the energy deposition.

As an illustration, Fig. 5.3 shows three snapshots of the temperature, density and radiative losses during the catastrophic cooling process: The left panels ($t = t_1$) show the loop as it is cooling predominantly around the apex as a result of footpoint-centered heating. In this early phase, the density is still monotonically decreasing with height and the radiative losses around the loop apex are small. The central panels ($t = t_2$) show the loop with a pronounced temperature minimum at the loop apex. A flow towards the loop apex has developed which is accreting mass and results in a density inversion. The loop top therefore cools even faster and starts radiating strongly: catastrophic cooling has set in. The right panels ($t = t_3$) finally show how the gravitationally unstable condensation region falls towards one footpoint. After it has drained, the low-density loop reheats and the cycle starts again. In Chap. 4, the physical processes leading to this evaporation-condensation cycle were studied, together with its application to small ($L = 10$ Mm) transition region loops, which can just barely be spatially resolved with the currently available instruments. This chapter focuses on plasma condensations in longer coronal loops ($L = 100$ Mm), where the same process can induce significantly stronger flows and greater variations in the spectral signature, due to the longer acceleration phase along the loop. More generally, the aim of this chapter is also to work out the different types of loop evolution that result from different damping lengths of the heating function.

It is interesting to note that a time-dependent evolution for time-independent heating over short damping lengths has already been described in a different context by Hearn et al. (1983) and Korevaar & Hearn (1989). However, they applied their results not to solar coronal loops, but to open coronal regions surrounding hot stars. A connection of their work to the results presented here will be pointed out in Chap. 8.

Cyclic evolution of coronal loops was studied for the first time by Kuin & Martens (1982). In their semi-analytical model, they treated the coronal loop as an integrated system, coupled to the underlying chromosphere. A comparison of their work with our hydrodynamical simulations is given in Chaps. 4 and 7.

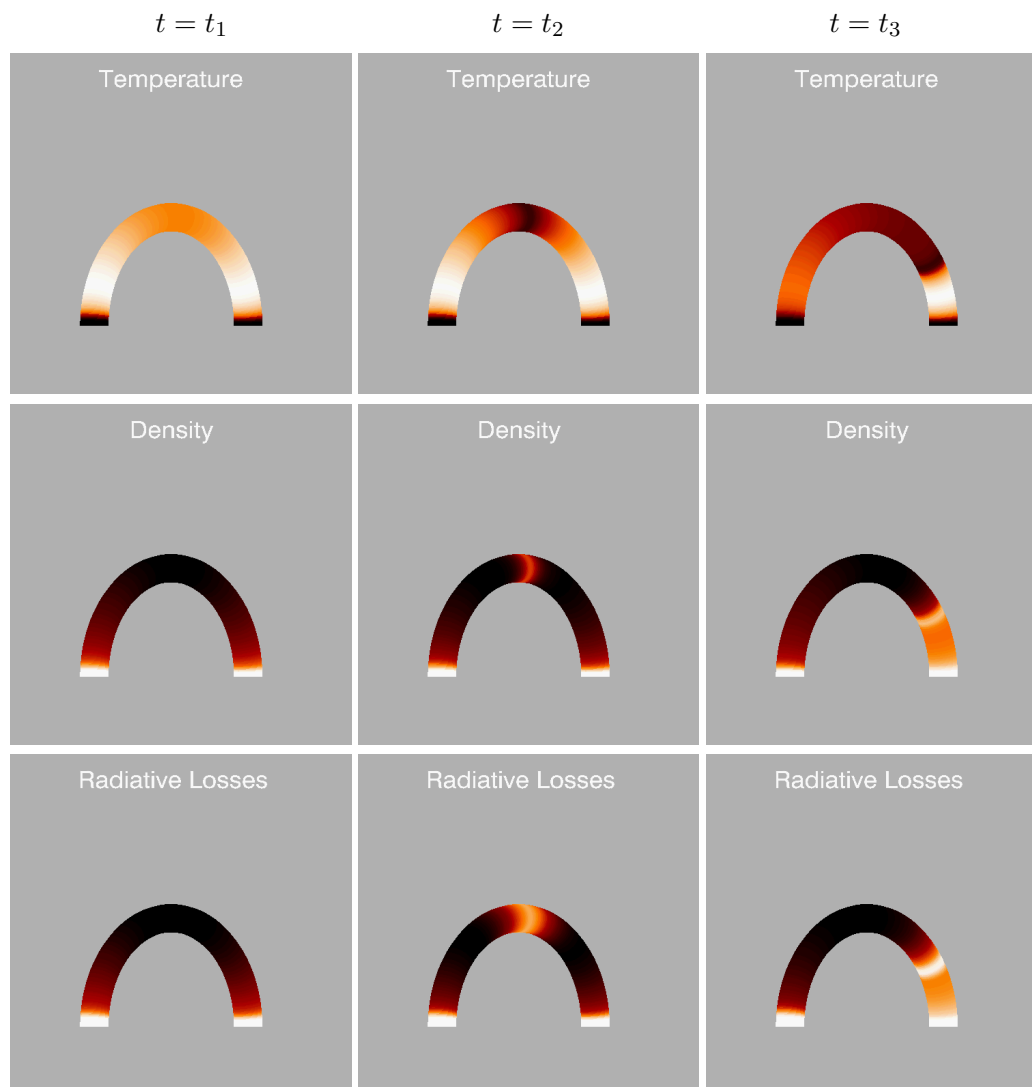


FIGURE 5.3: Illustration of the formation and fall of a condensation region. Left panels ($t = t_1$): Due to the footpoint-centered heating, the loop cools, predominantly around the apex. In the early phase, the density is still monotonically decreasing with height. Central panels ($t = t_2$): A flow towards the loop apex has developed which is accreting mass and results in a density inversion. The loop top therefore cools even faster and starts radiating strongly: catastrophic cooling has set in. Right panels ($t = t_3$): The condensation region is gravitationally unstable and falls towards one footpoint. After it has drained, the low-density loop reheats and the cycle starts again.

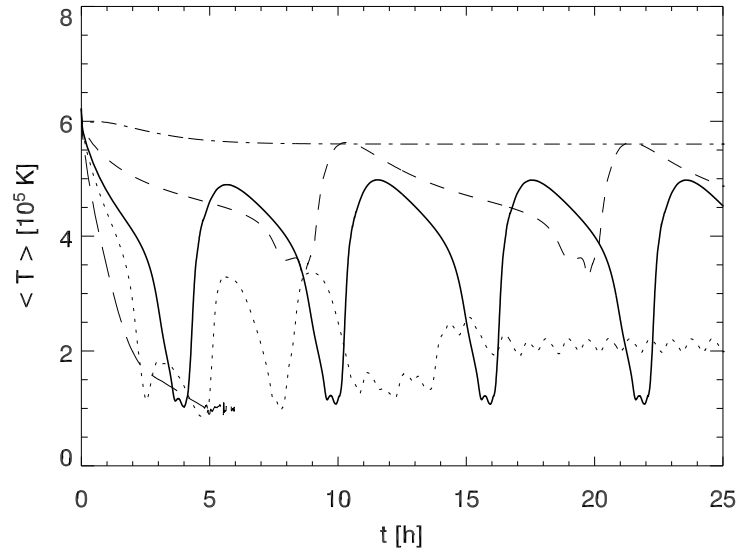


FIGURE 5.4: Evolution of mean temperature, $\langle T \rangle$, as a function of time, for four different damping lengths of the heating function: $H_m = 2$ Mm (dotted), $H_m = 3$ Mm (solid), $H_m = 5$ Mm (dashed), $H_m = 6$ Mm (dash-dotted). For comparison, the long-dashed line shows $\langle T \rangle(t)$ for a loop model where the heating is switched off at $t = 0$.

5.3 Results

5.3.1 Different Types of Loop Evolution

For large damping lengths ($H_m \geq 6$ Mm) and a prescribed energy flux as described in Sect. 5.1.1, a stable, static loop solution is attained. Figure 5.2 shows the temperature along the loop for $H_m = 6$ Mm, which has a mean temperature of $\langle T \rangle = 5.3 \cdot 10^5$ K.¹ For shorter damping lengths, when the heating is more concentrated at the footpoints, the loop loses its thermal equilibrium and exhibits a dynamic evolution. Figure 5.4 shows the mean temperature, $\langle T \rangle$, of a $L = 100$ Mm loop as a function of time for damping lengths of $H_m = 2, 3, 5$, and 6 Mm. It is found that for 2.5 Mm $< H_m < 6$ Mm, the loop shows a periodic variation of $\langle T \rangle$ due to the evaporation-condensation cycle as described in Chap. 4. For even shorter damping lengths ($H_m \leq 2.5$ Mm), the evolution of $\langle T \rangle$ is irregular and shows intermittency of hot phases and strongly fluctuating cool phases. This type of intermittent behavior is well-known from chaotic non-linear systems. For comparison, Fig. 5.4 displays also $\langle T \rangle(t)$ for a loop model where the heating is switched off at $t = 0$ (long-dashed line). In this case, the loop plasma simply drains on both sides of the loop with flow speeds of $v < 15$ km/s, and the loop cools down to chromospheric temperatures without any plasma condensation forming. Let us examine the different types of dynamic solutions in more

¹Throughout this work, the mean values are defined as the average quantities over the region of the loop which lies above the transition region, bounded by the points where the temperature crosses $T = 10^5$ K in both loop legs (the exact choice of this cut-off value does not significantly influence the results and could be set to any temperature $T \gtrsim 2 \cdot 10^4$ K).

detail to see which phenomena accompany the condensation process. Figure 5.5 displays space-time diagrams of the loop temperature, $T(z, t)$, for $H_m = 2, 3, 5$ Mm. The left and the center plot show two different kinds of recurrent formation of plasma condensations:

In the first case ($H_m = 5$ Mm), one condensation region forms at the loop apex and is then accelerated on its way down, resulting in flow velocities in the wake of the falling plasma blob of up to $v \approx 100$ km/s. When this condensation region encounters the transition region near the loop footpoint, it is strongly decelerated by the pressure gradient of the underlying plasma and the velocity profile forms a shock front. As the compression is approximately adiabatic, this leads to a transient heating of the transition region plasma. The direction in which the blob starts to move is decided by small asymmetries of the pressure around the loop apex. A small increase of the deposited energy in one loop leg (e.g. 1%) is sufficient to trigger a motion of the blob in the opposite direction. In Sect. 5.3.4, the velocity profiles of the flow will be discussed in more detail. A possible connection to the recent observations of falling plasma blobs by De Groof et al. (2004) will be studied in detail in Chap. 6.

The center plot of Fig. 5.5 shows the second type of recurrent condensations which occurs if the damping length is slightly reduced with respect to the first case ($H_m = 3$ Mm). Here, two condensation regions form simultaneously and then drain down both loop legs. Note that in agreement with the results obtained in Chap. 4 for short loops, the period of the condensation cycle decreases with decreasing damping length as the loss of equilibrium due to insufficient heating of the upper part of the loop occurs sooner.

The right panel of Fig. 5.5 shows the most complex evolution of this set of numerical experiments: As the heating is even more concentrated towards the footpoints, the evolution of temperature along the loop with time reflects the persistent battle between loop heating and radiative cooling: The loop first cools down from its initial state to $T \approx 1.1 \cdot 10^5$ K and forms two condensation regions at $t = 8\,000$ s (≈ 2.2 h). After these have drained, the loop starts reheating. Due to the concentration of the heating to low heights, however, not enough energy is deposited in the upper part of the loop to prevent it from repeated radiative cooling and condensation at $t = 12\,000$ s. At $t = 19\,000$ s, the loop recovers from its catastrophic cooling and enters a quiet, warm phase, during which the flow speed does not exceed $v = 16$ km/s. At $t = 25\,000$ s, a new instability sets in and leads to the formation of two new condensation regions whereupon flow speeds of up to $v = 95$ km/s are reached. The reflections of the shock fronts meet near the loop apex and yield to a transient temperature increase there. At $t = 30\,000$ s, a new phase of evolution starts: small condensation regions are recurrently formed in one leg of the loop, but due to the footpoint-centered heating function, the loop does not reach temperatures of more than $T = 3.9 \cdot 10^5$ K before collapsing again. At $t = 54\,000$ s, the loop enters a periodic phase where condensation regions are recurrently formed in the right loop leg. How long the different phases of loop evolution last is dependent on small variations in the radiative loss rate. “Chaotic” evolution of the loop for the entire duration of the longest simulation run ($2 \cdot 10^5$ s) was observed when including the non-equilibrium ionization of only hydrogen and helium, while the loop reached a periodic solution at $t = 54\,000$ s (as described above) when also accounting for the non-equilibrium ionization of carbon and oxygen.

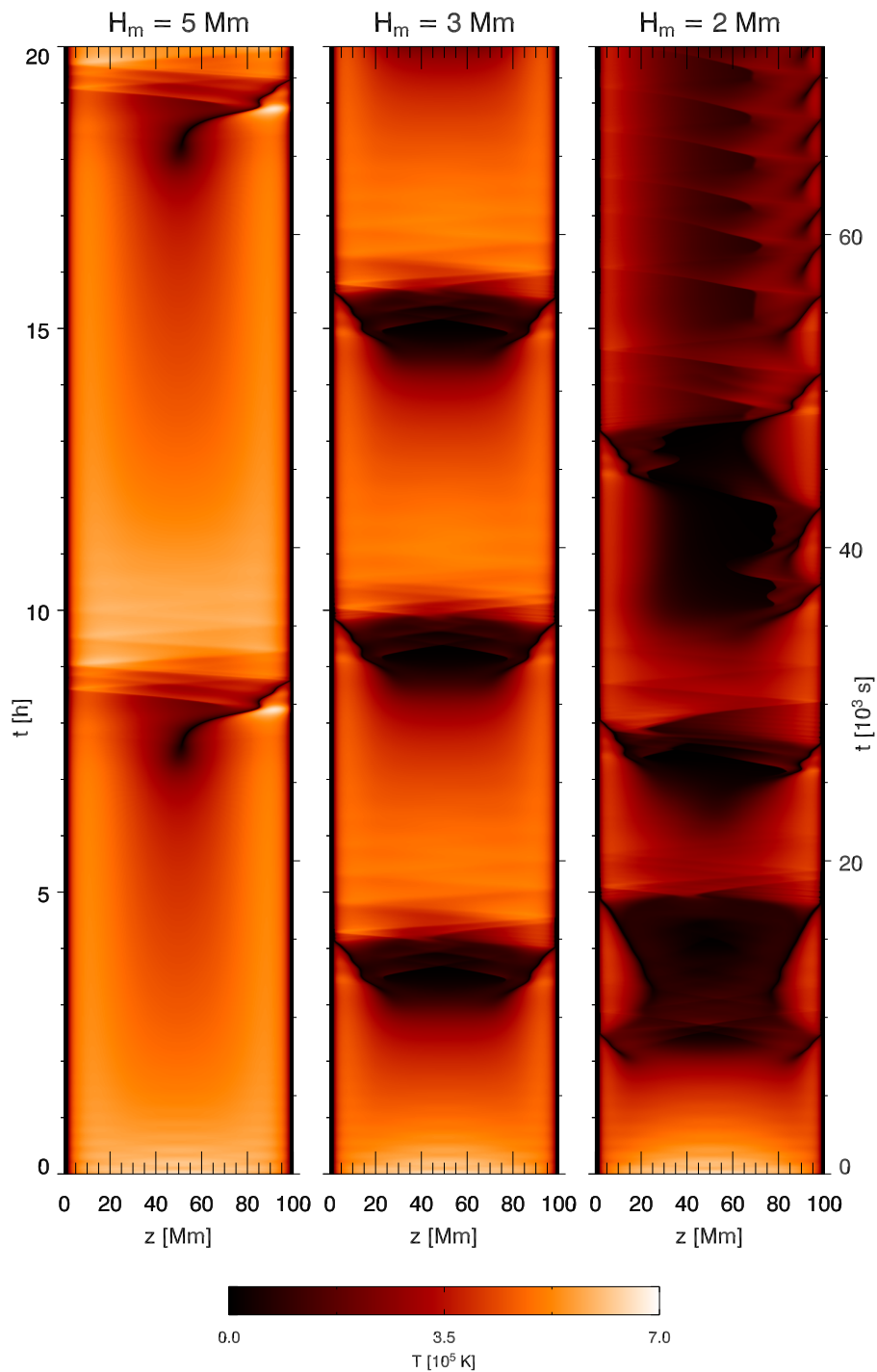


FIGURE 5.5: Evolution of the temperature along the loop, $T(z, t)$, for three different damping lengths of the heating function: $H_m = 5$ Mm (left), $H_m = 3$ Mm (center), $H_m = 2$ Mm (right). The loop footpoints are at $z = 0$ and 100 Mm, the apex is at $z = 50$ Mm.

5.3.2 Classification of Loop Evolution

One way of representing the temporal evolution of coronal loops is in terms of phase diagrams in $\langle p \rangle - \langle T \rangle$ space. Figure 5.6 shows such a phase diagram for a static loop ($H_m = 6$ Mm, *dash-dotted*), a periodically condensing loop ($H_m = 3$ Mm, *solid*), and an irregular loop ($H_m = 2$ Mm, *dotted*). It is seen that the stable loop approaches a fixed point in $\langle p \rangle - \langle T \rangle$ space, while the

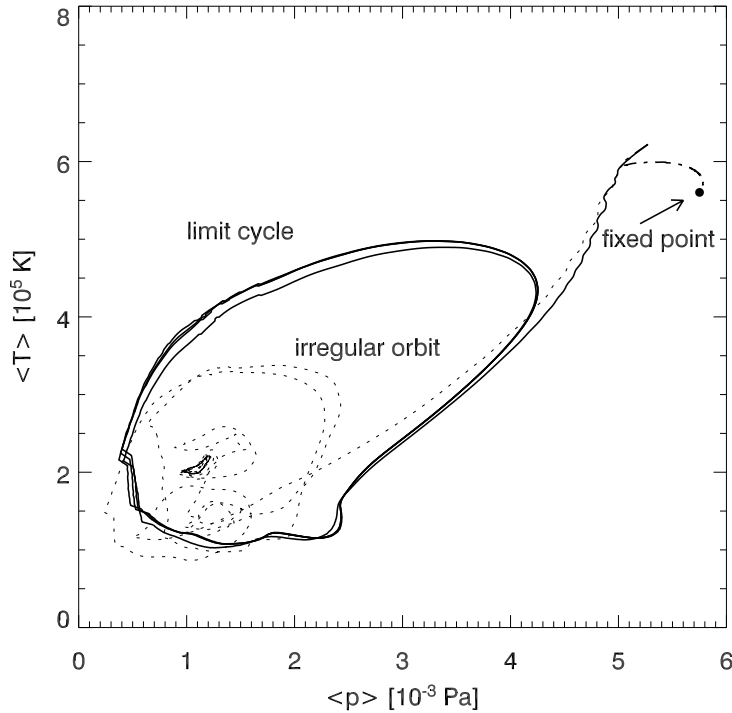


FIGURE 5.6: Mean temperature, $\langle T \rangle$, of the loop, as a function of mean pressure, $\langle p \rangle$, for a loop of total length $L = 100$ Mm. *Dotted*: $H_m = 2$ Mm, *solid*: $H_m = 3$ Mm, *dash-dotted*: $H_m = 6$ Mm.

periodically condensing loop traces out limit cycles. On the other hand, the irregular loop exhibits a pattern that is composed of a multitude of small intersecting paths, occasionally interrupted by larger cycles corresponding to the temporarily stable phases of the loop.

5.3.3 Where in a Coronal Loop do Condensation Regions Form?

In the beginning of the cooling process, the evolution of the temperature as a function of loop length is very similar for the two cases of $H_m = 3$ Mm and $H_m = 5$ Mm. This raises the question why two condensation regions form in the wing of the loop in one case and only one central condensation region in the other case, where the heating is less concentrated towards the footpoints.

Some Consideration on the Energetics

In order to better understand the formation of the condensation region it is also helpful to study the deposition and transport of the energy. If the ratio of the damping length to the loop length is large, stable coronal loops reach the maximum temperature near the loop top. In contrast, stable loops with a smaller ratio of damping length to loop length reach the peak temperature well below the apex and have a rather flat temperature profile in the central part of the loop. For instance, a stable 100 Mm long loop with $H_m = 6$ Mm reaches a maximum temperature of $5.9 \cdot 10^5$ K some 16 Mm above its footpoints, while the central 80 Mm, i.e. most of the loop, show only a 6% change in temperature, with a local temperature minimum of $5.6 \cdot 10^5$ K at the apex. In this model, the loop top is not predominately heated by the mechanical heating as defined in Eq. (5.1). The rapid exponential decrease of the heating can sustain high coronal temperatures only up to some 10 Mm height above each footpoint. Above that height the plasma is mainly heated by heat conduction. In an equilibrium situation this leads to a temperature dip at the loop apex. As the heat conduction is efficient at high temperatures the resulting temperature profile is rather flat in the upper part of the loop.

If the heating is more and more concentrated to the footpoints (by decreasing H_m), the peak temperature becomes smaller and occurs at lower heights. This reduces the heat input through heat conduction into the upper part of the loop, and finally the heat conduction can no longer balance the radiative losses and catastrophic cooling sets in. This clarifies why the catastrophic drop in temperature can set in over a very wide range of the loop, basically in the whole region between the temperature maxima (cf. middle and right panel of Fig. 5.5 and upper left panel of Fig. 5.7).

Off-center Formation of Condensation Regions

The upper left panel of Fig. 5.7 shows the temperature profiles of the $H_m = 3$ Mm loop for five different time steps. In the first time step, $t = 30\,000$ s, the loop is already in the cooling phase, and the temperature decreases with time throughout the central part of the loop. The cooling is dominated by radiation, with total radiative losses of $L_r = \Phi(T) \cdot n_e \cdot n_H \approx \Phi(T) \cdot n_e^2$. The radiative loss function, $\Phi(T)$, is determined by the ionization (non-)equilibrium of the model atoms included in the calculation and is therefore time-dependent. However, if the ionization of the loop plasma does not depart too strongly from equilibrium, the radiative losses peak around $T \approx 2 \cdot 10^5$ K, as shown in the upper right panel of Fig. 5.7. This means that plasma of a given electron density cools more efficiently at $T = 2 \cdot 10^5$ K than at $T = 4 \cdot 10^5$ K. On the other hand, the density enters quadratically into the radiative loss function, so that a local density enhancement anywhere leads to a strongly increased cooling. Let us concentrate on the time step $t = 31\,000$ s (*dotted line*) and compare the different panels on the left side of Fig. 5.7: It is seen that the total radiative losses have developed two local maxima in the wings of the loop, which subsequently lead to local density maxima at $t = 33\,000$ s (*dash-dotted line*). This initiates the formation of two condensation regions, as seen by the drastic density increase at later time steps. At the earlier time $t = 31\,000$ s, however, these local maxima are not yet accompanied by local density maxima and arise at a temperature of $T \approx 3 \cdot 10^5$ K (right center panel of Fig. 5.7), which is not the location of the maximum of the radiative loss function, $\Phi(T)$. The total radiative losses, $L_r \approx \Phi(T) \cdot n_e^2$, however, peak here and hence lead to the formation of lateral condensation regions. The lower right panel of Fig. 5.7 shows the strong density decrease towards the cooler center of the loop

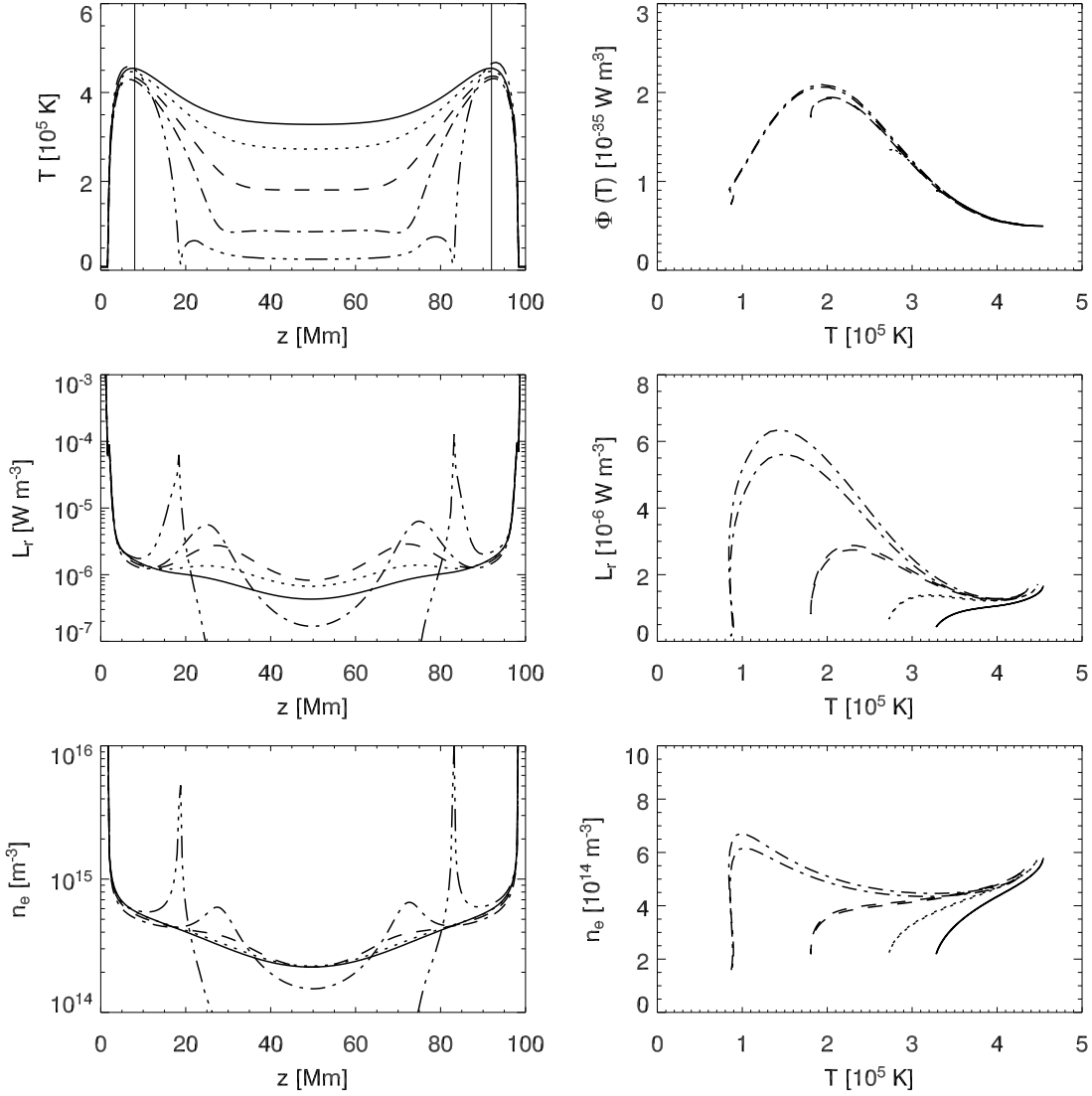


FIGURE 5.7: Formation of two simultaneous, lateral condensation regions for $H_m = 3$ Mm. *Left* panels, as functions of loop length: loop temperature (*top*), total radiative losses (*middle*), electron density (*bottom*). *Right* panels, as functions of loop temperature: radiative loss function (*top*), total radiative losses (*middle*), electron density (*bottom*). The following time steps are plotted: $t = 30\,000$ s (*solid*), $t = 31\,000$ s (*dotted*), $t = 32\,000$ s (*dashed*), $t = 33\,000$ s (*dash-dotted*), $t = 34\,000$ s (*dash-dot-dotted*). The *right* panels display only data of the central part of the loop, between the two vertical lines shown in the *upper left* panel, for the first 4 time steps. In some cases (*dashed* and *dash-dotted* curves in the *middle* and *lower right* panels) two branches are seen because of a slightly different evolution of the two loop legs.

which prevents the formation of a central condensation region.

Formation of Central Condensation Regions

Let us now compare the results obtained for a damping length of $H_m = 3$ Mm with those for $H_m = 5$ Mm. In the upper left panel of Fig. 5.8, the temperature profiles of the $H_m = 5$ Mm loop for six different time steps are plotted. As in the previous case, the loop is in its cooling phase, with a local temperature minimum at the loop apex, and cools fastest around the apex. In contrast to the $H_m = 3$ Mm case, however, the density gradient, $\partial n_e / \partial z$, near the apex is significantly shallower than in the previous case. This is due to the larger damping length which means that a larger fraction of the energy is dissipated higher up in the loop.² Therefore, a local maximum of the total radiative losses forms at the loop apex at $t = 22\,000$ s (middle left panel, *dotted line*). The middle right panel displays the total radiative losses, L_r , as a function of temperature, and it is seen that for $T < 4 \cdot 10^5$ K, $L_r(T)$ increases monotonically with decreasing temperature. Consequently, a local density maximum forms at the loop apex at $t = 26\,000$ s (lower left panel, *dash-dotted line*) and evolves by catastrophic cooling into a condensation region.

5.3.4 Formation of a Shock Front

In a hydrostatic configuration, the gravitational force acting on the plasma is balanced by the pressure gradient. As an illustration of a temporarily static phase of the coronal loop with $H_m = 3$ Mm, the upper left panel of Fig. 5.9 shows the component of the gravitational acceleration parallel to the loop, $g_{\parallel}(z)$, and the acceleration due to the pressure gradient, $\nabla p(z) / \rho(z)$, along the coronal part of the loop at $t = 32\,000$ s. It is seen that these two quantities compensate each other, and due to this equilibrium, the plasma in the loop is nearly static (the velocity is displayed in the upper right panel). At $t = 34\,400$ s, however, a loss of equilibrium has occurred and the gravitational force is no longer balanced by the pressure gradient (lower left panel): In the central part of the loop, the pressure gradient has dropped to very small values, while close to the footpoints, it is more than an order of magnitude higher than the gravitational acceleration. The reason why ∇p becomes much smaller in the central part of the loop than in hydrostatic equilibrium is the drastic decrease of the temperature (cf. Fig. 5.7, upper left panel) which causes a strong decrease in the pressure. This explains the velocity profile seen in the lower right panel: In the central part of the loop, the plasma is accelerated to velocities very close to the free-fall speed, indicated by the *dashed line*, and then strongly decelerated in the lower parts of the loop, resulting in a characteristic shock profile (Positive values of v denote a flow in the positive z -direction. A downflow in the left loop leg ($z < 50$ Mm) is thus characterized by velocities $v < 0$, while a downflow in the right loop leg ($z > 50$ Mm) has velocities $v > 0$).

5.3.5 Velocity Profiles and Acceleration of the Condensation Region

In order to compare these results with the velocities and accelerations deduced from observations of “moving blobs” in coronal loops, I concentrate in this section on the falling condensation region

²The larger damping length also results in a higher temperature in general. When the cooling phase sets in, the $H_m = 5$ Mm loop has a maximum temperature of $T = 5.8 \cdot 10^5$ K compared to $T = 5.2 \cdot 10^5$ K for the $H_m = 3$ Mm loop (cf. also the mean temperatures plotted in Fig. 5.4).

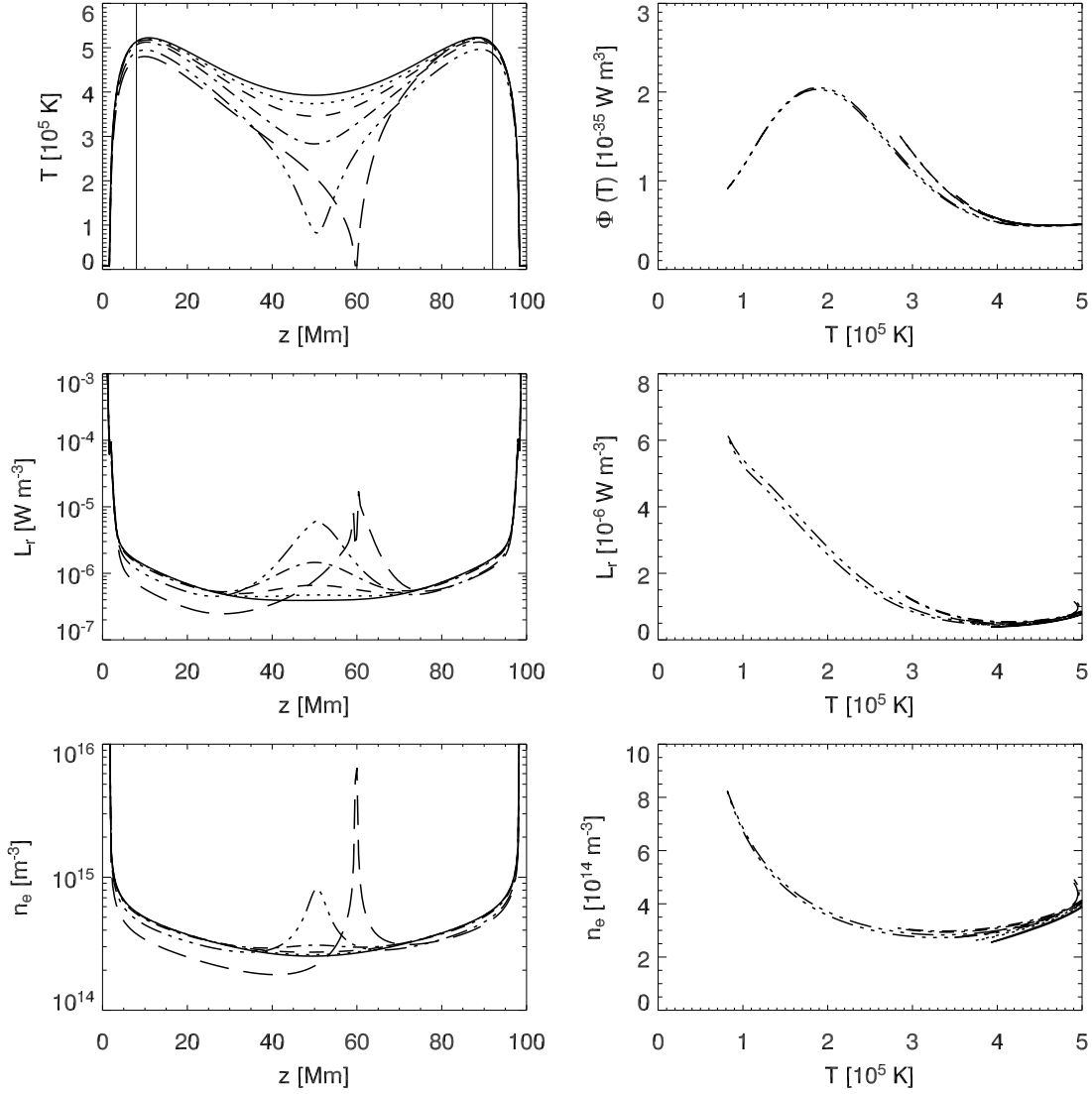


FIGURE 5.8: Formation of a central condensation region for $H_m = 5$ Mm. *Left panels*, as functions of loop length: loop temperature (*top*), total radiative losses (*middle*), electron density (*bottom*). *Right panels*, as functions of loop temperature: radiative loss function (*top*), total radiative losses (*middle*), electron density (*bottom*). The following time steps are plotted: $t = 20\,000$ s (*solid*), $t = 22\,000$ s (*dotted*), $t = 24\,000$ s (*dashed*), $t = 26\,000$ s (*dash-dotted*), $t = 28\,000$ s (*dash-dot-dotted*), $t = 30\,000$ s (*long dashes*). The *right panels* display only data of the central part of the loop, between the two vertical lines shown in the *upper left* panel, for the first five time steps.

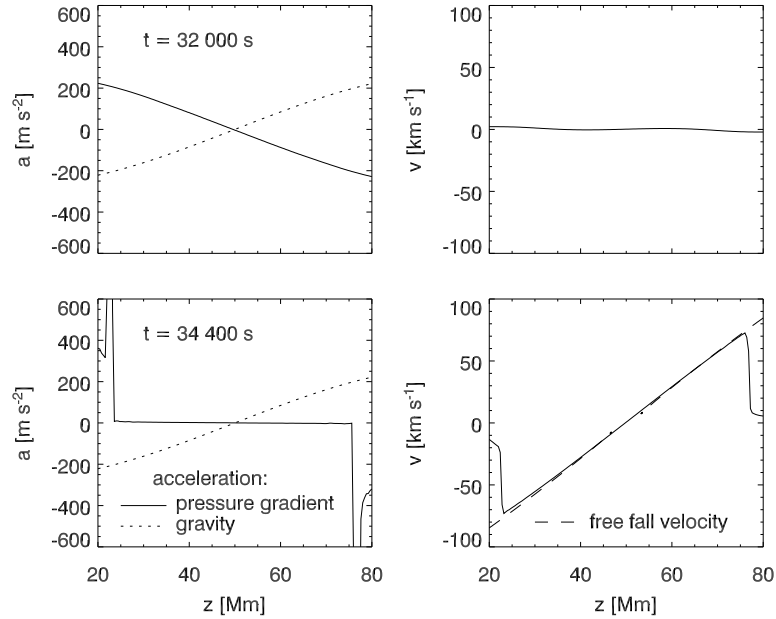


FIGURE 5.9: Formation of a shock front for $H_m = 3$ Mm. Gravitational acceleration, $g_{\parallel}(z)$ (dotted), and acceleration due to the pressure gradient, $\nabla p(z)/\rho(z)$ (solid) for $t = 32\,000$ s (top row) and $t = 34\,400$ s (bottom row). In the lower right plot, the free-fall velocity profile is indicated by a dashed line.

around $t = 30\,000$ s of the simulation run with $H_m = 5$ Mm. Figure 5.10 shows the velocity profile for $t = 31\,200$ s (solid line) and a velocity profile corresponding to a free fall of a test particle along the loop, which has a height of $h = 33.2$ Mm (dashed line). The maximum of the free-fall velocity is $v_{\max} = \sqrt{2gh} = 135$ km/s. Comparing the free-fall velocity profile with the velocity in the right half of the loop, it is seen that from $z = 50 - 70$ Mm the flow is faster than free fall, while it is slower for $z = 70 - 100$ Mm. The dotted line displays the local sound speed; from $z = 60 - 65$ Mm, the flow is supersonic. The fact that $v_{\text{apex}} = 50$ km/s immediately shows that there is a force acting on the loop plasma, which turns out to be the pressure force originating from the pressure difference between the wake of the moving condensation region and the rest of the loop behind the condensation region, which is located at $z = 85$ Mm in this plot. In Fig. 5.11 the velocity and acceleration of the center of the condensation region are plotted as a function of time. For this purpose, the condensation region is defined as the interval in which the temperature drops below $T = 10^5$ K (alternatively, a threshold for the density or the radiative losses could be used). The increasing velocity in the left half of the upper panel shows how the blob is being accelerated up to $v = 33$ km/s. It can be seen in the lower panel that for $t < 29\,500$ s, the acceleration is only a little smaller than g_{\parallel} , i.e. the free-fall case. After $t = 30\,600$ s, however, the pressure of the compressed plasma underneath has become so large (cf. Sect. 5.3.1) that the blob is now effectively decelerated. At $t = 31\,140$ s, the blob stops and even bounces 1 Mm upwards before falling again. After a second deceleration phase the blob drains through the loop's footpoint at $t = 32\,840$ s. The maximal acceleration of the blob during its fall is $a = 54$ m/s².

It has to be stressed that this loop model is one-dimensional, so that in reality the deceleration

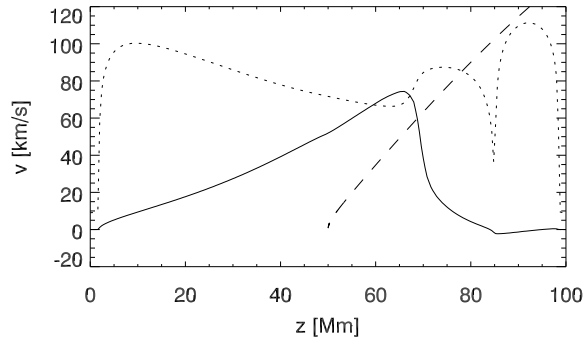


FIGURE 5.10: Comparison between the velocity profile for $H_m = 5$ Mm at $t = 31\,200$ s (*solid line*) with the free-fall velocity from the loop apex at 50 Mm to the right footpoint at 100 Mm (*dashed*) and the local sound speed at $t = 31\,200$ s (*dotted line*).

process may not be as vigorous as in the simulation described here. If the magnetic field is weak, the enhanced pressure of a region of dense plasma will distort the magnetic field which can lead to a lateral expansion of the dense plasma and a storage of energy in the surrounding plasma and magnetic field (Athay & Holzer 1982). Mackay & Galsgaard (2001), on the other hand, carried out two-dimensional simulations of the evolution of a density enhancement in a stratified atmosphere and found that a sufficiently strong magnetic field enables the density enhancement to maintain its shape as it falls, and indeed results in the dense blob rebounding several times.

The deceleration of the plasma blob in the model is caused by the same mechanism as proposed by Schrijver (2001) and yields a blob acceleration which is significantly lower than solar gravity and is consistent with the values of $a = 80 \pm 30$ m/s² reported by Schrijver (2001). The maximal *blob* velocities obtained from the simulations shown here are smaller than the maximal velocities of up to 100 km/s reported by Schrijver (2001) and 60 – 110 km/s (De Groof et al. 2004), while the maximal *flow* velocities that are obtained ($v_{\max} = 75$ km/s for $H_m = 5$ Mm, $v_{\max} = 74$ km/s for $H_m = 3$ Mm, and $v_{\max} = 128$ km/s for $H_m = 2$ Mm) are of the same order. In the simulations, the highest flow speeds are reached in the wakes of the falling plasma blobs. However, increasing the loop length results in a longer acceleration path, so that higher *blob* velocities are obtained for loops longer than 100 Mm. Simulations of longer loops where higher blob speeds are reached will be presented in Chap. 6, together with a comparison with observational data.

5.3.6 Spectral Signature of Catastrophic Cooling and Downflows

As the numerical code used in this work consistently solves the ionization rate equations for different atomic species, the emission of a large number of coronal and transition region spectral lines can be calculated, including the effects of non-equilibrium ionization. In this context, the emission in the lines of CIV (154.8 nm, formation temperature $T_f \approx 10^5$ K) and OV (63.0 nm, $T_f \approx 2.2 \cdot 10^5$ K) is of particular interest since the 160 nm passband filter of TRACE is dominated by CIV emission above the solar limb, and the OV line is frequently observed with SOHO/CDS. Let us analyze the simulation run with $H_m = 5$ Mm and focus on the same period that was dis-

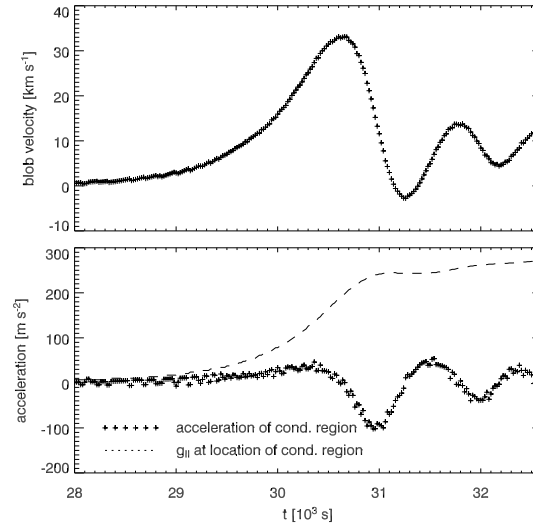


FIGURE 5.11: Velocity (*top*) and acceleration (*bottom*) of the condensation region for $H_m = 5$ Mm. The blob is accelerated by gravity and then slowed down by the pressure of the compressed transition region plasma underneath. The *dashed line* in the lower panel shows the effective gravitational acceleration, $g_{||}$, at the respective position of the blob.

cussed in the previous section.

Figure 5.12 displays the intensities and mean Doppler shifts, $\langle v_D \rangle$, for C IV (154.8 nm) and O V (63.0 nm). Both quantities are integrated over the right half of the loop, excluding the footpoints, and the Doppler shifts are calculated as seen from above and converted to velocity units. It is seen in the upper panel that the blob brightens strongly in both spectral lines while falling, and reaches its maximal intensity shortly before draining through the footpoint. The maximal Doppler shifts occur around $t = 30.5$ s when the blob reaches its maximal velocity. The maximal Doppler shifts are $\langle v_D \rangle = 25$ km/s for C IV (154.8 nm) and $\langle v_D \rangle = 22$ km/s for O V (63.0 nm). Both lines are redshifted due to the blob's motion towards the solar surface. Larger maximal Doppler shifts would result if no averaging over the entire right half of the loop was performed. To visualize the variation of line shifts and intensity with time, the line profiles of C IV (154.8 nm) and O V (63.0 nm) for different points of time during the fall of the condensation region are plotted in Fig. 5.13. It is seen that the line profiles are redshifted as the blob falls while the line intensity increases (cf. Fig. 5.12). The Doppler shifts that would be measured in these lines will of course depend on the aspect angle that loop is viewed at. In order to calculate Doppler shifts which can directly be compared with measurements with the CDS instrument on SOHO, one needs to consider not only the spatial resolution of the instrument, but also the finite temporal resolution due to the raster-scan process.

For an overview of temperature, velocity and emission for a small part of the simulation run with $H_m = 2$ Mm, Fig. 5.14 shows a cutout from Fig. 5.5 (right panel), together with the velocity field and the corresponding emission in the two spectral lines of C IV (154.8 nm) and O V (63.0 nm). It is seen that the condensation regions are accompanied by strong transient brightenings in both

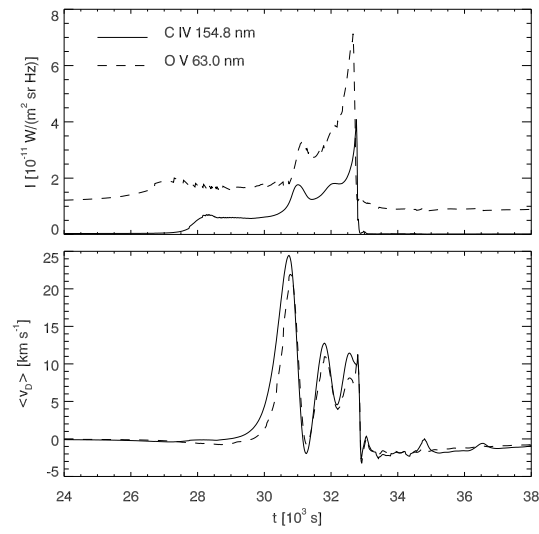


FIGURE 5.12: Variation of total intensity (*top*) and mean Doppler shift (*bottom*) due to the falling condensation region, integrated over the right half of $H_m = 5$ Mm loop. The *solid line* displays C IV (154.8 nm), the *dashed line* O V (63.0 nm).

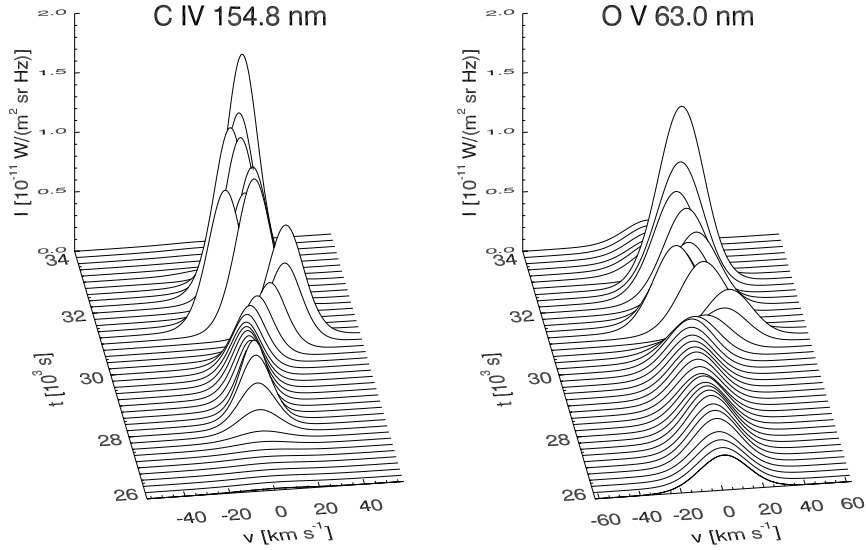


FIGURE 5.13: Line profiles of C IV (154.8 nm) and O V (63.0 nm) during the fall of the condensation region ($H_m = 5$ Mm) as seen from above. The flow towards the solar surface results in a redshift of around 10 km/s and the emission stops abruptly when the condensation region drains through the footpoint.

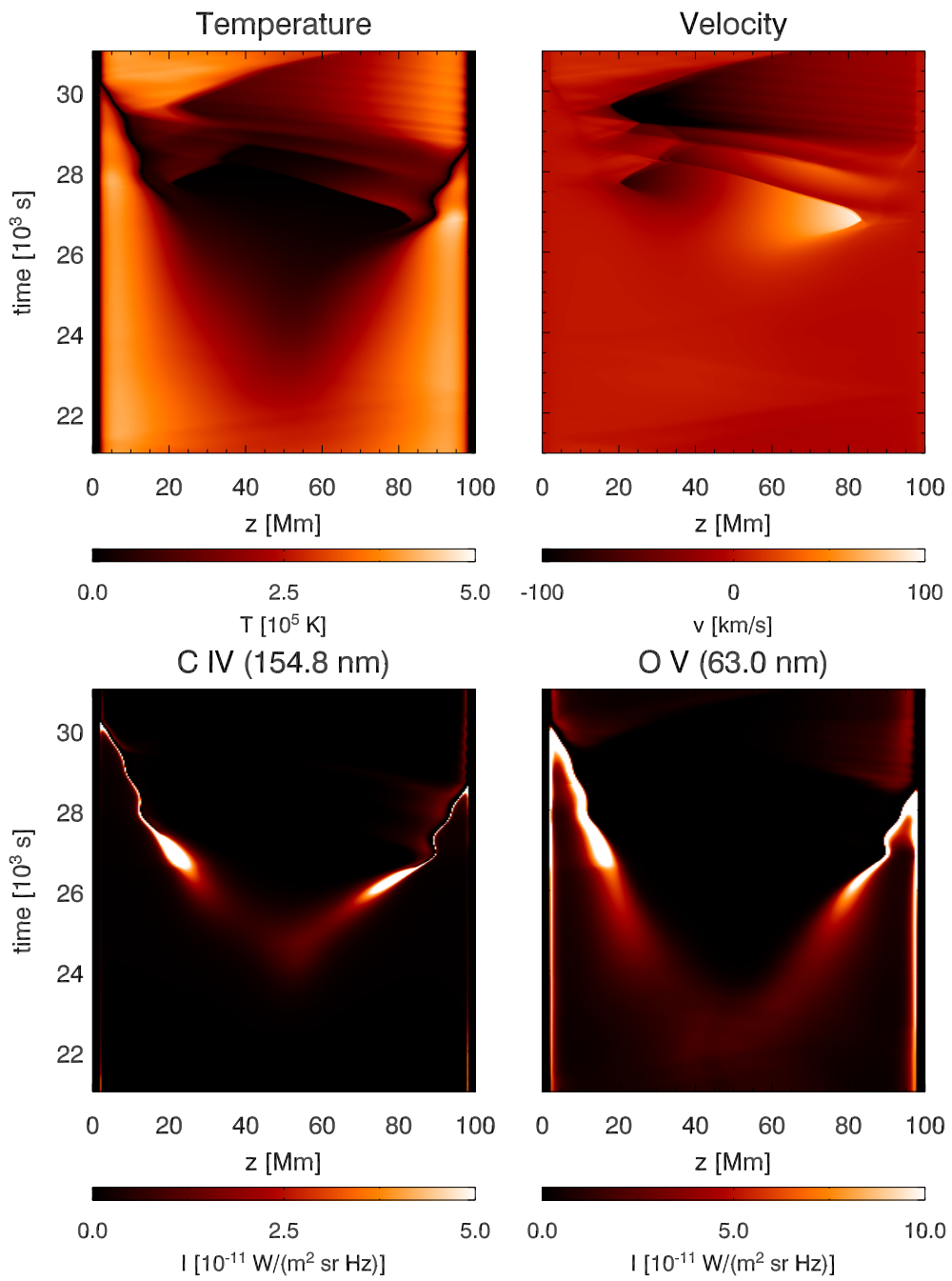


FIGURE 5.14: Formation of two condensation regions in a coronal loop for $H_m = 2$ Mm. The *upper left* plot shows the evolution of temperature along the loop, the *upper right* plot shows the corresponding velocities. The *lower left* plot displays the emission in C IV (154.8 nm), the *lower right* plot the emission in O V (63.0 nm.)

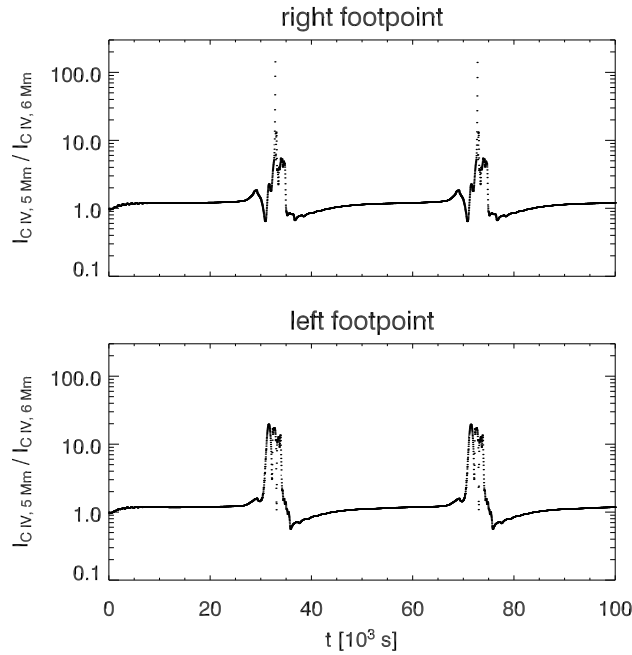


FIGURE 5.15: Relative intensity, $I_{H_m=5 \text{ Mm}}/I_{H_m=6 \text{ Mm}}$, in C IV (154.8 nm) at the left (*upper panel*) and right (*lower panel*) footpoints.

lines. As the O V (63.0 nm) line is formed at higher temperatures than the C IV (154.8 nm) line, a small time delay is observed between the occurrence of the brightenings in the two lines. The wiggles in the path of the condensation region are due to the strong deceleration of the blob by the transition region plasma (cf. Sect. 5.3.5).

When the condensed plasma blob falls down the leg of the loop, it compresses the underlying plasma, which results in a transient temperature rise of the plasma underneath and a strong brightening around the footpoint of the loop when the plasma blob encounters the transition region. Figure 5.15 shows the variation of the emission in C IV (154.8 nm) at the loop footpoints ($z = 2 \text{ Mm}$ and $z = 98 \text{ Mm}$) as a function of time. The intensity from this highly dynamic model run with $H_m = 5 \text{ Mm}$ is scaled by the respective intensity from the stable model run for $H_m = 6 \text{ Mm}$ (cf. Fig. 5.4). This is done in order to highlight the dynamics in the C IV emission. It is observed that the intensity at the right footpoint (draining direction of the condensation region, lower panel) increases for a short time by more than two orders of magnitude and by more than one order of magnitude at the left footpoint. The latter effect takes place because the rarefaction wave following the falling condensation region pulls up plasma from the lower transition region to higher temperatures which leads to the strong transient brightening in the C IV (154.8 nm) line.

5.4 Comparison to Observations and Discussion

Several features of the numerical simulations presented here are in good agreement with recent observations from different instruments, so that I propose the condensation-evaporation cycle as a

possible common explanation.

Let us briefly sum up the observational evidence and its analysis: The TRACE observations of Schrijver (2001) show strong transient brightenings in the spectral lines of Ly_α and CIV (154.8 nm), developing initially near the loop tops. Thereafter cool plasma slides down on both sides of the loops, forming clumps which move with velocities of up to 100 km/s but show a downward acceleration of $80 \pm 30 \text{ m/s}^2$, significantly less than the solar surface gravity. After a detailed analysis, Schrijver (2001) concluded that the observed brightenings are due to the radiation of relatively dense blobs of falling plasma which are “embedded in more tenuous cool matter or in plasma at a different temperature”. He argued that the reduced acceleration may be caused by the cooling plasma underneath the radiating blobs which could slow down the fall. Referring to the work of Mok et al. (1990), he suggested that the observed catastrophic cooling could be explained by a drastic and fast reduction of the heating scale height which would result in a strong decrease of the heating at the loop apex.

De Groof et al. (2004) analyzed a high-cadence time series of simultaneous EIT (30.4 nm) and Big Bear H_α data and found intensity variations in a coronal loop which propagated from the top towards the footpoint. The measured speeds of the blobs are compatible with a free fall in the upper part of the loop but are significantly smaller in the lower part of the loop. Testing different hypotheses concerning the origin of the intensity variations, the authors rejected slow magneto-acoustic waves as an explanation for the observations. Instead, they favored flowing plasma blobs to account for the observed intensity variations.

The simulations presented here strongly support catastrophic cooling as the key mechanism to explain these sets of observations and provide further insight into the physical processes. In contrast to the work of Mok et al. (1990), it is now possible to synthesize optically-thin emission lines forming in the transition region and corona which directly reproduce the transient brightenings in, e.g., the CIV (154.8 nm) line. The suggestion of Schrijver (2001) is proven that the falling plasma blobs are decelerated by the underlying plasma and a quantitative agreement for the acceleration of the blobs is obtained. Furthermore, it is found that this region is strongly compressed by the falling condensation region which leads to a strong transient brightening of the loop footpoint.

The main novelty that these simulations provide, however, is the finding that catastrophic cooling is not necessarily initiated by a sudden decrease of the heating or the heating scale height. I support the presumption of Schrijver (2001) that a “drastic and fast reduction of the heating scale height suffices” to trigger the formation of cool condensations. In fact, this is what is happening in the initial phase of all dynamic loop simulations presented here, when the heating scale height is instantaneously reduced. Moreover, it is shown that catastrophic cooling does not have to be the result of a time-dependent heating scale height, but can also result from a slowly evolving loss of equilibrium at the loop apex as a natural consequence of loop heating predominantly at the footpoints. On the other hand, it is hardly possible to trigger catastrophic cooling at all by just decreasing the amount of heating if this decrease is not accompanied by a decrease of the heating scale height (cf. Sect. 5.3.1).

A small heating scale height rather than a heating function with time-dependent amplitude thus seems to be the key element for catastrophic cooling. These statements are important as they show that time-dependent phenomena observed in coronal loops do not demand time-dependent driving mechanisms (although many of them exist) but can also be the result of basic radiative or hydrodynamic instabilities.

The question has been raised whether a higher temperature of the loops would significantly alter

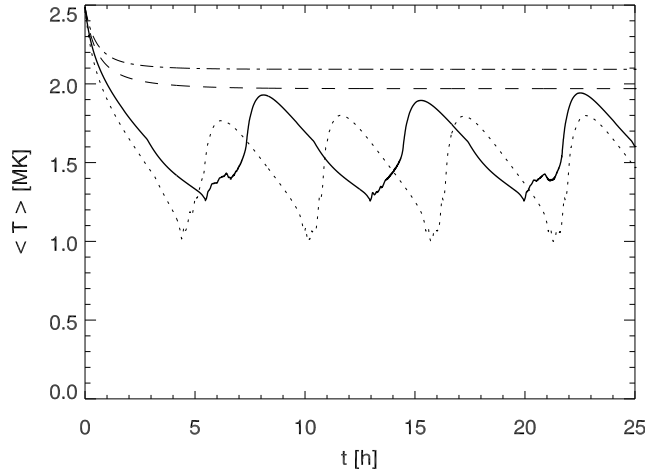


FIGURE 5.16: Evolution of mean temperature, $\langle T \rangle(t)$, using an increased mechanical energy flux of $F_{m0} = c \cdot 10^4 \text{ W/m}^2$, for four different damping lengths of the heating function: $H_m = 2 \text{ Mm}$ (dotted), $H_m = 3 \text{ Mm}$ (solid), $H_m = 5 \text{ Mm}$ (dashed), $H_m = 6 \text{ Mm}$ (dash-dotted).

their evolution. An additional set of simulations was therefore carried out where the mechanical energy flux was increased to $F_{m0} = c \cdot 10^4 \text{ W/m}^2$ while keeping all other parameters constant. This results in a start model with $T_{\text{max}} = 2.7 \text{ MK}$ and $\langle T \rangle = 2.5 \text{ MK}$ and recurrently condensing loops with maximal temperatures of $\langle T \rangle_{\text{max}} = 1.8 - 1.9 \text{ MK}$. The evolution of the mean temperature of these loop models is displayed in Fig. 5.16. It is seen that the general behavior remains unchanged, in the sense that loops with a heating scale height below a certain threshold undergo periodic evolution. Compared to cooler loops with a lower heating rate, the increased heating rate results in a slight reduction of this threshold value, which is the expected result. It has to be kept in mind that the loop length also significantly affects the maximal loop temperature so that longer loops reach much higher temperatures for a given mechanical energy flux.

Comparing the results of the current model with observations, it has to be stressed that the observed blob speeds are significantly smaller than the observed ones and the periods are lower than the time scale estimated by Schrijver (2001). However, as mentioned in Sect. 5.3.5, simulations for a $L = 300 \text{ Mm}$ model loop (which corresponds to the estimated length of the loop analyzed by De Groof et al. (2004)) yield blob speeds of the order of 100 km/s and periods of up to several days. A comparison of these results with observational data will be presented in Chap. 6.

In this model the implicit assumption is made that the heating rate is not affected by the catastrophic cooling, even though the density and gas pressure change significantly while the condensation sets in (compare, for example, the average pressure in Fig. 5.6 or the density in Figs. 5.7 and 5.8). However, even during the condensation phase the plasma- β remains below 0.03 when assuming a reasonable value of 1 mT (10 Gauss) for the magnetic field. Thus, throughout one deals with a low- β plasma, where the magnetic field is presumably unperturbed by the plasma. Therefore, when assuming a magnetically-dominated heating mechanism like flux braiding (Galsgaard & Nordlund 1996; Gudiksen & Nordlund 2002) one would expect the average

heating rate to remain constant (and decay exponentially with height), regardless of the dynamic evolution of the plasma.

5.5 Summary

The model calculations of coronal loops presented in this chapter reproduce observations of catastrophic cooling and high-speed downflows, using a very simple, time-independent heating function. The non-linearity of the energy equation results in a loss of equilibrium which triggers a highly dynamic loop evolution. No external time-dependent driving mechanism is necessary to explain rapid cooling and evacuation of loops. Coronal loops can exhibit cyclic behavior, with a wide range of periods, as well as irregular solutions. The time-dependent emission of optically-thin spectral lines has been synthesized and directly compared to observations giving a good qualitative match to the observed properties of catastrophic cooling of coronal loops.

6 High-Speed Coronal Rain

Abstract

At high spatial and temporal resolution, coronal loops are observed to have a highly dynamic nature. Recent observations with SOHO and TRACE frequently show localized brightenings “raining” down towards the solar surface. What is the origin of these features? In this chapter for the first time a comparison of observed intensity enhancements from an EIT shutterless campaign with non-equilibrium ionization simulations of coronal loops is presented in order to reveal the physical processes governing fast flows and localized brightenings. It is shown that catastrophic cooling around the loop apex as a consequence of footpoint-concentrated heating offers a simple explanation for these observations. An advantage of this model is that no external driving mechanism is necessary as the dynamics result entirely from the non-linear character of the problem.

6.1 Introduction

The upper solar atmosphere, i.e. the transition region and corona, is highly complex and magnetically structured. Recent space observations, especially with SOHO and TRACE, have revealed that coronal loops, magnetically closed structures in the upper solar atmosphere, are intrinsically dynamic, and intensity enhancements (“blobs”) are often seen to propagate along these loops. As was pointed out in Chap. 5, spectroscopic investigations show that these intensity variations have different signatures in UV spectral lines formed at different temperatures and exhibit Doppler shifts of $v = 20 - 100 \text{ km s}^{-1}$. Recently, [De Groof et al. \(2004\)](#) observed propagating intensity variations in the He II 30.4 nm band with the Extreme-Ultraviolet Imaging Telescope (EIT). The dominant part of the plasma emitting in this spectral band has temperatures of $T = 6 - 8 \cdot 10^4 \text{ K}$. Plasma seen in this spectral band in higher layers of the solar atmosphere is thus considerably cooler than its surroundings. This can be the result of plasma draining from a prominence or material cooling down after a flare. However, when evidence for these two processes is lacking, the nature of these intensity variations is difficult to explain. While slow magneto-acoustic waves may in general account for propagating intensity variations, this explanation of the features observed in the EIT shutterless campaign from 11 July 2001 was ruled out by [De Groof et al. \(2004\)](#).

Another possible explanation which has been proposed in Chaps. 4 and 5 (see also [Müller et al. 2003](#); [Müller et al. 2004](#)) is the scenario of the “evaporation-condensation cycle”. In the previous chapters it was shown that localized brightenings can be the result of catastrophic cooling of a loop which is predominantly heated at the footpoints. The heating leads to an evaporation of plasma into the coronal loop which then cools rapidly due to a loss of thermal equilibrium. The confined region of “condensed” plasma subsequently falls down under the effect of gravity in the form of a cool plasma blob. In Chap. 5 the evolution, speed and spectral signature of these traveling condensation regions was described, and a possible connection to the recent EIT observations

was pointed out. Compared to the loops described in Chap. 5, the loop structure seen in the data from the EIT shutterless campaign is larger (with an estimated loop length of about $L = 300$ Mm compared to the $L = 100$ Mm models of Chap. 5) and the observed blob velocities are higher. Even so, encouraged by the general features of the model, new simulations were carried out with changes suggested by the EIT observations. For the models presented here, the loop geometry inferred from the EIT data was adopted and also a higher heating rate was used to reach apex temperatures of around 3 MK as suggested, e.g. by TRACE observations of large active region loops.

6.1.1 Loop Heating

The energy input into the coronal loop is parametrized in the same way as in Chaps. 4 and 5 by specifying the energy flux at the footpoints of the loop, F_{m0} , and assuming a mechanical energy flux that is constant up to a height z_1 and then decreases exponentially for $z \geq z_1$ as

$$F_m(z) = F_{m0} \exp[-(z - z_1)/H_m] \quad (6.1)$$

with a damping length H_m . In the models presented below, H_m will be varied between 2 and 30 Mm for a loop of $L = 300$ Mm length. For the mechanical energy flux, $F_{m0} = c \cdot 10^4$ W/m² will be used, with the normalization constant $c = 1/(1 - \exp[-(L/2 - z_1)/H_m])$ and $z_1 = 1.75$ Mm. The normalization constant ensures that the total energy input into the loop is constant, irrespective of the damping length H_m . The heating rate, i.e. the energy deposition per unit time and unit volume, is given by the divergence of the energy flux, $Q_m = -\nabla F_m$. With the damping length H_m it can be controlled whether the heating is concentrated near the footpoints or is more evenly distributed along the loop.

6.1.2 Initial State

The coronal loop model studied here has a total length of 300 Mm, composed of a semicircular arch of 298 Mm length and a vertical stretch of 1 Mm length at each end. A static initial state is obtained by prescribing a large energy dissipation length of $H_m = 30$ Mm, which results in a loop apex temperature of $T = 3.3$ MK. The temperature along the loop of the initial state is plotted in Fig. 6.1.

6.2 Effect of the Damping Length on the Loop Evolution

6.2.1 Recurrent Condensations in Long Loops

The most important conclusion reached in Chaps. 4 and 5 was the fact that a thermal instability can give rise to a highly dynamic evolution of solar coronal loops. It was worked out in Chap. 5 that the scale height of the energy dissipation (the so-called damping length) acts as a control parameter of this non-linear system and determines whether there exists a stable solution. If this is not the case, thermal non-equilibrium can lead to *catastrophic cooling*, a self-amplifying process by which the radiative losses increase strongly over a short time scale, and result in a confined region of high-density plasma (the *condensation region*), which then slides down the loop legs due to gravity.

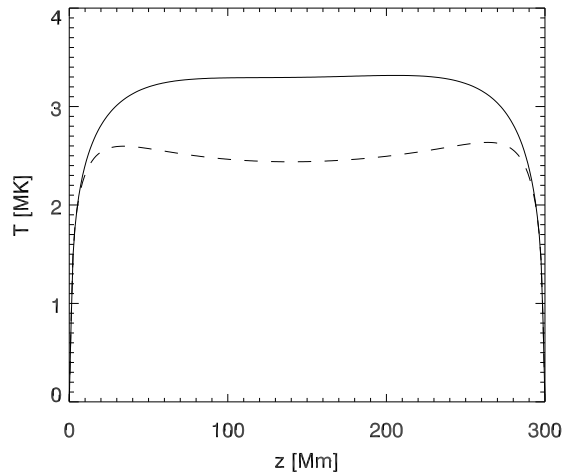


FIGURE 6.1: Temperature along the coronal loop. Initial stable state (solid line, $H_m = 30$ Mm) and another stable solution for $H_m = 12$ Mm (dashed line).

The maximum velocity of the falling condensation region is determined by its formation height and the loop plasma underneath the condensation region. It was found in Chap. 5 that the pressure of the transition region plasma can efficiently slow down the falling “blob” so that its maximum velocity may be substantially slower than the free-fall speed. Compared to observations of catastrophic cooling in coronal loops (Schrijver 2001; De Groof et al. 2004), the results were encouraging in the sense that the formation of such high-density regions was indeed possible without any time-dependent driving mechanism, but not fully satisfying as the deduced blob velocities of $30 - 40 \text{ km s}^{-1}$ were lower than the observed ones (up to 100 km s^{-1}).

For the new loops models with $L = 300$ Mm, Fig. 6.2 displays the mean temperature, $\langle T \rangle$, as a function of time for three different damping lengths. In agreement with the results of Chap. 5, it is found that the period of the condensation cycle increases with increasing damping length, until finally a stable solution is reached. For damping lengths close to the limit of stability, the period of the cycle can become very long. A model with $H_m = 8$ Mm was run for 10 days of solar time and showed a period of $P = 4.15$ days. Figure 6.3 shows the evolution of the mean temperature, $\langle T \rangle$, as a function of mean pressure, $\langle p \rangle$. In this plot, periodic solutions trace out cycles in $\langle p \rangle - \langle T \rangle$ space while stable solutions reach fixed points. It is seen that also in this parameter regime the loop evolution can be classified into stable solutions and dynamic solutions.

The main effects of the longer loop length and higher energy flux (with respect to the models presented in Chap. 5) are as follows: For a given loop length, a higher heating rate leads to a higher loop temperature and a higher density, while for a fixed energy flux of $F_{m0} = 10^4 \text{ W/m}^2$, the mean loop temperature of *stable* loops with small damping lengths ($H_m \leq 10$ Mm) does not depend strongly on the loop length. However, the range of damping lengths for which the loops exhibit recurrent condensations increases with loop length. For more details on the effects of the different loop parameters on the loop evolution, the reader is referred to Chap. 8.

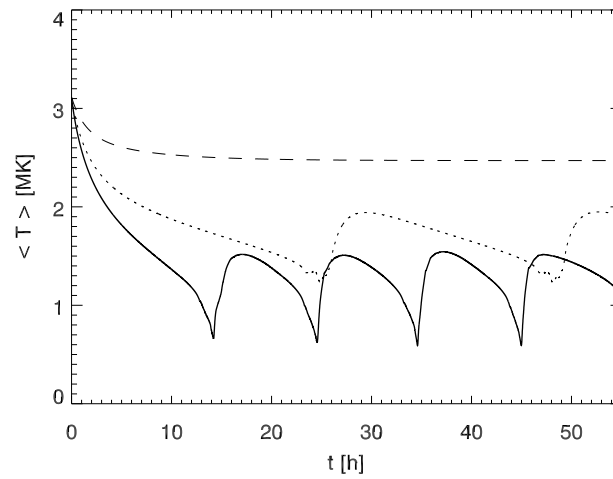


FIGURE 6.2: Evolution of mean temperature, $\langle T \rangle$, as a function of time, for different damping lengths of the heating function: $H_m = 2$ Mm (solid), $H_m = 5$ Mm (dotted), and $H_m = 12$ Mm (dashed).

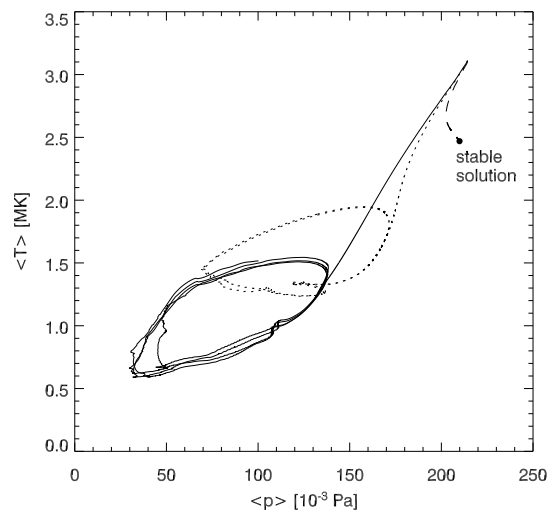


FIGURE 6.3: Mean temperature, $\langle T \rangle$, of the loop, as a function of mean pressure, $\langle p \rangle$, for a loop of total length $L = 300$ Mm. Solid line: $H_m = 2$ Mm, dotted: $H_m = 5$ Mm, dashed: $H_m = 12$ Mm.

6.2.2 Slow and Fast Blobs

Having introduced the general characteristics of possible solutions, let us now focus on the evolution of the dynamic solutions with the aim of deducing the speed of the plasma blobs which result from the catastrophic cooling process. In Fig. 6.4 space-time diagrams of the loop temperature, $T(z, t)$, are plotted for damping lengths of $H_m = 2, 3, 5$ Mm. All three models show the recurrent condensations which have been described in detail in Chap. 5. It was pointed out in Chap. 5 that the highest velocities occur in the wake of a falling blob where the density is low. However, for a comparison with observations, the proper motions of the density enhancements themselves have to be calculated. The maximal blob speeds are 48 km s^{-1} for the run with $H_m = 5$ Mm and 42 km s^{-1} for the run with $H_m = 3$ Mm. This shows that the blobs are strongly decelerated on their way down since the maximal free-fall speed from the loop apex, h_{max} , is $v_{\text{ff}} = \sqrt{2Gm_{\odot}h_{\text{max}}/(r_{\odot}(r_{\odot} + h_{\text{max}}))} = 215 \text{ km s}^{-1}$.

I would now like to draw the reader's attention to the simulation run with $H_m = 2$ Mm. Every time after a condensation region has formed, e.g. around $t_1 = 13$ h and $t_2 = 24$ h, a second temperature minimum occurs, and the shallow slope of its motion in the (z, t) -plane indicates very high speeds. Figure 6.5 displays the temperature for this part of the simulation, along with the velocity along the loop. This plot shows that the second condensation is accompanied by very fast flows of up to 230 km s^{-1} in the wake of the falling blob. Figure 6.6 displays the blob speed as a function of time for both the first and the second condensation region. While the first blob only reaches a velocity of around 25 km s^{-1} , the second blob moves with a velocity of up to 90 km s^{-1} .

It is seen that after a short period of nearly free fall (between $t = 14.0 - 14.1$ h), the blob is strongly decelerated and even bounces upwards shortly ($t = 14.2 - 14.3$ h). It was pointed out in Chap. 5 that in the case of a weak magnetic field the deceleration process may in reality not be as vigorous as in this one-dimensional simulation, because the enhanced pressure of such a high-density region will distort the magnetic field. However, the findings of Mackay & Galsgaard (2001) show that a sufficiently strong magnetic field can indeed result in the dense blob rebounding several times.

6.2.3 Formation of the Second Condensation Region

The phenomenon that a second region of enhanced density can form in the wake of another condensation region has not been reported before and shall be explained in detail. First of all, compared to the $L = 100$ Mm loops studied in Chap. 5 with maximal apex temperatures below $7 \cdot 10^5$ K, the more strongly heated $L = 300$ Mm loop models studied here have apex temperatures of around 3 MK and correspondingly higher pressures. Therefore the formation of a condensation region, where the temperature drops to around 10^4 K on a very short time scale, results in a much higher pressure gradient on both sides of the condensation region. The resulting inflows towards the pressure minimum collide and produce shocks. These pressure pulses then travel away from the condensation region to both sides and lead to a transient compression of the loop plasma they encounter on their way. Even a small compression leads to a noticeable increase of the radiative losses and these radiative losses in turn give rise to enhanced cooling which results in a local density maximum. The condition for the formation of a condensation region are herewith fulfilled, and the density enhancement cools more strongly than its surroundings: catastrophic cooling sets in.

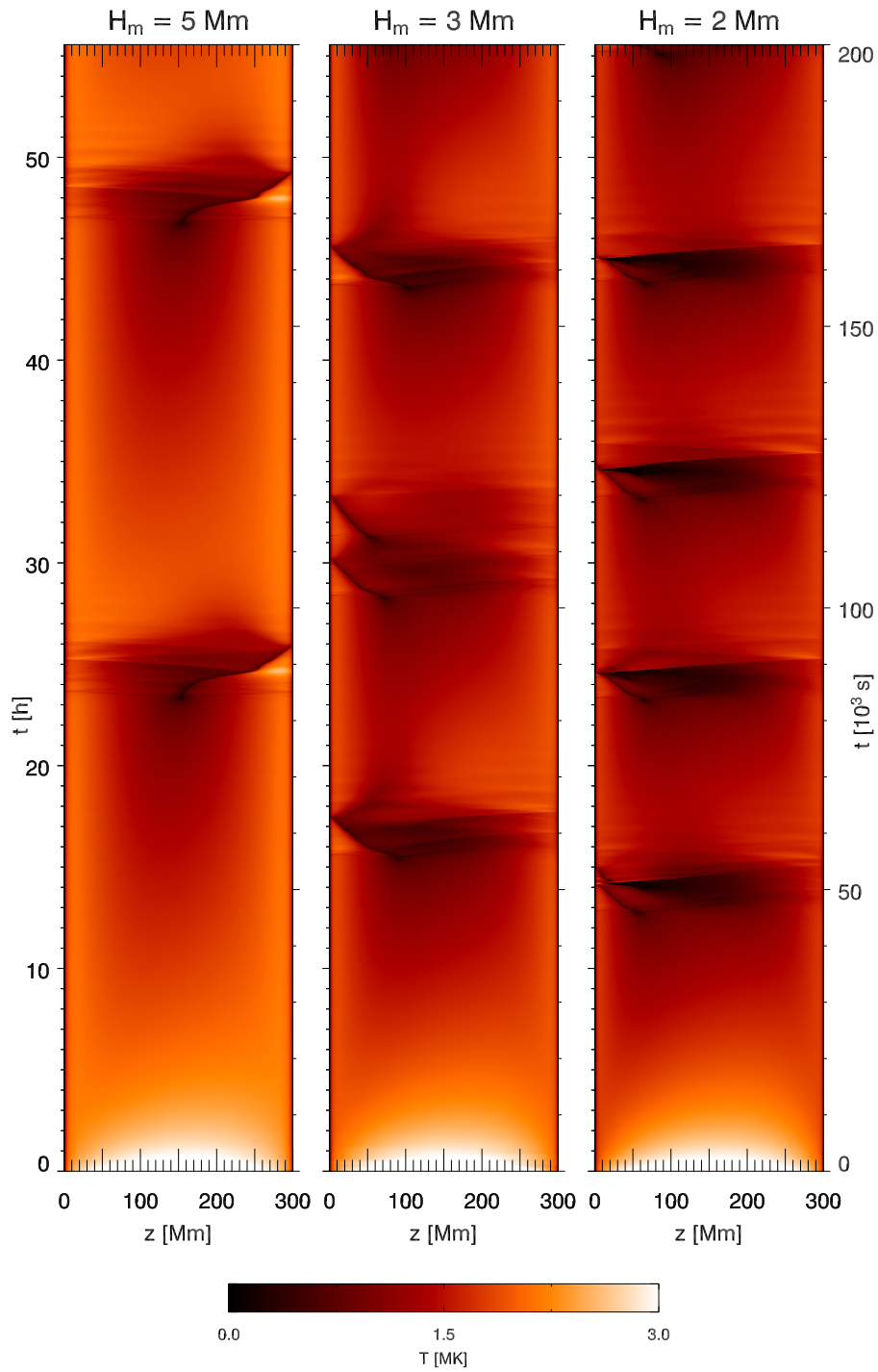


FIGURE 6.4: Evolution of the temperature along the loop, $T(z, t)$, for three different damping lengths of the heating function: $H_m = 5$ Mm (left), $H_m = 3$ Mm (center), $H_m = 2$ Mm (right). The loop footpoints are at $z = 0$ and 300 Mm, the apex is at $z = 150$ Mm.

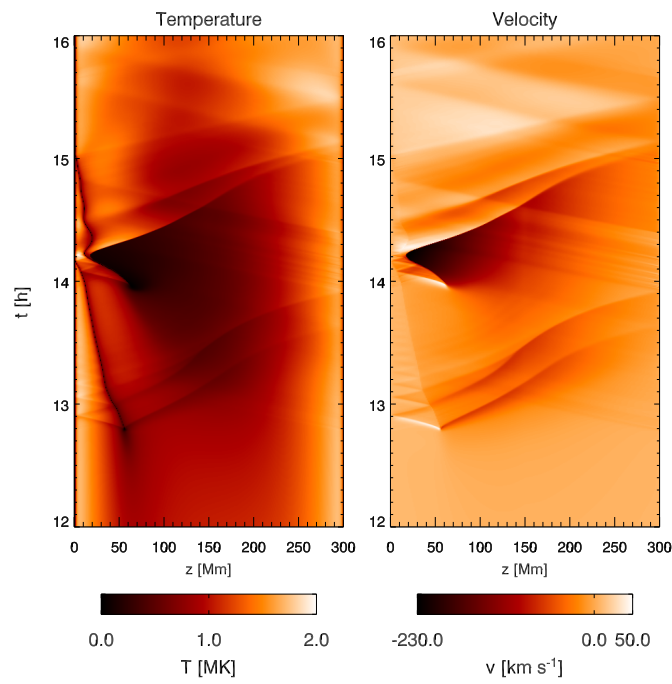


FIGURE 6.5: Formation of the fast blob. The *left* plot shows the temperature $T(z, t)$ for a damping length of $H_m = 2$ Mm, the *right* plot displays the corresponding velocities.

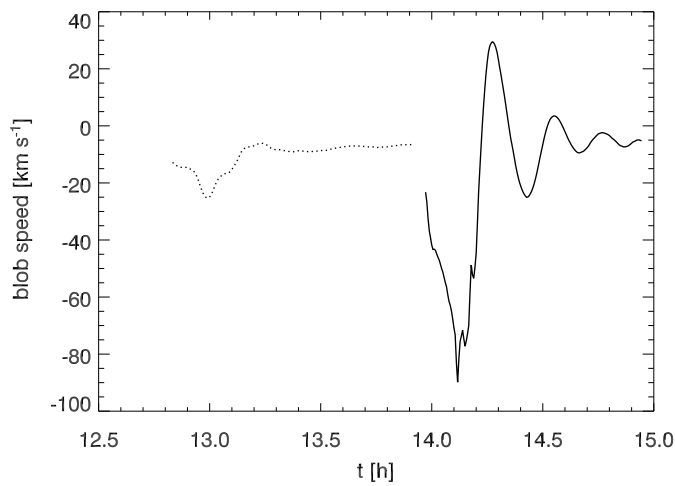


FIGURE 6.6: Proper motion of the slow blob (*dotted line*) and the fast blob (*solid line*).

This evolution is displayed in Fig. 6.7: At time $t_1 = 46\,060$ s (*solid lines*), the first condensation region has formed and appears as a narrow region with strongly decreased temperature and pressure, and strongly enhanced radiative losses and electron density. At time t_2 (*dotted lines*), the condensation region has traveled around 5 Mm to the left, and a temperature and density perturbation is seen to propagate towards the loop apex. At time t_3 (*dashed lines*), this perturbation has led to a local maximum in the radiative losses (indicated by the right black dot and vertical lines), while the electron density is also perturbed, but does not show a local maximum yet.

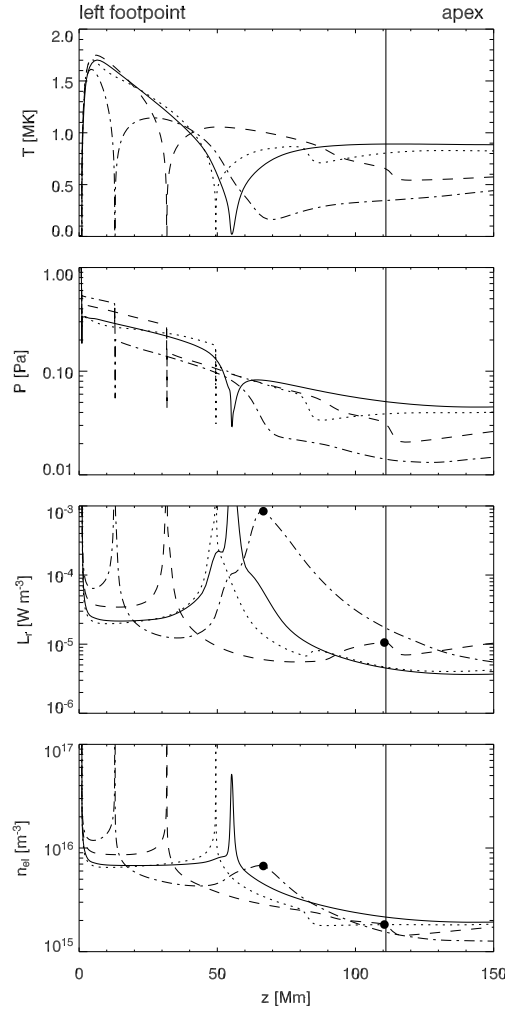


FIGURE 6.7: Formation of the second condensation region. From top to bottom: temperature, pressure, total radiative losses and electron density along the left half of the loop for $t_1 = 46\,060$ s (*solid*), $t_2 = 46\,500$ s (*dotted*), $t_3 = 47\,720$ s (*dashed*) and $t_4 = 50\,120$ s (*dash-dotted*). The black dots mark the second maximum of the radiative losses which is triggered by the shock front (indicated by *vertical lines*) originating from the first condensation region.

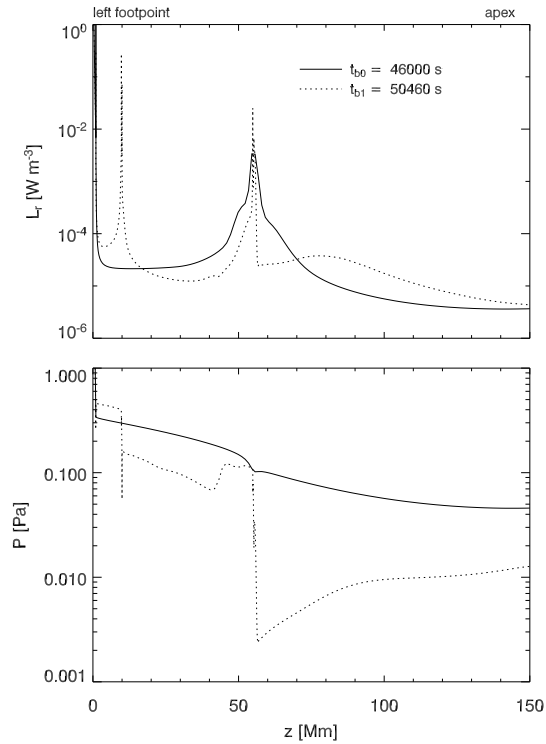


FIGURE 6.8: Radiative losses (*top*) and pressure (*bottom*) for two time steps of the simulation. The solid line in the upper panel shows the enhanced radiation from the first blob, formed around $t_{b0} = 46000$ s. The dotted line ($t_{b1} = 50460$ s) has two maxima: the one at $z = 10$ Mm stems from the first blob which has moved towards the left footpoint, while the second one at $z = 55$ Mm indicates the second blob. The lower panel shows that at the same location, the pressure downstream of the second blob (at t_{b1}) is lower than the pressure downstream of the first blob (at t_{b0}), which explains its higher speed.

Finally, at time t_4 (*dash-dotted lines*), the second condensation sets in, and the second region of strongly decreased temperature and pressure is accompanied by local maxima of the radiative losses and electron density (indicated by the left black dot). From the separation of the peaks it can already be seen that the second condensation region travels much faster than the first one.

What makes this density enhancement travel so much faster than the previous one? Figure 6.8 shows the total radiative losses (to indicate the blobs' positions) and the pressure for the slow and the fast blob for two time steps where the blobs are at the same location ($z \approx 53$ Mm). It is seen that the pressure downstream the leading blob is significantly higher than the one for the trailing blob. Therefore, the first blob is more strongly decelerated by the pressure of the underlying plasma, while the second one can travel in the low-pressure region in the wake of the first one.

6.3 Comparison with Observations

On 11 July 2001 from 16:00 UT until 18:28 UT, an “EIT shutterless campaign” was conducted which provided 120 high-cadence He II (30.4 nm) images of the north-eastern quarter disk of the

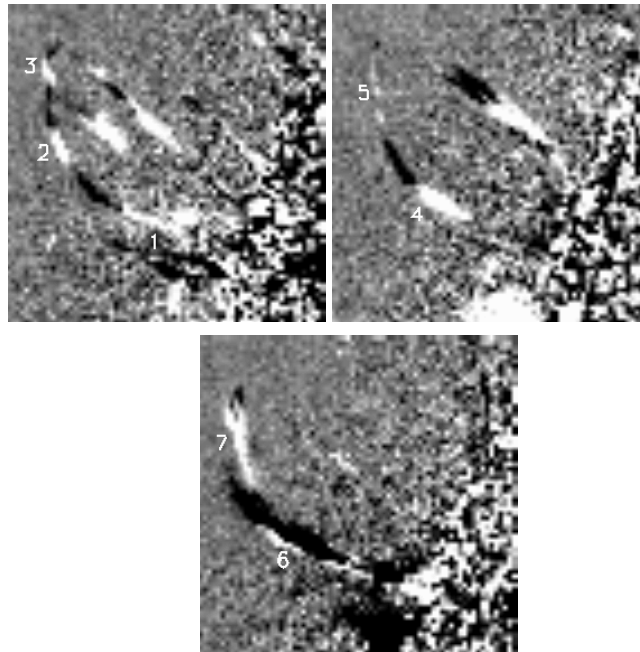


FIGURE 6.9: Three difference images taken at 16:27, at 17:09 and at 17:58 UT, in which seven propagating blobs with enhanced intensity can be identified.

Sun. In this observational program, which is planned every 3 months, the EIT shutter is kept open for more than 2 hours during which images are taken with a time cadence around 68 seconds. The sequence of 120 images is interrupted only by two gaps, allowing each for a LASCO C2 image in the framework of the EIT “CME watch program”. Instead of the normal full-disk field of view (FOV) of EIT, the shutterless program concentrates on a subfield of 416×416 pixels ($\approx 1082'' \times 1082''$), the north-eastern quarter disk in the sequence under analysis.

The most intriguing feature present in the data is an off-limb loop structure of approximately 100 Mm height which shows intensity variations propagating downwards during the whole sequence. Figure 6.9 displays three EIT difference images which allowed for the identification of seven propagating intensity variations (for details, cf. De Groof et al. 2004). Since there was no evident cause noticeable in the direct neighborhood of this loop, De Groof et al. (2004) studied the characteristics of the intensity variations propagating downwards in order to find out whether they could be interpreted as waves or as a flow. A multi-wavelength analysis of the time frame of the shutterless sequence revealed that the varying loop is unlikely to be flare-related (although a flare goes off south of the analyzed region) and that the bright blobs consist of cool plasma since they are only visible in the cool temperature bands of He II (30.4 nm) and $H\alpha$.

The propagating disturbances were analyzed in more detail by outlining the track along which they move down and investigating the behavior and speed of the bright blobs in a space-time diagram. Seven blobs were identified, propagating down along the loop track with speeds ranging from 30 to 120 km s^{-1} , increasing in time (see Fig. 6.10). The mean intensity enhancements caused by the disturbances range from 9 to 38 % or from 23 to 93 % of the background intensity depending on how the background subtraction is carried out. In order to interpret the intensity variations

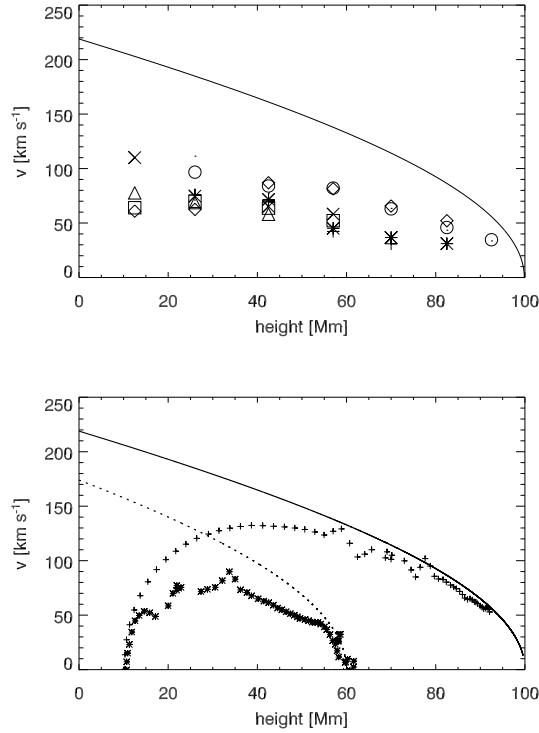


FIGURE 6.10: *Top*: Measured blob speeds as a function of height over the solar surface, together with the free-fall speed from a height of 100 Mm. The different symbols mark the different observed blobs. *Bottom*: Speed of the fast blob in the simulation with $H_m = 2$ Mm. Crosses and asterisks correspond to two runs with slightly different radiative losses. The solid line indicates a free fall from a height of 100 Mm, the dotted line corresponds to 60 Mm height.

as waves or flows, De Groof et al. (2004) compared the parameters found in the analysis with the typical parameters of slow magneto-acoustic waves observed in the solar corona. This comparison led to several anomalies, e.g. the blob speeds which are increasing and definitely higher than the local sound speed, the amplitudes which substantially exceeded the intensity enhancements seen in waves and the lack of any damping. Last but not least, slow waves are only observed propagating upwards while the bright blobs that are seen all move downwards. On the other hand, the hypothesis of falling/flowing plasma concentrations looks more promising.

The upper panel of Fig. 6.10 shows the observed blob speeds as a function of height over the solar surface, as measured by De Groof et al. (2004). The different symbols correspond to the different blobs which have been identified. In the upper part of the loop, the measured speeds are closely related to the theoretical free-fall speed from a height of 100 Mm, especially when taking into account the uncertainties concerning the projection angle, the curvature of the loop and the exact loop height. In the lower part of the loop, on the other hand, the speeds clearly deviate from the free-fall curve. The lower panel of Fig. 6.10 shows the speeds of the fast blobs from the catastrophic cooling models. It turns out that the exact location where a condensation region forms depends very sensitively on the radiative losses. In the simulations where the non-

equilibrium ionization of hydrogen, helium, carbon and oxygen were explicitly included in the calculations, the blobs formed at around 60 Mm height, while they appeared at greater heights when *a priori* radiative loss curves as functions of electron temperature for elements other than hydrogen and helium were used. The subsequent evolution of the plasma is very similar, therefore the blob speeds for both cases are plotted in Fig. 6.10, together with the velocity curves for a free fall from heights of 60 Mm and 100 Mm, respectively.

Despite the fact that the accurate measurement of blob speeds is difficult, especially in the lower part of the loop, we find at least a qualitative agreement between the observed blob speeds and those derived from the model. In their early phases the blobs are accelerated to nearly free-fall speeds as the main force acting on the plasma is the field-line projected component of the solar gravitational acceleration. As the blobs fall towards the solar surface, however, the speeds deviate more and more strongly from free fall since the blob is decelerated by the underlying plasma. In contrast to the model, most of the measured blob speeds do not show a significant decrease towards the solar surface, but only a strong deviation from free-fall speed. For two blobs, indicated by the rectangles and diamonds in Fig. 6.10, the speeds indeed decrease slightly in the last data points, but the number of blobs tracked is too low to make any general statement. Apart from possible shortcomings of the model, the lack of observations of decreasing speeds towards the solar limb may also be due to the fact that the loop's footpoints lie behind the limb or due to the difficulty of correct background subtraction which is described by De Groof et al. (2004). However, this is to our knowledge the first model which provides a simple physical mechanism leading to propagating intensity enhancements which reach velocities of the order of 100 km s^{-1} .

Time-slice diagrams of EIT data set indicate events where fast blobs catch up with blobs at lower speeds, but further analysis of more data sets is needed to confirm or reject this hypothesis. High-cadence observations of active regions above the limb in the He II (30.4 nm) band, H_α or C IV (154.8 nm) would help to shed more light onto the distribution of blob speeds as a function of height above the limb. Observations of blob speeds which are increasing during the first phase of the fall and then decreasing when the blob approaches the solar limb would strengthen our concept of falling plasma condensations that are decelerated by the pressure of the transition region. On the other hand, observations of blobs close to the limb at speeds significantly above 100 km s^{-1} would indicate that the part of the loop underneath the falling blob has been previously evacuated by a different process.

6.4 Spectral Signature of Fast Downflows

As already introduced in Chap. 5, spectral lines can be synthesized from the model to study the spectral signature of the catastrophic cooling process. In addition to the lines of C IV (154.8 nm, formation temperature $T_f \approx 10^5 \text{ K}$) and O V (63.0 nm, $T_f \approx 2.2 \cdot 10^5 \text{ K}$), also the He II (30.4 nm, $T_f \approx 8 \cdot 10^4 \text{ K}$) line has been synthesized here to facilitate a comparison of the model to the EIT observations. Figure 6.11 displays the intensities and mean Doppler shifts for all three lines. Both quantities are integrated over the left half of the loop, excluding the footpoints, and the Doppler shifts are calculated as seen from above and converted to velocity units. It is seen that both the first and the second condensation are accompanied by strong transient brightenings in all three spectral lines. For the first condensation region which forms higher up in the hot part of the loop, the brightening is strongest for the O V line which has the highest formation temperature of the three

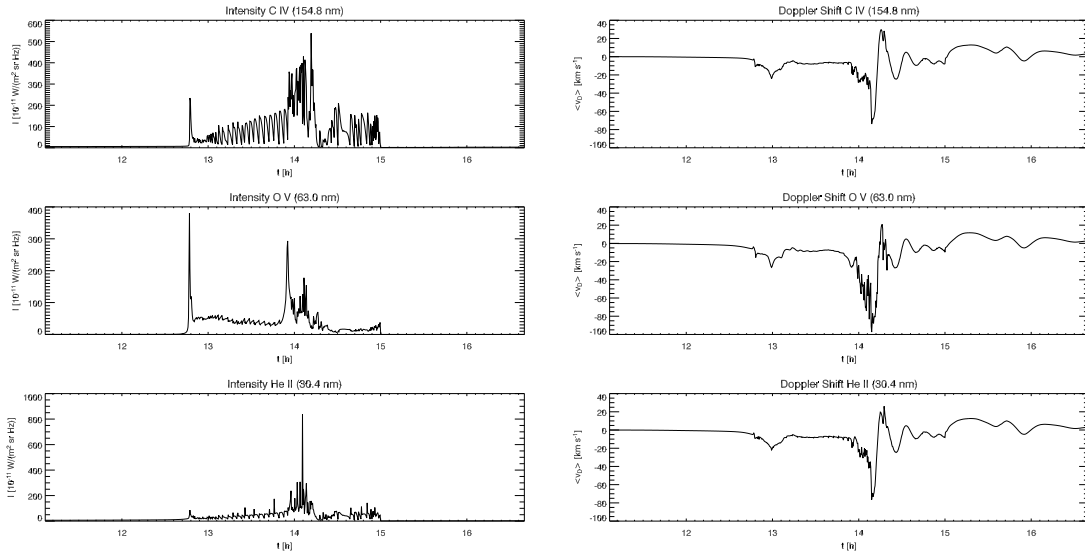


FIGURE 6.11: Variation of the total intensity (left) and Doppler shifts (right) of the lines of CIV (154.8 nm), O V (63.0 nm), and He II (30.4 nm) due to the falling condensation region, integrated over the left half of the loop.

lines. On the other hand, the second intensity increase around $t = 14$ h that is due to the second blob hitting the dense plasma of the cooler lower transition region is strongest for He II, which is the line with the lowest formation temperature. The periodic intensity fluctuations between the formation of the first and the second condensation region, which are seen predominantly in CIV, are caused by sound waves which are reflected back and forth between the strong pressure gradient near the condensation region and the transition region. The corresponding Doppler shifts in the lower panel reveal the different velocities associated with the two condensation events. While the integrated Doppler shifts do not exceed 24 km s^{-1} (for CIV), 26 km s^{-1} (for OV) and 22 km s^{-1} (for He II) in the first case, they reach up to 74 km s^{-1} , 98 km s^{-1} and 76 km s^{-1} , respectively, for the trailing blob. All three lines are redshifted due to the blobs' motions towards the solar surface. To visualize the variation of line shifts and intensity with time, Figure 6.12 shows the line profiles for different points of time during the fall of the second condensation region, starting at $t = 13.7$ h. The spectral lines are integrated over the left half of the loop, excluding the footpoints, and the loop is viewed from above. It is seen that the line profiles are strongly redshifted as the blob falls while the line intensities increase (cf. Fig. 6.11). The Doppler shifts that would be measured in these lines will of course depend on the aspect angle that loop is viewed at.

6.4.1 Footpoint Brightening

When the condensed plasma blob falls down the leg of the loop, it compresses the underlying plasma, which results in a transient temperature rise of the plasma underneath and a strong brightening around the footpoint of the loop when the plasma blob encounters the transition region. Following the description in Sect. 5.3.6, Fig. 6.13 shows the variation of the emission in the CIV (154.8 nm) line at the loop footpoints ($z = 0 - 3 \text{ Mm}$ and $z = 297 - 300 \text{ Mm}$) as a function of

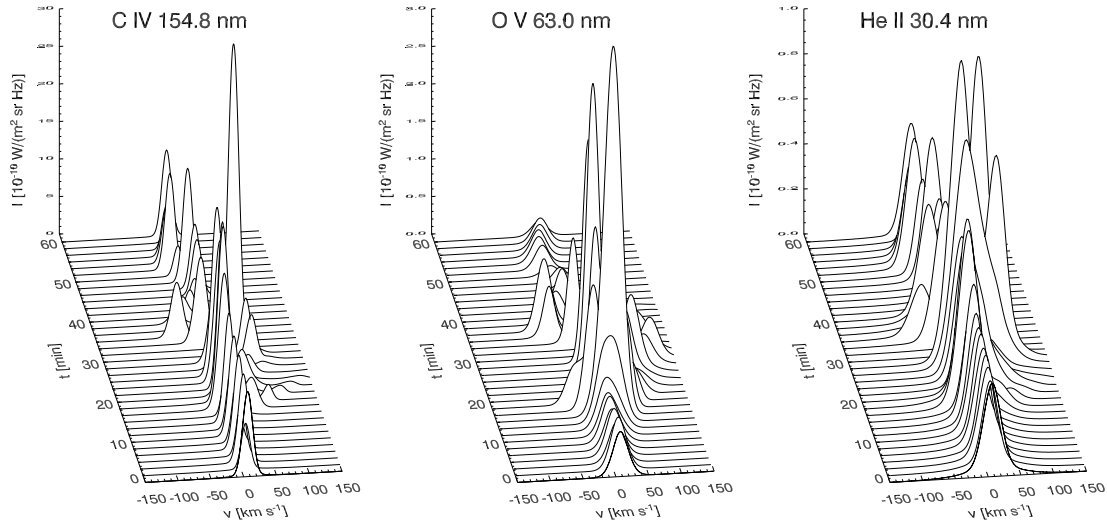


FIGURE 6.12: Spectral signature of the falling plasma blob. The line profiles of C IV (154.8 nm), O V (63.0 nm), and He II (30.4 nm) all show transient brightenings and strong redshifts when seen from above.

time. The intensity is scaled by the respective intensity from the initial model with $H_m = 30$ Mm in order to highlight the dynamics in the C IV emission.

Also for these loops it is observed that the intensity at the left footpoint (draining direction of the condensation region, upper panel) increases for a short time by more than two orders of magnitude and by more than one order of magnitude at the right footpoint. As has been pointed out before, the latter effect takes place because the rarefaction wave following the falling condensation region pulls up plasma from the lower transition region to regions of higher temperatures which leads to the strong transient brightening in the C IV (154.8 nm) line.

Figure 6.14 shows the brightening of a falling plasma blob observed with the Big Bear Solar Telescope in the chromospheric H_α line at $\lambda = 656.3$ nm. This data was acquired simultaneously with the EIT data, and the white lines outline the loop observed with EIT in He II (30.4 nm). Although the time evolution is seen best in movies of this data set, one can identify a faint moving feature in the lower part of the outlined loop which appears around 17:50 UT and brightens up shortly before encountering the solar limb. The formation process of the H_α line is complicated and cannot be treated using the “optically-thin” approximation. However, the strong and localized emission indicates regions of cool plasma at high densities, so that brightening blobs seen in the H_α line above the solar limb support our hypothesis of falling plasma blobs.

6.5 Summary

In this chapter, the scenario of the “evaporation-condensation cycle” has been applied for the first time to models of long active-region loops. It is found that the shocks caused by rapid cooling processes in hot loops can trigger further cooling events. The associated condensation regions, blobs of cool plasma with enhanced density and radiative losses, can subsequently be accelerated to very

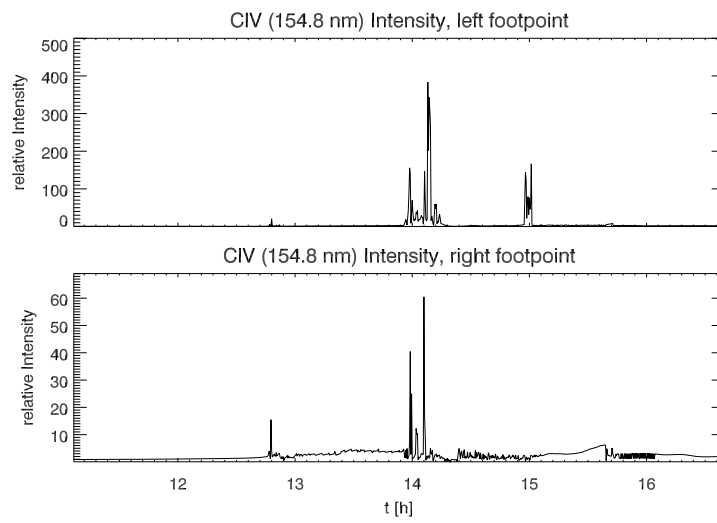


FIGURE 6.13: Footpoint brightening due to falling plasma blobs. The upper panel shows the relative intensity in the CIV (154.8 nm) line for the left footpoint of the loop, the lower panel the one for the right footpoint.

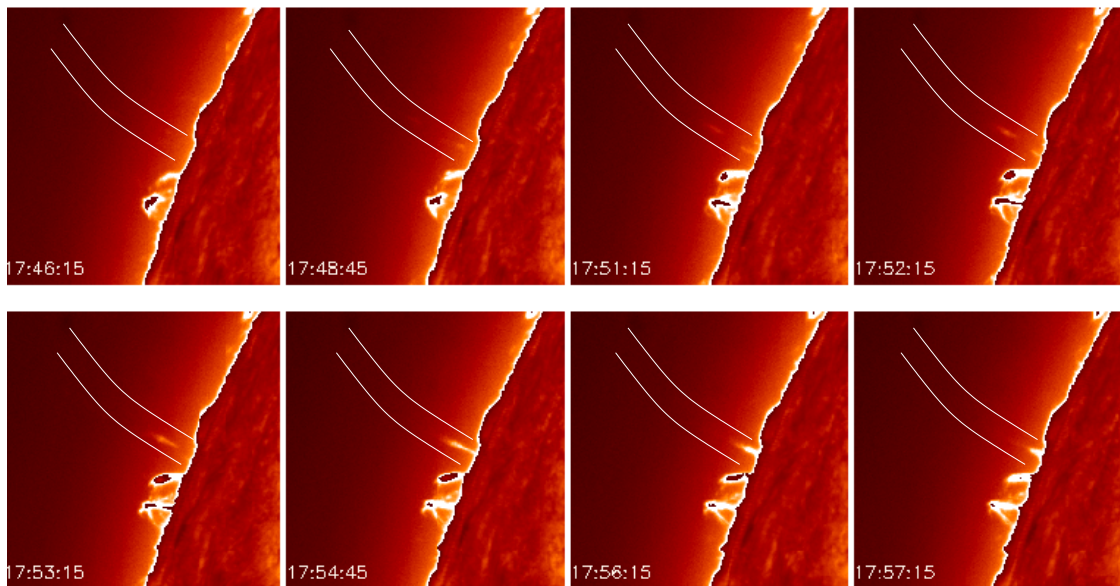


FIGURE 6.14: Brightening of a falling plasma blob observed with the Big Bear Solar Telescope in H_{α} . The loop structure seen with EIT in He II (30.4 nm) is marked by white lines. Courtesy of A. De Groof.

high velocities. While the leading condensation region is strongly decelerated by the underlying loop plasma, the trailing blob is traveling in the wake of the leading blob where the pressure is significantly lower. These blobs are initially traveling with almost free-fall speed and can reach velocities of the order of 100 km s^{-1} before their deceleration sets in in the lower regions of the atmosphere. The reason for the higher velocity of these blobs is the lower pressure in the wake of the leading blob. These fast blobs offer a possible explanation for the recent observations of propagating intensity enhancements by [De Groof et al. \(2004\)](#) and show that transient brightenings and high-speed downflows with a wide range of speeds can result from catastrophic cooling in coronal loops.

7 Coronal Loops as Non-Linear Systems

The finding that footpoint-heated coronal loops can undergo catastrophic cooling and exhibit both stable, periodic and irregular solutions rises the question whether such a system could be reasonably modeled by a set of coupled differential equations for a small set of mean variables. Prominent examples for this approach are, e.g., the predator-prey model of Lotka-Volterra, the Lorenz model (a simplified model for the Rayleigh-Bénard experiment) and the Brusselator model (which describes simple chemical reactions and was named after a working place of the Nobel price winner I. Prigogine). For a general treatment of this subject the reader is referred to [Honerkamp \(1994\)](#). In this chapter, a brief summary on attempts to establish such a simplified model is given, followed by an assessment of the conclusions that can be drawn from them.

Limit cycle solutions in coronal loops were first reported by [Kuin & Martens \(1982\)](#). In their pioneering work they studied the overall energy balance by integrating the energy equation over the entire loop length. For simplification, the radiative losses were parametrized as a power law and a constant heating rate per volume (i.e. no explicit space dependence) was assumed. From these assumptions, they derived a system of two coupled ordinary differential equations¹ for the dimensionless temperature, \bar{T} , and dimensionless density, \bar{n} :

$$\begin{aligned}\frac{d\bar{T}}{d\bar{t}} &= \frac{1}{\bar{n}} \left[1 - \bar{n}^2 \bar{\psi}(\bar{T}) - f\alpha(\bar{T} - 1) \right], \\ \frac{d\bar{n}}{d\bar{t}} &= f\alpha(1 - \bar{T}^{-1}).\end{aligned}\tag{7.1}$$

In these equations, \bar{t} parametrizes time, $\bar{\psi}$ the radiative losses, f is a factor that accounts for chromospheric evaporation (set to one in all cases treated by [Kuin & Martens \(1982\)](#)), and α represents a coupling parameter which is a function of the radiative losses, $\bar{\psi}(\bar{T})$. The coronal loop is thus reduced to a zero-dimensional system, characterized by mean values and coupled to the underlying chromosphere which acts as a heat reservoir. Depending on the value of α , either stable solutions or limit cycle solutions are obtained, with periods between several thousand seconds and about one day. The findings of Kuin & Martens are remarkable in the sense that the important physical processes, namely chromospheric evaporation, catastrophic cooling, and fast draining of the loop are accounted for in a fairly simple model. Different solutions of Eqns. (7.1) are displayed in Fig. 7.1. Depending on the value of the coupling parameter α , the system shows either nonlinear oscillations (case *a* and *b*) or stable static solutions (case *c*). For $\alpha = 1.1$ (case *d*) the evolution depends on the initial conditions and the regimes of stable and periodic solutions are divided by a separatrix (dashed line).

Some years later, their work was heavily criticized by [Craig & Schulkes \(1985\)](#) who tried to reconcile the Kuin & Martens model with the stability analysis of [McClymont & Craig \(1985a,b\)](#).

¹In the original work of [Kuin & Martens \(1982\)](#) the chromospheric evaporation factor, f , in the first of Eqns. (7.1) was omitted which was noticed by [Craig & Schulkes \(1985\)](#). However, since f is set to one throughout the work of [Kuin & Martens \(1982\)](#), this does not affect their results.

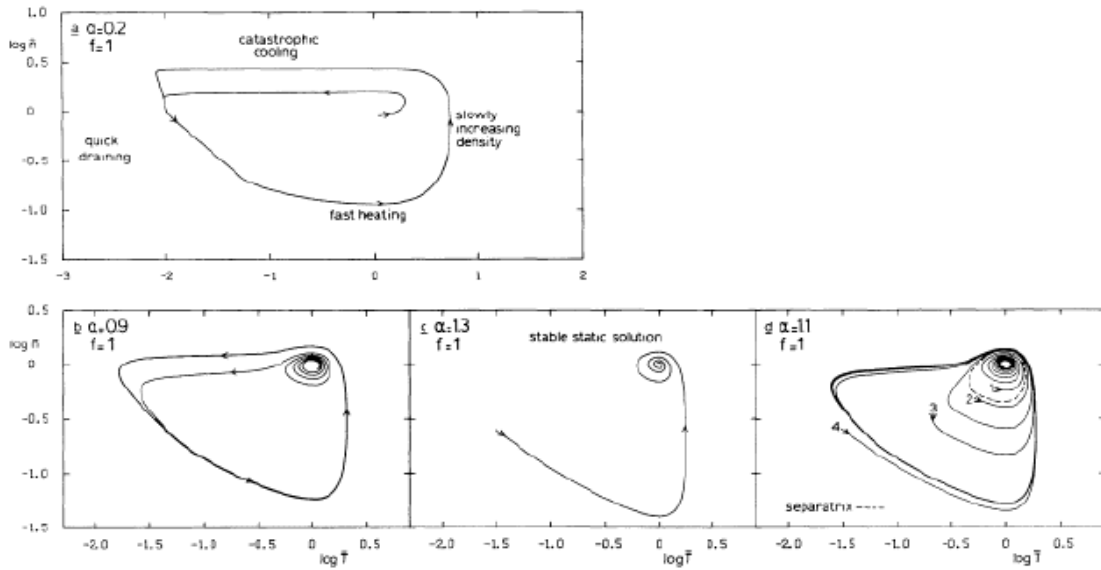


FIGURE 7.1: The solution of Eqns. (7.1) in the phase plane of dimensionless temperature and density. The arrows indicate the time evolution. Case *a* and *b* represent oscillating solutions, case *c* corresponds to a stable static solution. In case *d* the evolution depends on the initial conditions and the system can evolve either into a stable or an oscillating solution. From [Kuin & Martens \(1982\)](#), courtesy P. Martens.

They argued that the coupling factor introduced by [Kuin & Martens](#) was unphysical, but showed that a reconciliation with the work of [McClymont & Craig](#) was possible if this coupling parameter was incorporated correctly. They then found that limit cycles only exist for a coupling parameter above a critical value and argued that under the assumption of a heating function that is *independent of the position* along the loop this parameter range would be unphysical. In a later work, [Craig \(1990\)](#) reexamined the problem by using a one-dimensional coronal loop model and stated that his simulations – which used a constant heating function per unit mass – did not support the limit cycle hypothesis. According to his model, unstable loops collapse and then form “cool loop equilibria” at chromospheric temperatures.

An interesting contribution was made some years later by [Gomez et al. \(1990a,b\)](#) but has not received a lot of attention ever since. They extended the model of [Kuin & Martens](#) to a model with a more detailed treatment of the coupling between the chromosphere and the corona and derived a set of coupled differential equations for perturbations in the density and pressure. The free parameters in their model are the loop length, the heating rate, and a parameter γ which describes the amplitude of a discontinuity of the heating rate between the loop base and the corona. For these equations, a linear stability analysis was carried out, and it was found that for a given loop length and value of γ the solution shows a Hopf bifurcation if the heating rate drops below a critical value. [Gomez et al. \(1990b\)](#) showed furthermore that this Hopf bifurcation is subcritical, which means that there is no stable solution connecting the two branches of the bifurcation around the critical point. They estimated a period of the limit cycle of 20 – 30 min and stated that the amplitudes of their limit cycles were considerably lower than those found by [Kuin & Martens \(1982\)](#).

From the analysis presented in this thesis, I reach the following conclusions concerning the connection of time-dependent “global” loop models and simplified models in which a coronal loop is only characterized by mean quantities: Firstly, the importance of the early work of [Kuin & Martens \(1982\)](#) has to be emphasized. The solutions of the relatively simple set of two coupled differential equations they deduced can be related to the physical processes of chromospheric evaporation, condensation and draining, and the physically and observationally important periodic solutions are found. The criticism concerning the simplicity of the model by [Craig & Schulkes \(1985\)](#) seems partly justified, but one has to bear in mind that many detailed processes which can already be accounted for in one-dimensional time-dependent models are necessarily simplified in both approaches. The finding of [Craig \(1990\)](#) that unstable loops saturate into loops in equilibrium at chromospheric temperatures may be right under the assumption of a heating mechanism that is constant per unit mass, but seems misleading without highlighting the fact that it is indeed the heating function which plays a crucial role regarding the question of stability.

The work presented in this thesis shows that the spatial distribution of a temporally constant heating function can act as a control parameter of the system. In that respect, it seems questionable whether more than a correct prediction of the general behavior of the described physical system can be deduced from simplified models which do not account for any spatial variation of variables along the loop.

8 Families of Loops: A Parameter Study

8.1 Introduction and Setup

Loops in the solar corona occur at a large range of different sizes, and also the amount and scale height of the heating are seen to vary. To obtain a better understanding of the regime in which coronal loops exhibit recurrent condensations due to thermal instability, a set of 100 simulations of coronal loops was carried out, covering a range of loop lengths, energy fluxes and damping lengths.

Specifically, loop lengths of $L = 100, 150, 200, 250,$ and 300 Mm, energy fluxes of $F_m = 100, 500, 1000,$ and $10\,000$ W/m², and damping lengths of $H_m = 2, 4, 6, 8,$ and 10 Mm were chosen. The energy fluxes used span the range indicated by [Withbroe & Noyes \(1977\)](#) who estimated a total coronal energy loss of 300 W/m² for the quiet sun and up to 10 000 W/m² for active regions. For each loop length, the simulation was started with a stable loop model with an energy flux of $F_0 = 10^3$ W/m² and a damping length of $H_m = L/4$. Figure 8.1 shows the loop temperature as a function of loop length for the different start models.

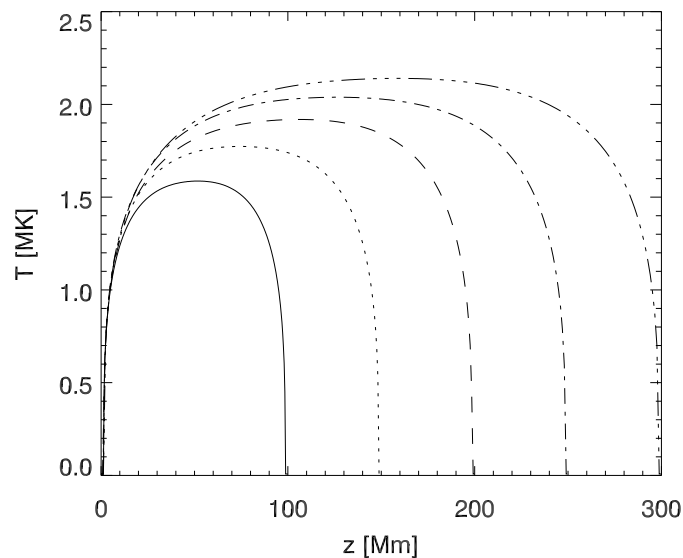


FIGURE 8.1: Loop temperature as a function of loop length for the start models with $L = 100$ Mm (*solid*), $L = 150$ Mm (*dotted*), $L = 200$ Mm (*dashed*), $L = 250$ Mm (*dash-dotted*), and $L = 300$ Mm (*dash-dot-dotted*).

Each simulation was initially run for 10^5 s, and for some runs the simulation time was ex-

tended up to $6 \cdot 10^5$ s whenever necessary to identify long periods. The time-integration scheme was set to fully implicit mode ($\alpha = 1$) to ensure maximal stability. In order to keep the parameter study computationally tractable, the non-equilibrium ionization rate for hydrogen and helium were solved along with the hydrodynamic equations, while the radiative losses for the other elements were interpolated from precalculated radiative loss curves as a function of electron temperature. A comparison with simulations in which the non-equilibrium radiative losses for more elements were included showed that this had some effect on the periods of the condensation cycles and the absolute values of the physical variables (cf. the models in Chap. 6, where non-equilibrium ionization of carbon and oxygen were included), but did not change the class of any solution, i.e. whether static or dynamic solutions were obtained. Since the goal of this parameter study is to work out the general character of the solutions for different loop parameters, this approach seemed reasonable. However, for a detailed study of the time-dependent emission and line shifts originating from a dynamic loop model, as much information as possible about the atomic processes should be included.

The simulations presented here are quite demanding in computing-time, since the time steps have to be temporally as small as 10^{-4} s, e.g. when a condensation region forms. The time needed to run one of the dynamic simulations for $t = 10^5$ s is of the order of 2 CPU days on a machine with 1.15 Ghz Alpha EV7 processors (the *HYADES* cluster at the ITA Oslo) and around 30% longer on a machine with 1.8 Ghz AMD Athlon processors (the *KABUL* cluster at the KIS Freiburg). The advantage of using an implicit code is that for static solutions, the time steps can be very large, so that these runs are completed within several hours. The disadvantage is that the matrix inversion which is part of the implicit scheme is not well-suited for parallelization. However, the large number of individual simulations which has been carried out could be conveniently distributed over several CPUs.

8.2 Classes of Solutions and Periods

According to the findings of Chap. 5, the time-dependent evolution of loop models can be grouped into three different classes: static solutions, periodic solutions, and irregular/chaotic solutions. An overview of the solution types for all realizations of the model is given in Table 8.1. Static solutions are denoted by the symbol S, while for periodic solutions the period P is given. The remaining solutions show irregular/chaotic behavior, indicated by the symbol C. The discrimination between periodic and irregular solutions is based on the evolution of the loops' mean temperature, $\langle T \rangle(t)$. All non-static solutions undergo recurrent condensation, but only those which show a clear periodic pattern in the mean temperature are classified as "periodic", while all others are classified as irregular. It should be noted that some of these solutions may relax into periodic solutions, as pointed out in Chap. 6. In two cases of the 100 simulations, namely for $F_0 = 10^2$ W/m², a damping length of $H_m = 2$ Mm and loop lengths of $L = 250$ Mm and 300 Mm, the models cooled down to very low temperatures and the time steps became exceedingly small, so that no convergence was reached (indicated by "nc" in Table 8.1). In three other cases, also for loop lengths of $L = 250$ Mm and 300 Mm and a damping length of $H_m = 2$ Mm, the time steps became exceedingly small during the formation of a condensation region before the prescribed simulation time was reached. In principle, most of these cases can be handled numerically, e.g. by adjusting the weights of the grid equation and increasing the number of iterations when calculating the ionization rate equa-

L [Mm]	H_m [Mm]	$F_0 = 10^2 \text{ W/m}^2$	$F_0 = 5 \cdot 10^2 \text{ W/m}^2$	$F_0 = 10^3 \text{ W/m}^2$	$F_0 = 10^4 \text{ W/m}^2$
100	2	C	$P = 18\,200 \text{ s}$	$P = 20\,800 \text{ s}$	$P = 20\,100 \text{ s}$
100	4	S	$P = 46\,800 \text{ s}$	S	S
100	6	S	S	S	S
100	8	S	S	S	S
100	10	S	S	S	S
150	2	C	C	$P = 26\,100 \text{ s}$	$P = 25\,700 \text{ s}$
150	4	S	$P = 43\,700 \text{ s}$	$P = 112\,500 \text{ s}$	$P = 38\,700 \text{ s}$
150	6	S	S	S	$P = 83\,000 \text{ s}$
150	8	S	S	S	S
150	10	S	S	S	S
200	2	C	$P = 18\,000 \text{ s}$	C	$P = 23\,400 \text{ s}$
200	4	S	$P = 57\,500 \text{ s}$	C	$P = 40\,300 \text{ s}$
200	6	S	S	S	$P = 59\,900 \text{ s}$
200	8	S	S	S	$P = 129\,300 \text{ s}$
200	10	S	S	S	S
250	2	nc	C	C	C
250	4	S	$P = 71\,600 \text{ s}$	$P = 112\,000 \text{ s}$	C
250	6	S	S	S	$P = 71\,600 \text{ s}$
250	8	S	S	S	$P = 285\,000 \text{ s}$
250	10	S	S	S	S
300	2	nc	C	$P = 18\,300 \text{ s}$	C
300	4	S	C	$P = 132\,200 \text{ s}$	$P = 27\,000 \text{ s}$
300	6	S	S	S	$P = 56\,300 \text{ s}$
300	8	S	S	S	$P = 78\,800 \text{ s}$
300	10	S	S	S	$P = 125\,900 \text{ s}$

TABLE 8.1: Solution classes and periods for loop models with different loop lengths, L , damping lengths, H_m , and energy fluxes, F_0 . Static solutions are denoted by S, periodic solutions by P (the period of the condensation cycle in seconds), and irregular/chaotic solutions by C.

tions. However, since the basic parameters of all simulations of this study should be identical if a reasonable comparison is to be made, this was not done. A comparison with similar runs with the next higher damping length indicated that the solutions are very likely irregular.

The main findings of the parameter can be summarized as follows:

- It is found that for energy fluxes of $F_0 \leq 10^3 \text{ W/m}^2$ and damping lengths of $H_m \geq 6 \text{ Mm}$, all loop models are stable. This shows that for loops between $L = 100 - 300 \text{ Mm}$ length and moderate energy fluxes, the limit of thermal instability is not strongly dependent on the ratio of the damping length to the loop length.
- Furthermore, the period of recurrent condensations for a given energy flux and loop length grows strongly upon approaching the limit of instability. However, they do not depend strongly on the loop length, which shows that it is not the time it takes for the condensation region to drain from the loop which determines the period, but the slower process of chromospheric evaporation and subsequent cooling of the coronal part of the loop before the instability sets in.

- Interesting cases of chaotic/irregular evolution are found for coronal loops with very short damping lengths, on the order of $H_m = 2$ Mm.
- A very high energy flux of $F_0 = 10^4$ W/m² has two effects. Firstly, it increases the rate of chromospheric evaporation which results in a higher density in the coronal part of the loop. This facilitates the formation of a condensation region since the radiative losses scale with the square of the electron density. As a result, the limit of stability increases to 12 Mm for $L = 300$ Mm loops. This phenomenon of overheated loops will be discussed in Sect. 8.4. On the other hand, a higher total energy flux also results in a higher energy deposition at a given height. For shorter loops ($L = 100$ Mm), this prevents the formation of a condensation region since heat conduction is efficient enough to balance the radiative losses around the loop apex. This explains why e.g. loops with a damping length of $H_m = 4$ Mm are stable for $L = 100$ Mm, but not for longer loop lengths.

8.3 Temperature and Density Variations

The mean temperature, $\langle T \rangle$, of all loop models is shown in Table 8.2. As in the previous chapters, the mean values are defined as the average quantities over the region of the loop which lies above the transition region, bounded by the points where the temperature crosses $T = 10^5$ K in both loop legs. If a single number is given, this corresponds to a stable solution, while a temperature range indicates a dynamic (periodic or irregular) solution. To avoid effects of the initial condition on the temperature ranges, these ranges are calculated using the second half of each simulation run only.

It is seen that for a given energy flux the mean loop temperatures increase as a function of damping length. This can be easily understood since a deposition of energy at greater heights results in lower radiative losses (due to the decreased density) and therefore more net heating. For dynamic solutions, the spread of mean temperatures for a given loop model is large: At a given point in time, the mean temperature of a dynamic loop can be lower than the mean temperature of a model with an energy flux F_0 which is ten times smaller.

Furthermore, it is seen that a static loop with a given mean temperature can be “produced” in two different ways: Either with a lower energy flux and a long damping length, or with a higher energy flux and a shorter damping length. As an illustration, Fig. 8.2 displays the ratios of temperature, electron density and total radiative losses along two $L = 150$ Mm loop models with an apex temperature of $T_{\text{top}} = 1.1$ MK, but different amounts of heating. The first one has an energy flux of $F_{0,1} = 10^3$ W/m² and a damping length of $H_{m,1} = 6$ Mm, while the second one has an energy flux of $F_{0,2} = 5 \cdot 10^2$ W/m² and a damping length of $H_{m,2} = 10$ Mm. It is by no means surprising that the model with the higher energy flux also radiates more strongly, but the comparison shows clearly that stable loops with a given apex temperature can be “overdense” compared to more uniformly heated loops if the heating is concentrated towards the footpoints. This agrees with the findings of [Aschwanden et al. \(2001\)](#), which will be discussed in Sect. 8.5.

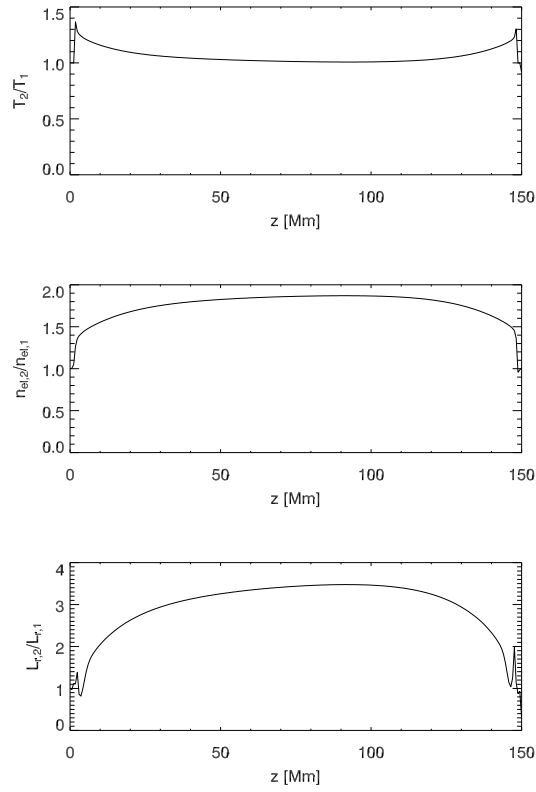


FIGURE 8.2: Comparison of two loop models with similar apex temperatures but different electron densities, n_e , and hence radiative losses, L_r . The top panel displays the temperature ratio along two $L = 150$ Mm loop models, one with an energy flux of $F_{0,2} = 5 \cdot 10^2$ W/m² and a damping length of $H_{m,2} = 10$ Mm, the other one with $F_{0,1} = 10^3$ W/m² and $H_{m,1} = 6$ Mm. The middle and lower panel show the corresponding ratios of electron densities and radiative losses, respectively.

L [Mm]	H_m [Mm]	$F_0 = 10^2 \text{ W/m}^2$	$F_0 = 5 \cdot 10^2 \text{ W/m}^2$	$F_0 = 10^3 \text{ W/m}^2$	$F_0 = 10^4 \text{ W/m}^2$
100	2	69-337	214-639	363-928	1000-1804
100	4	465	464-853	965	1730
100	6	541	895	1108	2090
100	8	589	969	1191	2265
100	10	624	1018	1249	2384
150	2	180-241	121-693	54-971	994-1722
150	4	463	379-789	544-1034	1321-1898
150	6	545	900	1103	1489-2191
150	8	598	987	1205	2051
150	10	641	1048	1278	2278
200	2	200-252	216-614	140-847	438-1874
200	4	472	272-771	646-911	1215-1883
200	6	553	897	1094	1448-2096
200	8	608	990	1204	1724-1929
200	10	654	1057	1284	2167
250	2	nc	200-540	184-802	547-1798
250	4	479	303-644	406-962	762-1829
250	6	557	908	1107	1449-1958
250	8	613	1000	1217	1569-2213
250	10	659	1069	1298	2224
300	2	nc	300-558	336-690	491-1543
300	4	478	377-711	860-931	1045-1660
300	6	560	901	1089	1231-2011
300	8	618	997	1207	1454-2127
300	10	665	1068	1293	1572-2291

TABLE 8.2: Mean temperatures in units of 10^3 K for loop models with different loop lengths, L , damping lengths, H_m , and energy fluxes, F_0 .

L [Mm]	H_m [Mm]	$F_0 = 10^2 \text{ W/m}^2$	$F_0 = 5 \cdot 10^2 \text{ W/m}^2$	$F_0 = 10^3 \text{ W/m}^2$	$F_0 = 10^4 \text{ W/m}^2$
100	2	0.43-2.21	3.08-9.69	3.41-16.53	24.53-90.88
100	4	2.66	3.04-9.66	12.92	51.07
100	6	2.60	8.17	12.02	45.64
100	8	2.54	7.85	11.53	43.15
100	10	2.52	7.66	11.20	41.64
150	2	0.59-1.21	0.90-7.02	0.71-12.11	22.73-61.78
150	4	1.96	2.60-7.02	10.81-11.34	26.55-58.56
150	6	2.02	6.17	9.90	24.13-58.22
150	8	1.99	5.96	9.49	46.61
150	10	1.97	5.81	9.22	43.94
200	2	0.42-1.00	1.10-5.61	1.45-9.69	8.74-57.73
200	4	1.42	2.17-5.77	8.59-9.34	21.10-49.34
200	6	1.43	5.26	8.15	22.95-49.04
200	8	1.42	5.12	7.87	41.55-45.64
200	10	1.42	5.02	7.66	38.18
250	2	nc	1.24-4.55	0.86-8.61	0.86-8.61
250	4	1.17	1.86-4.87	2.91-8.06	16.52-65.09
250	6	1.19	4.00	6.52	20.77-49.73
250	8	1.19	3.93	6.35	19.16-43.21
250	10	1.20	3.87	6.21	29.95
300	2	nc	0.85-3.46	1.64-6.40	4.47-39.10
300	4	0.96	1.84-3.76	6.16-6.23	18.08-41.22
300	6	0.96	3.54	6.04	16.63-38.57
300	8	0.96	3.51	5.95	18.02-39.62
300	10	0.97	3.48	5.85	18.11-40.15

TABLE 8.3: Mean electron densities in units of 10^{14} m^{-3} for loop models with different loop lengths, L , damping lengths, H_m , and energy fluxes, F_0 .

8.4 Overheated Loops

An inspection of the loop models with intermediate damping lengths of $H_m = 6 - 8$ Mm reveals another interesting aspect, namely an alternative way of triggering a thermal instability. For all loop models with $L \geq 150$ Mm it is seen that stable solutions are obtained for energy fluxes up to $F_0 = 10^3$ W/m², while a larger energy flux of $F_0 = 10^4$ W/m² results in a thermal instability with recurrent condensations.

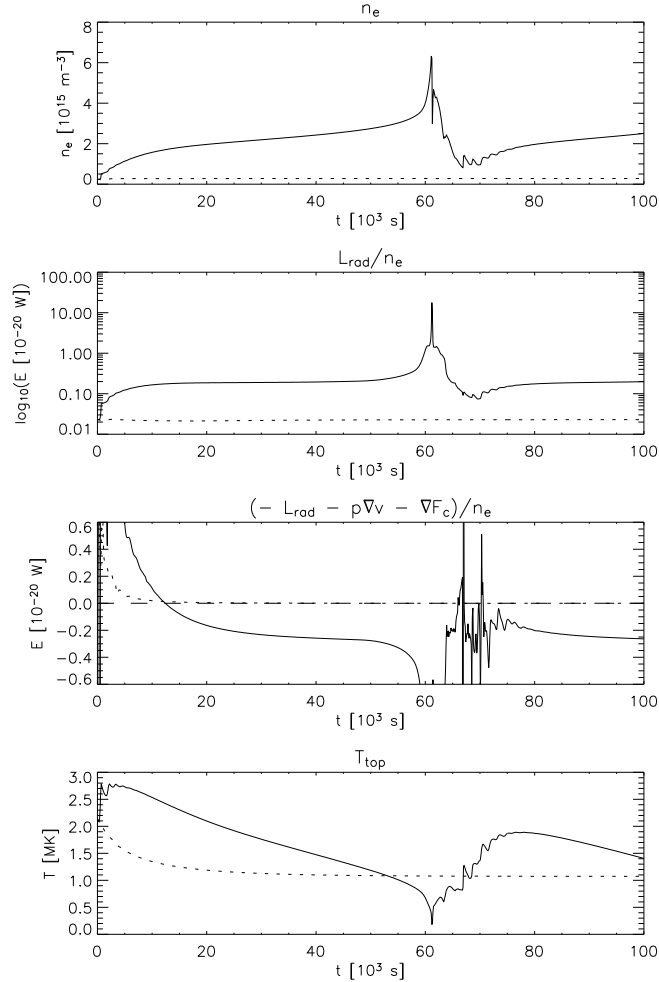


FIGURE 8.3: Energy balance at the loop apex for $L = 300$ Mm loop models with energy fluxes of $F_0 = 10^3$ W/m² (dotted lines) and $F_0 = 10^4$ W/m² (solid lines), and a damping length of $H_m = 6$ Mm. From *top to bottom*: Electron density, n_e , radiative losses per particle, the sum $(-L_{\text{rad}} - p\nabla v - \nabla F_c)$ per particle (negative values indicate that the loop apex is losing energy), and the temperature at the loop top.

Figure 8.3 shows a comparison of the energy balance at the loop apex for two $L = 300$ Mm loop models with a damping length of $H_m = 6$ Mm and two different energy fluxes of $F_0 = 10^3$ W/m² and $F_0 = 10^4$ W/m². Both models were started from the static initial model with $F_0 = 10^3$ W/m² and a damping length of $H_m = L/4$ (displayed in Fig. 8.1).

In the case of the more strongly heated loop (solid lines), the apex temperature rises initially from $T_{\text{top,start}} = 2.1 \text{ MK}$ to $T_{\text{top}} = 2.8 \text{ MK}$ as a result of the higher energy flux (bottom panel of Fig. 8.3). However, once the system has adjusted to the increased heating rate, the energy balance at the loop apex soon becomes negative. This is illustrated in the third panel of Fig. 8.3, where the sum of the radiative losses, L_{rad} , the adiabatic compression, $p\nabla v$, and the divergence of the conductive flux, ∇F_c , are plotted.

On the other hand, the less strongly heated loop (dotted lines) cools down to $T_{\text{top}} = 1.1 \text{ MK}$ since the energy flux of $F_0 = 10^3 \text{ W/m}^2$ is now dissipated in lower regions of the loop ($H_m = 6 \text{ Mm}$ compared to $H_m = L/4 = 75 \text{ Mm}$ of the start model) and reaches a static equilibrium solution with constant radiative losses, temperature and electron density at the loop apex.

For the more strongly heated loop, the apex electron density continuously increases with time until a thermal instability sets in around $t = 60 \cdot 10^3 \text{ s}$. The reason for this is that the enhanced energy flux, F_0 , evaporates continuously chromospheric plasma into the loop while this process eventually ceases for lower energy fluxes when the loop approaches an equilibrium. This can be seen in Fig. 8.4 where the mass flux, $\rho \cdot v$, at the location $z = 20 \text{ Mm}$ in the left loop leg is plotted. It is seen that the mass flux into the coronal part of the loop vanishes after several 10^3 s for $F_0 = 10^3 \text{ W/m}^2$ (dotted line), while for $F_0 = 10^4 \text{ W/m}^2$ (solid line) it remains at a positive value of around $2 \cdot 10^{-8} \text{ kg m}^{-2} \text{ s}^{-1}$ until the thermal instability sets in around $t = 60 \cdot 10^3 \text{ s}$ and initiates an even stronger upflow in the left loop leg.

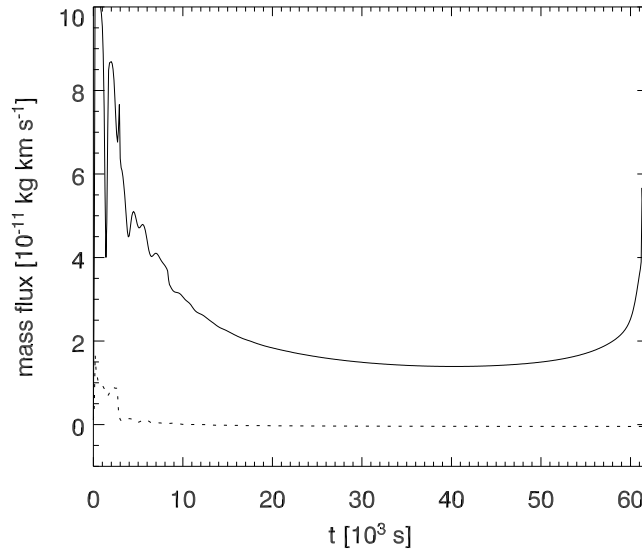


FIGURE 8.4: Mass flux, $\rho \cdot v$, at $z = 20 \text{ Mm}$ into the coronal part of the loop for the two loop models with energy fluxes of $F_0 = 10^3 \text{ W/m}^2$ (dotted line) and $F_0 = 10^4 \text{ W/m}^2$ (solid line). In the case of the lower heating rate, chromospheric evaporations stops as the loop approaches an equilibrium configuration, while the more strongly heated loop is continuously filled. Around $t = 60 \cdot 10^3 \text{ s}$, a thermal instability sets in which results in an even higher mass-accretion rate.

This phenomenon is particularly interesting for two reasons: Firstly, it provides an extension of

the parameter range in which footpoint-centered heating of coronal loops can give rise to thermal instabilities and dynamic loop evolution. If the energy flux into the transition region and corona is temporarily enhanced for a given patch of the solar surface, this can trigger a thermal instability of coronal loops which were stable before. Such a transient increase of the energy flux can for example be the result of magnetic flux eruption or magnetic reconnection processes.

Secondly, it establishes a connection between thermal instabilities in coronal loops and instabilities and subsequent relaxation oscillations of open coronae. It has been found by [Hearn & Vardavas \(1981\)](#), [Hammer \(1982\)](#) and [Souffrin \(1982\)](#) that the classical picture of an infinitely extended corona breaks down when the energy flux exceeds a certain limit which depends on the damping length over which the energy is dissipated in the corona.

It was suggested by [Hearn et al. \(1983\)](#) that these overheated coronae undergo global relaxation oscillations, during which an extended corona becomes unstable and collapses into two coronal shells. The outer shell eventually contracts and absorbs the inner shell so that again one extended corona is formed which becomes subsequently unstable. This was later confirmed by more detailed time-dependent numerical calculations by [Korevaar & Hearn \(1989\)](#). The parameters used in their calculations were quite different from the solar case, as they modeled the hot O star ζ Ori which has a mass of $44.7 M_{\odot}$, a radius of $28.7 R_{\odot}$ and an effective temperature of 31 000 K. However, the general behavior of the two modeled systems is very similar: The increased heating of lower parts of the corona increases the density in the outer regions which gives rise to enhanced radiative losses. Above a certain limit, thermal conduction can no longer balance the radiative losses and the corona collapses. These findings have found additional confirmation by the work of [Tziotziou et al. \(1998\)](#) who calculated a grid of coronal models for different energy fluxes and distributions and found that relaxation oscillations occur when the energy input exceeds a certain limit. Using a different numerical approach, [Hammer \(1985\)](#) computed a large number of hydrostatic shell models and localized a boundary line in the parameter space of energy flux and damping length that separates normal extended coronae from coronal shells. The evaporation-condensation cycle which has been shown to be a versatile mechanism to explain the dynamic evolution of coronal loops is very similar to the idea of collapsing and rebuilding coronae.

8.5 Comparison with Hydrostatic Models

A parameter study of 500 hydrostatic loop models with non-uniform heating was carried out by [Aschwanden et al. \(2001\)](#) and compared to observations with TRACE and EIT. They found that most of the observed loops could not be explained by the classical “RTV scaling law” ([Rosner et al. 1978](#)), which assumes a constant pressure and heating along the loop, because the observed loops seemed to be nearly isothermal along their coronal segments, showed an enhanced density and pressure compared to loops with uniform heating, and were visible over a much larger height range than the hydrostatic scale height.

Their parameter study consisted of a set of 500 models with loop lengths between 8 and 600 Mm length which all had an apex temperature of 1 MK. They assumed symmetric, static loops, and solved iteratively for the temperature and pressure distribution along a half-loop. The radiative losses were parametrized as a function of temperature. Apart from the fixed apex temperature, the other boundary conditions were a footpoint temperature of 0.1 MK and a vanishing conductive flux both at the footpoint and the apex. [Aschwanden et al. \(2001\)](#) found that stably stratified loops

were obtained for long damping lengths, while for short damping lengths ($H_m \leq 6.3$ Mm for a total loop length of $L = 100.8$ Mm, $H_m \leq 8.0$ Mm for $L = 201$ Mm, $H_m \leq 12.6$ Mm for $L = 401$ Mm), no *static* solutions could be found numerically. In a narrow regime of intermediate damping lengths, they found unstably stratified loops with a density inversion at the loop apex. Comparing the model results with TRACE observations, the authors found that only 30% of the observed loops were compatible with hydrostatic steady state solutions, and that the best fits were obtained for damping lengths of $H_m = 12 \pm 5$ Mm.

The parameter study presented here is in good agreement with the work of [Aschwanden et al. \(2001\)](#) and covers the regime where the authors could not find any static solutions, since for the loops in this regime no equilibrium solutions exist. Therefore, time-dependent models are needed to obtain any information about this parameter regime.

It should be emphasized for clarification that the argument that footpoint-centered heating leads to higher loop densities holds for a given apex temperature, and this is not so much because the heating is centered in the lower parts of the loop but because a larger heat flux is needed to sustain this specific apex temperature if the energy is dissipated at lower heights.

In contrast to [Aschwanden et al. \(2001\)](#), who derived an empirical relation between the critical damping length, below which no static solutions exist, and the loop length ($H_{m,\text{crit}} \approx \sqrt{L/2}$), the ensemble of 100 loop models calculated here do not support a simple parametrization of the critical damping length as the function of loop length, but it is found that the critical damping length also depends on the energy flux.

The two approaches of solving the hydrostatic equations with parametrized radiative losses on the one hand, and solving the time-dependent hydrodynamic equations with non-equilibrium ionization on the other hand complement each other. While the first approach makes the calculation of a very large ensemble of loops feasible, the second approach can cover the regime where no equilibrium solutions exist.

8.6 Plots of Loop-Averaged Variables

The general time evolution for a large number of loop models can be compared most easily by plotting different loop-averaged variables, such as the mean temperature, the mean density and the mean pressure, as a function of time, or by plotting two variables, e.g. $\langle T \rangle$ and $\langle p \rangle$, as a function of each other. Also here the mean values are defined as the average quantities over the region of the loop which lies above the transition region, bounded by the points where the temperature crosses $T = 10^5$ K in both loop legs. Figures 8.5 – 8.9 show the mean loop temperatures as a function of time for loop length of $L = 100, 150, 200, 250, 300$ Mm, respectively, and in Figs. 8.10 – 8.14 the corresponding $\langle T \rangle$ – $\langle p \rangle$ -diagrams are displayed. As has been mentioned before, the periodic evolution of loops appears in the form of limit cycles in the $\langle T \rangle$ – $\langle p \rangle$ -diagrams, while static solutions reached fixed points.

Additional plots of the corresponding mean electron densities and mean pressures as a function of time are given in the appendix in Figs. 8.10 – 8.14 and Figs. A.1 – A.5, respectively.

8.6.1 Time Evolution of Mean Temperature

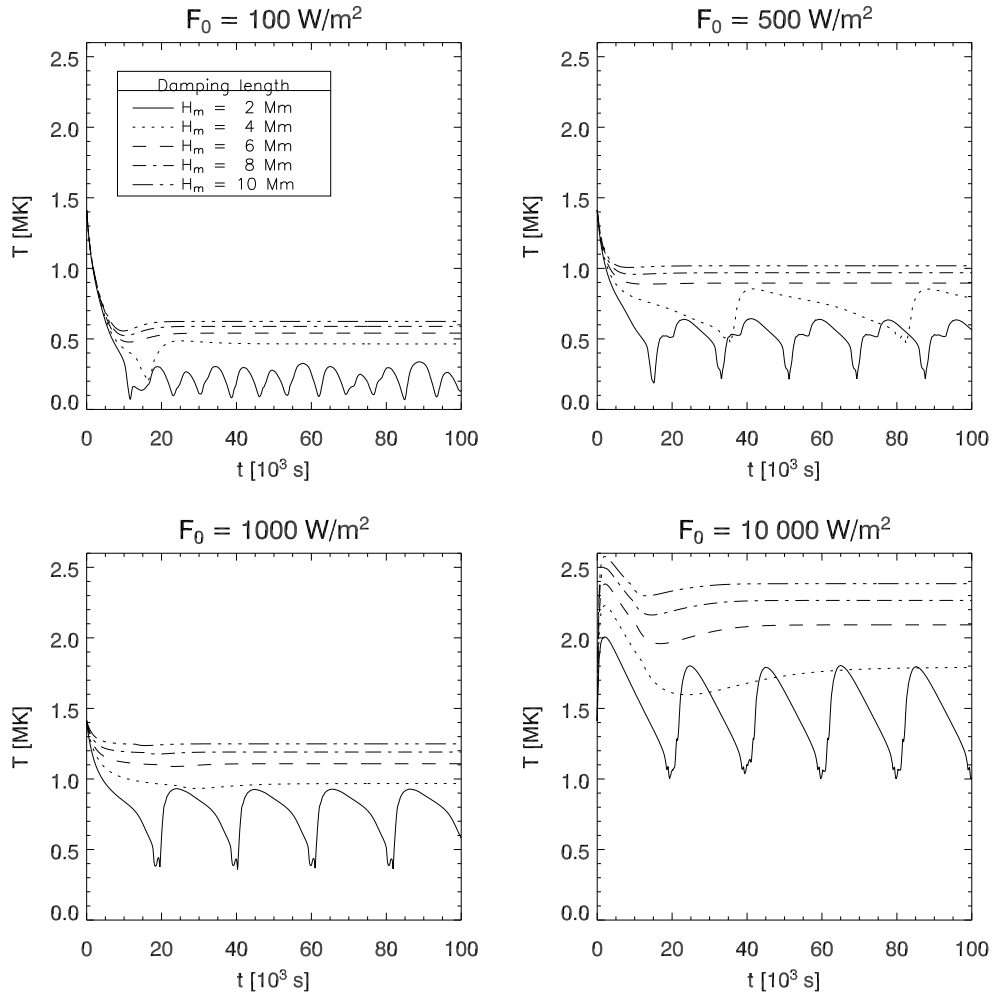


FIGURE 8.5: Mean loop temperature as a function of time for $L = 100$ Mm loop models and energy fluxes of $F_0 = 10^2, 5 \cdot 10^2, 10^3, 10^4 \text{ W/m}^2$.

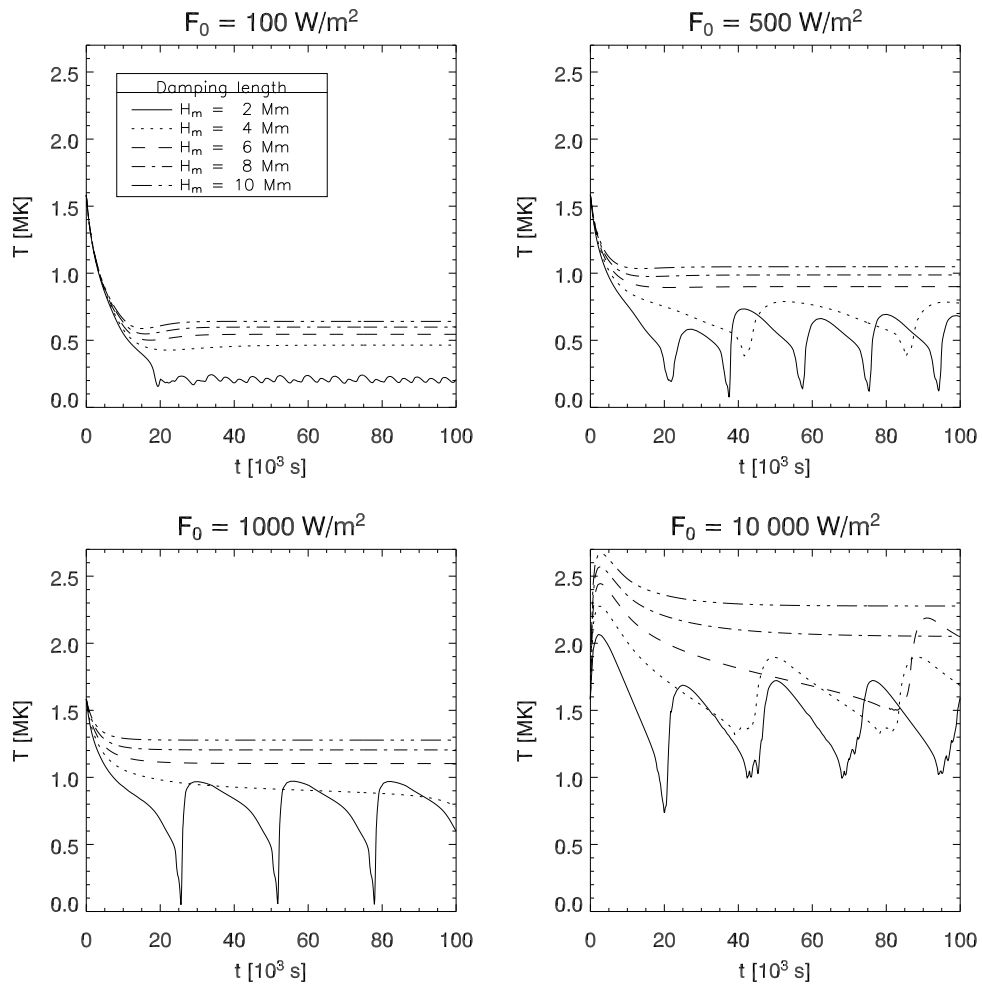


FIGURE 8.6: Mean loop temperature as a function of time for $L = 150$ Mm loop models and energy fluxes of $F_0 = 10^2, 5 \cdot 10^2, 10^3, 10^4 \text{ W/m}^2$.

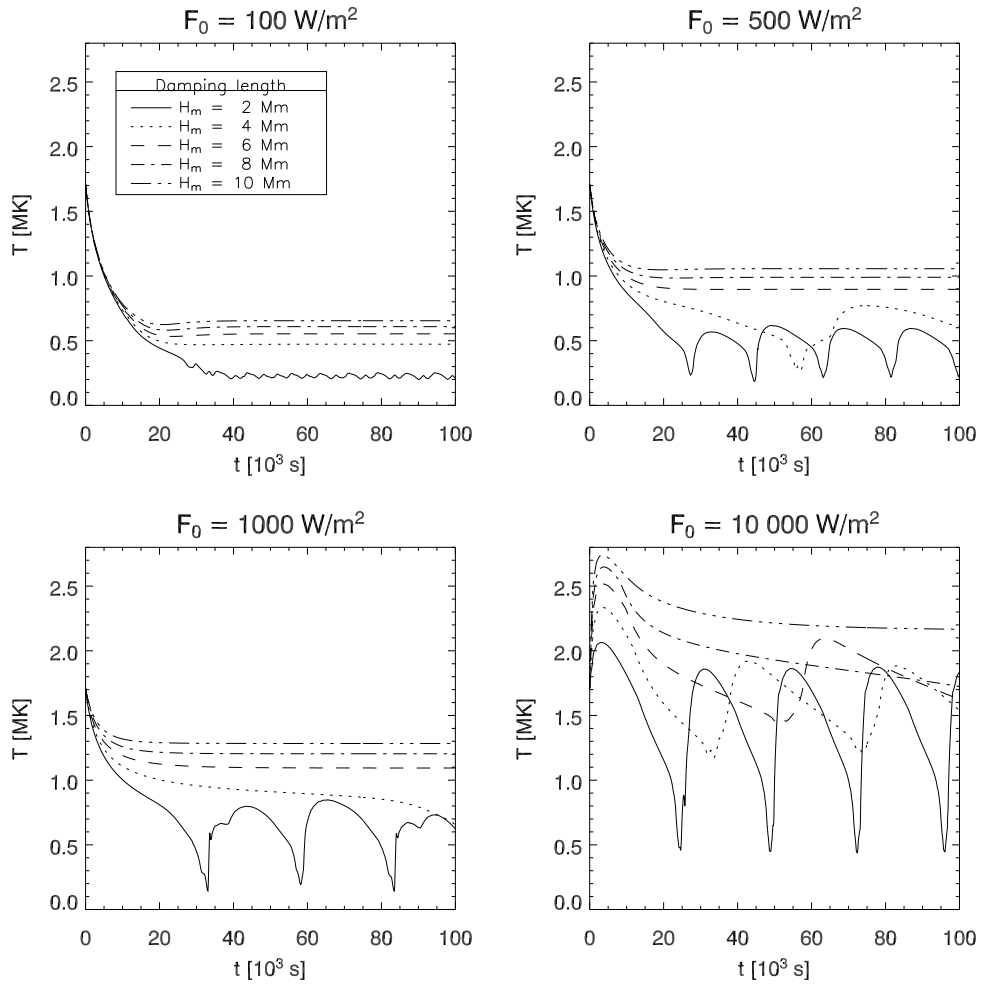


FIGURE 8.7: Mean loop temperature as a function of time for $L = 200$ Mm loop models and energy fluxes of $F_0 = 10^2, 5 \cdot 10^2, 10^3, 10^4 \text{ W/m}^2$.

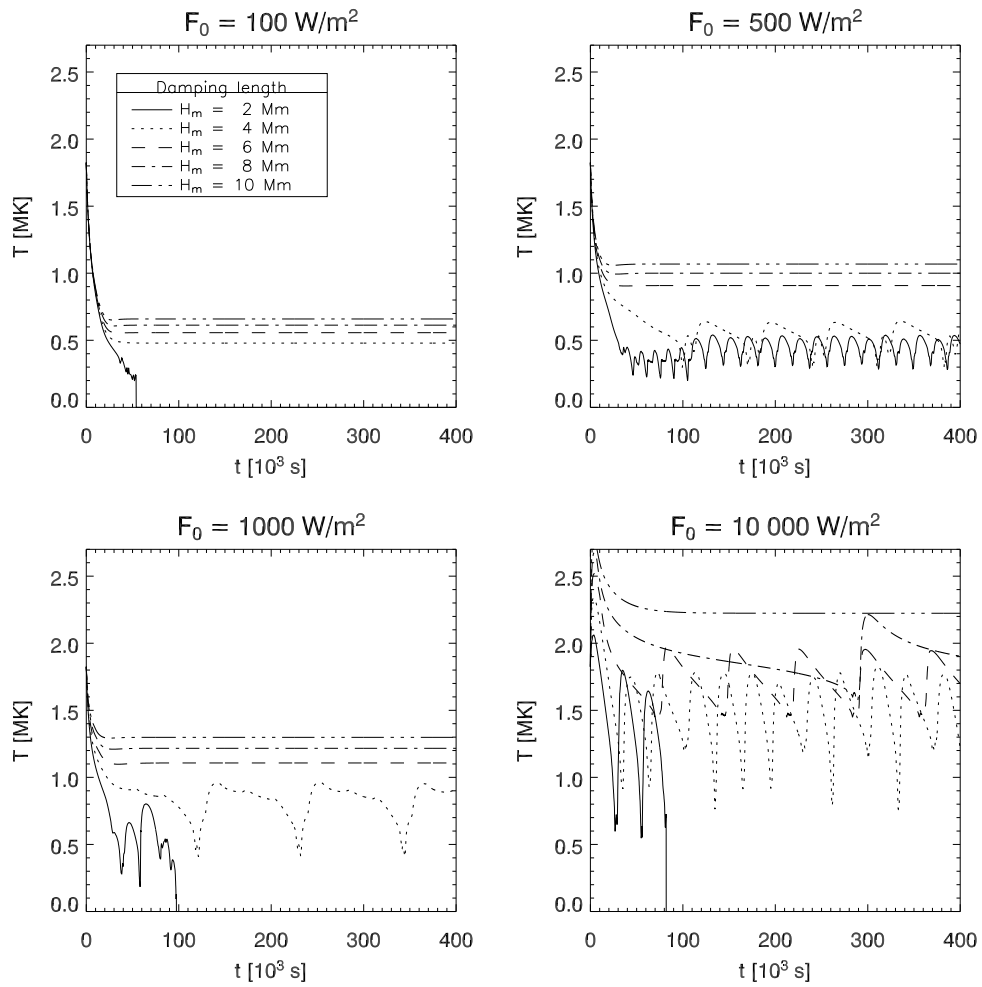


FIGURE 8.8: Mean loop temperature as a function of time for $L = 250$ Mm loop models and energy fluxes of $F_0 = 10^2, 5 \cdot 10^2, 10^3, 10^4$ W/m². Note that all simulations of this set were run for $t = 4 \cdot 10^5$ s.

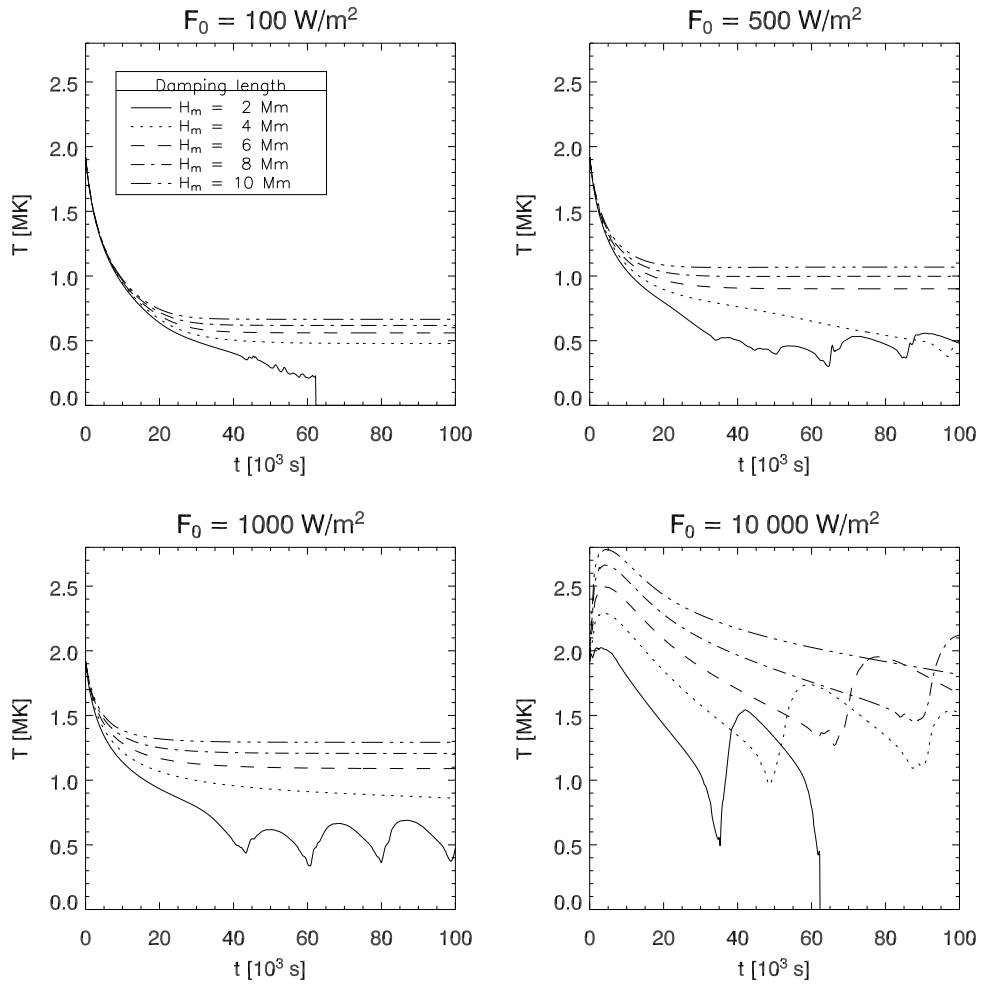


FIGURE 8.9: Mean loop temperature as a function of time for $L = 300$ Mm loop models and energy fluxes of $F_0 = 10^2, 5 \cdot 10^2, 10^3, 10^4 \text{ W/m}^2$.

8.6.2 Pressure-Temperature Diagrams

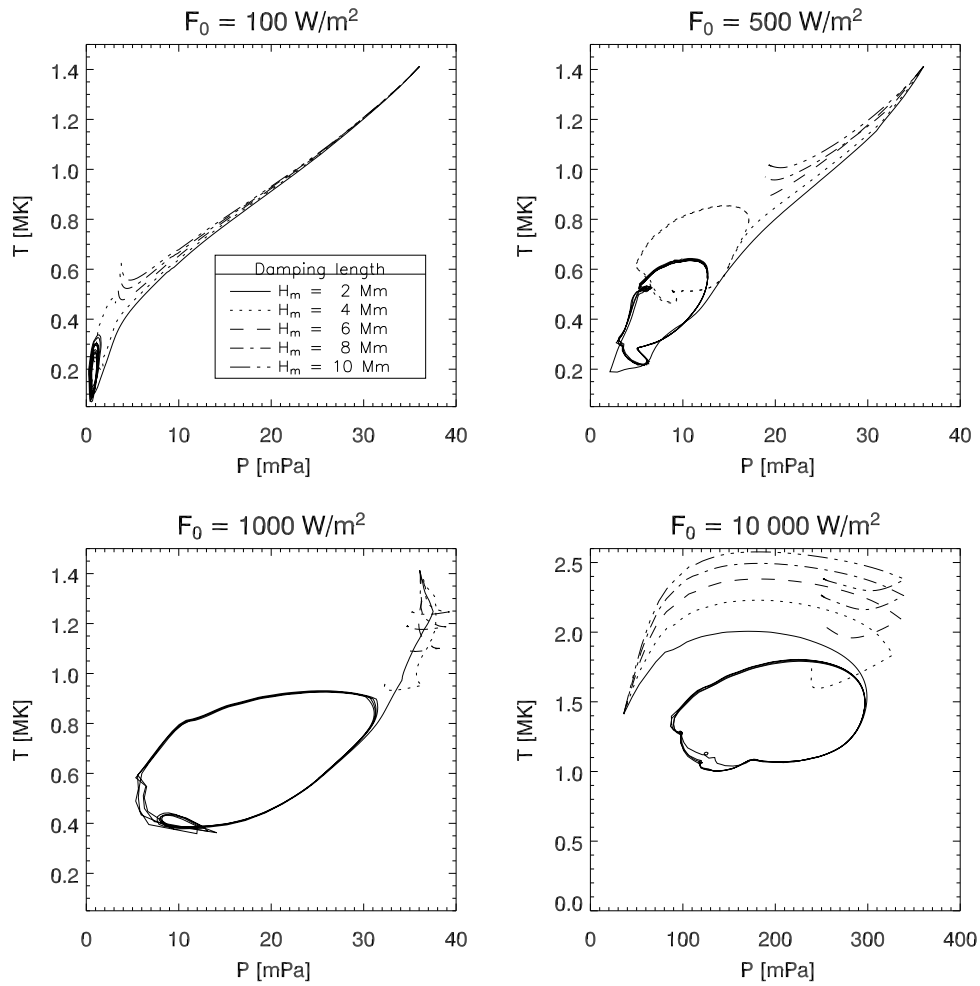


FIGURE 8.10: Mean temperature as a function of mean pressure for $L = 100$ Mm loop models and energy fluxes of $F_0 = 10^2, 5 \cdot 10^2, 10^3, 10^4 \text{ W/m}^2$.

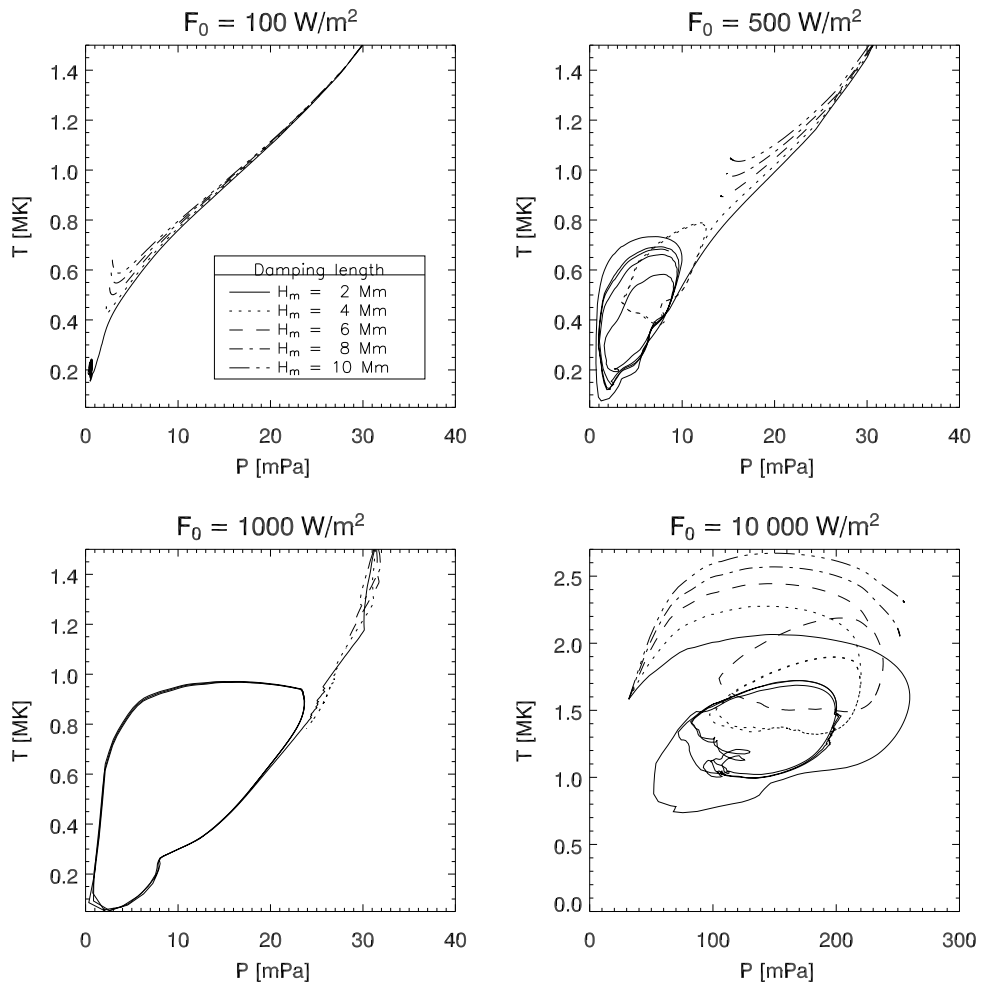


FIGURE 8.11: Mean temperature as a function of mean pressure for $L = 150$ Mm loop models and energy fluxes of $F_0 = 10^2, 5 \cdot 10^2, 10^3, 10^4 \text{ W/m}^2$.

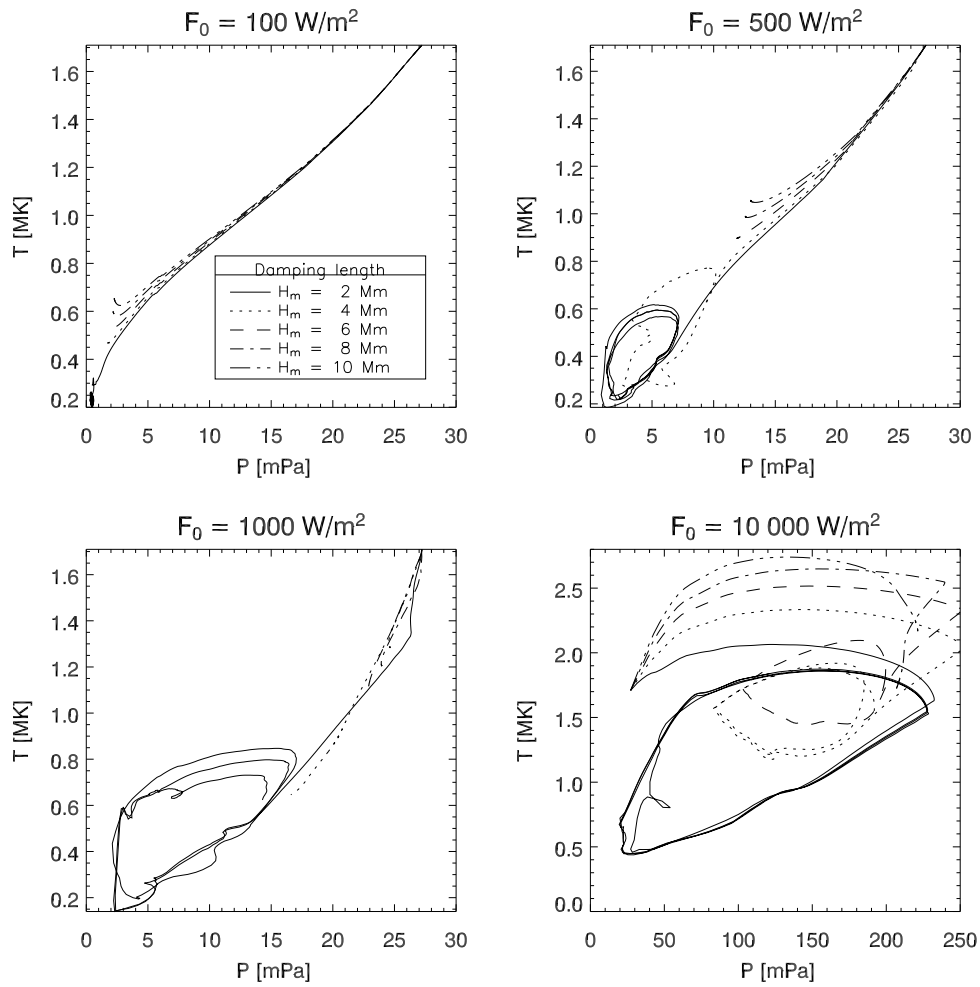


FIGURE 8.12: Mean temperature as a function of mean pressure for $L = 200$ Mm loop models and energy fluxes of $F_0 = 10^2, 5 \cdot 10^2, 10^3, 10^4 \text{ W/m}^2$.

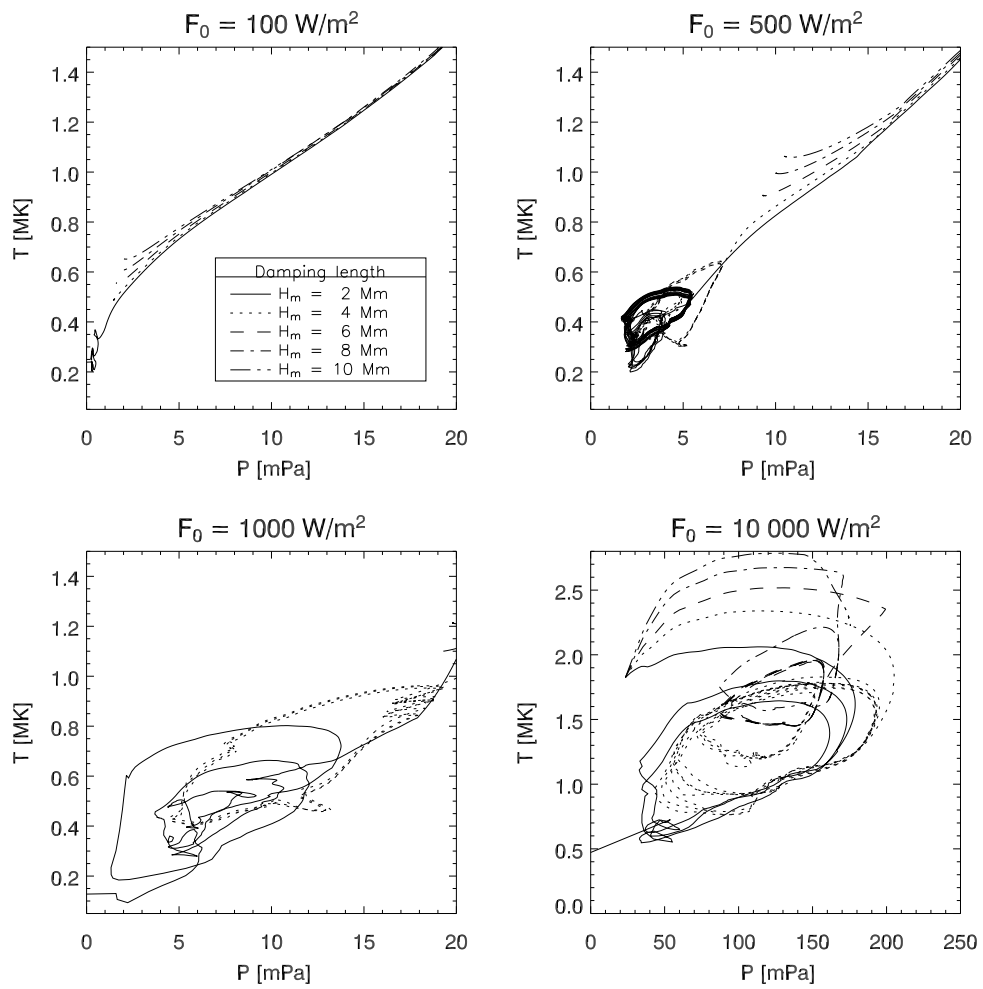


FIGURE 8.13: Mean temperature as a function of mean pressure for $L = 250$ Mm loop models and energy fluxes of $F_0 = 10^2, 5 \cdot 10^2, 10^3, 10^4 \text{ W/m}^2$.

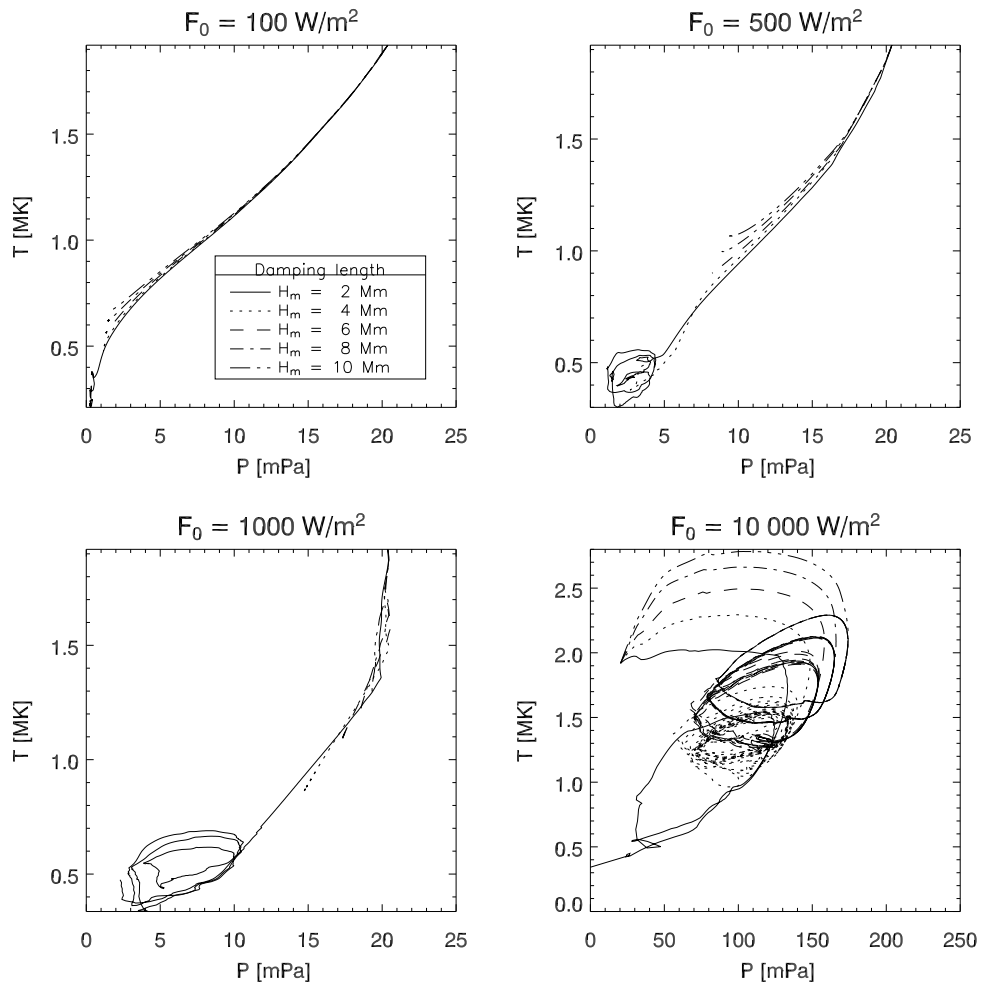


FIGURE 8.14: Mean temperature as a function of mean pressure for $L = 300$ Mm loop models and energy fluxes of $F_0 = 10^2, 5 \cdot 10^2, 10^3, 10^4 \text{ W/m}^2$.

9 Recent Multi-Wavelength Observations of Coronal Loops

The real challenge for any model lies in its confrontation with reality. Since 1996 and 1998, respectively, the two satellites SOHO and TRACE have provided us with various instruments to study the dynamics of the solar transition region and corona at unprecedented spectral and spatial resolution. Regarding studies of the dynamic evolution of coronal loops, the strength of SOHO lies in its spectrometers CDS (the Coronal Diagnostic Spectrometer) and SUMER (the Solar Ultraviolet Measurements of Emitted Radiation instrument). The TRACE observatory, on the other hand, is designed for recording images with a high spatial resolution of $1''$ with different spectral filters, sensitive to plasma at different temperatures. The best usage of the available information is made when one combines the strengths of several instruments by observing the same region on the sun in different wavelengths, recording both spectra and images.

In order to study plasma condensations, downflows and other time-variable phenomena in active region loops, especially at transition region temperatures, a joint observing program with the SOHO instruments CDS, SUMER, MDI (the Michelson Doppler Imager) and EIT (the Extreme ultraviolet Imaging Telescope) together with the TRACE instruments was carried out in May 2004. This program with the acronym JOP 174 was coordinated by T. Fredvik (CDS), O. Kjeldseth-Moe (CDS), W. Curdt (SUMER), K. Schrijver (TRACE) and T. Tarbell (TRACE). Since the data was acquired very recently, the data reduction and analysis is currently still in progress, but due to the timeliness of the goals of this study and its close connection to the models presented in this thesis, a few preliminary results of this observing campaign are presented here.

Figure 9.1 shows an active region above the limb, imaged by the TRACE instrument in two different wavelength bands. The left image was taken in the 160.0 nm pass band on 20 May 2004 at 19:10:24 UT. For observations above the solar limb, the emission in this band is dominated by the spectral lines of CIV (154.8 nm and 155.0 nm), formed at around $T \approx 0.1$ MK. The right image (taken on 20 May 2004, 19:10:53 UT) shows the same region on the sun, this time seen in the 17.1 nm pass band, which contains mainly emission from Fe IX and Fe X at $T \approx 0.65$ MK and 1 MK, respectively. In both images dark shading corresponds to high intensities and light shading to low intensities. It is seen that the CIV emission along the different strands of the loop system is much more “clumpy” than the emission seen in the Fe IX/X image. The latter shows also many more loop structures throughout the field of view, which are presumably too hot to be seen in the 160.0 nm pass band. An inspection of a time series of TRACE 160.0 nm images reveals that the structures which outline the loop system are in constant motion. Many of the bright “blobs” appear in the upper part of the loop system and then fall down along either side of the loop structures.

In order to probe the temperature of the plasma, raster scans of the CDS slit over the active region were performed. In the normal operation mode it takes 11 min to complete a raster scan of a $160'' \times 240''$ area with the $4'' \times 240''$ slit, so that loop dynamics on short time scales cannot be resolved. For this reason, Terje Fredvik developed a quick scan mode, in which an area of

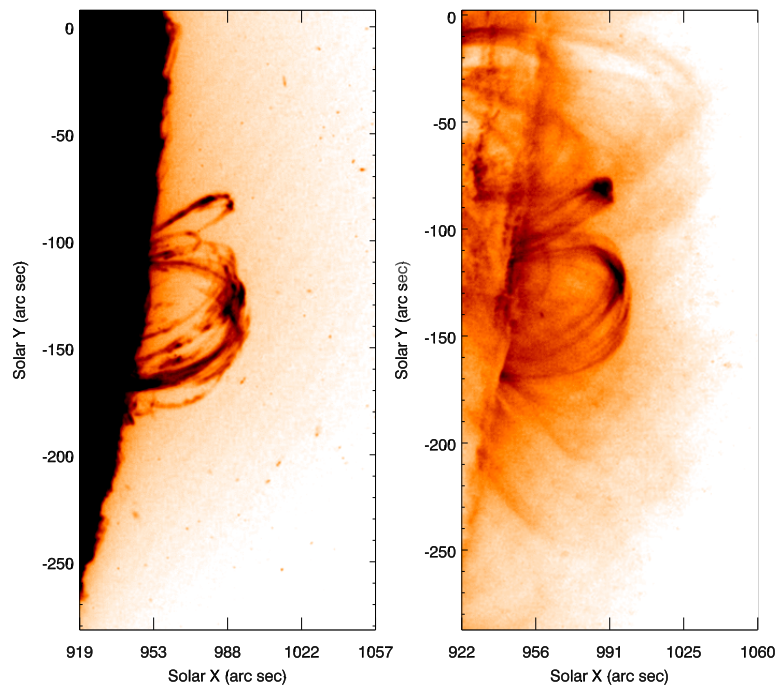


FIGURE 9.1: TRACE images of an active region above the limb. Left: 160.0 nm band, dominated by CIV (154.8 nm) and CIV (155.0 nm) at $T \approx 0.1$ MK when observing off-limb. Right: Fe IX/X (17.1 nm) band (mainly Fe IX and Fe X at $T \approx 0.65$ MK and 1 MK, resp.). Images courtesy of T. Fredvik.

$60'' \times 240''$ is scanned with the $4'' \times 240''$ slit with a step size of $8''$, i.e. twice the slit width. This reduces the time needed to accomplish one scan to approximately 2 min. The increased temporal resolution comes at the expense of lacking spatial information, so that the missing pixel rows have to be interpolated. However, as the strength of CDS lies in its spectra which sample a broad temperature range rather than in high spatial resolution, this scanning mode is preferable to study the dynamics of coronal loops, especially if the observations are accompanied by an imaging instrument such as TRACE.

Figures 9.2 and 9.3 show four snapshots of the same active region taken on 20 May 2004 at 19:11:50 UT, 19:59:21 UT, 20:57:05 UT and 21:12:53 UT. The left panels show TRACE images in the 160.0 nm passband, while the remaining three panels show CDS raster scans in the spectral lines of He I (58.4 nm, formed around 20 000 K), O V (63.0 nm, $T \approx 0.23$ MK) and Fe XVI (36.0 nm, $T \approx 2.7$ MK). Although the time evolution is much better seen in movies of the respective data sets, Figs. 9.2 and 9.3 illustrate clearly that coronal loops show very dynamic evolution on short time scales: At 19:11:50 UT the loop system is strongly emitting in the CIV passband, indicating that the loops are filled with plasma at a temperature around 10^5 K. Bright “blobs” are seen to move downwards along the loop structures, often accelerated in the early phase of their fall. The CDS rasters show localized brightenings as well, but due to the limited spatial resolution

of the CDS instrument and the undersampling of the rastering process (which causes the vertical stripes in the rasters) individual structures of the loop system can hardly be resolved. Within the next 90 min (lower panel of Fig. 9.2 and upper panel of Fig. 9.3) it is observed that the loop system vanishes almost completely and then “magically” reappears around 15 min later (lower panel of Fig. 9.3).

A movie of the TRACE images in the 160 nm pass band suggests that plasma drains in “clumps” through the loop legs, and also the time series of the CDS He I and O V rasters show features which brighten up while moving downwards. Although the line-of-sight velocities of the plasma are presumably rather small since we are looking at structures that are oriented largely perpendicular to the observing direction, future work will include a detailed analysis of the Doppler shifts of the various lines. In the CDS rasters of the Fe XVI (36.0 nm) line, which is formed at very high temperatures ($T \approx 2.7$ MK), the spatial brightness variations are much weaker, which supports the conjecture that the localized brightenings are associated with plasma at cooler temperatures. Figure 9.4 finally shows the relative intensities recorded in one single CDS detector pixel, located at $(x, y) \approx (990'', -75'')$, in four spectral lines which are formed at different temperatures. In this region, the TRACE movie shows a rather simple, isolated loop structure along which a bright blob is seen to propagate downwards. It is seen that in the beginning of the time series, the intensity in the hot Fe XVI line (36.0 nm, $T \approx 2.7$ MK) is high and then drops sharply around 19:00 UT. At the same time, the relative intensity in Mg IX (36.8 nm, $T \approx 1$ MK) rises strongly, reaches a peak at 19:10 UT and then decreases again. A similar transient rise of the intensity is found for O V (63.0 nm, $T \approx 0.23$ MK) and O III (59.9 nm, $T \approx 0.1$ MK). The intensity peak of O V is shifted by around 15 min in time with respect to the hotter Mg IX line, while the O III peak seems to be slightly shifted with respect to the O V peak. Although a more detailed analysis is needed, which is in progress but not part of this work, we note that this observation is consistent with a dense, cool plasma blob, surrounded by hotter material, which is moving past the detector pixel.

To conclude this section, we state that a first inspection of the new data from the joint observing program 174 supports the concept of plasma condensation in coronal loops, accompanied by localized brightenings and fast downflows. The ongoing analysis of these data will help to further evaluate our hydrodynamic model and to indicate areas where improvement is needed to obtain a good match between the observations and the model.

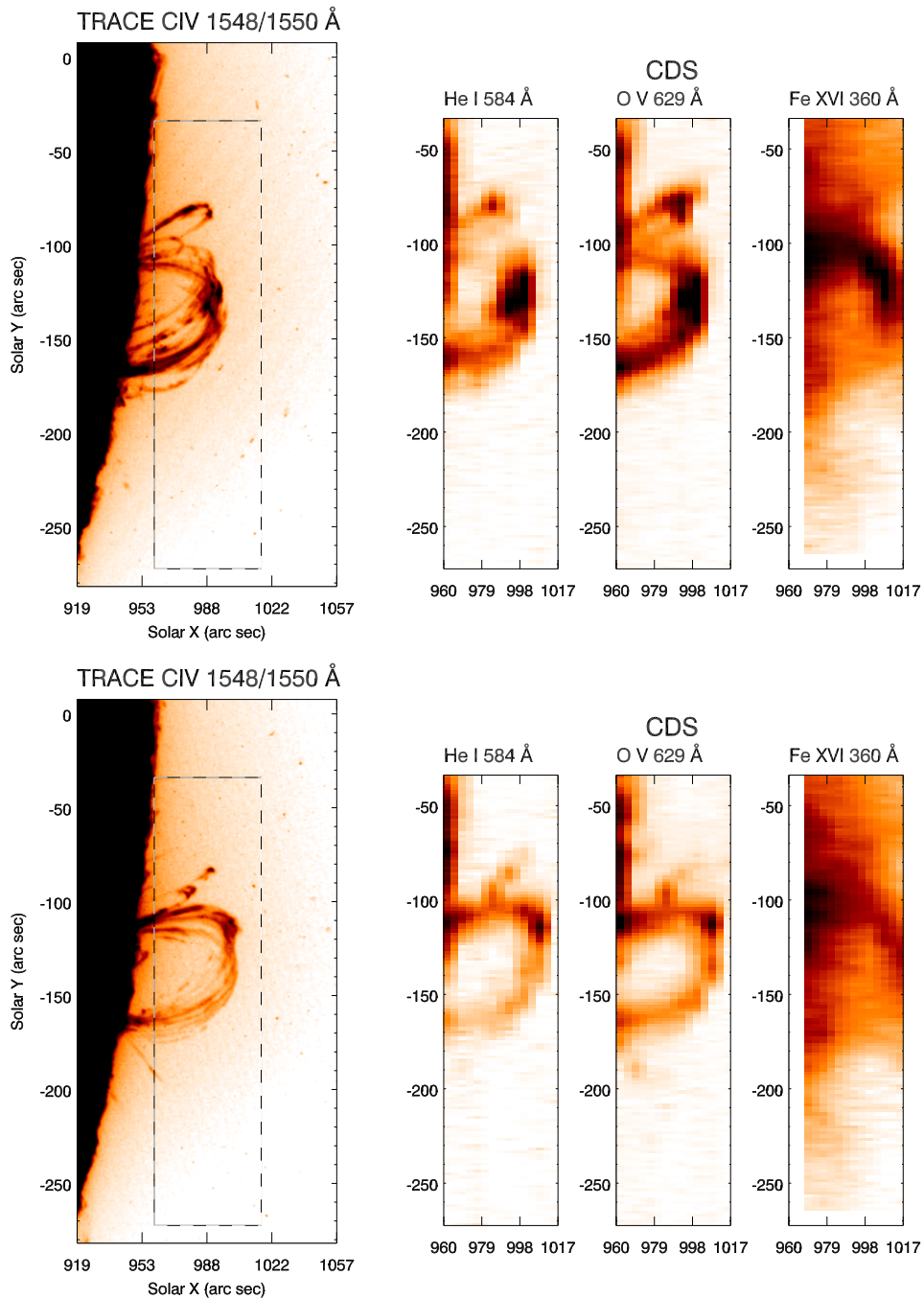


FIGURE 9.2: Nearly simultaneous images with TRACE and CDS in different wavelength bands. From left to right: TRACE 160.0 nm band (above the limb mainly C IV, $T \approx 0.1$ MK), CDS He I (58.4 nm, $T \approx 20\,000$ K), CDS O V (63.0 nm, $T \approx 0.23$ MK), Fe XVI (36.0 nm, $T \approx 2.7$ MK). The upper image was taken on 20 May 2004 at 19:11:50 UT, the lower one at 19:59:21 UT. The dashed boxes in the TRACE images indicate the location of the CDS rasters. (Courtesy of T. Fredvik.)

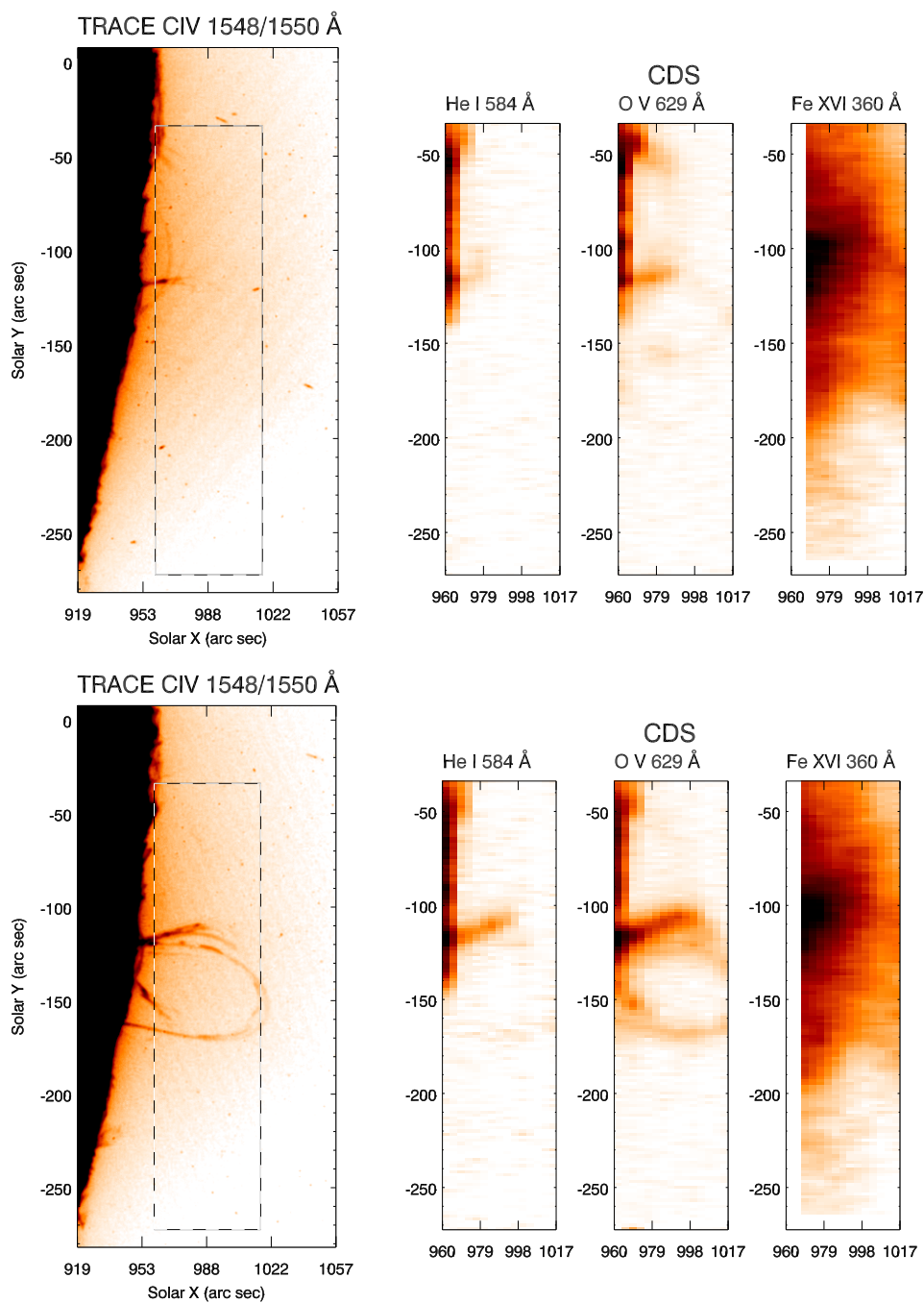


FIGURE 9.3: Nearly simultaneous images with TRACE and CDS in different wavelength bands. From left to right: TRACE 160.0 nm band (above the limb mainly CIV, $T \approx 0.1$ MK), CDS He I (58.4 nm, $T \approx 20\,000$ K), CDS O V (63.0 nm, $T \approx 0.23$ MK), Fe XVI (36.0 nm, $T \approx 2.7$ MK). The upper image was taken on 20 May 2004 at 20:57:05 UT, the lower one at 21:12:53 UT. The dashed boxes in the TRACE images indicate the location of the CDS rasters. (Courtesy of T. Fredvik.)

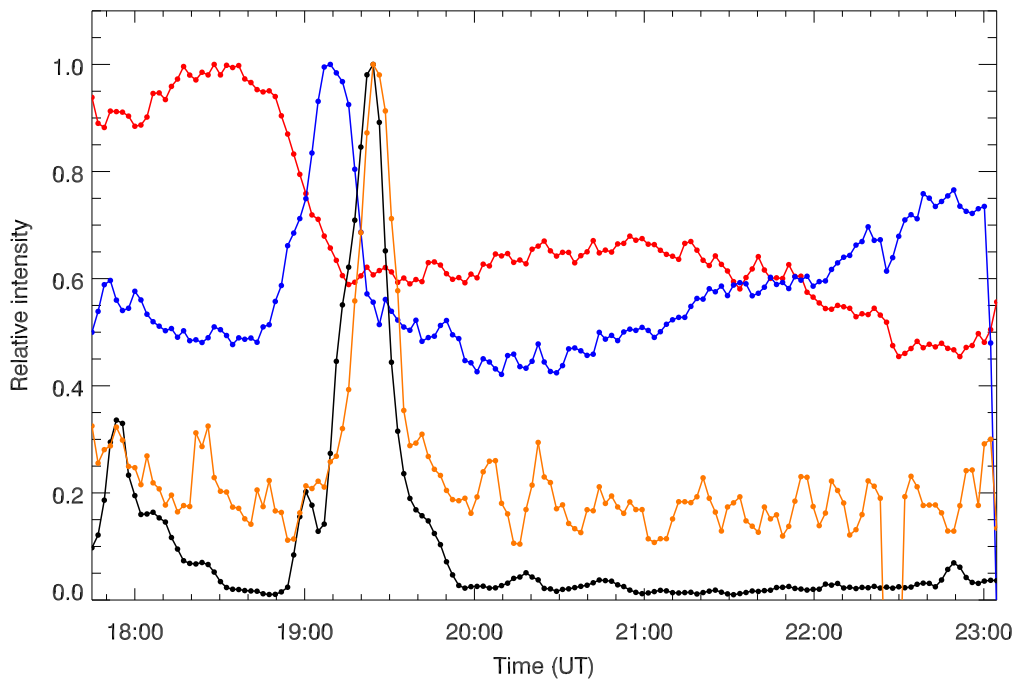


FIGURE 9.4: Relative intensity as a function of time for four emission lines formed at different temperatures, recorded in one single detector pixel located at $(x, y) \approx (990'', -75'')$. The cadence is approximately 2 minutes. *Red*: Fe XVI (36.0 nm, $T \approx 2.7$ MK), *blue*: Mg IX (36.8 nm, $T \approx 1$ MK), *black*: O V (63.0 nm, $T \approx 0.23$ MK), *orange*: O III (59.9 nm, $T \approx 0.1$ MK). (Courtesy of T. Fredvik.)

10 Discussion & Outlook

The work presented in this thesis shows that solar coronal loops can evolve very dynamically even under the assumption of a temporally constant heating if the heating is concentrated close to the footpoints of the loops. In this case, the non-linearity of the energy equation results in a loss of equilibrium which triggers a highly dynamic loop evolution. This dynamic evolution can be understood on the basis of an evaporation-condensation cycle: Plasma is first evaporated by coronal heating from the cool and dense chromosphere into the corona, then condenses in the coronal part of the loop as a result of thermal instability, drains towards the footpoints of the loop and finally evaporates again. In that respect, the term “coronal rain” which has been coined to describe the phenomenon of plasma blobs which appear at high altitudes of the corona and then fall towards the solar surface seems very appropriate as the processes of evaporation and condensation resemble indeed the familiar rain on earth.

The damping length of the energy dissipation in the coronal loop acts as a control parameter of this non-linear system. For large damping lengths, corresponding to heating which is more evenly distributed over the loop, static solutions are obtained, while for shorter damping lengths periodic solutions are found. For very short damping lengths, the evolution of the loop becomes very complex and irregular.

The dynamic loop scenario is interesting in several aspects: Firstly, it can account for transient brightenings in transition region lines, originating from small loops which are barely resolved with the current generation of space instruments. In that respect, simultaneous observations of several spectral lines which are formed at different temperatures, e.g. C IV (154.8 nm), O V (63.0 nm), and O VI (103.2 nm) would be advantageous in order to verify if this phenomenon is as common as it seems. The fact that the dynamic loop models can show strong emission in lines formed at temperatures below 10^5 K and at the same time relatively weak emission in lines formed at higher temperatures seems promising with respect to the outstanding “emission measure problem”, i.e. the fact that current models cannot account for the increased emission of the solar atmosphere at cooler temperatures. Secondly, the model calculations shown here can explain recent observations of catastrophic cooling and high-speed downflows in coronal loops as a result of a coronal heating mechanism which is concentrated at low heights. It is found that no external time-dependent driving mechanism is necessary to explain the observed rapid cooling and evacuation of loops. As the model solves the non-equilibrium rate equations consistently with the dynamic equations, the time-dependent emission of optically-thin spectral lines can be synthesized and directly compared to observations. A good match to the observed properties of catastrophic cooling of coronal loops is found. These results strengthen the hypothesis that coronal heating is concentrated towards the footpoints of loops. Such knowledge is very useful to limit the number of possible coronal heating mechanisms.

Future efforts in coronal loop modeling should also focus on models for high-temperature loops which will be observed with the next generation of EUV and X-ray instruments which are part of the *Solar-B* mission and the *Solar Dynamics Observatory* (SDO). These two space missions

are scheduled for launch in 2005 and 2008, respectively. Using the most accurate atomic data available, the time-dependent emission in many different spectral lines should be calculated for different models, followed by the calculation of the resulting transmission through different filters. This will be particularly useful for the interpretation of results from imaging instruments with multiple filters (such as the *Atmospheric Imaging Assembly* for SDO) and will help to reduce the ambiguities that one encounters when dealing with filter-ratio techniques.

One of the major challenges in solar physics is the identification of the physical processes which heat the solar corona. This problem has to be approached from different angles: On the one hand, detailed numerical magneto-hydrodynamical simulations, preferably in three spatial dimensions, are needed to investigate the structure of the solar corona and its coupling to the underlying atmospheric layers. On the other hand, observable quantities have to be calculated from the magneto-hydrodynamic models in order to compare the results of these models with observations. In a very recent work Peter et al. (2005) calculated for the first time emission-line spectra from the three-dimensional numerical model of Gudiksen & Nordlund (2002) under the assumption of ionization equilibrium and found strong evidence for magnetic flux braiding mechanism to be the dominant heating process of the magnetically-closed corona of the sun. Such a forward-modeling approach is of great use to compare theoretical results with observations and can also be applied to models of the coronae of other stars. In many cases, however, the solar plasma is not in ionization equilibrium, and the resulting effects should ultimately be included in a comprehensive model. However, the computational expense of additionally solving the ionization rate equations in a three-dimensional model of even a small part of the solar corona is currently too high to be feasible. Thus, innovative approaches are needed to evaluate whether non-equilibrium effects can be reasonably accounted for in a simplified way. For the time being, the effects of non-equilibrium ionization can therefore only be studied with models of one spatial dimension. Another advantage of one-dimensional models is the fact that many more realizations can be carried out in a given time which makes it possible to explore the parameter space of possible solutions.

As far as an extended comparison of the predictions of this work with observations is concerned, the analysis of the data acquired in the framework of the *Joint Observing Program 174*, combined with ongoing modeling efforts, will provide further insight into the dynamics of solar coronal loops.

Appendix

A Appendix

A.1 Effect of Atomic Composition on Instabilities in Shock Waves

It is important to note that the onset of instabilities in plasmas depends also on the details of atomic physics. In this section two examples are given which do not correspond very closely to the problem modeled in this thesis but seem nevertheless worthwhile to note in a broader context.

[Grun et al. \(1991\)](#) showed in a laboratory experiment that, depending on the ambient gas, the shock fronts of Taylor-Sedov-type blast waves can be either stable or unstable. In their experiment, a high-power laser pulse was released on a polystyrene foil, which created a blast wave produced by the expansion of ablation plasma from the foil's surface. When this experiment was carried out in a nitrogen-filled chamber, the shock front of the blast wave remained stable, while an instability set if the chamber was filled with xenon gas. The authors explained this result by the different adiabatic indices of the two gases: They argued that the lower adiabatic index of xenon ($\gamma_{Xe} = 1.06 \pm 0.02$) makes the gas radiate more strongly than the neon gas ($\gamma_N = 1.3 \pm 0.1$). In a later work [Laming & Grun \(2002\)](#) and [Laming & Grun \(2003\)](#) carried out detailed atomic physics calculations which could not only explain the previous results of [Grun et al. \(1991\)](#) but also explained why this instability was not found in other experiments, e.g. by [Edwards et al. \(2001\)](#). [Laming & Grun \(2002\)](#) argued that the fundamental reason for the stability of blast waves in a neon gas was not the fact that it is "inherently less radiative" than xenon, but that its radiation is more suppressed by the electron density than in the case of xenon (the higher density reduces the radiative cooling rate by electron collisional depopulation of excited levels).

[Smith & Rosen \(2003\)](#) investigated the formation of shocks in interstellar molecular clouds and found that fast shocks can be unstable because the production of CO and H₂O molecules in the cooling layer alters the cooling function significantly. They found a strong dependence of the atomic composition of the cloud on the cloud's stability (an instability only sets in at sufficiently high C and O abundances) and showed furthermore that cooling layers of hydrodynamic molecular shocks can exhibit cyclic or even chaotic collapse and reformation.

A.2 Further Data From the Parameter Study

A.2.1 Time Evolution of Mean Electron Density

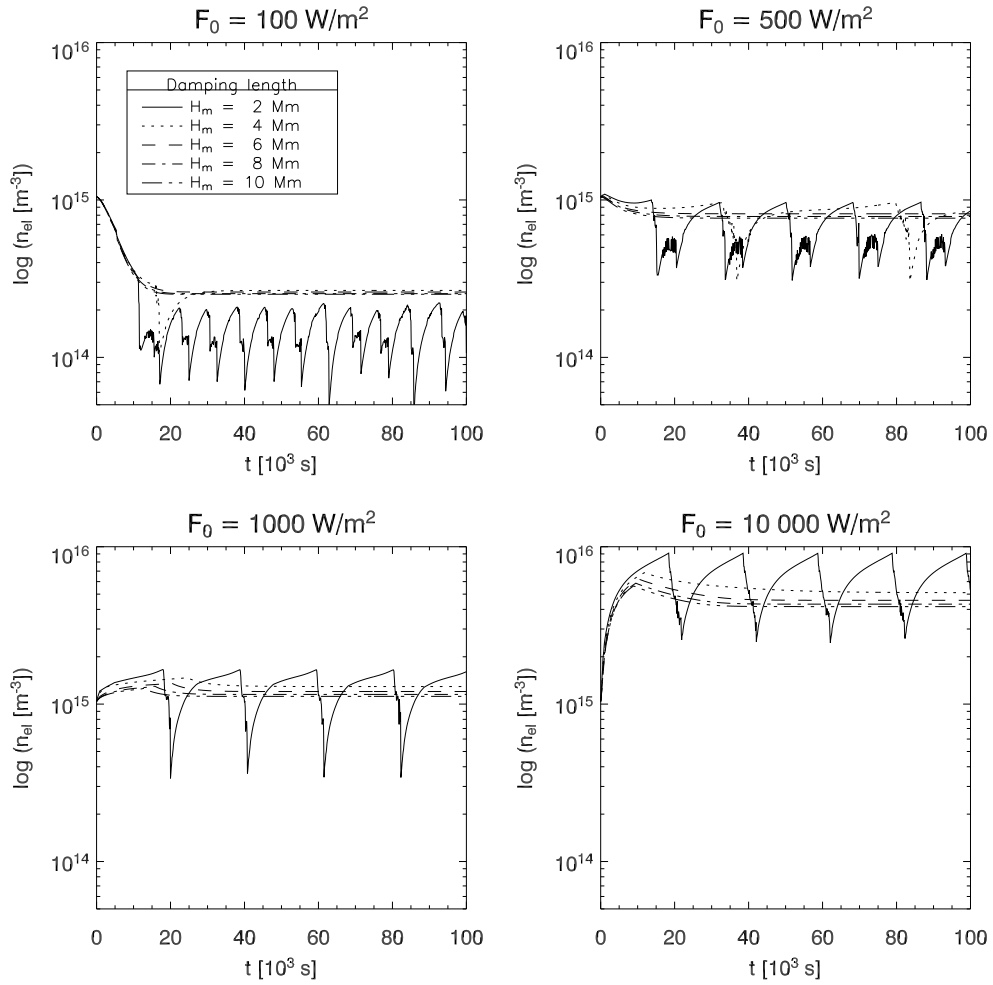


FIGURE A.1: Mean electron density as a function of time for $L = 100$ Mm loop models and energy fluxes of $F_0 = 10^2, 5 \cdot 10^2, 10^3, 10^4 \text{ W/m}^2$.

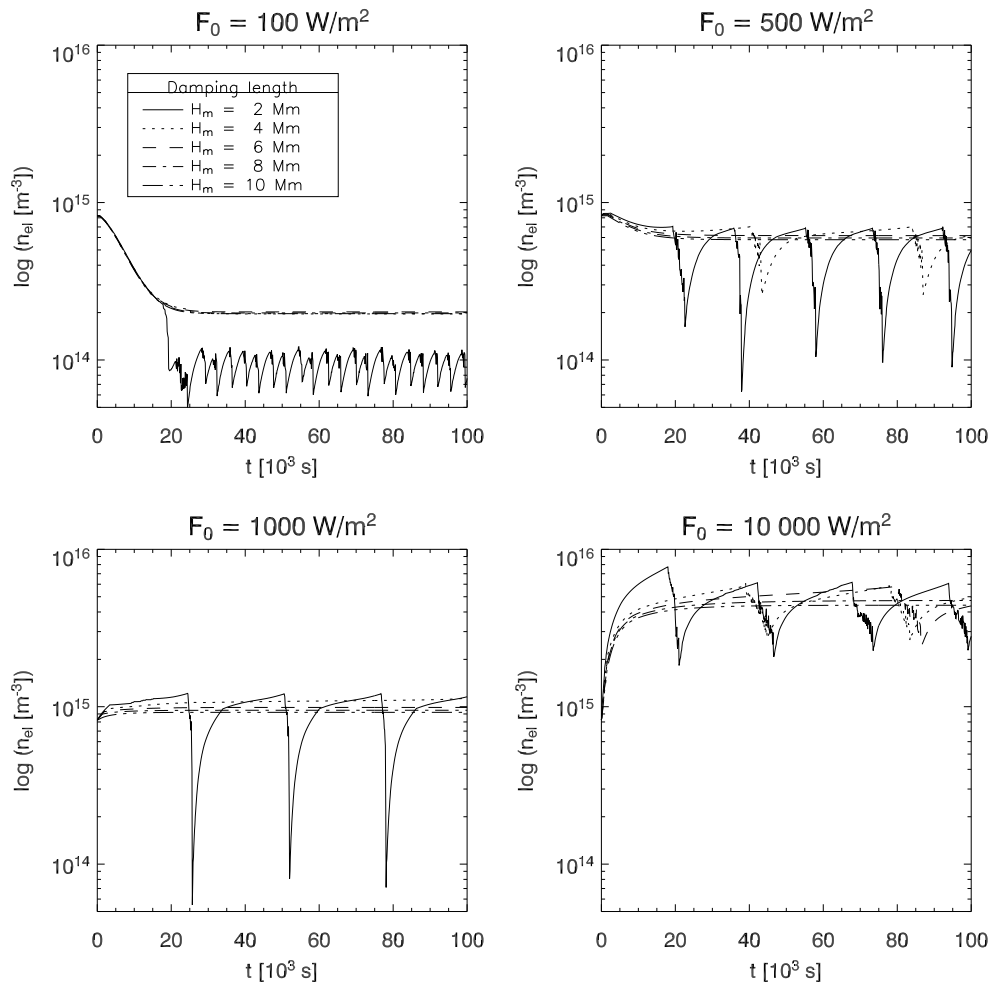


FIGURE A.2: Mean electron density as a function of time for $L = 150$ Mm loop models and energy fluxes of $F_0 = 10^2, 5 \cdot 10^2, 10^3, 10^4 \text{ W/m}^2$.

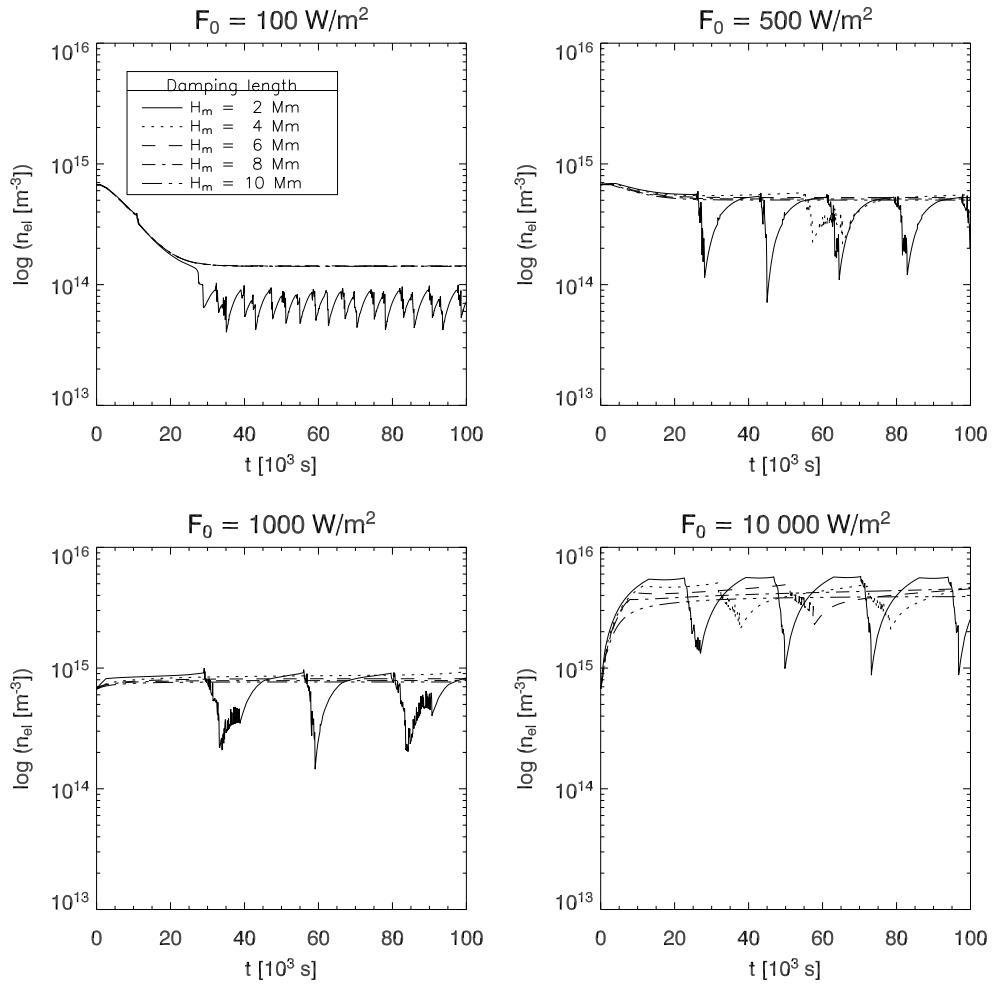


FIGURE A.3: Mean electron density as a function of time for $L = 200$ Mm loop models and energy fluxes of $F_0 = 10^2, 5 \cdot 10^2, 10^3, 10^4 \text{ W/m}^2$.

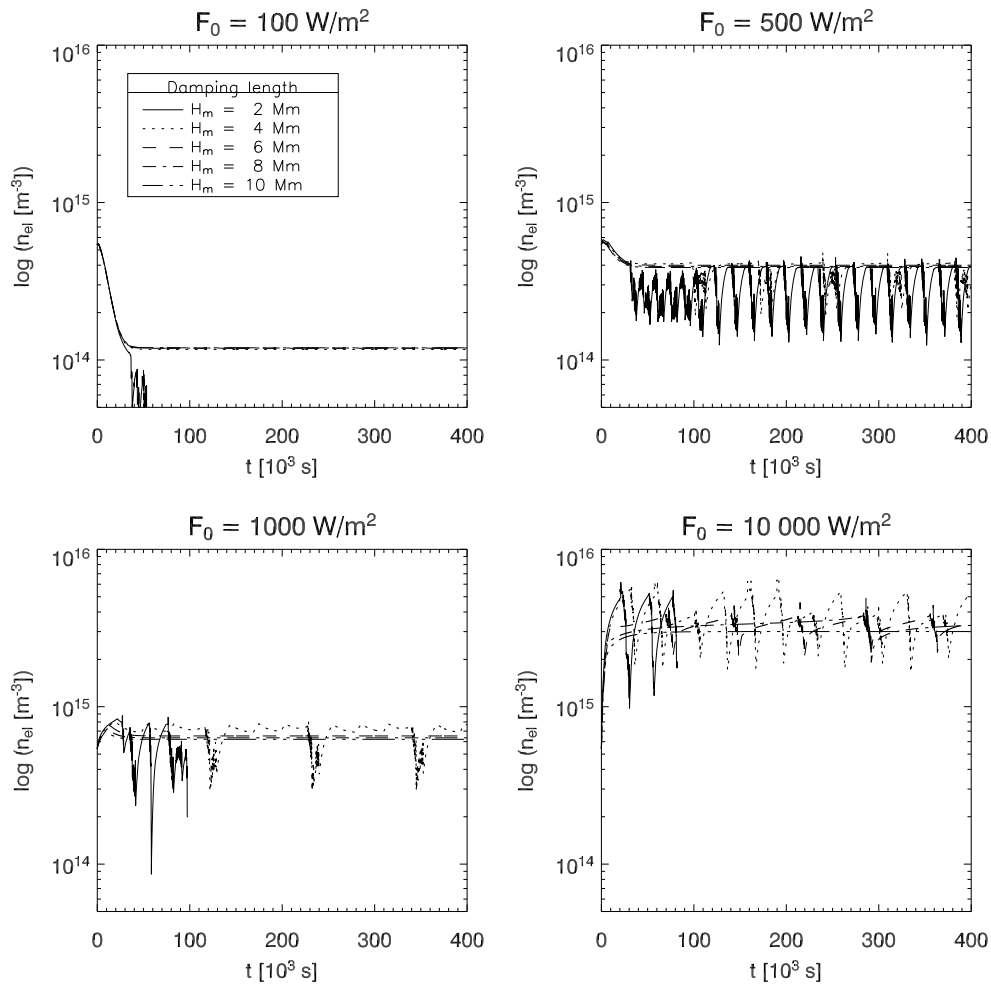


FIGURE A.4: Mean electron density as a function of time for $L = 250$ Mm loop models and energy fluxes of $F_0 = 10^2, 5 \cdot 10^2, 10^3, 10^4 \text{ W/m}^2$. Note that all simulations of this set were run for $t = 4 \cdot 10^5$ s.

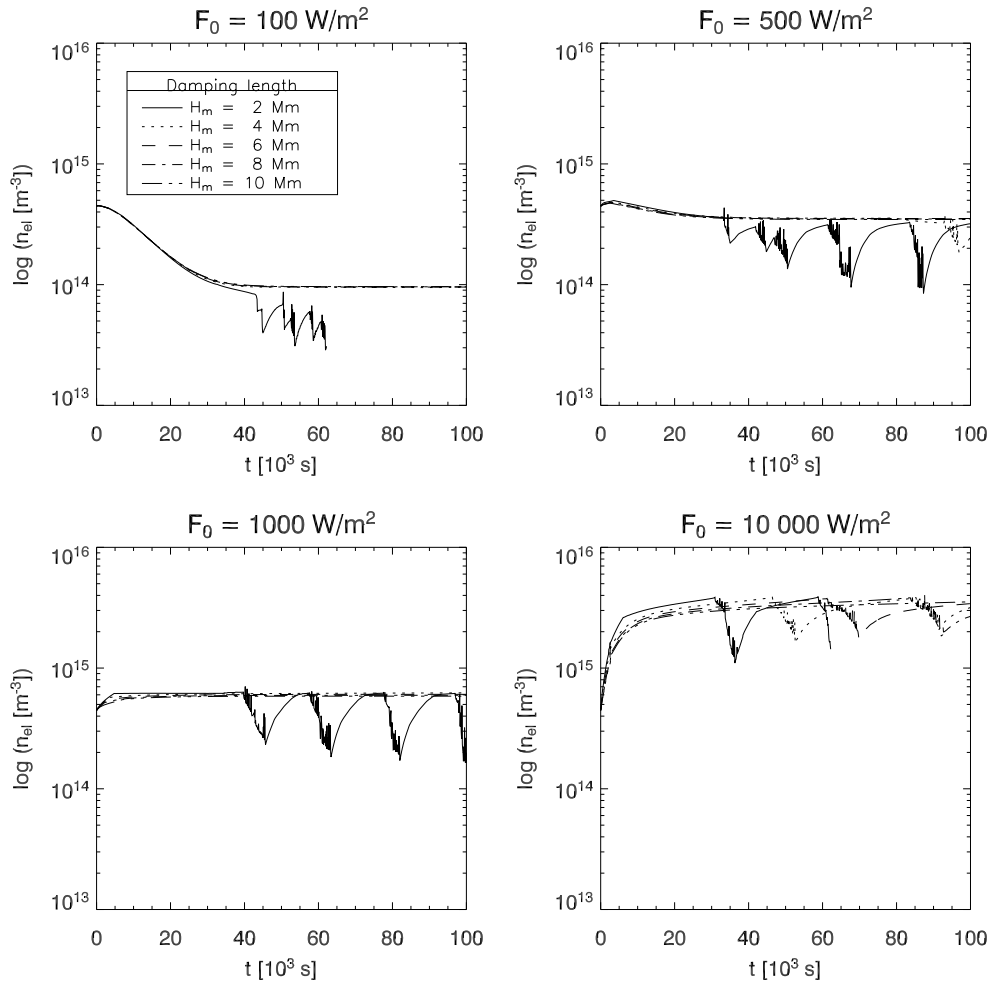


FIGURE A.5: Mean electron density as a function of time for $L = 300 \text{ Mm}$ loop models and energy fluxes of $F_0 = 10^2, 5 \cdot 10^2, 10^3, 10^4 \text{ W/m}^2$.

A.2.2 Time Evolution of Mean Pressure

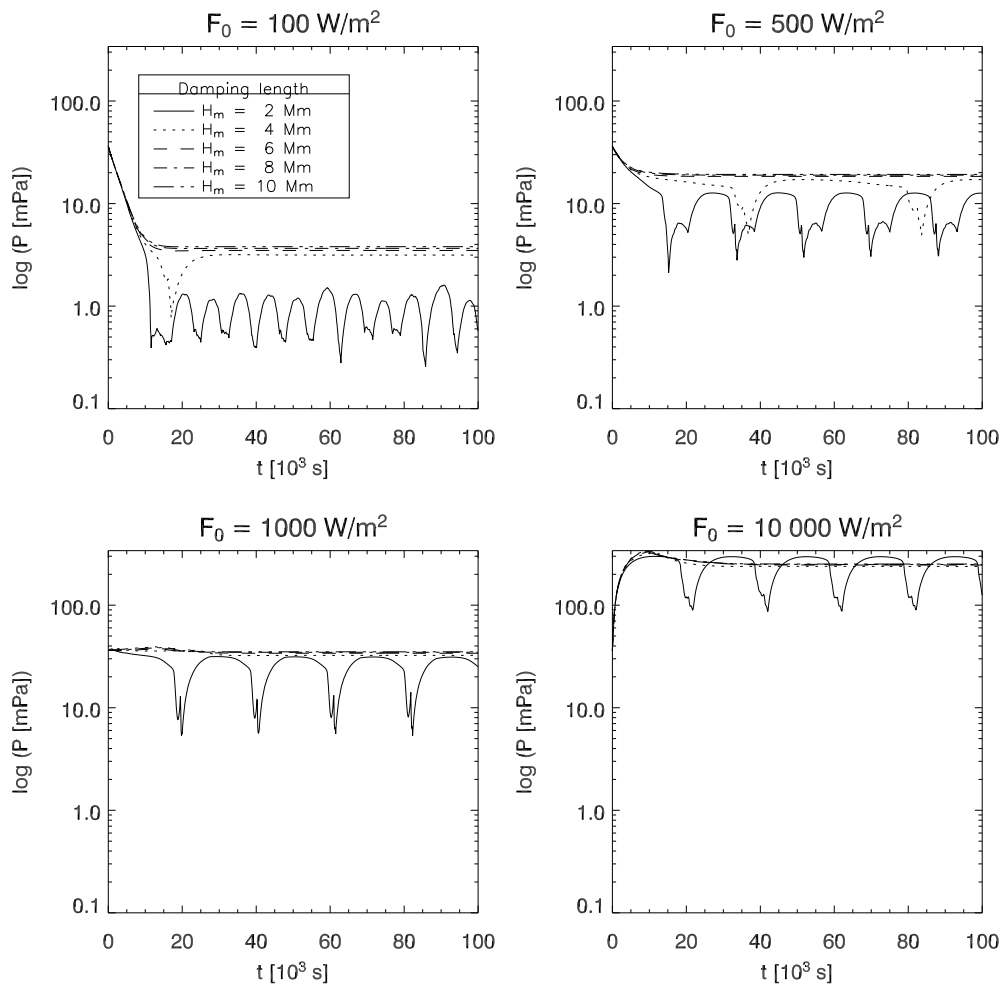


FIGURE A.6: Mean pressure as a function of time for $L = 100 \text{ Mm}$ loop models and energy fluxes of $F_0 = 10^2, 5 \cdot 10^2, 10^3, 10^4 \text{ W/m}^2$.

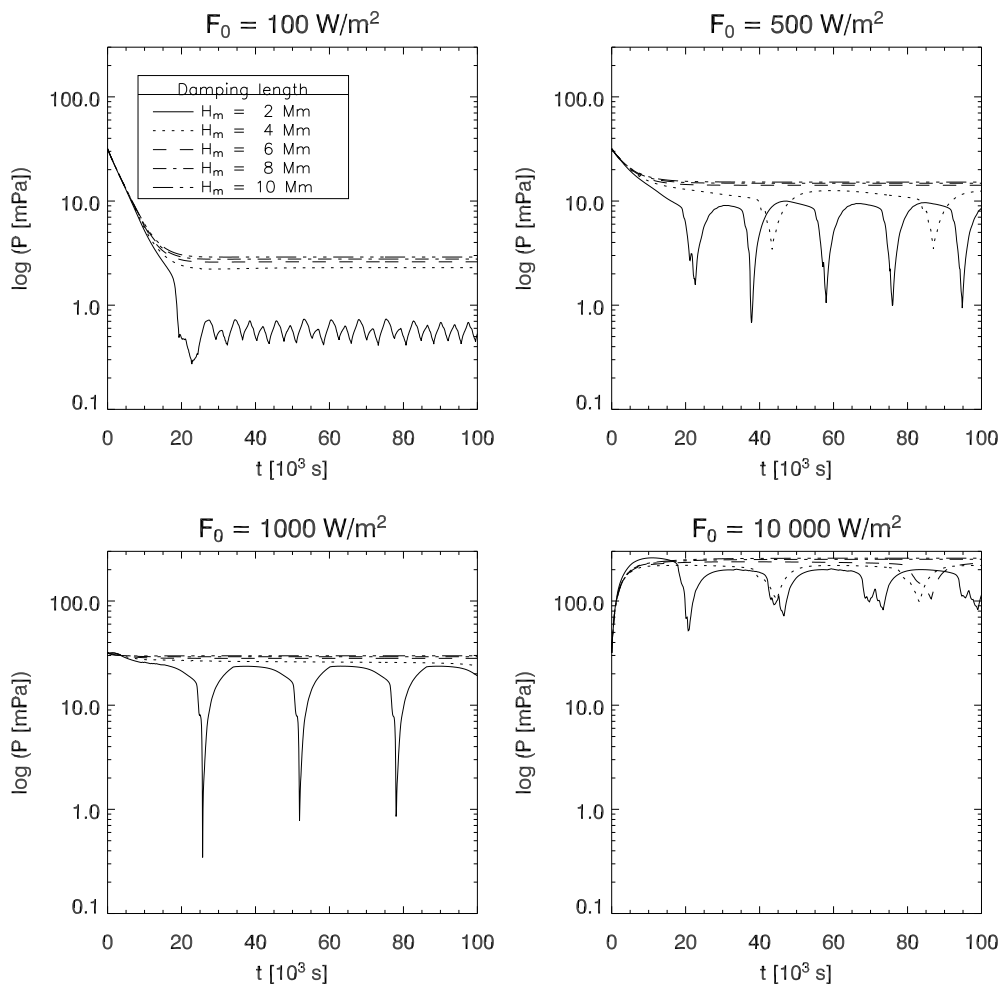


FIGURE A.7: Mean pressure as a function of time for $L = 150$ Mm loop models and energy fluxes of $F_0 = 10^2, 5 \cdot 10^2, 10^3, 10^4 \text{ W/m}^2$.

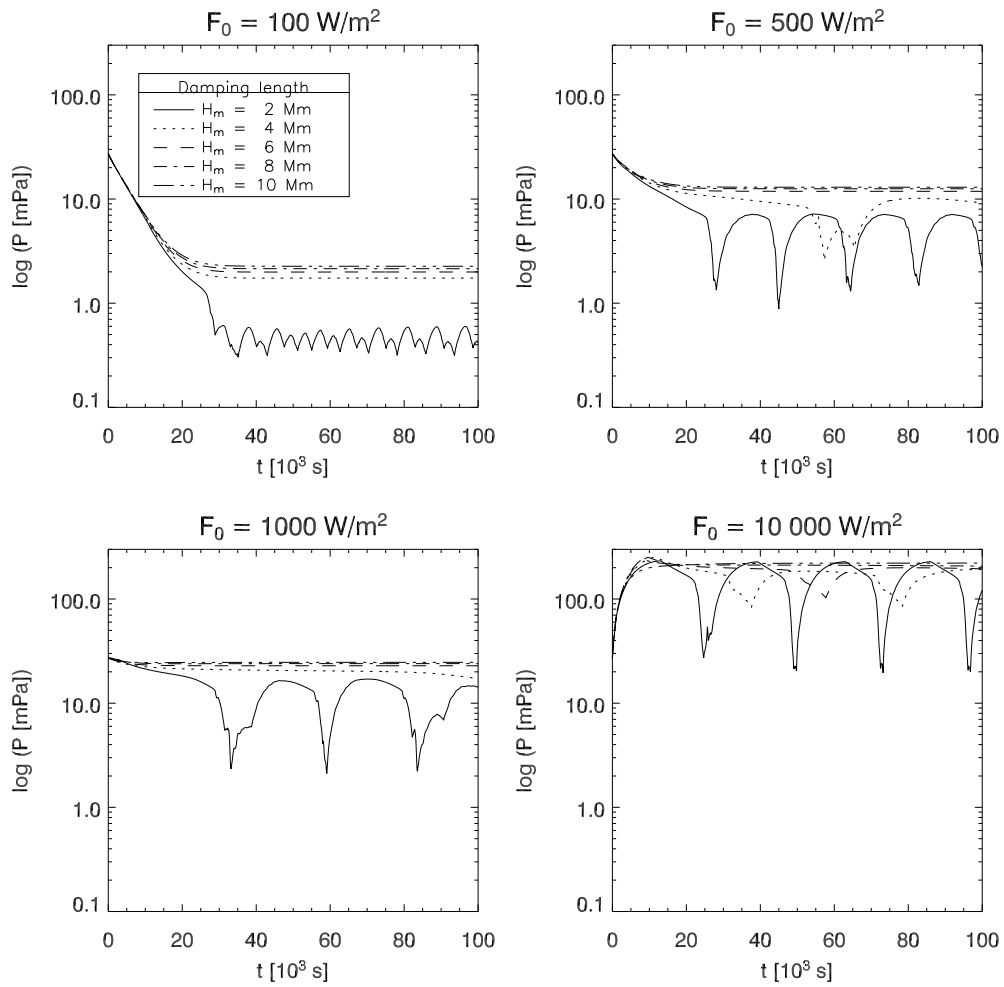


FIGURE A.8: Mean pressure as a function of time for $L = 200 \text{ Mm}$ loop models and energy fluxes of $F_0 = 10^2, 5 \cdot 10^2, 10^3, 10^4 \text{ W/m}^2$.

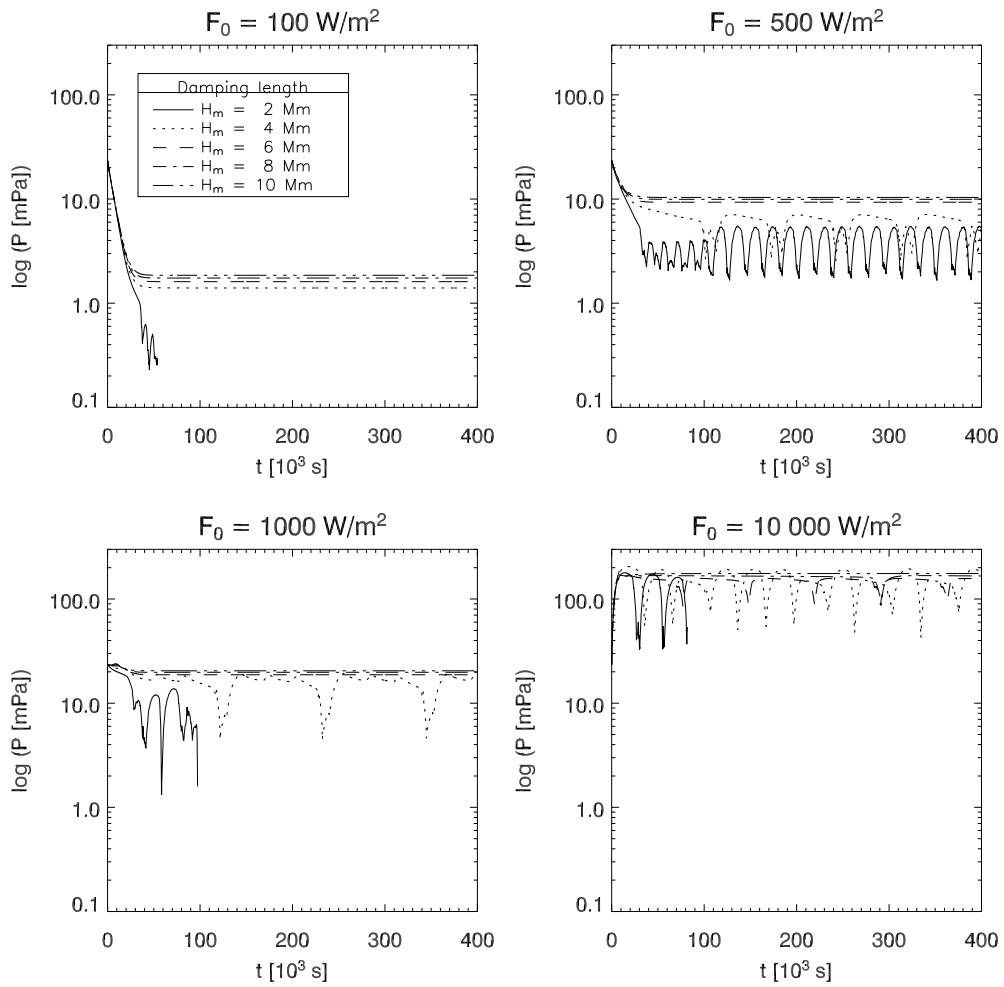


FIGURE A.9: Mean pressure as a function of time for $L = 250$ Mm loop models and energy fluxes of $F_0 = 10^2, 5 \cdot 10^2, 10^3, 10^4 \text{ W/m}^2$. Note that all simulations of this set were run for $t = 4 \cdot 10^5 \text{ s}$.

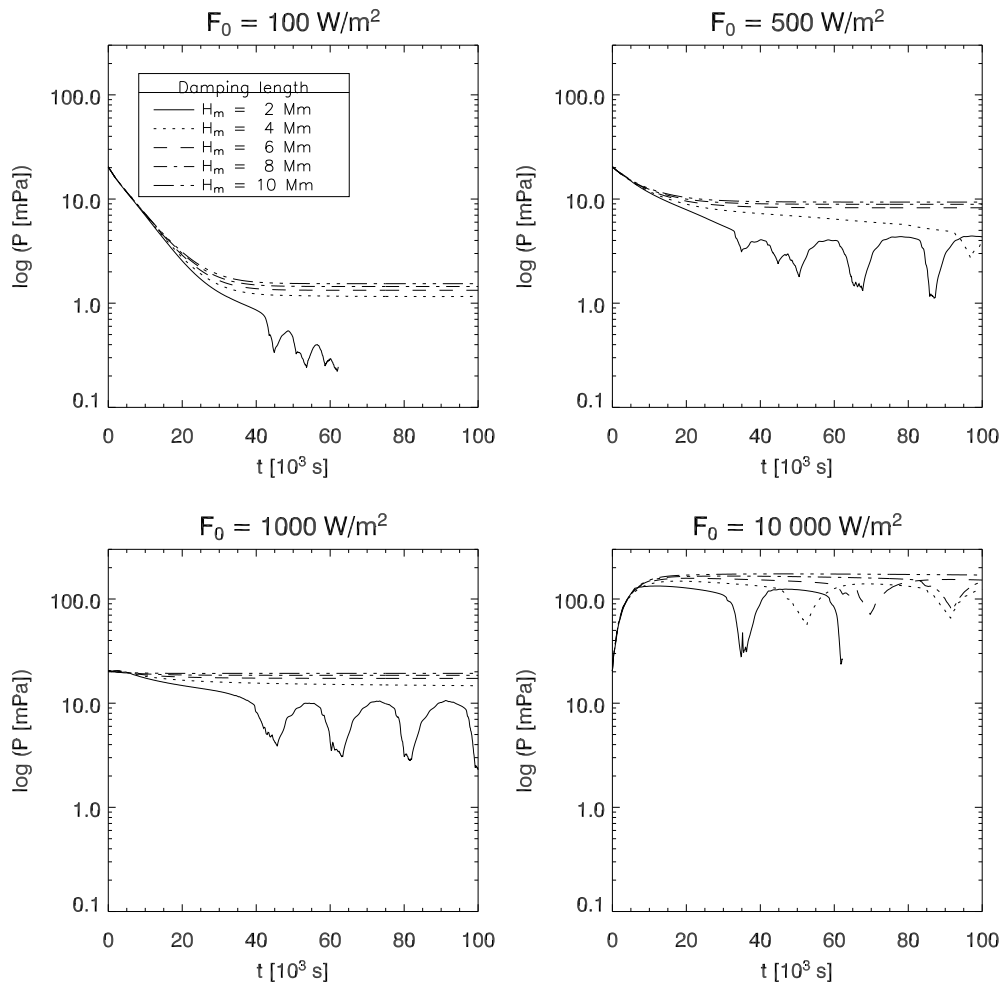


FIGURE A.10: Mean pressure as a function of time for $L = 300 \text{ Mm}$ loop models and energy fluxes of $F_0 = 10^2, 5 \cdot 10^2, 10^3, 10^4 \text{ W/m}^2$.

A.3 List of Physical Constants

Symbol	Name	Value
a_0	Bohr radius	$5.2918 \cdot 10^{-11} \text{ m}$
c	speed of light	$2.9979 \cdot 10^8 \text{ m s}^{-1}$
G	gravitational constant	$6.6742 \cdot 10^{-11} \text{ m}^3 \text{ kg}^{-1} \text{ s}^{-2}$
g_{\odot}	solar surface gravity	274 m s^{-2}
h	Planck's constant	$6.626 \cdot 10^{-34} \text{ Js}$
k	Boltzmann's constant	$1.3807 \cdot 10^{-23} \text{ J K}^{-1}$
m_e	electron mass	$9.1094 \cdot 10^{-31} \text{ kg}$
m_{\odot}	solar mass	$1.9889 \cdot 10^{30} \text{ kg}$
R_A	astronomical unit	$1.4960 \cdot 10^{11} \text{ m}$
r_{\odot}	solar radius	$6.960 \cdot 10^8 \text{ m}$
κ_0	Spitzer's thermal conduction coefficient	$1.1 \cdot 10^{-11} \text{ W m}^{-1} \text{ s}^{-1} \text{ K}^{-7/2}$
μ_0	magnetic permeability of the vacuum	$4\pi \cdot 10^{-7} \text{ V s A}^{-1} \text{ m}^{-1}$

Bibliography

- Aldrovandi, S. M. V. & Pequignot, D. 1973, *A&A*, 25, 137 [3.2.4](#)
- Alfvén, H. 1942, *Arkiv. f. Mat. Astron. Fysik*, 29 B, 1 [1.1.2](#)
- Allen, C. W. 1973, *Astrophysical quantities* (University of London, Athlone Press, London) [3.2.4](#)
- Antiochos, S. K. & Klimchuk, J. A. 1991, *ApJ*, 378, 372 [4.3.3](#)
- Antiochos, S. K., MacNeice, P. J., & Spicer, D. S. 2000, *ApJ*, 536, 494 [4.1](#)
- Antiochos, S. K., MacNeice, P. J., Spicer, D. S., & Klimchuk, J. A. 1999, *ApJ*, 512, 985 [4.1](#), [5.2](#)
- Antiochos, S. K. & Noci, G. 1986, *ApJ*, 301, 440 [4.1](#)
- Aris, R. B. 1962, *Vectors, Tensors and the Basic Equations of Fluid Mechanics* (Prentice Hall, Englewood Cliffs, New Jersey) [2.7](#)
- Arnaud, M. & Rothenflug, R. 1985, *A&AS*, 60, 425 [3.2.4](#)
- Aschwanden, M. J., Nightingale, R. W., & Alexander, D. 2000, *ApJ*, 541, 1059 [4.1](#), [4.2](#), [5.1.1](#)
- Aschwanden, M. J., Schrijver, C. J., & Alexander, D. 2001, *ApJ*, 550, 1036 [1.3](#), [4.1](#), [4.2](#), [5.1.1](#), [8.3](#), [8.5](#)
- Athay, R. G. & Holzer, T. E. 1982, *ApJ*, 255, 743 [5.3.5](#)
- Beyer, H. F. & Shevelko, V. P. 2003, *Introduction to the Physics of Highly Charged Ions* (Institute of Physics Publishing, Bristol) [3](#)
- Biermann, B. 1941, *Vierteljahresschrift Astron. Ges.*, 76, 194 [1.1.2](#)
- Biermann, L. 1951, *Z. Astrophys.*, 29, 274 [1.1.6](#)
- Cally, P. S. 1990, *ApJ*, 355, 693 [4.1](#)
- Cally, P. S. & Robb, T. D. 1991, *ApJ*, 372, 329 [4.1](#)
- Carlsson, M. 2003, private communication [2.1](#)
- Carlsson, M. & Stein, R. F. 1995, *ApJ*, 440, L29 [1.1.3](#)
- Chandrasekhar, S. 1961, *Hydrodynamic and Hydromagnetic Stability* (International Series of Monographs on Physics, Clarendon, Oxford) [4.3.6](#)

- Courant, R., Friedrichs, K. O., & Lewy, H. 1928, *Math. Ann.*, 100, 32 [2.2](#)
- Craig, I. J. D. 1990, *A&A*, 234, L12 [7](#)
- Craig, I. J. D. & Schulkes, R. M. S. M. 1985, *ApJ*, 296, 710 [7](#), [1](#)
- De Groof, A., Berghmans, D., van Driel-Gesztelyi, L., & Poedts, S. 2004, *A&A*, 415, 1141 [1.2.2](#),
[1.3](#), [5](#), [5.1](#), [5.3.1](#), [5.3.5](#), [5.4](#), [5.4](#), [6.1](#), [6.2.1](#), [6.3](#), [6.3](#), [6.5](#)
- Dere, K. P., Bartoe, J.-D. F., & Brueckner, G. E. 1989, *Sol. Phys.*, 123, 41 [1.2.2](#)
- Dorfi, E. A. & Drury, L. O. 1987, *J. Comp. Phys.*, 69, 175 [2.8](#)
- Dowdy, J. F., Rabin, D., & Moore, R. L. 1986, *Sol. Phys.*, 105, 35 [1.1.4](#), [4.1](#)
- Edlén, B. 1942, *Z. Astrophys.*, 22, 30 [1.1.5](#)
- Edwards, M. J., MacKinnon, A. J., Zweiback, J., et al. 2001, *Phys. Rev. Lett.*, 87, 085004 [A.1](#)
- Fabricius, J. 1611, *De Maculis in Sole Observatis (Wittenbergae)* [1.1.2](#)
- Feldman, U., Dammasch, I. E., & Wilhelm, K. 2000, *Space Sci. Rev.*, 93, 411 [4.1](#)
- Feldman, U., Dammasch, I. E., & Wilhelm, K. 2001, *ApJ*, 558, 423 [4.1](#)
- Fredvik, T. 2002, private communication [4.4](#)
- Gabriel, A. H. 1976, *Royal Society of London Philosophical Transactions Series A*, 281, 339
[1.1.4](#)
- Galsgaard, K. & Nordlund, Å. 1996, *J. Geophys. Res.*, 101, 13445 [5.4](#)
- Gomez, D., Sicardi Schifino, A., & Ferro Fontan, C. 1990a, *ApJ*, 352, 318 [7](#)
- Gomez, D., Sicardi Schifino, A., & Ferro Fontan, C. 1990b, *ApJ*, 352, 326 [7](#)
- Grotian, W. 1939, *Naturwissenschaften*, 27, 214 [1.1.5](#)
- Grun, J., Stamper, J., Manka, C., Resnick, J., & Burris, R. 1991, *Phys. Rev. Lett.*, 66, 2738 [A.1](#)
- Gudiksen, B. V. 2004, PhD thesis, Stockholm University [1.1.5](#)
- Gudiksen, B. V. & Nordlund, Å. 2002, *ApJ*, 572, L113 [1.1.5](#), [5.1.1](#), [5.4](#), [10](#)
- Hale, G. E. 1908a, *ApJ*, 28, 100 [1.1.2](#)
- Hale, G. E. 1908b, *ApJ*, 28, 315 [1.1.2](#)
- Hale, G. E. & Nicholson, S. B. 1938, *Magnetic observations of sunspots, 1917-1924 (Carnegie Institution of Washington, Washington, D.C.)* [1.1.2](#)
- Hammer, R. 1982, *ApJ*, 259, 767 [8.4](#)

- Hammer, R. 1985, in *The Origin of Nonradiative Heating/Momentum in Hot Stars*, ed. A. Underhill (NASA-CP 2358), 125–129 [8.4](#)
- Hansteen, V. 1993, *ApJ*, 402, 741 [2](#), [4.1](#)
- Hansteen, V. H. & Leer, E. 1995, *J. Geophys. Res.*, 100, 21577 [4.2](#)
- Hawley, J. F., Smarr, L. L., & Wilson, J. R. 1984, *ApJS*, 55, 211 [2.4](#), [2.5](#)
- Hearn, A. G., Kuin, N. P. M., & Martens, P. C. H. 1983, *A&A*, 125, 69 [5.2](#), [8.4](#)
- Hearn, A. G. & Vardavas, I. M. 1981, *A&A*, 98, 230 [8.4](#)
- Hoffmeister, C. 1943, *Z. Astrophys.*, 22, 265 [1.1.6](#)
- Honerkamp, J. 1994, *Stochastic Dynamical Systems : Concepts, Numerical Methods, Data Analysis* (VCH, Weinheim) [7](#)
- Hood, A. W. & Priest, E. R. 1980, *A&A*, 87, 126 [1.3](#)
- Janev, R. K., Langer, W. D., & Evans, K. 1987, *Elementary Processes in Hydrogen-Helium Plasmas – Cross Sections and Reaction Rate Coefficients* (Springer Series on Atoms and Plasmas, Springer, Berlin) [3.2.4](#)
- Judge, P. G. & Meisner, R. 1994, in *The Third SOHO Workshop, Solar Dynamic Phenomena and Solar Wind Consequences*, ed. J. J. Hunt (ESA SP-373, ESTEC, Noordwijk) [3.2.4](#)
- Karpen, J. T., Antiochos, S. K., Hohensee, M., Klimchuk, J. A., & MacNeice, P. J. 2001, *ApJ*, 553, L85 [4.1](#), [5.2](#)
- Kjeldseth-Moe, O. & Brekke, P. 1998, *Sol. Phys.*, 182, 73 [1.2.2](#), [5.1](#)
- Korevaar, P. 1989, PhD thesis, Utrecht University [2](#)
- Korevaar, P. & Hearn, A. G. 1989, *A&A*, 224, 141 [5.2](#), [8.4](#)
- Korevaar, P. & van Leer, B. 1988, *A&A*, 200, 153 [2.6](#)
- Kuin, N. P. M. & Martens, P. C. H. 1982, *A&A*, 108, L1 [1.3](#), [4.3.5](#), [5.2](#), [7](#), [7](#), [1](#), [7.1](#), [7](#)
- Kuin, N. P. M. & Poland, A. I. 1991, *ApJ*, 370, 763 [2.1](#)
- Laming, J. M. & Grun, J. 2002, *Phys. Rev. Lett.*, 89, 125002 [A.1](#)
- Laming, J. M. & Grun, J. 2003, *Physics of Plasmas*, 10, 1614 [A.1](#)
- Levine, R. H. & Withbroe, G. L. 1977, *Sol. Phys.*, 51, 83 [1.2.2](#), [5.1](#)
- Mackay, D. H. & Galsgaard, K. 2001, *Sol. Phys.*, 198, 289 [5.3.5](#), [6.2.2](#)
- Mariska, J. T. 1992, *The Solar Transition Region* (Cambridge Astrophysics Series, Cambridge University Press, New York) [3](#), [3.1.1](#), [3.1](#), [3.2](#), [4.1](#)

- McClymont, A. N. & Craig, I. J. D. 1985a, *ApJ*, 289, 820 7
- McClymont, A. N. & Craig, I. J. D. 1985b, *ApJ*, 289, 834 7
- Mok, Y., Drake, J. F., Schnack, D. D., & van Hoven, G. 1990, *ApJ*, 359, 228 5.4
- Müller, D. A. N., Hansteen, V. H., & Peter, H. 2003, *A&A*, 411, 605 5.1, 5.2, 6.1
- Müller, D. A. N., Peter, H., & Hansteen, V. H. 2004, *A&A*, 424, 289 6.1
- Owczarek, J. A. 1964, *Fundamentals of Gas Dynamics* (International Textbook Co., Scranton, Pennsylvania) 2.7
- Parker, E. N. 1988, *ApJ*, 330, 474 1.1.5
- Parker, E. N. 1991, in *Proc. Miniworkshop on Physical Processes in the Solar Transition Region*, ed. P. Maltby & E. Leer (Inst. Theor. Astrophys., Oslo), 63 1.1.5
- Peter, H. 2000, *A&A*, 360, 761 1.1.4, 4.1
- Peter, H. 2001, *A&A*, 374, 1108 1.1.4, 1.6
- Peter, H., Gudiksen, B. V., & Nordlund, Å. 2005, *ApJ*, in press 10
- Peter, H. & Judge, P. G. 1999, *ApJ*, 522, 1148 4.1
- Reeves, E. M. 1976, *Sol. Phys.*, 46, 53 1.1.4
- Rosner, R., Tucker, W. H., & Vaiana, G. S. 1978, *ApJ*, 220, 643 1.2.3, 4.1, 8.5
- Scheiner, C. 1611, *Rosa Ursina* (Bracciano) 1.1.2
- Schrijver, C. J. 2001, *Sol. Phys.*, 198, 325 1.2.2, 1.3, 4.4, 5.1, 5.3.5, 5.4, 5.4, 6.2.1
- Serio, S., Peres, G., Vaiana, G. S., Golub, L., & Rosner, R. 1981, *ApJ*, 243, 288 1.2.3, 4.2, 5.1.1
- Shull, J. M. & van Steenberg, M. 1982, *ApJS*, 48, 95 3.2.4
- Smith, M. D. & Rosen, A. 2003, *MNRAS*, 339, 133 A.1
- Souffrin, P. 1982, *A&A*, 109, 205 8.4
- Spadaro, D., Lanzafame, A. C., Consoli, L., et al. 2000, *A&A*, 359, 716 4.4
- Spitzer, L. 1962, *Physics of Fully Ionized Gases* (Interscience, New York (2nd edition)) 2.1
- Stix, M. 2002, *The sun: An Introduction* (Springer, Berlin) 1, 1.2.1
- Tziotziou, K., Martens, P. C. H., & Hearn, A. G. 1998, *A&A*, 340, 203 8.4
- Van Leer, B. 1974, *J. Comp. Phys.*, 14, 361 2.4, 2.9
- Vernazza, J. E., Avrett, E. H., & Loeser, R. 1981, *ApJS*, 45, 635 1.1.4, 1.4, 4.3.1

von Neumann, J. & Richtmyer, R. D. 1950, *J. Appl. Phys.*, 21, 232 [2.1](#)

Wilson, J. R. 1978, in *Sources of Gravitational Radiation*, ed. L. Smarr (Cambridge University Press, Cambridge), 423 [2.4](#)

Winkler, K.-H. A., Norman, M. L., & Mihalas, D. 1984, *J. Quant. Spectrosc. Radiat. Transfer*, 31, 473 [2.7](#), [2.7](#)

Withbroe, G. L. & Noyes, R. W. 1977, *ARA&A*, 15, 363 [8.1](#)

Young, C. A. 1895, *The Sun* (D. Appleton and Company, New York) [1.8](#)

Abbreviations of Journal Names

Abbreviation	Full Journal Name
Adv. Space Res.	Advances in Space Research
A&A	Astronomy and Astrophysics
A&AS	Astronomy and Astrophysics Supplement Series
ApJ	Astrophysical Journal
ApJS	Astrophysical Journal Supplement Series
ARA&A	Annual Review of Astronomy and Astrophysics
Arkiv. f. Mat. Astron. Fysik	Arkiv för Matematik, Astronomi och Fysik
J. Appl. Phys.	Journal of Applied Physics
J. Comp. Phys.	Journal of Computational Physics
J. Geophys. Res.	Journal of Geophysical Research
J. Quant. Spectrosc. Radiat. Transfer	Journal of Quantitative Spectroscopy and Radiative Transfer
Math. Ann.	Mathematische Annalen
MNRAS	Monthly Notices of the Royal Astronomical Society
Phys. Rev. Lett.	Physical Review Letters
Sol. Phys.	Solar Physics
Space Sci. Rev.	Space Science Reviews
Vierteljahresschrift der Astron. Ges.	Vierteljahresschrift der Astronomischen Gesellschaft
Z. Astrophys.	Zeitschrift für Astrophysik

Acknowledgments

My sincerest thanks go to my two advisors, PD Dr. Hardi Peter at the Kiepenheuer-Institut für Sonnenphysik in Freiburg and Prof. Dr. Viggo Hansteen at the Institute of Theoretical Astrophysics in Oslo. It has been both a pleasure and a challenge to work with them. Hardi's vast supply of new ideas and constructive comments was always helpful and initiated new thoughts and experiments. I appreciated the freedom I had been given in defining my work, knowing that I could ask for his advice at any time. He provided me with all the support I needed and established the cooperation with Viggo in Oslo. On the other hand, I am especially indebted to Viggo for passing on his decadal experience in numerical modeling and for letting me work with his numerical code which set the base for this work. He also provided me with the unique opportunity of carrying out the second half of this work at the University of Oslo in the framework of the European Research Training Network "Turbulence in Space Plasmas".

At the Kiepenheuer-Institut, I would like to thank Prof. Dr. Michael Stix for his support and interest in my work and for being the official supervisor in its early stage, Dr. Rolf Schlichenmaier for being a great running companion, Dr. Wolfgang Dobler for knowing answers to (not only) computer-related questions most people do not even dare to ask, Dr. Reiner Hammer for stimulating discussions about coronal physics, for bringing up the idea of overheated loops and for serving as an internal referee, the extended "Spielzimmer" for enjoyable coffee breaks and entertainment, Dr. Peter Caligari for keeping the computers running and Prof. Dr. Oskar von der Lühe for raising my interest in solar physics as an undergraduate student.

At the Institute of Theoretical Astrophysics, my thanks go to Prof. Dr. Mats Carlsson for generous support and advice, to Prof. Dr. Egil Leer, Dr. Øivind Wikstøl and Dr. Eirik Endeve for showing me what Norwegian winter really is about, Dr. Luc Rouppe van der Voort for being a great office mate, the "kaffeklubben" for redefining the coffee experience, Terje Fredvik for teaching me about CDS observations, Dr. Boris Gudiksen for proof-reading a part of this work and all the friends and colleagues at KIS and ITA for making work at these two institutes so enjoyable.

Furthermore, I would like to thank Dr. Jim Klimchuk, Dr. Spiro Antiochos and Dr. Judy Karpen at the Naval Research Lab in Washington, D.C., for their hospitality and enlightening discussions during my visit and Dr. Bernhard Fleck at the NASA Goddard Space Flight Center for supporting my participation in the CDS observing campaign.

My sincere thanks go to all my friends who made sure that life was always much more than just science. To mention only a few, I could always count on Ralf Haug, Sadik Hafizović, Corinna Unger, Anna Kathinka Dalland Evans, Terje Fredvik, Rikke Gåsholt and Paola Testa, wherever on this planet any one of them happened to be. Very special thanks go to Dorothea von Trotha for everything we have been sharing. I especially would like to express my gratitude to my parents and my sister for their steady support and encouragement. Wherever life has taken me, they were always there.

The financial support of the European Commission, the German Research Council (*Deutsche Forschungsgemeinschaft*), the Kiepenheuer-Institut für Sonnenphysik, the Institute of Theoretical Astrophysics, and the scholarship of the German National Merit Foundation (*Studienstiftung des deutschen Volkes*) are greatly acknowledged.

Curriculum Vitae

Daniel Müller

*28.07.1976 in Göttingen/Germany

Education

- 05/2002 – 10/2004 : Binational Ph. D. thesis in physics, Kiepenheuer Institute for Solar Physics, Freiburg/Germany, and Institute of Theoretical Astrophysics, Oslo/Norway
- 08/2000 – 08/2001 : Diploma thesis, Kiepenheuer Institute for Solar Physics, Freiburg/Germany, Title: *Polarization of lines in the spectrum of a sunspot penumbra*
- 06/1999 – 11/2001 : Diploma studies in physics (Hauptstudium), Albert-Ludwigs-Universität Freiburg/Germany
- 08/1998 – 05/1999 : Graduate studies in physics, University of Texas at Austin/USA
- 10/1996 – 07/1998 : Diploma studies in physics (Grundstudium), Albert-Ludwigs-Universität Freiburg/Germany
- 08/1989 – 05/1996 : Christian-von-Dohm-Gymnasium (High School), Goslar/Germany

Professional Affiliations

- 09/2004 – : Member of the Centre of Mathematics for Applications, University of Oslo/Norway
- 01/2004 – : Scientist, Institute of Theoretical Astrophysics, Oslo/Norway
- 11/2001 – 12/2003 : Scientist, Kiepenheuer Institute for Solar Physics, Freiburg/Germany
- 11/2001 – 12/2001 : Visiting Scientist, Institute of Theoretical Astrophysics, Oslo/Norway
- 06/1999 – 11/2001 : Research Assistant, Kiepenheuer Institute for Solar Physics, Freiburg/Germany
- 08/1999 – 12/1999 : Research Assistant, Ultracold Atomic Physics Group, University of Texas at Austin/USA

Awards & Grants

- 01/2004 – : Fellowship of the European Research Training Network “Turbulence in Space Plasmas”
- 10/2002 – : Ph. D. scholarship of the German National Merit Foundation (Studienstiftung des deutschen Volkes)
- 07/2002 – : Research grant of the German Research Council (Deutsche Forschungsgemeinschaft)
- 1998 – 1999 : University Honor List, University of Texas at Austin/USA
- 1998 – 1999 : Graduate scholarship of the University of Texas at Austin/USA
- 1996 – 2002 : Scholarship of the German National Merit Foundation